# Fingerprinting Source Fluids of Iron Oxide-Copper-Gold and Iron Oxide-Apatite Deposits Using Traditional and Non-Traditional Stable Isotope Geochemistry

**by**

**Tristan Morgan Childress**

A dissertation submitted in partial fulfillment
of the requirements for the degree of
Doctor of Philosophy
(Earth and Environmental Sciences)
in the University of Michigan
2019

Doctoral Committee:

Professor Adam Charles Simon, Chair
Research Professor Jeffery Alt
Associate Professor Rebecca D. Hardin
Professor Emeritus Stephen Kesler
Professor Kyger Lohmann

If you awaken from this illusion and you understand that black implies white, self implies other, life implies death (or shall I say, death implies life), you can feel yourself – not as a stranger in the world, not as something here on probation, not as something that has arrived here by fluke - but you can begin to feel your own existence as absolutely fundamental.

– Alan Watts, “The Dream of Life”

Tristan Morgan Childress

tristanc@umich.edu

ORCID iD: 0000-0002-2827-9379

## DEDICATION

This work is dedicated to my family who has supported me throughout my academic career and dealt with the long distance with love and grace. To my mother, Sharon, who has encouraged me to reach higher and think outside the boundaries of convention. To my father, Tony, who taught me to love and respect the outdoors. To my sister, Tiffany, a true role model of someone who can not only raise a wonderful family, but also build a successful career simultaneously. To her husband and sons, Mark, Brandt, and Fischer, who lift my spirits whenever I'm home. Finally, to my late grandparents, Colene and Eugene Morgan and Arnette Childress, who taught me the virtues of hard honest work, and who I miss every day.

## ACKNOWLEDGEMENTS

First off, I must thank my dissertation committee, Drs. Kacey Lohmann, Steve Kesler, Jeffrey Alt, and Rebecca Hardin, for all of their time, comments, encouragement, and discussion over the past few years, which made my thesis all the stronger and more enjoyable to read. I must sincerely thank my advisor, Dr. Adam Simon, who took a chance bringing me to the University of Michigan and encouraged me through all of my hard work that has helped me become the geologist I am today.

Without the incredible assistance of Drs. Ilya Bindeman and Jim Palandri at the University of Oregon and Dr. Craig Lundstrom and Zhenhao Zhou at the University of Illinois Urbana-Champaign I would have never managed such quality isotopic data in such efficient time. Ilya and Jim are an oxygen isotope powerhouse (seriously, I'm jealous of their setup) and ran so many samples for my research I have lost count. I must especially thank Craig, who managed to not only assist me in my Fe isotope analyses, teaching me how to run the instrument, but also managed to deal with all the technical headaches I caused, and for that I am very grateful. These gentleman taught me invaluable lessons regarding isotopes as well as mass spectrometry.

This research has taken me to Chile several times over the years, a beautiful country with lovely people, bursting with culture. While there I met many great geologists, namely my coauthors Drs. Martin Reich and Fernando Barra. Their knowledge of Chilean geology and the

iron oxide deposits is incredible, and spending even a few days with them was worth more than any short course. During that time I met many of their students who became great friends during our time in the Atacama, and who I am certain will go on to become great geologists like their advisors.

While working in the office here at the University of Michigan, I met many great professors and researchers with whom I could chat about science or life. Dr. Aaron Wolf hosted the MRM group that encouraged us to "think deeper" and more critically about what is happening in the earth's mantle and core (as well as what's going on in outer space), and how that relates to my own research in the Earth's crust. Dr. Jamie Gleeson has been a great next door friend who was always up for a beer and chat and is always in good spirits. Drs. Nathan Niemi and Ben van der Pluijm provided a much needed insight into tectonics and mapping, and great laughs along the way.

The camaraderie within our department has always been impressive. Beginning in the first year office I became great friends with now Dr. Brian Konecke who I also lived with during my first year (and probably had too many beers with). I could always destress with my cohort at the bar after a hard day's work. I will always remember the long talks Brian, Laura Motta, and I had about rocks, spiritualism, and aliens (we are the "crazy" ones). A big thanks goes out to all of the students here now and in the past that have helped me both academically and mentally over the years.

The Simon lab group has been a cornerstone in my academic career, and always will be. Dr. Laura Bilenker was an amazing mentor and very close friend who taught me everything I needed to know about iron isotopes when I first arrived here, and helped me through some of the harder mental challenges of being a PhD student through the years, for which I will always be

grateful. Drs. Liz Tannis, Jaayke Knipping, Adrian Fiege, and Tom Hudgins were great mentors and always great for a laugh. Nikita la Cruz, official member of the "El Simon Dream Team" along with Brian and I, has been an incredible officemate, roommate, and friend. Thank you for putting up with Ravi "singing" in the night and playing hide and seek in your bedroom. Honorary lab cousin and cat-god parent Xiaofei Pu has taken great care of my cats Ravi and Norah while I was away at Red Dog Mine during the summers, and we are eternally grateful for you. Daniel Korfeh and Gephen Sadove were the best office mates I could have asked for, and Daniel in particular always pushed me to ask "Why!? Why is there so much titanium in magnetite??" I have no doubt that our newest lab members, Maria AR Mustafa and Jackie Wrage, will live up to the excellence in this lab group and excel in their studies.

I would never have made it this far in my career without the initial guidance and friendship of Dr. Kerry McCarney-Castle, who was head of the research project I worked on at the South Carolina Geological Survey prior to beginning at the University of Michigan. She can lay claim to my original geological role model. And a special thanks goes out to all of the great people I worked with during the summers at Red Dog Mine, who helped me take a step back from my research to understand the bigger picture of how geology fits into society on a grander scale.

The past several years of research has introduced me to so many wonderful and intelligent people, all of whom I am not able to mention here, but to all of whom I am sincerely grateful and appreciative.

## TABLE OF CONTENTS

## LIST OF TABLES

### CHAPTER II



### CHAPTER III



### CHAPTER IV



### APPENDIX

## LIST OF FIGURES

### CHAPTER II



### CHAPTER III

**CHAPTER IV**

## ABSTRACT

Iron oxide deposits have provided important amounts of metal to society since the dawn of the Iron Age. In 2017 alone, they supplied 2.4Gt of raw iron ore globally, in addition to other valuable elements (e.g. Au, Ag, Cu, and Co). In order to meet industry's growing resource demand, it is imperative to test and refine current genetic models that explain the occurrence of these deposits. On the basis of their elemental contents, iron oxide deposits are divided into two distinct groups: the iron oxide–copper–gold (IOCG) and iron oxide–apatite (IOA) deposits. Nearly a century of geological research has produced several working models to explain how they formed, but agreement is lacking. Two predominant models invoke magnetite mineralization either directly from a magma or from hydrothermal fluids, where the occurrence of both types requires multiple fluid sources. Additionally, previous studies have hypothesized IOAs may form the deeper roots of some IOCG deposits, citing similarities among ore related minerals and the occurrence of both deposit types both spatially and temporally, and have proposed an IOA-IOCG continuum model. If we are to explore for more deposits of these types, it is imperative to test and refine these models, which is the objective of this thesis research. After a brief introductory chapter, Chapter II deals with models for the Proterozoic Pea Ridge and Pilot Knob IOA deposits of Missouri, USA. Stable Fe and O isotopes and trace elements in the ore forming magnetite from these deposits indicate a silicate magma source for the magnetite ore bodies and at least three generations of magnetite. Two generations grew from a hydrothermal fluid, while one high-Ti variety crystallized from a magma. These observations

suggest a new genetic model that incorporates the occurrence of both hydrothermal and magmatic magnetite via magnetite microlite flotation where orthomagmatic magnetite may be enveloped by a buoyant Fe-rich fluid within a magma that further precipitates hydrothermal magnetite. This new model demonstrates that both magmatic and hydrothermal magnetite may originate from a single source. Chapter III focuses on the Jurassic Mantoverde IOCG deposit in Chile. It compares Fe and O isotopes and trace element contents of Mantoverde magnetite and hematite to the same minerals in the neighboring Los Colorados IOA deposits. The isotopes and trace elements indicate that both early magnetite and late hematite were sourced from a silicate magma. Similar isotopic signatures and cooling trends in trace element concentrations at Los Colorados support the previously proposed IOA-IOCG continuum hypothesis. In Chapter IV, triple O, H, and Fe isotopes were analyzed in the ore forming iron oxides of the enigmatic near-surface El Laco IOA deposits of Chile. This combination of isotopic measurements reveal that magnetite was sourced from a silicate magma and, when interpreted in combination with drill core data, indicate magnetite in these deposits formed from an evolving magmatic fluid that crystallized orthomagmatic and hydrothermal magnetite. Significantly, this supports the magnetite microlite flotation model that is compatible with all of these observations. This research effectively rules out other genetic models, and links IOAs and IOCGs in a continuum model. Future refinement of these models is key to better understanding of the petrologic and hydrothermal processes that form these important deposits, as well as to bolster exploration strategies for the IOAs and IOCGs.

# CHAPTER I

# INTRODUCTION

## IRON OXIDE DEPOSITS

Iron oxide deposits are broadly defined as bodies of rock containing > 10% low-Ti iron oxides such as magnetite and hematite, where individual deposits may contain millions to billions of tons of iron ore. These deposits are differentiated based on their unique elemental contents. They often contain economically significant concentrations of Cu, Au, REE, P, U, Ag, and Co. Ages of these deposits range from the Archean through the Cenozoic, are often stratigraphically or structurally controlled, and are temporally and spatially associated with intense and voluminous Na-Ca-K metasomatism. In contrast, these iron oxide deposits generally lack well defined tectonic and igneous correlations, which has led to a disparity in genetic models (Barton, 2014).

Iron oxide deposits are primarily divided into their Cu- and Au-rich and Cu- and Au-poor, P-rich endmembers - the iron oxide–copper–gold (IOCG) and iron oxide–apatite (IOA) deposits (both with their own subdivisions). Several models have been proposed to explain the origin of IOCGs and IOAs: 1) the magmatic-hydrothermal model, where a metal bearing fluid evolved from a silicate magma may transport and deposit metals (e.g., Pollard, 2006; Nyström et al., 2008; Rieger et al., 2010, 2012; Jonsson et al., 2013); 2) the non-magmatic hydrothermal

model, where metal scavenging meteoric fluids or basinal brines derived from evaporites circulate through the crust, accumulate metals, and later deposit them (e.g., Barton and Johnson, 1996; Sillitoe and Burrows, 2002; Benavides et al., 2007); 3) the metamorphic hydrothermal model, where fluids are derived from metamorphic devolatilization of continental crust which then scavenge metals from host rocks and redeposit them (e.g. Fisher and Kendrick, 2008); 4) the immiscible Fe-rich melt model, where a volatile- and Fe-rich melt separates from an initially Fe-rich silicate melt and is later emplaced in the crust (Nyström and Henríquez, 1994; Travvisany et al., 1995; Naslund et al., 2002; Barton, 2014); and 5) the magmatic magnetite flotation model, where a silicate magma grows magnetite crystals which are then wetted by exsolving Fe-rich fluids, lowering their overall density and floating them upward in a magma where they may be erupted into the overlying crust (e.g. Knipping et al., 2015a,b; Ovalle et al., 2018; Simon et al, 2018). The hydrothermal fluid models (1, 2, and 3) require a heat source (an underlying magma or the crustal geothermal gradient) to transport or circulate fluids, whereas all models incorporate previously existing geologic structures in order to deposit their metal contents, either by direct precipitation from an Fe-rich fluid or metasomatic replacement of host rocks.

Iron oxide deposits have been exploited by humanity dating back as early 43,000 years to the Lion Cave in Swaziland, South Africa (Dart and Beaumont, 1971), where humans mined hematite to be used as red pigments for decoration. The earliest known iron artifacts, small decorative iron beads mined and refined from meteorite iron, were uncovered from burial graves in northern Egypt circa 3200 B.C.E (Rehren et al., 2013). The onset of widespread ironworking has thrust humanity into ongoing and unwavering technological advance. Undoubtedly, iron is and has been a major factor in the success of humanity, bringing humankind out of the Bronze Age and into the Iron Age by 1200 B.C.E. For most contemporary humans, iron has become the

foundation of society, forming the structural skeletons of skyscrapers, the bodies and engines of automobiles, and a primary component of everyday objects in our offices and households. Humanity's constant and growing demand for development comes with an inherent demand for resources. The United States Geological Survey reports a global production (and consumption) of 2.4 billion metric tons of iron ore for 2017 (USGS, 2018), roughly a volume of $1km^3$. In addition, with the onset of consumer electronics and computing-based technology, elements such as Au, Ag, Cu, Co, and the rare earths are being consumed at higher and higher rates. This presents the difficult question: How will humanity continue to meet rapidly increasing resource metal demand for the foreseeable future? Geologists must continuously refine their knowledge and understanding of the geologic processes which concentrate metals in the earth's crust. In this dissertation, I test competing geological models of iron oxide deposit formation by applying traditional and non-traditional stable isotopic systems to and analyze trace element abundances in magnetite and hematite in several iron oxide deposits that exist in a range of geologic settings and geologic time.

## IRON OXIDE CHEMISTRY

Magnetite ($Fe^{2+}Fe_3{}^{+2}O_4$) is the primary iron ore mineral in IOA deposits, whereas magnetite and hematite ($Fe^{3+}{}_2O_3$) are typically found in IOCG deposits. Magnetite exhibits an inverse spinel crystalline structure where ferric iron occupies the tetrahedral coordination site and ferric ($Fe^{3+}$) and ferrous ($Fe^{2+}$) occupy the octahedral sites. A wide variety of cation substitute in each of these sites due to similar ionic radii. Primarily Mg, Mn, Zn, and Ni substitute for ferric iron, and Al, V, and Cr substitute for ferrous iron. Titanium occurs in magnetite via coupled substitution of $Fe^{2+}$ in the tetrahedral sites and $Ti^{4+}$ for $Fe^{3+}$ in the octahedral sites. Titanium can occur as a continuous solid solution between magnetite and

ulvöspinel ($Fe^{2+}{}_2Ti^{4+}O_4$) above 600 ℃, and will typically exsolve as ilmenite at lower temperatures ($Fe^{2+}Ti^{4+}O_3$). Trace element substitution is highly dependent on temperature and oxygen fugacity, and will occur in greater amounts at higher temperature and lower oxygen fugacity (Nadoll et al., 2014). This observation makes magnetite (and its oxidation product, hematite) a powerful tool when deciphering its original mineralizing conditions.

Until recently, magnetite and hematite have traditionally only been examined for their stable O isotopes. Delta notation of isotopic systems is defined as:

$$\delta^{a}X_{sample}\ (‰) = [({}^{a}X/{}^{b}X)_{measured} / ({}^{a}X/{}^{b}X)_{standard} - 1] * 1000 \qquad (1)$$

where *X* is the element of interest, *a* is typically the more abundant isotope of *X*, and *b* is the less abundant isotope. This delta notation provides a ratio of the isotopic content of a sample in question and a well-known standard material, normalized to values of permil (‰). When applied to magnetite and hematite and compared to other natural samples, ratios of $^{18}O$ and $^{16}O$ (represented by $\delta^{18}O$ notation) can provide geologic information such as the source of O, the degree of post-depositional mineral alteration, and even the temperature at which the iron oxide crystallized (e.g. magnetite-diopside isotope thermometer; Matthews et al., 1983). Indeed, O isotopes have been well studied in ore forming systems (Taylor 1974), and have been the basis of many studies and conclusions of the iron oxides in IOA and IOCG deposits. However, O isotopes are easily altered from their original ratios by secondary hydrothermal fluids (ubiquitous in IOA and IOCG ore forming systems), obscuring or completely obliterating the original isotopic signatures of their minerals.

More recent studies have found "non-traditional" Fe stable isotopes to be particularly useful when applied to iron oxide systems, thanks to a rapidly growing database of natural

samples, experiments, and first principles modeled data (Dauphas et al., 2017 and references therein). Ratios of $^{54}Fe$ and $^{56}Fe$ (represented by $\delta^{56}Fe$ notation) isotope abundances in iron oxide minerals are more resistant to secondary alteration than are the abundances of H and O (Frost et al., 2007, Weis, 2013, Bilenker et al., 2016, Childress et al., 2016, 2019), and will only significantly deviate from their original signature (to lighter values) via extensive coupled dissolution and reprecipitation reactions with hydrothermal fluids, as has been reported for the Mineville IOA deposit (Bilenker et al., 2016) and the Dannemora (Sweden) and Chagangnuoer (China) Fe-skarn-type deposits (Weis, 2013; Günther et al., 2017). Using the paired Fe–O stable isotope systems for individual samples of iron oxides allows for clearer interpretation of the source fluids, style of deposition, and subsequent degree of alteration, where Fe isotopes may provide a clearer signature of the initial source fluids, and O isotopes may reveal secondary processes affecting the iron oxides.

Additionally, ratios of H stable isotopes $H^1$ and $H^2$ (represented by either $\delta^2H$ or $\delta D$ notation) can be used to further support interpretations based on the Fe–O stable isotope systems. Minerals will typically incorporate fluid inclusions as they grow, which provide geochemical information regarding the fluids which precipitated those minerals. Analyzing fluid inclusions in iron oxides and the hydrous iron oxide goethite for their $\delta^2H$ ratios will provide further information regarding the source of fluids, potential mass-dependent fractionation processes during mineral precipitation, and degree of alteration (Taylor, 1974).

## TESTING IOA AND IOCG MODELS

The models described above involve distinct geologic processes, metal and fluid sources, and each model will ultimately result in a unique geochemical signature, both in the isotopes and the trace elements contained within the ore-forming minerals, primarily magnetite and hematite.

Iron oxides formed via high-temperature (>500 ℃) hydrothermal processes are expected to incorporate greater amounts of mobile trace elements (Si, Al, Mn, Ca) as mineral inclusions or within the iron oxide crystalline structure, as opposed to iron oxides formed at low temperatures (<500 ℃) (Dupuis and Beaudoin, 2011; Nadoll et al., 2014). Similarly, magnetite formed from magmas will incorporate greater amounts of the relatively hydrothermal fluid-incompatible trace elements Ti and V into their crystalline structure, as opposed to hydrothermally derived magnetite that tends to contain very low Ti and V contents (Dare et al., 2014). Isotopic ratios in magnetite are primarily dependent on their source reservoir as well as the temperature of mineral formation. Magmatically derived magnetite tends to exhibit a well-defined narrow range of heavy values of $\delta^{56}Fe$ and $\delta^{18}O$ (and relatively heavy $\delta^{2}H$) in comparison to meteoric sources which typically exhibit much lighter values (Taylor, 1974; Bindeman, 2008; Weis, 2013; Bilenker et al., 2016), and magnetite formed as a result of immiscible Fe-rich melts will exhibit isotopic ratios similar to that of their parental silicate melt (Lester et al., 2013). If there are multiple generations of iron oxides, this will be evident in their unique textures, isotopic ratios, and trace element abundances (e.g. Knipping et al., 2015).

## APPLICATION OF FE, O, AND H ISOTOPIC SYSTEMS AND TRACE ELEMENT ANALYSIS TO IOA AND IOCG DEPOSITS

I apply traditional O and H, non-traditional Fe isotopes and analyze trace elements to geochemically characterize the ore-forming iron oxides of four geologically and temporally distinct iron oxide ore deposits: The Proterozoic Pea Ridge and Pilot Knob IOA deposits of Missouri, USA, and the Jurassic Mantoverde manto-type IOCG and the Plio-Pleistocene El Laco IOA deposits of northern Chile. Historically, when attempting to decipher the timing of mineralization events and mineral/mineralizing fluid provenance(s) of IOA deposits, researchers

have overwhelmingly focused on gangue minerals associated with main-stage iron oxide deposition. However, these minerals effectively only act as proxies when trying to understand the formation conditions of the iron oxide minerals. In this dissertation, I geochemically characterize the most modally abundant, ore-forming minerals magnetite and hematite to directly characterize the ore forming fluids.

**Chapter II** examines magnetite from the Mesoproterozoic Pea Ridge and Pilot Knob deposits of Missouri, USA, hosted in rhyolitic tuffs and coeval granites. The Pea Ridge orebody displays porphyritic textures, with magnetite phenocrysts occurring in a fine-grained magnetite matrix (Emery, 1968; Nuelle et al., 1992). The Pilot Knob deposit contains large zoned magnetite and hematite crystals and zones of fine-grained magnetite in contact with host rocks. Magnetite analyzed in this study from both deposits exhibits magmatically derived isotopic signatures in both deposits, and revealed three textural generations of magnetite range with $TiO_2$ contents that range from 0.06 to 15.93 wt % at Pea Ridge. This combination of magmatic $\delta^{18}O$ and $\delta^{56}Fe$ stable isotope ratios and the observation of three distinct magnetite generations that range from magmatic-hydrothermal to orthomagmatic in regards to their Ti contents indicate a combination of magmatic and magmatic-hydrothermal processes. This chapter is published in *Economic Geology*, **111**, 2033-2044.

**Chapter III** examines early-stage magnetite and late-stage hematite from the Jurassic manto-type Mantoverde IOCG deposit of Chile. This is the first application of the paired $\delta^{56}Fe$-$\delta^{18}O$ isotopic systems to IOCG deposits. Within the Andean Cretaceous IOCG province, many IOCG deposits are spatially and temporally associated with IOA deposits, and it has been suggested that IOCG and IOA mineralization form a continuum, where magmatic fluids deposit S- and metal-poor minerals at depth (IOA) and continue upwards in the crust to deposit S- and

metal-rich minerals at surface (IOCG) (Benavides et al., 2007; Barra et al., 2017; Simon et al., 2018). The paired $\delta^{56}Fe$–$\delta^{18}O$ data indicate a magmatic source for both magnetite and hematite (i.e. early and late stage mineralization). The trace element and isotopic data from both magnetite and hematite reveal iron oxide grew from a cooling magmatic fluid. The sum of Fe and O isotopic data and trace element data is largely in agreement with the IOA-IOCG continuum hypothesis. This chapter was accepted pending revisions to the journal *Mineralium Deposita*, and is expected to be published in early 2019.

In **Chapter IV** I apply the Fe, triple O, and H stable isotopic systems to the iron oxides of the Plio-Pleistocene El Laco IOA orebodies of Chile. Previous works have only applied O stable isotopes to these deposits. El Laco is a unique IOA deposit due to the fact that the orebodies apparently formed at and near the surface of the crust, resulting in what appears texturally similar to basalt flows (Park, 1961). To test the often suggested hydrothermal replacement (Rhodes and Oreskes, 1999; Sillitoe and Burrows, 2002; Dare et al., 2015) and immiscible Fe-rich melt formation (Naslund et al., 2002; Velasco et al., 2016; Tornos et al., 2016, 2017) models we analyze bulk iron oxides of primarily magnetite with minor hematite and goethite. In this study, isotopic analyses reveal unequivocal magmatic signatures in magnetite with minor meteoric alteration to hematite and goethite. The sum of this data in combination with historical data from El Laco disallow for both the non-magmatic-hydrothermal and immiscible Fe-rich models to explain the iron oxide deposits at El Laco, and are most easily explained by a combination of magnetite precipitation from a combination of magmatic and magmatic-hydrothermal processes (Ovalle et al., 2018). This study will be submitted to *Economic Geology* for publication in 2019.

The research presented in this dissertation effectively tests five competing genetic models proposed for the Pea Ridge and Pilot Knob IOA deposits of Missouri, USA, and the Mantoverde

IOCG and El Laco IOA deposits of Chile using a relatively simple and affordable approach. By applying the paired Fe–O isotopic systems to the iron oxides, researchers and exploration geologists can determine which of the five major models best fit their deposits, and can readily determine whether or not the iron oxides were derived from magmatic or non-magmatic sources. Combining stable isotope analyses with textural and trace element analyses of the same samples will allow for further contextualization of the temperatures at which those iron oxide samples formed, the degree of alteration, and where those samples may exist within a modeled IOA or IOCG system. The paired Fe–O isotopic system can be an effective addition to the exploration geologist's toolbox, aiding to build time and cost efficient exploration strategies.

## REFERENCES


Barra F, Reich M, Rojas P, Selby D, Simon AC, Salazar E, Palma G (2017) Unraveling the origin of the Andean IOCG Clan: A Re-Os Isotope Approach. Ore Geology Reviews, 81:62–78.

Barton MD (2014) Iron oxide (–Cu–Au–REE–P–Ag–U–Co) systems, in Scott SD, ed., Geochemistry of mineral deposits. Amsterdam, Elsevier, Treatise on Geochemistry, 2nd ed., 13:515–541

Barton MD, Johnson DA (1996) Evaporitic-source model for igneous-related Fe oxide-(REE-Cu-Au-U) mineralization. Geology, 26:259–262.

Benavides J, Kyser TK, Clark AH, Oates CJ, Zamora R, Tarnovschi R, Castillo B (2007) The Mantoverde iron oxide-copper-gold district, III Región, Chile: the role of regionally derived, non-magmatic fluids in chalcopyrite mineralization. Economic Geology, 102:415–440.

Bilenker LD, Simon AC, Reich M, Lundstrom CC, Gajos N, Bindeman I, Barra R, Munizaga R (2016) Fe-O stable isotope pairs elucidate a high-temperature origin of Chilean iron oxide-apatite deposits. Geochimica et Cosmochimica Acta, 177:94–104

Bindeman I (2008) Oxygen isotopes in mantle and crustal magmas as revealed by single crystal analysis. Reviews in Mineralogy and Geochemistry, 69:445–478

Childress TM, Simon AC, Day WC, Lundstrom CC, Bindeman IN (2016) Iron and oxygen isotope signatures of the Pea Ridge and Pilot Knob magnetite-apatite deposits, Southeast Missouri, USA. Economic Geology, 111:2033–2044

Childress TM, Simon AC, Reich M, Barra F, Arce M, Lundstrom CC, Bindeman IN (2019) Formation of the Mantoverde iron oxide - copper - gold deposit, Chile: Insights from Fe and O stable isotopes and comparison to iron oxide - apatite deposits, *in review*

Dare SAS, Barnes S-J, Beaudoin G, Méric J, Boutroy E, Potvin-Doucet C (2014) Trace elements in magnetite as petrogenetic indicators. Mineralium Deposita, 49:785–796

Dart RA, Beaumont PB (1971) On a further radiocarbon date for ancient mining in southern Africa. South African Journal of Science, 67(1):10–11

Dare AS, Barnes S-J, Beaudoin G, Méric J, Boutroy E, Potvin-Doucet C (2014) Trace elements in magnetite as petrogenetic indicators. Mineralium Deposita, 49(7):785–796

Dauphas N, John SG, Rouxel O (2017) Iron isotope systematics. Reviews in Mineralogy and Geochemistry, 82:415–510

Dupuis C, Beaudoin G (2011) Discriminant diagrams for iron oxide trace element fingerprinting of mineral deposit types. Mineralium Deposita, 46:319–335

Emery JA (1968) Geology of the Pea Ridge iron orebody. Ridge JD, ed., Ore deposits of the United States, 1933-1967 (Graton-Sales volume): New York, American Institute of Mining, Metallurgial, and Petroleum Engineers, I:359–369

Fisher LA, Kendrick MA (2008) Metamorphic fluid origins in the Osborne Fe oxide-Cu-Au deposit, Australia: evidence from noble gases and halogens. Mineral Deposits, 43:483–497

Frost CD, Blanckenburg F von, Shoenberg R, Frost BR, and Swapp SM (2007), Preservation of Fe isotope heterogeneities during diagenesis and metamorphism of banded iron formation. Contributions to Mineral Petrology, 153:211–235

Günther T, Klemd R, Zhang X, Horn I, Weyer S (2017) In-situ trace element and Fe-isotope studies on magnetite of the volcanic-hosted Zhibo and Chagangnuoer iron ore deposits in the Western Tianshan, NW China. Chemical Geology, 453:111–127

Jonsson E, Valentin RT, Högdahl K, Harri C, Weis F, Nilsson KP, Skelton A (2013) Magmatic origin of giant 'Kiruna-type' apatite-iron-oxide ores in central Sweden. Scientific Reports, 3, doi: 10.1038/srep01644.

Knipping JL, Bilenker LD, Simon AC, Reich M, Barra F, Deditius AP, Lundstrom C, Bindeman I, Munizaga R (2015a) Giant Kiruna-type deposits form by efficient flotation of magmatic magnetite suspensions. Geology, 43:491–594

Knipping JL, Bilenker LD, Simon AC, Reich M, Barra F, Deditius AP, Wälle M, Heinrich CA, Holtz F, and Munizaga R (2015b) Trace elements in magnetite from massive iron oxide-apatite deposits indicate a combined formation by igneous and magmatic hydrothermal processes. Geochimica et Cosmochimica Acta, 171:15–38

Lester GW, Clark AH, Kyser TK, Naslund HR (2013a) Experiments on liquid immiscibility in silicate melts with $H_2O$, P, S, F and Cl: implications for natural magmas. Contributions to Mineralogy and Petrology, 166:329–349

Matthews A, Goldsmith JR, Clayton RN (1983) Oxygen isotope fractionation involving pyroxenes: the calibration of mineral-pair geothermometers. Geochimica et Cosmochimica Acta, 47:631–644

Nadoll P, Angerer T, Mauk JL, French D, Walshe J (2014) The chemistry of hydrothermal magnetite: A review. Ore Geology Reviews, 61:1–32

Naslund HR, Henriquez F, Nyström JO, Vivallo W, Dobbs FM (2002) Magmatic iron ores and associated mineralisation: examples from the Chilean high Andes and coastal Cordillera. In Hydrothermal Iron Oxide Copper–Gold A Global Perspective, 2 (ed. T. M. Porter). PGC Publishing, Adelaide, Australia, p. 207–226.

Nuelle LM, Day WC, Sidder GB (1992) Geology and mineral paragenesis of the Pea Ridge iron ore mine, Washington County, Missouri - origin of the rare-earth-element and gold-bearing breccia pipes. U.S. Geological Survey Bulletin, A1–A11

Knipping JL, Bilenker LD, Simon AC, Reich M, Barra F, Deditius AP, Lundstrom C, Bindeman I, Munizaga R (2015a) Giant Kiruna-type deposits form by efficient flotation of magmatic magnetite suspensions. Geology, 43:491–594.

Knipping JL, Bilenker LD, Simon AC, Reich M, Barra F, Deditius AP, Wälle M, Heinrich CA, Holtz F, and Munizaga R (2015b) Trace elements in magnetite from massive iron oxide-apatite deposits indicate a combined formation by igneous and magmatic hydrothermal processes. Geochimica et Cosmochimica Acta, 171:15–38.

Nyström, JO, Henríquez F (1994) Magmatic features of iron ores of the Kiruna-type in Chile and Sweden: Ore textures and magnetite geochemistry. Economic Geology, 89:820–839.

Nyström JO, Billström K, Henríquez F, Fallick AE, Naslund HR (2008) Oxygen isotope composition of magnetite in iron ores of the Kiruna type in Chile and Sweden: GFF [Geologiska Föreningen], 130:177–188.

Ovalle JT, La Cruz NL, Reich M, Barra F, Simon AC, Konecke, BA, Rodriguez-Mustafa MA, Deditius AP, Childress TM, Morata D (2018) Formation of massive iron deposits linked to explosive volcanic eruptions. Nature Scientific Reports, 8 no. 14855

Park CF Jr. (1961) A magnetite "flow" in northern Chile. Economic Geology, 56:431–436

Pollard PJ (2006) An intrusion-related origin for Cu-Au mineralization in iron oxide-copper-gold (IOCG) provinces. Mineralium Deposita, 41:179–187.

Rehren T, Belgya T, Jambon A, Káli G, Kasztovsky Z, Kis Z, Kovács I, Maróti B, Martinón-Torres M, Miniaci G, Pigott VC, Radivojević M, Rosta L, Szemtmiklósi L, Szőkefalvi-Nagy Z (2013) 5,000 years old Egyptian iron beads made from hammered meteoric iron. Journal of Archaeological Science, 40(12):4785-4792, doi:10.1016/j.jas.2013.06.002

Rieger AA, Marschik R, Díaz M, Hölzl S, Chiaradia M, Akker B, Spangenberg JE (2010) The hypogene IOCG mineralization in the Mantoverde district, northern Chile. Economic Geology, 105:1271–1299.

Rieger AA, Marschik R, Díaz M (2012) The evolution of the hydrothermal IOCG system in the Mantoverde district, northern Chile: new evidence from microthermometry and stable isotope geochemistry. Mineral Deposits, 47:359–369.

Sillitoe RM, Burrows DR (2002) New field evidence bearing on the origin of the El Laco magnetite deposit, northern Chile. Economic Geology, 97:1101–1109.

Simon AC, Knipping J, Reich M, Barra F, Deditius AP, Bilenker LD, Childress TM (2018) Kiruna-Type iron oxide-apatite (IOA) and iron oxide-copper-gold (IOCG) deposits form by a combination of igneous and magmatic-hydrothermal processes: evidence from the Chilean Iron Belt. Society of Economic Geologists Special Publications, 21:89–114

Taylor HP Jr (1974) The application of Oxygen and Hydrogen Isotope Studies to Problems of Hydrothermal Alteration and Ore Deposition. Economic Geology, 69:843–883

Tornos F, Velasco F, Hanchar JM (2016) Iron-rich melts, magmatic magnetite, and superheated hydrothermal systems: The El Laco deposit, Chile. Geology, 44(6):427–430

Tornos F, Velasco F, Hanchar JM (2017) The magmatic to magmatic-hydrothermal evolution of the El Laco deposit (Chile) and its implications for the genesis of magnetite-apatite deposits. Economic Geology 112(7):1595-1628

Travisany V, Henriquez F, Nyström JO (1995) Magnetite lava flows in the Pleito-Melon District of the Chilean iron belt: Economic Geology, 90:438–444.

United States Geological Survey (2018) Mineral Commodities Summary, 200p

Velasco F, Tornos F, Hanchar JM (2016) Immiscible iron-and silica-rich melts and magnetite geochemistry at the El Laco volcano (northern Chile): Evidence for a magmatic origin for the magnetite deposits. Ore Geology Reviews 79:346–366.

Weis F (2013) Oxygen and iron isotope systematics of the Grängesberg mining district (GMD), central Sweden: Unpublished Ph.D. Dissertation, Uppsala Universitet, Uppsala, Sweden, 77p.

# CHAPTER II

## IRON AND OXYGEN ISOTOPE SIGNATURES OF THE PEA RIDGE AND PILOT KNOB MAGNETITE-APATITE DEPOSITS, SOUTHEAST MISSOURI, USA


## ABSTRACT

New O and Fe stable isotope ratios are reported for magnetite samples from high-grade massive magnetite of the Mesoproterozoic Pea Ridge and Pilot Knob magnetite-apatite ore deposits and these results are compared with data for other iron oxide-apatite deposits to shed light on the origin of the southeast Missouri deposits. The $\delta^{18}O$ values of magnetite from Pea Ridge (n = 12) and Pilot Knob (n = 3) range from 1.0 to 7.0 and 3.3 to 6.7‰, respectively. The $\delta^{56}Fe$ values of magnetite from Pea Ridge (n = 10) and Pilot Knob (n = 6) are 0.03 to 0.35 and 0.06 to 0.27‰, respectively. These $\delta^{18}O$ and the $\delta^{56}Fe$ values suggest that magnetite crystallized from a silicate melt (typical igneous $\delta^{56}Fe$ ranges 0.06–0.49‰) and grew in equilibrium with a magmatic-hydrothermal aqueous fluid. We propose that the $\delta^{18}O$ and $\delta^{56}Fe$ data for the Pea Ridge and Pilot Knob magnetite-apatite deposits are consistent with the flotation model recently proposed by Knipping et al. (2015a), which invokes flotation of a magmatic magnetite-fluid suspension and offers a plausible explanation for the igneous (i.e., up to ~15.9 wt % TiO2 in magnetite) and hydrothermal features of the deposits.

## INTRODUCTION

The St. Francois Mountains terrane in southeast Missouri, USA, consists dominantly of early Mesoproterozoic (~1.48– 1.45 Ga) rhyolitic ash-flow tuffs intercalated with mafic to intermediate-composition flows and shallow intrusions (Fig. 2.1; Day et al., 2016). The volcanic sequence was intruded by hornblende-biotite granites coeval with emplacement of the high silica volcanic sequence. These volcanic rocks and associated volcanogenic breccias host several large-tonnage iron oxide-apatite (IOA) deposits, including Pea Ridge and Pilot Knob that are the focus of this study (see Kisvarsanyi, 1990; Marikos et al., 1990; Sims, 1990; Nuelle et al., 1992; Sidder et al., 1993b; Van Schmus et al., 1996; Gleason et al., 2000; King et al., 2008; Nold et al., 2014; Day et al., 2016). The Pea Ridge and Pilot Knob deposits were both economic iron orebodies, from which over 41 and 20 million metric tons (Mt) of iron ore were produced, respectively. Pea Ridge also hosts high concentrations of rare earth elements (REEs) in late-stage breccia pipes rich in monazite, xenotime, and apatite (Kisvarsanyi, 1990; Nuelle et al., 1992; Sidder et al., 1993b; Seeger et al., 2001; Aleinikoff et al., 2016; Ayuso et al., 2016). Numerous studies have documented crosscutting relationships among the orebodies, the host igneous rocks, and late-stage aplite dikes, as well as igneous textures in the magnetite orebodies, all of which have been interpreted as evidence for coeval magmatism and iron oxide mineralization in the St. Francois Mountains terrane (Kisvarsanyi, 1981; Seeger et al., 1989; Marikos et al., 1990; Nuelle et al., 1992; Sidder et al., 1993a, b; Nold et al., 2013, 2014; Day et al., 2016). The Missouri deposits share strong mineralogical and geochemical similarities, e.g., similar concentrations of TiO2 in magnetite (Mercer et al., 2015) to the namesake Kiruna magnetite-apatite deposits in Sweden (Dupuis and Beaudoin, 2011; Nold et al., 2013, 2014). Genetic models that have been proposed to explain the features observed in the Missouri deposits include growth of magnetite from high-

temperature, magmatic-hydrothermal fluids (e.g., Nuelle et al., 1991a; Sidder et al., 1993b), and crystallization of magnetite from an immiscible iron oxide-rich magma, which itself evolved a magmatic aqueous fluid that overprinted the igneous magnetite (e.g., Nold et al., 2013, 2014). However, other models have also been proposed that suggest some of the magnetite orebodies formed as sedimentary iron formations (Anderson, 1976; Nold, 1988) or exclusively by hydrothermal replacement of the host volcanic rocks (Crane, 1912; Panno and Hood, 1983). The Pilot Knob and Pea Ridge deposits contain as much as 60 to 90 vol % magnetite in the massive ores (Sidder et al., 1993b; Nold et al., 2014; Day et al., 2016). Several studies have described porphyritic textures in the Pea Ridge orebody, with the cores of magnetite crystals resembling magmatic phenocrysts occurring in a matrix of fine-grained magnetite (Emery, 1968; Nuelle et al., 1991a, b, 1992). Nold et al. (2014) reported that the Pilot Knob deposit also contains large zoned magnetite and hematite crystals, as well magmatic chill zones containing fine-grained magnetite on the edges of the ore-body, which they concluded are characteristic features of an iron-ore magma. Nold et al. (2013) and Day et al. (2016) suggested that similarities in mineralogy of the Pilot Knob magnetite ores and the coeval high Fe, mafic to intermediate-composition igneous suite are consistent with a genetic relationship between magnetite in the orebody and these host igneous rocks.

Gleason et al. (2000) used the homogeneity of Nd isotopes in ore samples and coeval igneous rocks to conclude that REEs in the breccia pipes that cut the Pea Ridge magnetite orebody are genetically related to the igneous rocks of the St. Francois Mountains terrane. These authors pointed out that significant REE mineralization could be attributed to the presence of high-temperature, high-salinity fluids identified in fluid inclusions in ore samples (e.g., Sidder et al., 1993b; Day et al., 2016). We note that Gleason et al. (2000) did not discuss whether the

proposed mineralizing brines were genetically related to (i.e., derived from) the coeval igneous rocks, or instead from a separate source. Fluid inclusion microthermometry data indicate that primary, three-phase (liquid, vapor, halite) quartz-hosted fluid inclusions in the magnetite ore zone of the Pea Ridge deposit have salinities of 54 to >60wt % NaCl equiv and trapping temperatures from 480° to >530°C (Sidder et al., 1993b). Oxygen isotope equilibration temperatures, calculated for quartz-magnetite pairs from 11 ore samples, range from 269° to 688°C and average 481°C (Johnson et al., 2013), which is consistent with the fluid inclusion homogenization temperatures and agrees with a quartz-magnetite oxygen isotope temperature of 480°C reported by Sidder et al. (1991). Johnson et al. (2013) presented oxygen isotope equilibration temperatures for apatite-magnetite pairs that range from 419° to 725°C. Johnson et al. (2013, 2016) point out that these temperatures are below the solidus for the ore assemblages, and that the data thus rule out a strictly igneous origin (i.e., via liquid immiscibility) for the deposits.

More than a century of investigations have produced a wealth of field, geochemical, petrographic, and geophysical data for the Missouri IOA deposits. However, in total the published data are inconclusive with respect to the source reservoir for iron in the ore-grade magnetite, and no available data uniquely fingerprint one genetic model for the deposits. In this study, we combine "traditional" stable isotope ratios of O ($^{18}O/^{16}O$) with less-traditional stable isotope ratios of Fe ($^{56}Fe/^{54}Fe$) for ore magnetite from Pea Ridge and Pilot Knob to evaluate a possible genetic link between the ore deposits and coeval magmatism. The O and Fe stable isotope data are compared with data for magnetite from similar deposit types such as Kiruna in Sweden and several deposits in the Chilean iron belt, as well as for unequivocally magmatic magnetite from a variety of igneous rock types (e.g., basalt, andesite, dacite), magnetite

precipitated from purely magmatic-hydrothermal aqueous fluids (e.g., porphyry ore deposits), and from low-temperature hydrothermal fluids (e.g., banded iron formations). Our results represent the first combined O and Fe isotope data published for the Pea Ridge and Pilot Knob magnetite deposits.

## GEOLOGIC BACKGROUND

The St. Francois Mountains terrane is a Mesoproterozoic igneous province that lies within the eastern granite-rhyolite province (Bickford and Mose, 1975; Lidiak et al., 1993; Bickford et al., 2015). Based on new geochemical data, the terrane is interpreted to have formed in a subduction zone environment, comprising igneous rocks of two distinct age ranges: an older (~1.48–1.45 Ga) sequence of volcanic and related plutonic rocks and a younger (~1.33–1.28 Ga) series of bimodal granite, mafic dikes, and gabbroic sills (Day et al., 2016, and references therein). The older igneous rocks are mainly high silica rhyolitic ignimbrite and associated volcaniclastic sedimentary rocks, with lesser amounts of basaltic to basaltic andesitic to volcanic and subvolcanic rocks (erroneously classified as "trachyte" in previous studies; Day et al., 2016). The volcanic rocks are variously intruded by hornblende-biotite granites that in places form ring complexes along presumed caldera structures, and granitic massifs (Kisvarsanyi, 1980; Sides et al., 1981). Several caldera structures have been identified that are interpreted to be the source of the high silica ignimbrites. All of the IOA and iron oxide-copper-gold (IOCG) deposits are hosted in the older early Mesoproterozoic sequence of volcanic rocks. The younger late Mesoproterozoic igneous episode represents a period of bimodal magmatism that resulted in the formation of highly evolved, two-mica, fluorine-rich "tin granites" and gabbroic sills, plutons, and mafic dikes that cut the older volcanic terrane (Kisvarsanyi, 1981, 1988; Bickford et al., 2015, and references therein).

There is evidence for several hydrothermal events in the region during the Mesoproterozoic (King et al., 2008; Aleinikoff et al., 2016; Neymark et al., 2016). One event at 1470 to 1466 Ma records the age of apatite within the magnetite ore at Pea Ridge (Neymark et al., 2016). Three later regional hydrothermal events occurred, with the youngest event at ca. 1100 Ma resetting feldspar δ18O values (Wenner and Taylor, 1976; King et al., 2008; Aleinikoff et al., 2016). The geologic details of the IOA and IOCG deposits in the Missouri district have been described in many publications and we refer interested readers to the review by Day et al. (2016). Herein, we briefly describe the Pea Ridge and Pilot Knob deposits from which the samples analyzed in this study were collected.

*Pea Ridge*

The Pea Ridge deposit is located in Washington County, Missouri, on the northern edge of the Ozark uplift (Fig. 2.1), a regional uplift zone covering ~40,000 mi2 across Missouri, Arkansas, and Oklahoma. Magnetite in the deposit was mined for iron ore from 1964 until 2001 (Nuelle et al., 1992; Nold et al., 2014); the mine is currently inactive. The deposit contains four mappable zones that are defined by different alteration assemblages and crosscutting relationships. In order of occurrence, from oldest to youngest, these are (1) amphibole-quartz zone, (2) magnetite ore zone, (3) hematite zone, and (4) silicified zone (Emery, 1968; Sidder et al., 1993b). Gangue minerals spatially associated with the magnetite deposit are predominantly apatite, with lesser amounts of quartz, pyrite, and monazite, and sparse chalcopyrite (Nuelle et al., 1991b); fluid inclusions are rare (Sidder, 1993a). The main magnetite iron orebody dips 75° SE to nearly vertical and strikes N 55° to 60° E (Husman, 1989), is approximately 760 m long and 100 to 200 m thick, and extends to an unknown depth. Four steeply dipping, REE-rich breccia pipes cut rocks along the footwall on the eastern margin of the deposit (Seeger et al.,

2001). The ore, hosted in rhyolitic pyroclastic rocks, averages >60% Fe (Emory, 1968) and consists mainly of magnetite that is fine grained, dense, and massive, without any foliation or lineation present. Subordinate hematite is common as pseudomorphic grains after magnetite, with the degree of replacement varying from minor rim alteration to complete replacement (Sidder et al., 1993b). Specular hematite occurs as discrete crystals, veinlets, irregular inclusions, and as crystals lining vugs (Nold et al., 2014).

Mercer et al. (2015) reported three distinct generations of magnetite in the Pea Ridge orebody, rhyolites, and mafic to intermediate-composition suite rocks in the deposit area. One generation of magnetite contains 2 to 6 wt % $TiO_2$, a second has 1 to 2 wt % $TiO_2$, and a third generation contains <0.8 wt % $TiO_2$. Mercer et al. (2015) interpreted the compositional and textural relationships among the three generations to indicate that the 2 to 6 wt % $TiO_2$ magnetite grains are magmatic, and were resorbed and overgrown by the magnetite having 1 to 2 wt % $TiO_2$. Magnetite grains that contain <0.8 wt % $TiO_2$ are disseminated throughout the matrix and are the modally predominant form of magnetite in the orebody.

*Pilot Knob*

The Pilot Knob deposit is located in Iron County, Missouri, about 40 km southeast of Pea Ridge (Fig. 2.1). The deposit was mined from 1968 to 1980; this mine is currently inactive. The Pilot Knob deposit comprises a series of tabular orebodies that strike northwest and dip moderately southwest, and approximately parallel the layering of the host andesitic and rhyolitic pyroclastic rocks of the older volcanic rock series. The deposit is ca. 500 m long, 700 m in downdip extent, and 100 m thick. Cambrian sedimentary rocks cover the deposit to an average depth of about 100 m (Nold et al., 2014). The minimum age of the deposit is constrained by the 120-m-thick crosscutting Shepherd Mountain Gabbro, which has a Sm-Nd isochron age of 1333

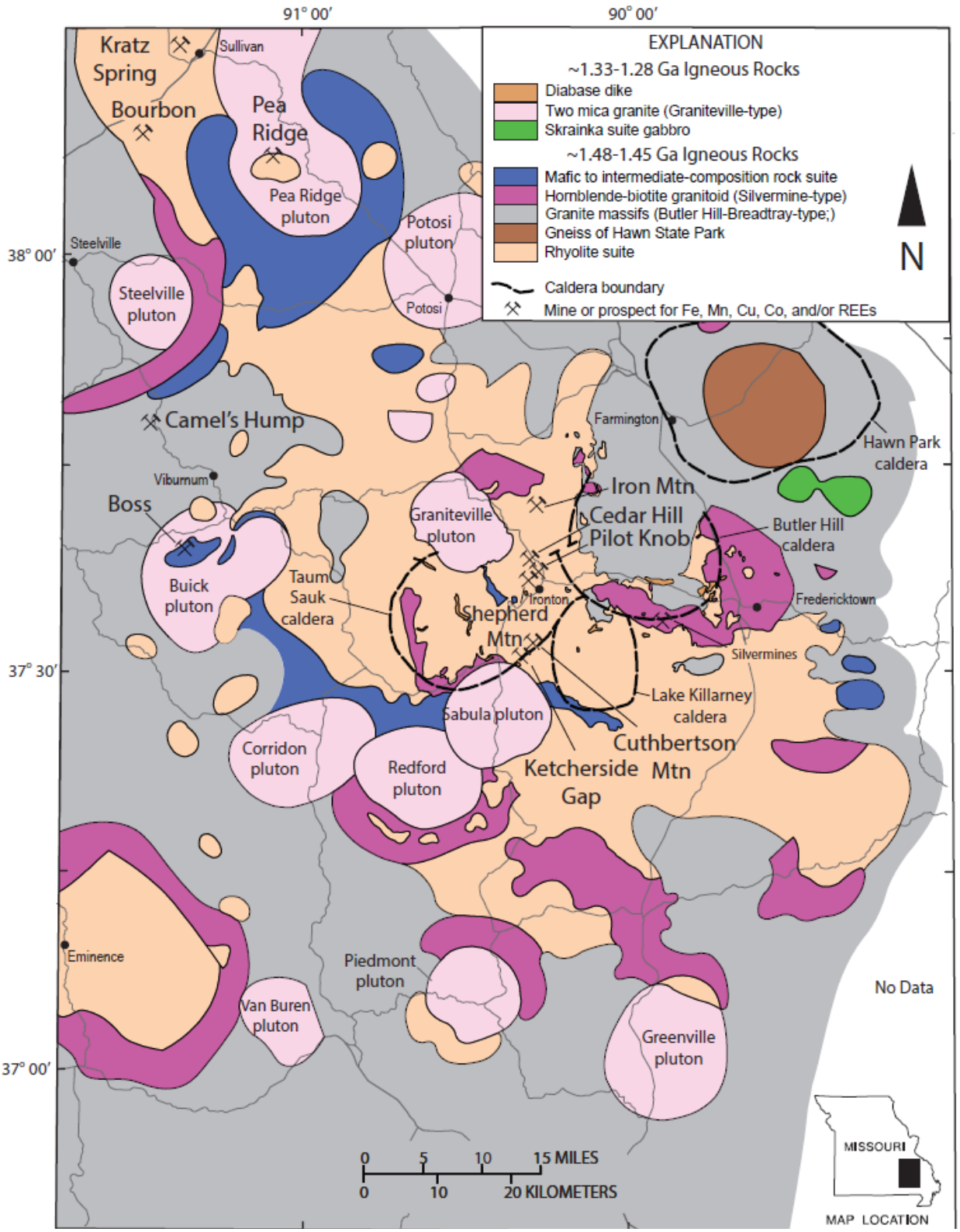


Figure 2.1: Geologic map of the Mesoproterozoic St. Francois Mountain terrane, southeast Missouri, USA, showing locations of Pea Ridge and Pilot Knob magnetite deposits. Modified from Day et al. (2016).

± 56 Ma (Lowell and Rämö, 1999). Two main ore types are recognized, one consisting of

relatively homogeneous, higher grade, black euhedral magnetite that forms the bulk of the orebody, and a relatively heterogeneous, lower grade magnetite-cemented breccia that forms an envelope around the higher grade ores. Nold et al. (2013, 2014) reported that the higher grade ore contains fine- to medium-grained magnetite interspersed with granular silicate minerals, mainly albitic plagioclase, together with minerals such as K-feldspar, quartz, and chlorite. Magnetite in the high-grade ore contains 0.02 to 0.68 wt % $TiO_2$; the lower grade ore is composed predominantly of larger magnetite grains, which typically display optically discernible zonation (Nold et al., 2013, 2014). Small inclusions of silicates, carbonates, sulfates, halides, and sulfides are present within the cores of low $TiO_2$ magnetite grains, whereas the rims are relatively free of inclusions (Nold et al., 2013). The rims of these zoned magnetite grains are slightly enriched in Fe and depleted in Al and Si, compared to the cores (Nold et al., 2014). In the surrounding lower grade orebody, magnetite is finer grained and disseminated in the host rhyolite tuff, in which host-rock porosity appears to have controlled the heterogeneous distribution of magnetite (Nold et al., 2014). Magnetite, and in some cases hematite, within this low-grade envelope surrounds volcanic shards, an observation that has stimulated debate as to whether the iron oxides are mainly hydrothermal replacement features (Panno and Hood, 1983), or primarily magmatic (Nold et al., 2014).

## SAMPLE SELECTION AND MAGNETITE CHARACTERIZATION

Seventeen samples from the Pea Ridge and Pilot Knob magnetite orebodies were provided by the U.S. Geological Survey and four samples from Pilot Knob were provided by John Nold of the University of Central Missouri. The samples from Pea Ridge were collected from the high-grade, massive magnetite ore zone at varying depths from the surface: 2,125,

2,275, 2,370, and 2,440 ft based on the maps of Seeger et al. (2001). Samples from Pilot Knob were collected from drill holes PKM-1086 (sample depth 918 ft), PKM-1098 (715 ft), PKM-1145 (830.1, 965.8, and 979.5 ft), PKM-1174 (1,348 ft), and PKM-2079 (1,160 ft).

A Cameca SX-100 electron probe microanalyzer (EPMA) and a JEOL 7800FLV field emission-scanning electron microscope (FE-SEM) at the University of Michigan were used to characterize magnetite ore samples as representative of those processed for Fe and O stable isotope analyses (Fig. 2.2). Instrumental conditions for the EPMA analyses were identical to those used in Knipping et al. (2015a, b) and Bilenker et al. (2016), and are reported in Table 2.1. Three generations of magnetite were identified in the samples (Fig. 2.2; Table 2.2). One generation consists of small (10–30 μm), subhedral to euhedral magnetite grains that contain <0.02 to 0.26 wt % TiO2. A second generation having a massive, spongy texture contains <0.02 to 0.35 wt % TiO2. A third generation of magnetite, localized within the massive spongy magnetite, contains 10.6 to 15.9 wt % TiO2. The presence of three discernible generations of magnetite and their compositions, as determined herein, are consistent with those reported by Mercer et al. (2015) for samples from the same orebody. In our study, it was not possible to physically separate the three generations of magnetite. The Fe and O stable isotope data reported here were obtained by processing and analyzing aggregates of these three generations of magnetite.

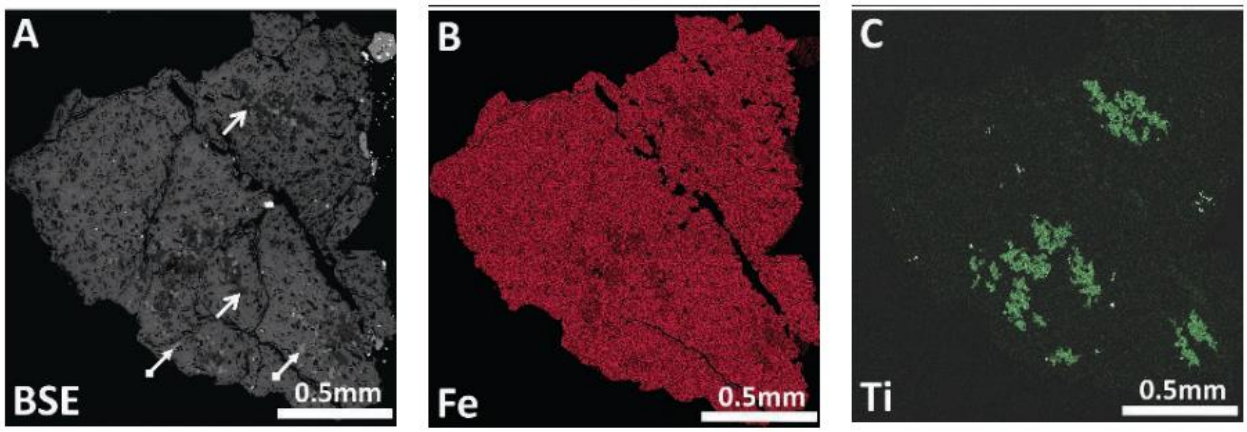


Figure 2.2: Images of a representative Pea Ridge magnetite grain processed for O and Fe stable isotope analyses. (A). Backscattered electron (BSE) image of three generations of magnetite are discernible by variations in gray hues. Most of the sample is magnetite that contains 0.02 to 0.35 wt % $TiO_2$ (magnetite generation Y, Table 2.2). White arrows with diamond tips point to brighter gray, subhedral to euhedral magnetite that contains 0.06 to 0.26 wt % $TiO_2$ (magnetite generation X, Table 2.2); arrows without diamond tips point to darker gray magnetite that contains 10.62 to 15.93 wt % $TiO_2$ (magnetite generation Z, Table 2.2). (B). Fe element map. (C). Ti element map.

## STABLE ISOTOPE ANALYTICAL METHODS

Whole magnetite samples were wrapped in weighing paper and crushed with a plastic-sheathed mallet to reduce the grain size to less than 1 mm. Magnetite grains were separated from the crushed material by use of a hand magnet wrapped in a Kimwipe. The separated grains of magnetite were then inspected using a binocular microscope at ~40× magnification to select the most uniform grains. Grain sizes between ~0.3 and 0.8 mm were chosen for O and Fe isotope analyses.

Grains selected for Fe analysis were further crushed to hasten acid digestion by use of an alumina-ceramic mortar and pestle that were rinsed in ethanol between samples to avoid contamination. Aliquots of polished magnetite grains from all samples were inspected at high magnification using backscattered electron (BSE) imaging on a Cameca SX-100 electron microprobe (SEM) and separately on a JEOL-7800FLV field emission-scanning electron

microscope (FE-SEM). The magnetite grains in the size fraction used for analyses were free of weathering features and are predominantly magnetite.

*Oxygen isotopes*

Oxygen isotope analyses of magnetite were conducted at the University of Oregon using a laser fluorination line coupled with a Thermo-Finnigan MAT 253 gas isotope ratio mass spectrometer used in dual inlet mode. Magnetite grains (2–3 mg) from each sample were subjected initially to low-power lasing, which was slowly increased in order to minimize jumping movements during fluorination with $BrF_5$. For samples that did not experience grain jumping, $O_2$ yields were close to the theoretical value of 100%. All data were compared to the Gore Mountain garnet standard, which was measured before, during, and after analysis of magnetite samples. Oxygen isotope values (Table 2.3) are reported relative to the international Vienna Standard Mean Ocean Water (VSMOW) standard. Average values for standard Gore Mountain garnet ($\delta^{18}$OGMG ± 1σ) over three days of measurements were 7.23 ± 0.10, 7.21 ± 0.11, and 7.19 ± 0.08‰. Analytical precision for individual analyses is ±0.10‰. The analytical values were adjusted by the difference between our measured standard values for each day and the recommended $\delta^{18}$O value of 6.52‰ for the Gore Mountain garnet standard.

*Iron isotopes*

Magnetite samples were subjected to ion chromatography to isolate Fe for isotopic analysis. Between ~0.3 and 0.7 mg of each sample was dissolved and dried down in aqua regia, again in 8N HCl, and then loaded into columns of AG1-X8 resin in 8N HCl, following the procedure described by Huang et al. (2011). Analyses were performed at the University of Illinois, Urbana-Champaign, using a Nu Plasma HR multi collector-inductively coupled plasma-

mass spectrometer (MC-ICP-MS) in dry plasma mode with a DSN-100 Desolvating Nebulizer System. All analyses were conducted following the double-spike method of Millet et al. (2012) to correct for instrumental mass bias and increase precision. Two aliquots of each sample were analyzed, and between each aliquot the international standard IRMM-14 was analyzed to monitor and correct for instrumental drift (Millet et al., 2012). The bracketing standard was also analyzed using the DSN-100 System. Iron isotope values (Table 2.3) are reported relative to IRMM-14, calculated by using the following equation:

$$\delta^{56}Fe_{sample}\ (‰) = [(^{56}Fe/^{54}Fe)_{measured}/(^{56}Fe/^{54}Fe)_{IRMM\text{-}14} - 1] * 1{,}000 \qquad (1)$$

The in-house standard UIFe was measured to an average $\delta^{56}$Fe value of 0.73 ± 0.01‰ (1SE, n = 16, two sessions over five months); the international standard BCR-2 yielded an average $\delta^{56}$Fe value of 0.08 ± 0.02‰ (1SE, n = 2; recommended value is 0.091 ± 0.011‰; Craddock and Dauphas, 2011).

## RESULTS

### *Oxygen isotope compositions of magnetite*

Stable O isotope ratios for magnetite are reported as $\delta^{18}$O values in Table 2.3 and Figure 2.3. The $\delta^{18}$O (±2σ) values for Pea Ridge magnetite samples collected at depths (from surface) of 2,125, 2,275, 2,370, and 2,440 ft are 4.56‰ (n = 1), 1.02‰ (n = 1), 4.32 ± 3.93‰ (n = 8), and 4.77 ± 0.78‰ (n = 2), respectively. Sample 954-5-205 from Pea Ridge was measured to be 5.50‰ (n = 1). The $\delta^{18}$O (±2σ) values for Pilot Knob magnetite from samples PK-1145 are 3.26, 6.68, and 6.21‰ for depths of 830.1, 965.8, and 979.5 ft, respectively.

### *Iron isotope compositions of magnetite*

Stable Fe isotope ratios for magnetite are reported as $\delta^{56}$Fe values in Table 2.3 and Figure 2.4. We highlight the fact that not all samples that were analyzed for O isotope ratios were analyzed for Fe isotopes. The average $\delta^{56}$Fe (±2σ) value for Pea Ridge magnetite is 0.17 ± 0.20‰ (n = 10), with a low of 0.03‰ and a high of 0.35‰. The average $\delta^{56}$Fe (±2σ) value for Pilot Knob magnetite is 0.18 ± 0.15‰ (n = 6), with a low of 0.06‰ and a high of 0.27‰.

## DISCUSSION

### *Constraints on the source reservoir of O and Fe in the Pea Ridge and Pilot Knob deposits*

*Oxygen isotopes: Previous studies:* There is a relative paucity of published O isotope data for the Missouri iron oxide deposits, albeit new work by Johnson et al. (2016) provides an important dataset to help understand the origin of these ore-forming systems. The early study of Wenner and Taylor (1976) presented $\delta^{18}$O data for 25 granites, 21 rhyolites, and 10 basaltic sills from the St. Francois Mountains terrane. They reported that the whole-rock and feldspar $\delta^{18}$O values increase systematically from 7 to 14 and 6 to 13‰, respectively, northeast to southwest, with increasing $\delta^{18}$O correlating with partial chloritization of hornblende (where present) and increasing degree of alteration of K-feldspar to a "brick-red" K-feldspar containing dust-sized hematite inclusions. Wenner and Taylor (1976) reported $\delta^{18}$O values that range from 7.5 to 9.5‰ for fresh, unaltered gabbro and basalt, and values ranging from 6.3 to 10.1‰ for altered diabase and basalt. Wenner and Taylor (1976) also reported $\delta^{18}$O values of 8.8 to 10.6‰ for primary igneous coarse-grained quartz (≥1.0 mm) from regional samples of the St. Francois Mountains; these $\delta^{18}$O values are consistent with $\delta^{18}$O values reported for quartz from most igneous rocks (Bindeman, 2008). In contrast, the $\delta^{18}$O values for fine-grained quartz (≤0.3 mm) showed spatial variability, becoming isotopically heavier from northeast to southwest, consistent with the whole-rock and feldspar data, and likely reflecting secondary alteration. Wenner and Taylor

(1976) also reported δD values for chlorite and, together with the $\delta^{18}O$ data for whole rocks, feldspar, and both coarse- and fine-grained quartz, concluded that the entire St. Francois Mountains terrane experienced low-temperature hydrothermal alteration several hundred m.y. after igneous activity and formation of the ore deposits. Wenner and Taylor (1976) proposed that meteoric surface waters were responsible for the ca. 1100 Ma hydrothermal alteration, characterized by $\delta^{18}O$ and δD values similar to modern-day meteoric waters found in warm climates, at low latitude and low elevation. Sidder et al. (1993a) reported a $\delta^{18}O$ value of 15.2‰ for quartz in the magnetite ore zone of the Pea Ridge deposit, and $\delta^{18}O$ values from 14.5 to 15.7‰ for quartz from the amphibole-quartz zone and the postmagnetite ore silicified zone, respectively. Sidder et al. (1993b) described quartz from the amphibole-quartz zone as forming both interstitial grains and massive pods 1 to 50 cm in diameter. Within the magnetite ore zone, quartz constitutes 1 to 10 modal % of the rock, present as interstitial grains to magnetite as well as in pods and linings of vugs. Sidder et al. (1993a) calculated equilibrium $\delta^{18}O$ temperatures up to 680°C for quartz-magnetite pairs for the premagnetite ore skarn alteration of the host rhyolitic tuff, and homogenization temperatures up to 530°C for primary halite-bearing (54–60 wt % NaCl equiv.) fluid inclusions in quartz from the magnetite ore zone. These observations were interpreted by Sidder et al. (1993b) to indicate that formation of the Pea Ridge iron orebody and REE-rich breccia pipes involved highly saline, high-temperature, magmatically derived hydrothermal fluids. A similar conclusion was reached by Hofstra et al. (2016), based on new fluid inclusion data.

King et al. (2008) reported $\delta^{18}O$ data for samples of the Royal Gorge Rhyolite from the Taum Sauk caldera (Fig. 2.1), including one sample of brecciated rhyolite ash-flow tuff at the Pilot Knob deposit. Their whole-rock $\delta^{18}O$ values range from 12.69 to 15.12‰ (avg $\delta^{18}O$ = 14.1

± 0.9‰; n = 6). These authors also presented $\delta^{18}O$ values for alteration-resistant zircon from the St. Francois Mountains terrane that vary from 5.8 to 8.2‰ (avg $\delta^{18}O = 7.3 \pm 1.1$‰), which are higher than the accepted mantle $\delta^{18}O$ value of 5.3‰, but consistent with those for zircons from Proterozoic rocks (i.e., $\delta^{18}O = 7.3 \pm 1.5$‰; Valley et al., 2005). The highest $\delta^{18}O$ value of 8.2‰ for zircon would correspond to a magmatic value of 10 to 10.5‰ (Trail et al., 2009). King et al. (2008) cited published Sm/Nd and U/Pb data (from Gonzales and Van Schmus, 2007) and attributed the elevated $\delta^{18}O$ (Zrc) values to a shift in the composition of post-Archean subducted sediments, coupled with assimilation of supracrustal rocks in subduction zone magmas.

*New data:* The O isotope data from this study are plotted in Figure 2.3 together with $\delta^{18}O$ data for other IOA deposits from Nyström et al. (2008), Jonsson et al. (2013), Weis (2013), Knipping et al. (2015a), and Bilenker et al. (2016). Results for $\delta^{18}O$ values in magnetite samples from Pilot Knob and Pea Ridge overlap those reported for magnetite from IOA deposits in the Kiruna district (i.e., Grängesberg and Kiruna) and several IOA deposits in the Chilean iron belt. We highlight the fact that none of the Pea Ridge and Pilot Knob samples has a $\delta^{18}O$ value below 0.9‰, which is interpreted as the lower limit for orthomagmatic (igneous) magnetite (cf. Taylor, 1967). Magnetite samples from other IOA deposits that have $\delta^{18}O$ values below 0.9‰ have been attributed to post-mineralization metasomatic alteration that affected the magnetite, which originally formed either by crystallization from a silicate melt or precipitation from a magmatic-hydrothermal fluid (Jonsson et al., 2013; Weis, 2013; Knipping et al., 2015a, b; Bilenker et al., 2016). The $\delta^{18}O$ ratios for magnetite from Pea Ridge range from 1.02 to 7.03‰ and for Pilot Knob from 3.26 to 6.68‰. The majority of magnetite samples (11 of 16) analyzed from Pea Ridge and Pilot Knob are isotopically heavier than the $\delta^{18}O$ range reported for orthomagmatic magnetite (Fig. 2.3). These heavier values (i.e., $4‰ \leq \delta^{18}O \leq 7‰$) are consistent with magnetite

that formed in equilibrium with a silicate melt. Considering that the magnetite ore bodies are hosted in time-equivalent volcanic rocks (Neymark et al., 2016) and radiogenic isotope evidence suggests a genetic relationship between the orebodies and magmatic host rocks (e.g., Gleason et al., 2000; Ayuso et al., 2016), it seems prudent to test this hypothesis.

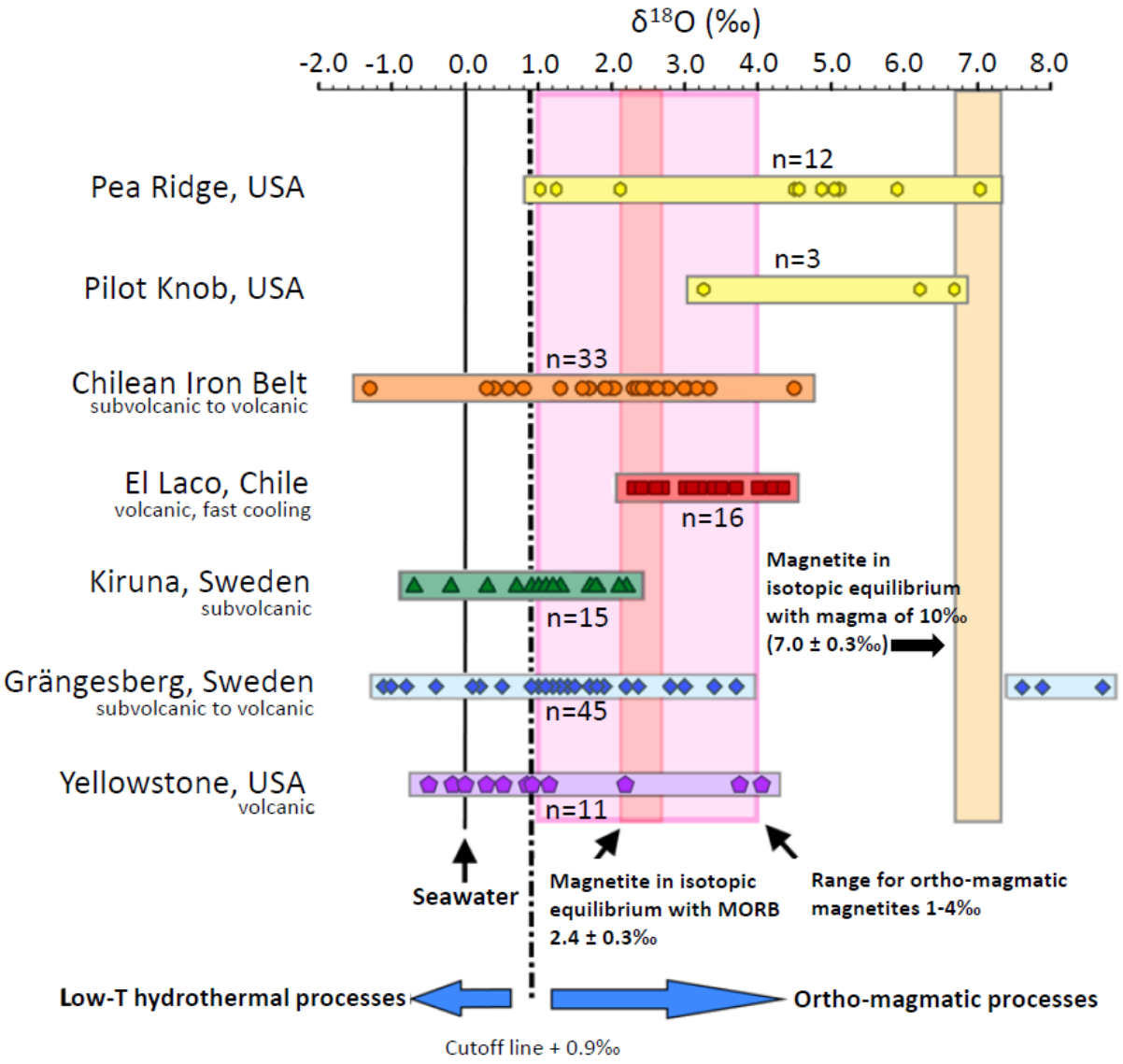


Figure 2.3: Oxygen isotope ($\delta^{18}O$) values for magnetite from Pilot Knob and Pea Ridge orebodies compared to those for other iron oxide-apatite deposits (adapted from Jonsson et al., 2013). Pink box ($\delta^{18}O$ = 1–4‰) is range for orthomagmatic magnetite (Taylor, 1967). Red box ($\delta^{18}O$ = 2.2–2.6‰) represents magnetite in equilibrium with mid-ocean ridge basalt (MORB). Pale orange box ($\delta^{18}O$ = 6.6–7.3‰) is magnetite in equilibrium with silicate magma having $\delta^{18}O$ of 10‰. Vertical dash-dot line represents cutoff between magnetite derived from silicate magma or magmatic-hydrothermal fluid, which in both cases would have $\delta^{18}O$ >0.9‰, and with low-temperature hydrothermal fluid having $\delta^{18}O$ <0.9‰

(cf. Jonsson et al., 2013). Literature sources for published $\delta^{18}O$ values for magnetite from Chilean iron belt, El Laco, Kiruna, Grängesberg, and Yellowstone are in Supplementary Table A.1. The 2σ uncertainties for all data points are smaller than the symbols, and are reported in Table 2.3.

*Potential source magmas:* We calculate the $\delta^{18}O$ values of theoretical parent magmas using the new $\delta^{18}O$ data presented here and published magnetite-melt fractionation factors. The host magmatic rocks of both Pea Ridge and Pilot Knob are predominantly rhyolite ash-flow tuff; however, spatially associated with these deposits are volumetrically abundant and possibly coeval, subvolcanic Fe-rich, mafic to intermediate-composition igneous intrusions (Day et al., 2016). Fractionation factors are used from Zhao and Zheng (2003) and equation (2):

$$\Delta^{18}O_{magnetite\text{-}magma} = \delta^{18}O_{magnetite} - \delta^{18}O_{magma}, \qquad (2)$$

to calculate the theoretical $\delta^{18}O$ isotope composition of a parent magma. A parent basalt or andesite would have $\delta^{18}O$ of 9.4 or 9.8‰, respectively, in equilibrium with magnetite that has a $\delta^{18}O$ value of 7‰ ($\Delta^{18}O_{magnetite\text{-}basalt} = -2.4$‰; $\Delta^{18}O_{magnetite\text{-}andesite} = -2.8$‰). A somewhat higher theoretical $\delta^{18}O$ value of about 10.3‰ is obtained for rhyolite magma by using $\Delta^{18}O_{magnetite\text{-}rhyolite}$ of –3.3‰. Values of $\delta^{18}O$ of 9 to 10‰ for a parent magma in equilibrium with magnetite that has a $\delta^{18}O$ value of 7‰ are generally slightly higher than those reported for fresh, unaltered igneous rock, but are consistent with the limited published $\delta^{18}O$ data reported for igneous rocks from the St. Francois Mountains terrane, as discussed above, and may also reflect later low-temperature hydrothermal alteration (cf. Wenner and Taylor, 1976).

We suggest that the new $\delta^{18}O$ data reported here for magnetite are consistent with a predominant magmatic source for O in magnetite within the massive magnetite ore zones of both the Pea Ridge and Pilot Knob deposits. The magnetite samples having the highest $\delta^{18}O$ values indicate an origin in equilibrium with a silicate melt (Fig. 2.3); samples with $\delta^{18}O$ values between ca. 1 and 4‰ indicate equilibrium with a moderate- to high-temperature, magmatic-

hydrothermal fluid (see also Johnson et al., 2016). Based on magnetite-water fractionation factors published by Cole et al. (2004), the lowest $\delta^{18}O$ values measured in magnetite from the Pea Ridge deposit are consistent with magnetite that grew in equilibrium with a high-temperature fluid evolved from a magmatic source (Fig. 2.3; cf. Hedenquist and Lowenstern, 1994). For example, a $\delta^{18}O$ value of 1.0‰ in magnetite requires a fluid with $\delta^{18}O$ = 8‰ at 600°C and 10‰ at 300°C, which is entirely consistent with reported O isotope values for magmatic-hydrothermal fluids generated in arc magma systems (Hedenquist and Lowenstern, 1994). We recognize that the lower $\delta^{18}O$ values could reflect reequilibration of magnetite during one of several hydrothermal events that overprinted the St. Francois Mountains terrane, which undoubtedly involved crustally derived fluids (King et al., 2008; Hofstra et al., 2016; Johnson et al., 2016). Similar observations have been made for magnetite in IOA deposits of the Grängesberg and Kiruna districts, Sweden (cf. Jonsson et al., 2013). However, complete dissolution and reprecipitation of magnetite shifts $\delta^{18}O$ to values of <0.9‰ (Fig. 2.3; Jonsson et al., 2013; Weis, 2013). Further, as discussed below, Fe isotope data for magnetite from the Pilot Knob and Pea Ridge deposits presented here are consistent with a magmatic source reservoir for iron in magnetite from the Pea Ridge and Pilot Knob magnetite deposits. The observed $\delta^{18}O$ values for magnetite do not allow us to directly resolve the origin of the heavy $\delta^{18}O$ composition of quartz within the deposits (e.g., Johnson et al., 2013, 2016). However, it is plausible that these heavy values for quartz reflect low-temperature hydrothermal alteration by crustal fluids that evolved from sedimentary rocks, which is evident in the comparison of $\delta^{18}O$ data from zircon and quartz (King et al., 2008; Barton, 2014).

*Iron isotopes:* The $\delta^{56}Fe$ values determined here average 0.17 ± 0.20‰ (n = 10) and 0.16 ± 0.13‰ (n = 6) for magnetite from the Pea Ridge and Pilot Knob deposits, respectively. These

values are similar to those for magnetite from other IOA deposits such as in the Grängesberg district, Sweden, and several deposits in the Chilean iron belt (Fig. 2.4; Weis, 2013; Knipping et al., 2015a, b; Bilenker et al., 2016). The data for Pea Ridge and Pilot Knob overlap $\delta^{56}$Fe values of magnetite from a variety of igneous rocks and are consistent with the magnetite-hosted iron in the orebodies having a genetic relationship with the coeval igneous rocks. The $\delta^{56}$Fe data for magnetite from IOA deposits such as Mineville (New York) and Grängesberg that plot outside the magmatic/magmatic-hydrothermal range (Fig. 2.4) were interpreted by Weis (2013) and Bilenker et al. (2016) to reflect hydrothermal alteration that shifted the Fe isotope compositions to lower $\delta^{56}$Fe values. For example, in the Mineville IOA deposit, primary magnetite was completely dissolved and reprecipitated (Valley et al., 2011), resulting in isotopically lighter Fe in secondary magnetite owing to Fe isotope fractionation between aqueous fluids and magnetite (cf. Heimann et al., 2008). If magnetite in the Pea Ridge and Pilot Knob deposits precipitated from an ore fluid that was meteoric in origin, this fractionation process would result in $\delta^{56}$Fe values of <0.0‰ (Fig. 2.4).

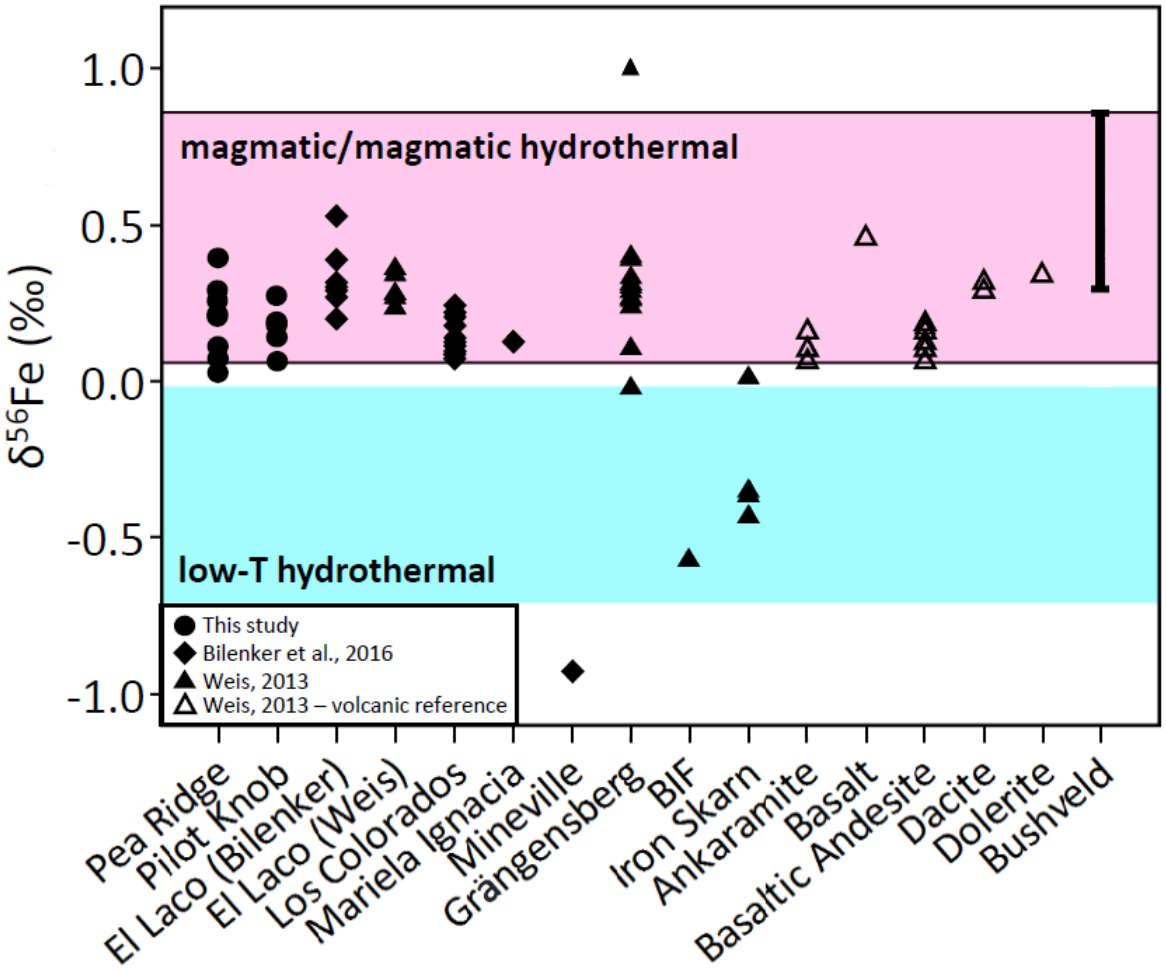


Figure 2.4: Iron isotope ($\delta^{56}$Fe) values of magnetite from Pilot Knob and Pea Ridge orebodies compared to those from other IOA ore deposits, igneous magnetite, magmatic-hydrothermal magnetite, and low-temperature hydrothermal magnetite (adapted from Bilenker et al., 2016). Data are from Weis (2013; triangles), Bilenker et al. (2016; diamonds), and this study (circles). Open triangles represent data for volcanic reference materials (Weis, 2013). Pink box encompasses complete range of $\delta^{56}$Fe values for magnetite from unaltered volcanic and plutonic rocks, based on data in Heimann et al. (2008) and Bilenker et al. (2016). Blue box encompasses complete range of $\delta^{56}$Fe values for magnetite from low-temperature hydrothermal ores, based on data in Anbar (2004), Shüßler (2008), and Severmann and Anbar (2009). The 2σ uncertainties for all data points are smaller than the symbols, and are reported in Table 2.3. The $\delta^{56}$Fe values from the literature are provided in Supplementary Table A.2.

The $\delta^{56}$Fe data presented here cannot be used alone to discriminate between models that invoke magnetite crystallization from an igneous melt versus magnetite that precipitated from a high-temperature, magmatic-hydrothermal fluid. However, the combination of new $\delta^{56}$Fe and $\delta^{18}$O stable isotope data, which argue for a predominant magmatic reservoir for Fe and O in

magnetite in the Pilot Knob and Pea Ridge orebodies (Figs. 2.3, 2.4), and the observation of local Ti-rich magnetite within the deposits (Fig. 2.2; Table 2.2; Mercer et al., 2015), allow us to suggest a new model for the Pea Ridge and Pilot Knob deposits.

*A fluid-suspension model for the magnetite at Pea Ridge and Pilot Knob magnetite deposits*

Knipping et al. (2015a, b) recently proposed a model that combines magmatic and magmatic-hydrothermal processes and offers a plausible explanation of interpreted magmatic and magmatic-hydrothermal features in many IOA deposits. Their model was based on an investigation of mineralization in the world-class Los Colorados IOA deposit in the Chilean iron belt. The model invokes magnetite crystallization from an intermediate-composition silicate melt, followed by volatile saturation of the melt and wetting of the magnetite crystals owing to the much more favorable surface tension properties between oxides and aqueous fluid, relative to silicate minerals (cf. Hurwitz and Navon, 1994; Matveev and Ballhaus, 2002). Coalescence of a buoyant, magnetite-fluid suspension allows the igneous magnetite to ascend through the magma chamber, most likely via hydraulic fractures created by tectonic stress changes in the magmatic system. Fast decompression allows the magnetite-fluid suspension to segregate into the fractures, and in the southeast Missouri deposits to percolate through porous and brecciated pyroclastic host rocks. Similar observations have been made for the Los Colorados deposit where diorite contains as much as 25 vol % magnetite adjacent to the main magnetite orebodies (Knipping et al., 2015a, b). Finally, during ascent of the magnetite-fluid suspension, magnetite growth continues during decompression and forms hydrothermal magnetite rims on igneous magnetite cores.

The textures reported for massive magnetite from Los Colorados are similar to those reported for magnetite from the Pea Ridge deposit where magnetite locally has cores interpreted

as igneous phenocrysts (Nuelle et al., 1992; Nold et al., 2014). Gangue mineral inclusions found in magnetite from this deposit are predominantly apatite, plus lesser amounts of quartz, pyrite, and monazite (Nuelle et al., 1991b). A polymineralic solid inclusion assemblage in magnetite is also present in the Los Colorados deposit (Deditius et al., 2015; Knipping et al., 2015a, b). These observations can be explained if minerals such as apatite were floated as part of the magnetite-fluid suspension, and/or by post-entrapment reactions between magnetite and the surrounding aqueous fluid that can precipitate mineral phases otherwise not stable at the formational temperature of the inclusions (cf. Matveev and Ballhaus, 2002). The high solubility of SiO2 in most magmatic-hydrothermal fluids easily accounts for the presence of quartz in the deposits (Newton and Manning, 2000). The presence of monazite likely reflects secondary fluid-induced alteration of primary REE-rich apatite (Harlov, 2015; Harlov et al., 2016); geochemical evidence (e.g., high Co/Ni ratios) presented by Reich et al. (2016) for pyrite from Los Colorados indicates that pyrite also can form from a cooling, magnetite-fluid suspension.

Magnetite in the Los Colorados deposit contains three-phase, halite-liquid-vapor fluid inclusions, which indicate a minimum salinity of 35 wt % NaCl equiv. for the magmatic-hydrothermal fluid that is invoked in the magnetite-fluid suspension model (Knipping et al., 2015a, b). This salinity is lower than those reported for hypersaline fluid inclusions in apatite from the magnetite ore zone in the Pea Ridge deposit (Hofstra et al., 2016). The highly saline fluid is a critical part of the Knipping et al. (2015a) model, because a fluid of this composition is able to transport significant amounts of Fe as $FeCl_2$ (cf. Simon et al., 2004; Bell and Simon, 2011), and also rare earth metals (cf. Reed et al., 2000; Tanis et al., 2012). At Los Colorados, the host diorite is brecciated and magnetite rich, with the proportion of magnetite increasing toward the contact with the massive magnetite orebody. These features are consistent with the proposed

fluid suspension having percolated into the host diorite where magnetite precipitated in open pore space and around igneous minerals in the diorite. The magnetite-fluid suspension model is also plausible for the magnetite-cemented breccia at Pilot Knob, which also contains a Fe-rich envelope around the magnetite deposit. After the majority of the magnetite in the ascending fluid is deposited to form the massive magnetite ore, the fluid, which still contains a high concentration of Fe (Simon et al., 2004), can percolate through the porous and permeable pyroclastic host rock where it precipitates magnetite in open space and around volcanic shards. It is also possible that magnetite replaced the volcanic groundmass. Textural evidence in support of this process was described by Nold et al. (2014) and is entirely consistent with the magnetite-fluid suspension model for IOA deposits proposed by Knipping et al. (2015a). We recognize that the model does not address every aspect of the Pea Ridge and Pilot Knob deposits. However, similarities between the geochemical and textural features of the Missouri IOA deposits and the Los Colorados IOA deposit are consistent with this genetic model.

## FINAL REMARKS

Stable Fe and O isotope data presented here suggest a magmatic source for the iron and oxygen in high-grade massive magnetite in the Mesoproterozoic Pea Ridge and Pilot Knob orebodies and provide new insights into the origin of these IOA deposits. The igneous $\delta^{18}O$ and δ56Fe signatures of the analyzed magnetite samples allow us to infer that meteoric fluids or basinal brines were not involved in formation of the deposits. Our new $\delta^{18}O$ and $\delta^{56}Fe$ data are consistent with a combination of magmatic and magmatic-hydrothermal growth of magnetite, and with the magnetite-fluid flotation model proposed recently for IOA deposits elsewhere.

## ACKNOWLEDGMENTS

Childress acknowledges funding from the Society of Economic Geologists Student Grant Program, the University of Michigan Earth & Environmental Sciences Turner Student Research Fund, and the University of Michigan Rackham Graduate School. Simon acknowledges funding from NSF EAR grants 1250239 and 1264560. John Slack (U.S. Geological Survey) and John Nold (University of Central Missouri) are thanked for providing samples. Christine Wawryk, Aaron Pietruszka, an anonymous referee, and guest editors John Slack, Louise Corriveau, and Murray Hitzman are thanked for their reviews, which significantly improved the paper both scientifically and stylistically.

Any use of trade, product, or firm names is for descriptive purposes only and does not imply endorsement by the U.S. Government.

## REFERENCES

Aleinikoff, J.N., Selby, D., Slack, J.F., Day, W.C., Pillers, R.M., Cosca, M.A., Seeger, C.M., Fanning, C.M., and Samson, I.M., 2016, U-Pb, Re-Os, and Ar/Ar geochronology of rare earth element (REE)-rich breccia pipes and associated host rocks from the Mesoproterozoic Pea Ridge Fe-REE-Au deposit, St. Francois Mountains, Missouri: Economic Geology, v. 111, p. 1883–1914.

Anbar, A.D., 2004, Iron stable isotopes: Beyond biosignatures: Earth and Planetary Science Letters, v. 217, p. 223–236.

Anderson, L.C., 1976, The Pilot Knob hematite deposit, Pilot Knob, southeast Missouri: M.S. thesis, Madison, Wisconsin, University of Wisconsin, 80 p.

Ayuso, R.A., Slack, J.F., Day, W.C., and McCafferty, A.E., 2016, Geochemistry, Nd-Pb isotopes, and Pb-Pb ages of the Mesoproterozoic Pea Ridge iron oxide-apatite–rare earth element deposit, southeast Missouri: Economic Geology, v. 111, p. 1935–1962.

Barton, M.D., 2014, Iron oxide (-Cu-Au-REE-P-Ag-U-Co) systems: Treatise on Geochemistry, 2nd ed., v. 13, p. 515–541.

Bell, A., and Simon, A.C., 2011, Experimental evidence for the alteration of the Fe3+/SFe of silicate melt caused by the degassing of chlorine-bearing aqueous volatiles: Geology, v. 39, p. 499–502. Bickford, M.E., and Mose, D.G., 1975, Geochronology of Precambrian rocks

in the St. Francois Mountains, southeast Missouri: Geological Society of America Special Paper 165, p. 1–48.

Bickford, M.E., Van Schmus, W.R., Karlstrom, K.E., Mueller, P.A., and Kamenov, G.D., 2015, Mesoproterozoic-trans-Laurentian magmatism: A synthesis of continent-wide age distributions, new SIMS U-Pb ages, zircon saturation temperatures, and Hf and Nd isotopic compositions: Precambrian Research, v. 265, p. 286–312.

Bilenker, L.D., Simon, A.C., Reich, M., Lundstrom, C.C., Gajos, N., Bindeman, I., Barra, R., and Munziga, R., 2016, Fe-O stable isotope pairs elucidate a high-temperature origin of Chilean iron oxide-apatite deposits: Geochimica et Cosmochimica Acta, v. 177, p. 94–104.

Bindeman, I., 2008, Oxygen isotopes in mantle and crustal magmas as revealed by single crystal analysis: Reviews in Mineralogy and Geochemistry, v. 69, p. 445–478.

Cole, D.R., Horita, J., Eniamin. V., Polyakov, V.B., Valley, J.W., Spicuzza, M.J., and Coffey, D.W., 2004, An experimental and theoretical determination of oxygen isotope fractionation in the system magnetite-H2O from 300 to 800°C: Geochimica et Cosmochimica Acta, v. 68, p. 3569–3585.

Craddock, P.R., and Dauphas, N., 2011, Iron isotopic compositions of geological reference materials and chondrites: Geostandards and Geoanalytical Research, v. 35, p. 101–123.
Crane, G.W., 1912, The iron ores of Missouri: Missouri Bureau of Geology and Mines, 2nd series, v. 10, p. 120–145.

Day, W.C., Slack, J.F., Ayuso, R.A., and Seeger, C.M., 2016, Regional geologic and petrologic framework for iron oxide ± apatite ± rare earth element and iron oxide copper-gold deposits of the Mesoproterozoic St. Francois Mountains terrane, southeast Missouri, USA: Economic Geology, v. 111, p. 1825–1858.

Deditius, A.P., Reich, M., Suvorova, A., Roberts, M., Rubanov, S., and Simon, A.C., 2015, Nano-geochemistry of trace elements in magnetite from the Los Colorados IOA deposit in Chile [abs.]: Geochemical Society, Goldschmidt 2015 Meeting, Prague, Czech Republic, Abstract Volume.

Dupuis, C., and Beaudoin, G., 2011, Discriminant diagrams for iron oxide trace element fingerprinting of mineral deposit types: Mineralium Deposita, v. 46, p. 319–335.

Emery, J.A., 1968, Geology of the Pea Ridge iron orebody, in Ridge, J.D., ed., Ore deposits of the United States, 1933-1967 (Graton-Sales volume): New York, American Institute of Mining, Metallurgical, and Petroleum Engineers, v. I, p. 359–369.

Gleason, J.D., Marikos, M.A., Barton, M.D., and Johnson, D.A., 2000, Neodymium isotopic study of rare earth element sources and mobility in hydrothermal Fe oxide (Fe-P-REE) systems: Geochimica et Cosmochimica Acta, v. 64, p. 1059–1068.

Gonzales, D.R., and Van Schmus, W.R., 2007, Proterozoic history and crustal evolution in southwestern Colorado: Insight from U/Pb and Sm/Nd data: Precambrian Research, v. 154, p. 31–70. Harlov, D.E., 2015, Apatite: A fingerprint for metasomatic processes: Elements, v. 11, p. 171–176.

Harlov, D.E., Meighan, C., Kerr, I., and Samson, I.M., 2016, Mineralogy, chemistry, and fluid-aided evolution of the Pea Ridge Fe oxide-(Y + REE) deposit, southeast Missouri, USA: Economic Geology, v. 111, p. 1963–1984.

Hedenquist, J.W., and Lowenstern, J.B., 1994, The role of magmas in the formation of hydrothermal ore deposits: Nature, v. 370, p. 519–527. Heimann, A., Beard, B.L., and Johnson, C.M., 2008, The role of volatile exsolution and subsolidus fluid/rock interactions in producing high 56Fe/54Fe ratios in siliceous igneous rocks: Geochimica et Cosmochimica Acta, v. 72, p. 4379–4396.

Hofstra, A.H., Meighan, C.J., Song, X., Samson, I., Marsh, E.E., Lowers, H.A., Emsbo, P., and Hunt, A.G., 2016, Mineral thermometry and fluid inclusion studies of the Pea Ridge iron oxide-apatite–rare earth element deposit, Mesoproterozoic St. Francois Mountains terrane, southeast Missouri, USA: Economic Geology, v. 111, p. 1985–2016.

Huang, F., Zhang, Z., Lundstrom, C.C., and Zhi, X., 2011, Iron and magnesium isotopic compositions of peridotite xenoliths from eastern China: Geochimica et Cosmochimica Acta, v. 75, p. 3318–3334. Hurwitz, S., and Navon, O., 1994, Bubble nucleation in rhyolitic melts: Experiments at high pressure, temperature, and water content: Earth and Planetary Science Letters, v. 122, p. 267–280.

Husman, J.R., 1989, Gold, rare earth element, and other potential by-products of the Pea Ridge iron ore mine: Missouri Department of Natural Resources, Contributions to Precambrian Geology 21, Open File Report OFR-89-78-MR, 18 p.

Johnson, C.A., Day, W.C., and Rye, R.O., 2013, Stable isotope geochemistry of the Pea Ridge iron oxide-rare earth element deposit, St. Francois Mountains, southeastern Missouri: Temperature of ore formation, source of hydrothermal fluid, and source of sulfur [abs.]: Geological Society of America Abstracts with Programs, v. 45, no. 7, p. 499.

Johnson, C.A., Day, W.C., and Rye, R.O., 2016, Oxygen, hydrogen, sulfur, and carbon isotopes in the Pea Ridge magnetite-apatite deposit, southeast Missouri, and sulfur isotope comparisons to other iron deposits in the region: Economic Geology, v. 111, p. 2017–2032.

Jonsson, E., Valentin, R.T., Högdahl, K., Harri, C., Weis, F., Nilsson, K.P., and Skelton, A., 2013, Magmatic origin of giant “Kiruna-type” apatite-iron-oxide ores in central Sweden: Scientific Reports, v. 3, p. 1644, doi:10.1038/ srep01644.

King, E.M., Trzaskus, A.P., and Valley, J.W., 2008, Oxygen isotope evidence for magmatic variability and multiple alteration events in the Proterozoic St. Francois Mountains, Missouri: Precambrian Research, v. 165, p. 49–60.

Kisvarsanyi, E.B., 1980, Granitic ring complexes and Precambrian hot-spot activity in the St. Francois terrane, Mid-continent region, United States: Geology, v. 8, p. 43–47.

——1981, Geology of the Precambrian St. Francois terrane, southeastern Missouri: Missouri Geological Survey, Reports of Investigations, v. 64, 60 p. ——1988, Precambrian ring complexes and mineralization in southeast Missouri, in Kisvarsanyi, G., and Grant, S.K., eds., Proceedings volume of the North American conference on tectonic control of ore deposits and the vertical and horizontal extent of ore systems: Rolla, Missouri, University of Missouri, p. 312–321.

——1990, General features of the St. Francis and Spavinaw granite-rhyolite terranes and the Precambrian metallogenic region of southeast Missouri: U.S. Geological Survey Bulletin 1932, p. 48–57.

Knipping, J.L., Bilenker, L.D., Simon, A.C., Reich, M., Barra, F., Deditius, A.P., Lundstrom, C., Bindeman, I., and Munizaga, R., 2015a, Giant Kiruna-type deposits form by efficient flotation of magmatic magnetite suspensions: Geology, v. 43, p. 491–594.

Knipping, J.L., Bilenker, L.D., Simon, A.C., Reich, M., Barra, F., Deditius, A.P., Wälle, M., Heinrich, C.A., Holtz, F., and Munizaga, R., 2015b, Trace elements in magnetite from massive iron oxide-apatite deposits indicate a combined formation by igneous and magmatic hydrothermal processes: Geochimica et Cosmochimica Acta, v. 171, p. 15–38.

Lidiak, E.G., Bickford, M.E., and Kisvarsanyi, E.B., 1993, Proterozoic geology of the eastern Midcontinent region: Geological Society of America, Decade of North American Geology, v. C-2, p. 259–270.

Loewen, M.W., and Bindeman, I., 2016, Oxygen isotope thermometry reveals high magmatic temperatures and short residence times in Yellowstone and other hot-dry rhyolites compared to cold-wet systems: American Mineralogist, v. 101, p. 1222–1227.

Lowell, G.R., and Rämö, O.T., 1999, Petrology and geochemistry of the Shepherd Mountain Gabbro: Implications for basalt genesis at 1.33 Ga in southeast Missouri [abs.]: Geological Society of America Abstracts with Programs, v. 31, p. 32.

Marikos, M.A., Nuelle, L.M., and Seeger, C.M., 1990, Geologic mapping and evaluation of the Pea Ridge iron ore mine (Washington County, Missouri) for rare earth element and precious metals potential—a progress report: U.S. Geological Survey Bulletin 1932, p. 76–81.

Matveev, S., and Ballhaus, C., 2002, Role of water in the origin of podiform chromitite deposits: Earth and Planetary Science Letters, v. 203, p. 235–243.

Mercer, C.N., Watts, K.E., Meighan, C.J., and Bennett, M.M., 2015, Mineral and melt inclusion constraints on the petrogenesis of regional magmas and magnetite ore from the Pea Ridge (IOA-REE) and Boss Bixby (IOCG) deposits, USA [abs.]: Society of Economic Geologists Annual Meeting, 2015, Hobart, Tasmania, Abstract Volume.

Millet, M.A., Baker, J.A., and Payne, C.E., 2012, Ultra-precise stable Fe isotope measurements by high resolution multiple-collector inductively coupled plasma mass spectrometry with a 57Fe-58Fe double spike: Chemical Geology, v. 304, p. 18–25.

Newton, R.C., and Manning, C.E., 2000, Quartz solubility in concentrated aqueous NaCl solutions at deep crust-upper mantle metamorphic conditions: 2-15 kbar and 500-900°C: Geochimica et Cosmochimica Acta, v. 64, p. 2993–3005.

Neymark, L.A., Holm-Denoma, C.S., Pietruszka, A.J., Aleinikoff, J.N., Fanning, C.M., Pillers, R.M., and Moscati, R.J., 2016, High spatial resolution U-Pb geochronology and Pb isotope geochemistry of magnetite-apatite ore from the Pea Ridge iron oxide-apatite deposit, St. Francois Mountains, southeast Missouri, USA: Economic Geology, v. 111, p. 1915–1933.

Nold, J.L., 1988, The Pilot Knob hematite deposit, Iron County, Missouri—a Proterozoic volcano-sedimentary iron deposit [abs.]: Geological Society of America Abstracts with Programs, v. 20, no. 7, p. A141.

Nold, J.L., Davidson, P., and Dudley, M.A., 2013, The Pilot Knob magnetite deposit in the Proterozoic St. Francois Mountains terrane, southeast Missouri, USA: A magmatic and hydrothermal replacement iron deposit: Ore Geology Reviews, v. 53, p. 446–469.

Nold, J.L., Dudley, M.A., and Davidson, P., 2014, The southeast Missouri (USA) Proterozoic iron metallogenic province—types of deposits and genetic relationships to magnetite-apatite and iron oxide-copper-gold deposits: Ore Geology Reviews, v. 57, p. 154–171.

Nuelle, L.M., Kisvarsanyi, E.B., Seeger, C.M., Day, W.C., and Sidder, G.B., 1991a, Structural setting and control of the Pea Ridge magnetite deposit, Middle Proterozoic St. Francois terrane, Missouri [abs.]: Geological Society of America Abstracts with Programs, v. 23, no. 5, p. A292.

Nuelle, L.M., Seeger, C.M., Day, W.C., and Sidder, G.B., 1991b, Rare earth element- and gold-bearing breccia pipes of the Pea Ridge iron ore mine, Washington County, Missouri: Society for Mining, Metallurgy, and Exploration, Inc., Preprint, 14 p.

Nuelle, L.M., Day, W.C., and Sidder, G.B., 1992, Geology and mineral paragenesis of the Pea Ridge iron ore mine, Washington County, Missouri— origin of the rare-earth-element and gold-bearing breccia pipes: U.S. Geological Survey Bulletin 1989, p. A1–A11.

Nyström, J.O., Billström, K., Henríquez, F., Fallick, A.E., and Naslund, H.R., 2008, Oxygen isotope composition of magnetite in iron ores of the Kiruna type in Chile and Sweden: GFF [Geologiska Föreningen], v. 130, p. 177–188.

Panno, S.V., and Hood, W.C., 1983, Volcanic stratigraphy of the Pilot Knob iron deposits, Iron County, Missouri: Economic Geology, v. 78, p. 972–982.

Reed, M.J., Candela, P.A., and Piccoli, P.M., 2000, The distribution of rare earth elements between monzogranitic melt and the aqueous volatile phase in experimental investigations at 200 MPa and 800°C: Contributions to Mineralogy and Petrology, v. 140, p. 251–262.

Reich, M., Simon, A.C., Deditius, A., Barra, F., Chryssoulis, S., Lagas, G., Tardani, D., Knipping, J., Bilenker, L., Sanchez-Alfaro, P., Roberts, M.P., and Munizaga, R., 2016, Trace element signature of pyrite from the Los Colorados iron oxide-apatite (IOA) deposit, Chile: A missing link between Andean IOA and iron oxide copper-gold systems?: Economic Geology, v. 111, p. 743–761.

Seeger, C.M., Nuelle, L.M., and Marikos, M.A., 1989, Massive silicification and late stage quartz veining in the Pea Ridge Fe-REE deposit, southeast Missouri [abs.]: Geological Society of America Abstracts with Programs, v. 21, no. 6, p. 34.

Seeger, C.M., Nuelle, L.M., Day, W.C., Sidder, G.B., Marikos, M.A., and Smith, D.C., 2001, Geologic maps and cross sections of mine levels at the Pea Ridge iron mine, Washington County, Missouri: U.S. Geological Survey Miscellaneous Field Studies Map MF-2353.

Severmann, S., and Anbar, A.D., 2009, Reconstructing palaeoredox conditions through a multitracer approach: The key to the past is the present: Elements, v. 5, p. 359–364.

Shüßler, J., 2008, Controls on stable iron isotope variations in magmatic systems—significance of mineral-melt isotopic fractionation in experiments and nature: Ph.D. thesis, Hannover, Germany, Faculty of Natural Science, Gottfried Wilhelm Leibniz Universität, 165 p.

Sidder, G.B., Nuelle, L.M., Day, W.C., Rye, R.O., Seeger, C.M., and Kisvarsanyi, E.B., 1991, Paragenesis and conditions of formation of the Pea Ridge iron and rare-earth element deposit, Missouri [abs.]: Geological Society of America Abstracts with Programs, v. 23, no. 5, p. A292.

Sidder, G., Day, W., and Rye, R., 1993a, Fluid inclusion and stable isotope data for the Pea Ridge Fe-REE orebody, Missouri [abs.]: Geological Society of America Abstracts with Programs, v. 25, no. 3, p. 81.

Sidder, G.B., Day, W.C., Nuelle, L.M., Seeger, C.M., and Kisvarsanyi, E.B., 1993b, Mineralogic and fluid-inclusion studies of the Pea Ridge iron-rare-earth-element deposit, southeast Missouri: U.S. Geological Survey Bulletin 2039, p. 205–216.

Sides, J.R., Bickford, M.E., Shuster, R.D., and Nusbaum, R.I., 1981, Calderas in the Precambrian terrane in the St. Francois Mountains, southeastern Missouri: Journal of Geophysical Research, v. 86, no. B11, p. 10,349–10,364.

Simon, A.C., Pettke, T., Candela, P.A., Piccoli, P.M., and Heinrich, C.A., 2004, Magnetite solubility and iron transport in magmatic-hydrothermal environments: Geochimica et Cosmochimica Acta, v. 68, p. 4905–4914.

Sims, P.K., 1990, Geologic setting and ages of Proterozoic anorogenic rhyolite-granite terranes in the central United States: U.S. Geological Survey Bulletin 1932, p. 40–47.

Tanis, E.A., Simon, A.C., Tschauner, O., Chow, P., Xiao, Y., Shen, G., Hanchar, J.M., and Frank, M., 2012, Solubility of xenotime in 2 M HCl aqueous fluid from 1.2 to 2.6 GPa and 300 to 500°C: American Mineralogist, v. 97, p. 1708–1713.

Taylor, H.P., 1967, Oxygen isotope studies of hydrothermal mineral deposits, in H.L. Barnes, ed., Geochemistry of hydrothermal ore deposits: New York, Holt, Rinehart and Winston, p. 109–142.

Trail, D., Bindeman, I.N., Watson, E.B., and Schmitt, A.K., 2009, Experimental calibration of oxygen isotopic fractionation factors between quartz and zircon: Geochimica et Cosmochimica Acta, v. 73, p. 7110–7126.

Valley, J.W., Lackey, J.S., Cavosie, A.J., Clechenko, C.C., Spicuzza, M.J., Basei, M.A., Bindeman, I.N., Ferreira, V.P., Sial, A.N., King, E.M., Peck, W.H., Sinha, A.K., and Wei, C.S., 2005, 4.4 billion years of crustal maturation: Oxygen isotope ratios of magmatic zircon: Contributions to Mineralogy and Petrology, v. 150, p. 561–580.

Valley, P.M., Hanchar, J.M., and Whitehouse, M.J., 2011, New insights on the evolution of the Lyon Mountain Granite and associated Kiruna-type magnetite-apatite deposits: Adirondack Mountains, New York State: Geosphere, v. 7, p. 357–389.

Van Schmus, W.R., Bickford, M.E., and Turek, A., 1996, Proterozoic geology of the east-central Midcontinent basement: Geological Society of America Special Paper 308, p. 7–32.

Weis, F., 2013, Oxygen and iron isotope systematics of the Grängesberg mining district (GMD), central Sweden: Ph.D. dissertation, Uppsala, Sweden, Uppsala Universitet, 77 p.

Wenner, D.B., and Taylor, H.P., 1976, Oxygen and hydrogen isotope studies of a Precambrian granite-rhyolite terrane, St. Francois Mountains, southeastern Missouri: Geological Society of America Bulletin, v. 87, p. 1587–1598.

Zhao, Z.F., and Zheng, Y.F., 2003, Calculation of oxygen isotope fractionation in magmatic rocks: Chemical Geology, v. 193, p. 59–80

## TABLES

Table 2.1: Oxygen and iron stable isotope ratios of magnetite measured in this study from the Pea Ridge and Pilot Knob iron oxide-apatite orebodies

| Location | Sample | Depth (ft) | $\delta^{18}O$ (‰) | 2σ | $\delta^{56}Fe$ (‰) | 2σ |
|---|---|---|---|---|---|---|
| Pea Ridge, USA | PR-148 | 2125 | 4.56 | 0.06 | | |
| | PR-153 | 2275 | 3.18 | 0.04 | | |
| | PR-158 | 2275 | | | 0.26 | 0.08 |
| | PR-18 | 2370 | 2.12 | 0.04 | 0.32 | 0.05 |
| | PR-64A | 2370 | 4.87 | 0.10 | 0.20 | 0.05 |
| | PR-65 | 2370 | 5.10 | 0.06 | | |
| | PR-73 | 2370 | 1.24 | 0.06 | | |
| | PR-77A | 2370 | 5.11 | 0.08 | 0.21 | 0.02 |
| | PR-82A | 2370 | 5.90 | 0.06 | 0.10 | 0.02 |
| | PR-82B | 2370 | 7.03 | 0.04 | 0.03 | 0.02 |
| | | | | | 0.07 | 0.05 |
| | PR-163 | 2370 | 1.02 | 0.06 | | |
| | PR-37 | 2440 | 4.50 | 0.06 | 0.07 | 0.05 |
| | PR-144 | 2440 | 5.04 | 0.08 | 0.26 | 0.09 |
| | | | | | 0.10 | 0.02 |
| | 954-5-205 | ? | 5.50 | 0.08 | | |
| Pilot Knob, USA | PK-1145-830.1 | 830.1 | 3.26 | 0.08 | | |
| | PK-1145-965.8 | 965.8 | 6.68 | 0.08 | 0.19 | 0.03 |
| | PK-1145-979.5 | 979.5 | 6.21 | 0.06 | 0.24 | 0.04 |
| | PK-1086-918[1] | 918 | | | 0.14 | 0.05 |
| | PK-1098-715[1] | 715 | | | 0.18 | 0.03 |
| | PK-1174-1348[1] | 1348 | | | 0.06 | 0.05 |
| | PK-2079-1160[1] | 1160 | | | 0.27 | 0.06 |

[1]Sample provided by Dr. John Nold of the University of Central Missouri

| Table 2.2: Analytical conditions for electron probe microanalysis (EPMA) | | | | |
|---|---|---|---|---|
| 20kV, 30 nA, focused; MDL is mean detection limit | | | | |
| **Element/Line** | **Crystal** | **Standard** | **Counting time [s]** | **MDL [Oxide wt%]** |
| Mg/Kα | TAP | geikielite | 100 | 0.02 |
| Al/Kα | TAP | zoisite | 100 | 0.02 |
| Si/Kα | LTAP | wollastonite | 100 | 0.01 |
| Ca/Kα | PET | wollastonite | 100 | 0.01 |
| Ti/Kα | PET | ilmenite | 120 | 0.02 |
| V/Kα | LLIF | $V_2O_5$ | 120 | 0.01 |
| Cr/Kα | LLIF | $Cr_2O_3$ | 100 | 0.01 |
| Mn/Kα | LLIF | rhodondite | 100 | 0.01 |
| Fe/Kα | LLIF | magnetite | 20 | 0.03 |

Table 2.3: EPMA data for three generations of magnetite (see Figure 2.2) in Pea Ridge sample PR-144, reported in weight percent oxides. Blank spaces indicate an analysis that was below detection limit as reported in Table 2.2. The generations X, Y, Z are shown in Figure 2.2 and described in the Figure 2.2 caption.

| Magnetite Generation | MgO | $Al_2O_3$ | $SiO_2$ | CaO | $TiO_2$ | $V_2O_3$ | $Cr_2O_3$ | MnO | FeO | Total |
|---|---|---|---|---|---|---|---|---|---|---|
| **X** | | | 0.03 | | | 0.06 | 0.01 | | 93.07 | 93.19 |
| | | 0.02 | 0.02 | | | 0.07 | 0.01 | | 92.96 | 93.11 |
| | | | 0.02 | | | 0.06 | | 0.05 | 93.08 | 93.23 |
| | | 0.02 | 0.05 | | | 0.06 | | 0.06 | 92.95 | 93.14 |
| | | 0.04 | 0.02 | | | 0.06 | 0.01 | | 93.38 | 93.52 |
| | | | 0.01 | | | 0.06 | | | 93.39 | 93.51 |
| | | | 0.02 | | | 0.07 | | 0.04 | 93.50 | 93.64 |
| | | 0.03 | 0.02 | | | 0.06 | | 0.03 | 93.19 | 93.36 |
| | | | 0.02 | | 0.25 | 0.06 | | 0.01 | 92.77 | 93.12 |
| | | | 0.03 | | | 0.06 | | 0.02 | 93.15 | 93.28 |
| | | | 0.02 | | | 0.06 | | | 93.29 | 93.40 |
| | | 0.04 | 0.02 | | 0.09 | 0.07 | | 0.02 | 93.33 | 93.56 |
| | | 0.02 | 0.04 | | 0.26 | 0.05 | 0.01 | 0.01 | 92.68 | 93.08 |
| | | | 0.03 | | 0.14 | 0.05 | | 0.01 | 93.41 | 93.67 |
| | | 0.02 | 0.02 | | 0.06 | 0.06 | 0.01 | 0.02 | 93.45 | 93.64 |
| | | 0.07 | 0.10 | | 0.20 | 0.06 | 0.01 | 0.01 | 92.54 | 93.00 |
| | | | 0.03 | | 0.25 | 0.05 | 0.01 | | 92.55 | 92.91 |
| | | | 0.02 | | 0.15 | 0.06 | | | 93.06 | 93.34 |
| | | 0.02 | 0.02 | | | 0.06 | 0.01 | | 93.16 | 93.28 |
| | | | 0.02 | | | 0.06 | | 0.02 | 93.38 | 93.48 |
| | | | 0.02 | | | 0.06 | | 0.02 | 92.96 | 93.08 |
| **Y** | | 0.06 | 0.02 | | | 0.04 | | | 90.26 | 90.39 |
| | | 0.05 | 0.02 | | | 0.07 | | | 89.85 | 89.98 |
| | | 0.09 | 0.02 | | 0.05 | 0.10 | 0.01 | | 89.81 | 90.06 |
| | | 0.06 | 0.01 | | 0.09 | 0.07 | 0.03 | | 89.95 | 90.21 |

| | | | | | | | | | |
|---|---|---|---|---|---|---|---|---|---|
| | | 0.06 | 0.02 | 0.13 | 0.05 | | | 90.33 | 90.57 |
| | | 0.06 | 0.03 | 0.02 | 0.08 | | | 90.23 | 90.41 |
| | | 0.08 | 0.02 | 0.35 | 0.06 | 0.01 | | 89.59 | 90.11 |
| | | 0.06 | 0.02 | | 0.07 | 0.02 | | 89.96 | 90.23 |
| | | 0.03 | 0.02 | | 0.07 | 0.01 | | 89.91 | 90.04 |
| | | 0.07 | 0.02 | | 0.10 | | | 90.52 | 90.71 |
| | | 0.12 | 0.01 | | 0.05 | | | 90.51 | 90.68 |
| | | 0.04 | 0.01 | | 0.07 | | | 89.81 | 89.94 |
| **Z** | 0.05 | 0.03 | 0.02 | 15.93 | 0.03 | 0.02 | 0.02 | 74.96 | 91.03 |
| | 0.04 | 0.05 | 0.01 | 13.14 | 0.05 | | 0.02 | 77.57 | 90.90 |
| | 0.04 | 0.04 | 0.02 | 13.26 | 0.05 | | 0.01 | 77.84 | 91.27 |
| | 0.05 | 0.04 | 0.03 | 10.62 | 0.07 | 0.01 | 0.02 | 80.17 | 90.99 |
| | 0.04 | 0.04 | 0.02 | 13.10 | 0.05 | | 0.02 | 77.31 | 90.58 |
| | 0.19 | 0.03 | 0.01 | 15.08 | 0.04 | | 0.05 | 76.32 | 91.72 |
| | 0.10 | 0.06 | 0.02 | 14.48 | 0.05 | | 0.03 | 75.77 | 90.49 |
| | 0.04 | 0.06 | 0.02 | 14.71 | 0.04 | | 0.01 | 75.89 | 90.79 |
| | 0.05 | 0.03 | 0.01 | 13.11 | 0.05 | | 0.02 | 77.68 | 90.97 |
| | 0.06 | 0.04 | 0.01 | 14.80 | 0.05 | | 0.02 | 76.15 | 91.13 |

# CHAPTER III

## FORMATION OF THE MANTOVERDE IRON OXIDE - COPPER - GOLD DEPOSIT, CHILE: INSIGHTS FROM FE AND O STABLE ISOTOPES AND COMPARISON TO IRON OXIDE - APATITE DEPOSITS


## ABSTRACT

The Mantoverde iron oxide – copper – gold (IOCG) deposit, Chile, contains hundreds of millions of tonnes (Mt) of mineable iron oxide and copper sulfide ore. While there is agreement that mineralization at Mantoverde was caused by hydrothermal fluid(s), there is a lack of consensus for the role(s) that non-magmatic vs. magmatic fluid(s) played during the evolution of the mineralized system. In order to overcome the extensive hydrothermal overprint at Mantoverde, which is known to disturb most conventional stable isotope systems (e.g., oxygen), we report the first $\delta^{56}Fe$ and $\delta^{18}O$ pairs for early-stage magnetite and late-stage hematite that fingerprint the source of the ore fluids for these modally dominant oxide minerals in the Mantoverde system. Magnetite $\delta^{56}Fe$ values range from 0.46 ± 0.04 ‰ to 0.58 ± 0.02 ‰, and average 0.51 ± 0.16 ‰ (n = 10; 2σ). Three hematite $\delta^{56}Fe$ values were measured to be 0.34 ± 0.10 ‰, 0.42 ± 0.09 ‰, and 0.46 ± 0.06 ‰. Magnetite $\delta^{18}O$ values range from 0.69 ± 0.04 ‰ to 4.61 ± 0.05 ‰ and average 2.99 ± 2.70 ‰ (n = 9; 2σ). Hematite $\delta^{18}O$ values range from -1.36 ± 0.05 ‰ to 5.57 ± 0.05 ‰ and average 0.10 ± 5.38 ‰ (n = 6; 2σ). These new $\delta^{56}Fe$ and $\delta^{18}O$ values complement published data for isotopes of Re, Os, C, O, S, Sr, Pb, Ar, Kr, Xe and halogen ratios for samples from hypogene mineralization, and fingerprint a magmatic-hydrothermal fluid as the predominant ore forming fluid responsible for IOCG mineralization in the Mantoverde deposit.

## INTRODUCTION

Iron oxide - copper - gold (IOCG) deposits contain anomalous concentrations of magnetite and/or hematite and Cu- and Au-bearing sulfides. Since the discovery in the 1970s of the giant Precambrian Olympic Dam deposit in Australia, the largest discovered deposit of this type, investigations of IOCG deposits have focused on determining the source reservoir(s) of the ore-forming fluids (and their contained metals) responsible for mineralization (Roberts and Hudson 1983; Hitzman et al. 1992; Porter 2000). Iron oxide - copper - gold deposits occur globally, are commonly associated with crustal extension related to subduction zone tectonism (Sillitoe 2003; Richards and Mumin 2013a,b; Montreuil et al. 2016), and ages of mineralization range from the Archean to the Cenozoic (Groves et al. 2010; Barton 2014). The deposits typically exhibit variable quantities of their namesake metals, containing up to several billion tonnes of Fe ore and hundreds of millions of tonnes of Cu ore, and some deposits contain elevated and mineable grades of light rare earth elements (LREE), P, U, Ag, Co, Ba and F (Sillitoe 2003; Williams et al. 2005; Groves et al. 2010; Barton 2014). Despite decades of studies, and multiple comprehensive genetic models (Mumin et al. 2010; Richards and Mumin 2013a,b; Barton 2014; Simon et al. 2018), consensus on the formation of IOCG deposits remains elusive. Disagreement on a genetic model stems from a lack of correlation between IOCG deposits and specific tectonic or magmatic settings and a lack of geochemical constraints on the source of the ore fluids required for efficient metal transport and mineralization. Working hypotheses proposed to explain the origin of the ore-forming fluids include: 1) a magmatic-hydrothermal fluid evolved from a silicate magma (e.g., Pollard 2006; Nyström et al. 2008; Rieger et al. 2010, 2012; Jonsson et al. 2013; Knipping et al. 2015a,b; Reich et al. 2016); 2) non-magmatic hydrothermal fluids such as meteoric fluids or basinal brines driven by heat from

either a magma body or the crustal geotherm (e.g., Barton and Johnson 1996; Sillitoe and Burrows 2002; Benavides et al. 2007); 3) metamorphic hydrothermal fluids derived from metamorphic devolatilization and water-rock interaction (Fisher and Kendrick 2008); and 4) a magmatic-hydrothermal fluid evolved from a volatile-bearing iron oxide melt, which itself evolved via liquid immiscibility from a silicate magma (Nyström and Henríquez 1994; Travvisany et al. 1995; Naslund et al. 2002; Barton 2014). However, it is relevant to note that no single genetic model explains the formation of the whole spectrum of IOCG deposits, and it has been proposed that the smaller and rarer Phanerozoic IOCG deposits formed in tectonic settings where conditions similar to those in the Precambrian were replicated (Groves et al. 2010; Richards and Mumin 2013a,b).

Within the Andean Cretaceous IOCG province, many IOCG deposits are spatially and temporally associated with Kiruna-type iron oxide - apatite (IOA) deposits, which have been suggested to be the sulfur-poor end member of ore systems that contain both IOA and IOCG mineralization. Sillitoe (2003) reported that IOCG deposits in general are associated with calcic, potassic and sodic alteration, and that IOCG systems transition at depth to IOA mineralization. Sillitoe (2003) hypothesized that Andean IOCG deposits formed from magmatic-hydrothermal fluids, which evolved and scavenged metals, Cl and S from intermediate to mafic composition magmas, and were channeled toward the surface via ductile and brittle fault systems (e.g., Atacama Fault System). Recent studies at the world class Los Colorados IOA deposit, Chile, support the hypothesis for a genetic connection between IOCG and Kiruna-type IOA deposits (Knipping et al. 2015a,b; Bilenker et al. 2016; Reich et al. 2016; Barra et al. 2017). These aforementioned studies report and discuss data that are consistent with IOCG mineralization resulting from a magmatic-hydrothermal fluid, which contains sufficient dissolved metals and S

after IOA ore formation to form IOCG mineralization at shallower levels of the crust. These studies do not eliminate the potential presence and importance of non-magmatic fluids, which may mix with ascending S- and metal-enriched magmatic-hydrothermal fluids and promote mineralization. Data from many studies indicate that fluids from different geologic sources (i.e., basinal brines, meteoric water, magmatic-hydrothermal fluid) play a role in the evolution of IOCG deposits (Williams et al. 2005; Groves et al. 2010; Barton 2014). However, the degree of influence these secondary, non-magmatic fluids had on ore formation remains controversial, and the primary source reservoir of ore metals remains unconstrained.

In this study, we focus on the world class Mantoverde IOCG deposit in northern Chile (Fig. 3.1). New stable Fe and O isotope data are reported for magnetite and hematite that fingerprint a magmatic source reservoir for these modally dominant constituents in the Mantoverde orebodies. The data complement published data for isotopes of Re, Os, C, O, S, Sr, Pb, Ar, Kr, Xe, and halogen ratios for samples from hypogene mineralization, and are consistent with a magmatic-hydrothermal ore forming fluid for magnetite and sulfide mineralization at Mantoverde. We also present stable Fe and O isotope data from IOA deposits in the Chilean Iron Belt and other mineralized districts and use the combined data set to discuss the evolution of Mantoverde as part of a continuum where S-Cu-Au-poor iron oxide - apatite mineralization represents the deeper levels of mineralized systems that transition from IOA mineralization at depth to IOCG mineralization at shallow levels of the crust.

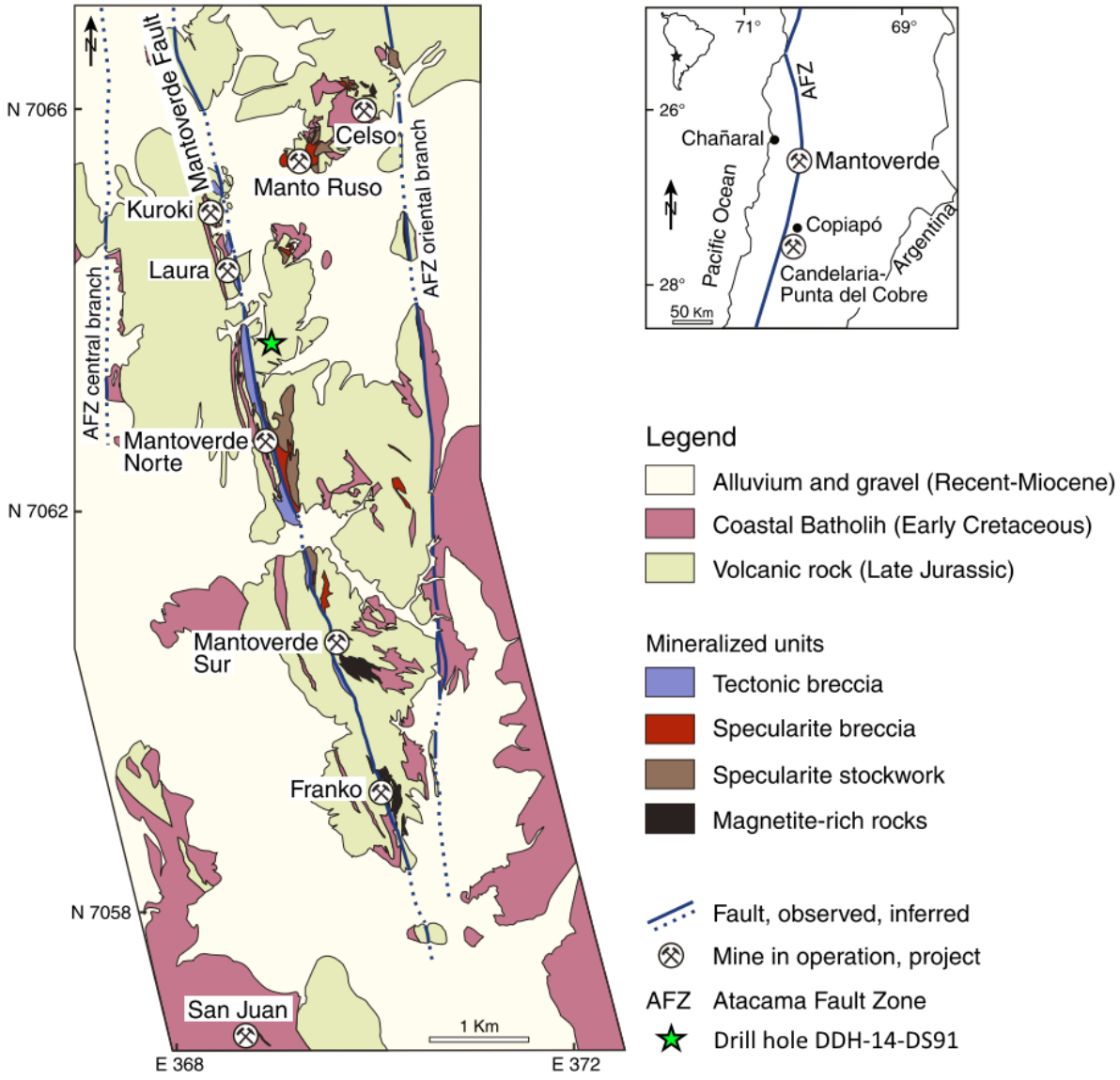


Figure 3.1: Map of the Mantoverde district showing general district geology, structures, iron oxide deposits; the location of the drill hole from samples were collected is shown. The inset shows the general location of the deposit relative to Copiapó, Chile. Figure from Rieger et al. (2012).

## GEOLOGIC BACKGROUND AND PREVIOUS STUDIES AT MANTOVERDE

The Mantoverde deposit is located approximately 50 km east of the Pacific coastline in northern Chile along the Atacama Fault Zone (AFZ) in what has become known as the Chilean Iron Belt (CIB). The formation of the CIB is associated with the subduction of the Aluk plate

under the South American continent. Subduction led to arc and associated back-arc basin formation during Jurassic – Early Cretaceous magmatism, which developed on late-Paleozoic to Triassic basement (Mpodozis and Ramos 1990). Late Jurassic andesitic volcaniclastic conglomerates, breccias, or flows make up the majority of rock types within the CIB. These volcanic rocks were subsequently intruded by Cretaceous granitoids of the Chilean Coastal Batholith (Lara and Godoy 1998), including subalkaline to alkaline, metaluminous, magnetite series, I-type granitoids of the calc-alkaline suite ranging from diorite to granodiorite, tonalite, and monzodiorite to quartz monzodiorite, all of which range in age from 90 to 130 Ma (Rieger et al. 2010; Barra et al. 2017). The majority of volcanic rocks within the Mantoverde IOCG district belong to the Late Jurassic La Negra Formation and Early Cretaceous Punta del Cobre Formation (Benavides et al. 2007). The Mantoverde IOCG deposits themselves are hosted in basaltic andesite and andesite flows and volcaniclastic rocks correlated with the La Negra Formation (Lara and Godoy 1998). The regionally extensional, north-south trending strike-slip Atacama Fault Zone transects both the arc and basement rocks, and the region is covered by Neogene to Quaternary alluvial and colluvial deposits.

The central and eastern branches of the Atacama Fault Zone in the Mantoverde district mark the western and eastern limits of IOCG mineralization in the Mantoverde system, and are connected by the NW-trending, east-dipping Mantoverde Fault, which is interpreted to be a scissor fault (Fig. 3.1; Zamora and Castillo 2001; Rieger et al. 2012). The Mantoverde Fault is considered to be the main ore fluid conduit and hosts the majority of ore mineralization in the deposit. Mineralization styles at Mantoverde include specularite-cemented hydrothermal breccias, specularite stockwork zones, magnetite-rich zones where magnetite occurs as cement in hydrothermal breccias, stockworks, and disseminations, and tectonic breccias (Vila et al. 1996;

Rieger et al. 2010). The Mantoverde deposit can be described as a zoned system, with magnetite occurring at depth and hematite occurring at shallow or distal levels of the Mantoverde Fault. The oxidation level reaches between 200 and 250 m below the surface and marks the transition of the supergene zone to the hypogene zone where pyrite and chalcopyrite are commonly present (Rieger et al. 2012). The host rocks are characterized by intense K-metasomatism, silicification, and carbonatization and lack district scale Na and/or Ca alteration (Marschik and Fontboté 2001; Rieger et al. 2010).

Mineralization at Mantoverde is interpreted to be the result of three major fluid events that define the paragenetic stages as described by Rieger et al. (2010): 1) the early Iron Oxide Stage, 2) the Sulfide Stage, and 3) the Late Stage. Benavides et al. (2007) recognized slightly different paragenetic relations and separated them into stages I, II, III, and IV, where stage I is responsible for magnetite mineralization, stage II is responsible for hydrolytic alteration resulting in minor hematite and pyrite, stage III is responsible for the majority of hematite mineralization, and stage IV resulted in the terminal calcite and quartz veining. We follow the paragenetic scheme of Rieger et al. (2010). Magnetite formed during the Iron Oxide Stage at deeper levels of the system, at temperatures between 278 and 530 °C (median = 435 °C), whereas hematite crystallized at more shallow levels at temperatures between 208 and 468 °C (median = 334 °C). These temperature ranges are based on fluid inclusion microthermometry of primary, hypersaline, magnetite- and hematite-bearing L-V-S fluid inclusions hosted in Iron Oxide Stage quartz that is temporally equivalent to magnetite and hematite (Benavides et al. 2007; Rieger et al. 2012). Calculated salinities vary from 32 to 64 wt. % NaCl eq., with a median salinity of 42 wt. % NaCl eq. (Rieger et al. 2012).

Sulfide Stage sulfide mineralization, which paragenetically follows Iron Oxide mineralization stage and occurred before late-stage calcite (Rieger et al., 2012), accounts for the bulk of pyrite and chalcopyrite in the Mantoverde district. The temperature range for the sulfide mineralization was bracketed by the homogenization temperatures for the Iron Oxide stage described above and by fluid inclusion homogenization temperatures for L-V-S and L-V inclusions hosted in late-stage calcite (Rieger et al. 2012). Three-phase L-V-S fluid inclusions homogenize by halite dissolution from 221 to 325 °C (median = 266 °C), with salinities ranging from 33 to 40.2 wt. % NaCl eq. (mean = 35.7 wt. %); one inclusion homogenized at 462 °C by vapor bubble disappearance. Two-phase L-V inclusions homogenize by halite dissolution from 160 °C to 322 °C (median = 244 °C), with salinities ranging from 30.1 to 40.0 wt. % NaCl eq. (mean =34.3 wt. %).

Several studies report isotope data for host rocks, gangue minerals, and fluid inclusions associated with mineralization in the Mantoverde district, including isotopes of C, O, S, Sr, Pb, and noble gas isotopes of Ar, Kr, and Xe (Benavides et al. 2007, 2008; Rieger et al. 2010, 2012; Marschik and Kendrick 2015). Benavides et al. (2007) reported overlapping $\delta^{34}S$ values for pyrite and chalcopyrite that range from -6.8 to +11.2 ‰. Those authors pointed out that Iron Oxide Stage pyrite, cogenetic with main stage magnetite, has a narrow range of $\delta^{34}S$ values from -0.6 to +2 ‰, whereas pyrite from main Sulfide Stage (Stage II of Benavides et al. 2007) of mineralization yielded a wider range of $\delta^{34}S$ values from -1.2 to +9.1 ‰. The youngest generation of sulfides in the district yielded a wider range of $\delta^{34}S$ values from +1.4 to +11.2 ‰. Rieger et al. (2010) reported $\delta^{34}S$ values for hypogene chalcopyrite and pyrite associated with Iron Oxide Stage magnetite that range from -6 to 3 ‰ and 1 to 11 ‰, respectively. A decreasing trend of $\delta^{34}S$ values in chalcopyrite was observed from north to south in the district

(approximately 5 km from the Manto Ruso deposit in the far north to Manto Sur deposit in the south), and may be related to depth within the system, controlled by the tilting of the hanging wall block of the Mantoverde fault. Deeper magnetite-rich portions of the system were tilted upward and are exposed to the south, whereas more shallow, more oxidized, and hematite-rich portions of the system were tilted downward and are exposed to the north (Mantos Copper, written communication). Rieger et al. (2010) offered an alternative explanation for this trend, suggesting that the southern part of the district could represent the proximal upflow zone of mineralizing fluids, and the northern part the proximal outflow zone. Both Benavides et al. (2007) and Rieger et al. (2010) concluded that the $\delta^{34}S$ data require a magmatic-hydrothermal ore fluid for the main magnetite and sulfide stages, and that a non-magmatic fluid was present during later stages of mineralization. These studies demonstrate that at Mantoverde, the $\delta^{34}S$ values from sulfides from the magnetite-rich ores, which make up the bulk of the hypogene ore, preclude mixing of a significant volume of a non-magmatic fluid. Rieger et al. (2010) also point out that mixing of a metal-bearing magmatic fluid and a sulfate-bearing non-magmatic fluid would result in low $\delta^{34}S$ values in the oxidized hematite-rich zones, and higher $\delta^{34}S$ values in the reduced magnetite-rich zones, which is the opposite of what is observed at Mantoverde.

Strontium isotope data for the Mantoverde district are published in Rieger et al. (2010) for altered volcanic rocks and hydrothermal calcite. The initial Sr isotope data from altered volcanic rocks range between igneous (0.703 to 0.705) and Early Cretaceous seawater (0.70235 to 0.70746; Jones et al. 1994). Calcite has an initial Sr isotope signature consistent with either an igneous Sr source or equilibration with an igneous source. Rieger et al. (2010) concluded that the Sr isotope data are compatible with a cooling magmatic-hydrothermal fluid that mixed with meteoric fluids, possibly coeval seawater. Rieger et al. (2010) also reported Pb isotope

compositions for chalcopyrite from Sulfide Stage sulfides. Their values of Pb isotope compositions of chalcopyrite define a narrow range that overlaps with Pb isotope compositions from Early Cretaceous plutonic rocks from the Candelaria-Punta del Cobre district near Copiapó (Lucassen et al. 2006). Considering that the Pb isotopes were measured in Sulfide Stage chalcopyrite, these Pb isotope data were interpreted by Rieger et al. (2010) to indicate that Pb and Cu were likely derived from Early Cretaceous magmatism and not the Jurassic country rocks, and concluded that the Pb isotope values are consistent with a (predominantly) magmatic source for Pb and Cu. Further work by Rieger et al. (2012) found that $\delta^{13}C$ isotopes of calcite intimately associated with hematite from Late Stage mineralization indicate that a fluid in equilibrium with calcite would exhibit a $\delta^{13}C$ between -5.0 and -3.0 ‰. This Late Stage fluid lies between upper mantle and marine limestone or subducted carbon $\delta^{13}C$ values (-5 ‰ and -1 ‰, respectively), and indicates the significance of magmatic fluids even during the latest mineralization at Mantoverde.

Marschik and Kendrick (2015) reported noble gas (Ar, Kr, Xe) and halogen (Cl, Br, I) compositions of fluid inclusions in hydrothermal quartz and calcite from the Mantoverde district. They report $^{40}Ar/^{36}Ar$ ratios that indicate crustal or mantle-derived excess $^{40}Ar$ in fluid inclusions in most samples, with salinities for these fluid inclusions that range from 3.5 to 64 wt. % NaCl eq. and Br/Cl and I/Cl molar halogen abundance ratios that are comparable to, but do not distinguish among, mantle, magmatic-hydrothermal fluid, and bittern sedimentary formation water values. The authors highlight that these values show no evidence of the involvement of evaporites, precluding halite dissolution as the dominant source of fluid salinity, and conclude that their findings are compatible with mixing of magmatic-hydrothermal fluids and evaporated seawater modified by interaction with back-arc basin sediments.

## METHODS

Magnetite and hematite were sampled from a single drill core provided by Mantos Copper (Fig. 3.1). The aim of sample selection was to select iron oxides that were free of gangue minerals, to quantify the trace element chemistry of magnetite in selected samples, and to quantify stable Fe and O isotope concentrations in magnetite and hematite from those same samples.

### *Sample selection*

Access to drill core samples was provided by Mantos Copper. Samples were collected from drill core DDH-14-DS91, located just north of Mantoverde Norte pit, and are representative of multiple mineralization styles. The surface elevation of this drill hole is approximately 1008 meters above sea level (m.a.s.l.) with a western azimuth. Samples in this study were collected from a core depth of 262 m to 492 m. Several fragments of rock from each sampled depth were prepared for electron probe micro analyses (EPMA). Additionally, samples from five depths (291, 340, 355, 456, 492 m) were cut into thin sections for transmitted and reflected light microscopy. For isotope analyses, magnetite grains were sampled where present, and hematite from veinlets was sampled where magnetite was not present. Iron oxides are not abundantly present at all depths and consequently were not sampled at every depth. See Table 3.1 for a list of analyses conducted for samples from each depth.

### *Hand sample descriptions*

Massive magnetite is the modally dominant mineral in the upper parts of the core, from 262 m to 314 m, and becomes more disseminated with depth. Magnetite is a modally minor

mineral, or absent, in the lower section of the core. Potassium feldspar and chlorite are the dominant matrix forming minerals throughout the core, with common but varying amounts of sericite after K-feldspar throughout. Pyrite is a major mineral in the upper parts of core (262 to 314 m) where it occurs as large blotches and filling veins. Chalcopyrite is a modally minor (<5 vol. %) mineral and occurs with greater abundance than pyrite in the K-feldspar-rich samples at depth. Specularite veinlets (≤1-2 mm), K-feldspar veinlets (0.5-1.5 mm), and calcite veinlets (0.2-5 mm) occur pervasively throughout the drill core, and quartz occurs as a minor mineral in some K-feldspar veinlets. Samples at depths ≥331.7 m have greater amounts of K-feldspar alteration, with the K-feldspar matrix containing large blotches of microcline and thin specularite (<0.5 mm), pyrite (~1 mm), and chalcopyrite (~1 mm) veinlets. See Fig. 3.2 for photos of representative hand samples and Table 3.2 for mineralization styles from nearby deposits.

*Sample preparation for stable isotope analysis*

Samples of massive magnetite (e.g., Fig. 3.2A) were wrapped in weighing paper and crushed with a plastic-sheathed mallet to reduce the grain size to less than 1 mm and disaggregate magnetite and gangue minerals. Magnetite grains were separated from the crushed material by use of a hand magnet wrapped in a Kimwipe. Hematite veinlets were broken open with the plastic-sheathed mallet, whereupon hematite (e.g., Fig. 3.2B) was easily friable with the use of a plastic scraper. The separated grains of magnetite and hematite were then inspected using a binocular microscope at ~40x magnification to pick the most uniform grains and to remove any other remaining minerals. Grain sizes of magnetite between ~0.3 and 0.8 mm and of hematite between ~0.1 and 0.6 mm were selected for O and Fe isotope analyses.

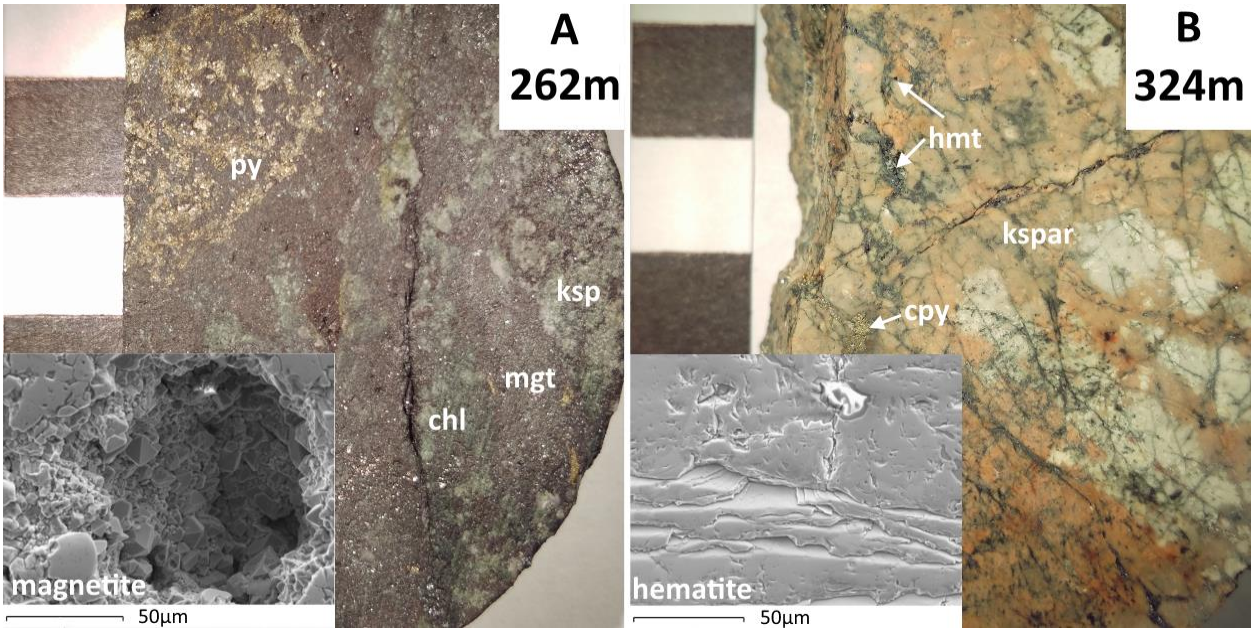


Figure 3.2: Hand sample photographs of drill core DDH-14-DS91, located at 368875m E 7063667m N, surface elevation approximately 1008masl with a western azimuth, and ranging from a core depth of 262m to 492m. The pictured samples were chosen to demonstrate the range of textural and mineralogical composition throughout the drill core. Scale bars equal 1 cm per square. Inset BSE images of representative magnetite and hematite sampled for O and Fe isotope analysis and trace element EPMA. BSE 262 shows cavity in massive magnetite filled with magnetite octahedra approximately 20µm and less. BSE 324 shows cleavage planes in hematite (var. specularite). Bright areas indicate surface charging. Mgt = magnetite, ksp = K-feldspar, py = pyrite, hmt = hematite, cpy = chalcopyrite, chl = chlorite, scp = scapolite.

Grains selected for Fe isotope analysis were further crushed to hasten acid digestion by use of an alumina ceramic mortar and pestle that were cleaned with ethanol between samples to avoid contamination. Aliquots of polished magnetite and hematite grains from all samples were inspected at high magnification by using backscattered-electron (BSE) imaging on a Cameca SX-100 scanning electron microscope (SEM) and separately on a JEOL-7800FLV field emission-scanning electron microscope (FE-SEM); both instruments are located at the University of Michigan Electron Microbeam Analysis Lab (EMAL). Magnetite analyzed in this study does not display specularite textures (i.e., from mushketovization of specularite) and is more consistent with magnetite from Stage I mineralization described by Benavides et al. (2007) and

the paragenetic “mt II” from the Iron Oxide Stage as described by Reiger et al. (2010). Hematite is interpreted to be that of Stage III mineralization described by Benavides et al. (2007) and Late Stage mineralization by Rieger et al. (2010) due its occurrence as veinlets and matrix enclosing angular to subangular fragments of K-feldspathized and chloritized host rock and. The magnetite and hematite grains in the size fraction used for analyses were free of weathering features and contain minimal inclusions.

*EPMA and FE-SEM*

For this study, EPMA and an FE-SEM were used to acquire BSE images and to characterize the concentrations of the trace elements Mg, Al, Si, Ca, Ti, V, Cr, and Mn in magnetite and late-stage hematite samples representative of those processed for Fe and O stable isotope analyses. The instrumental conditions for the EPMA analyses were identical to those used in Knipping et al. (2015a, b) and Bilenker et al. (2016), utilizing a 20 kV, 30 nA, focused beam with counting times of either 100 or 120 seconds for trace elements. Microprobe analysis conditions are reported in Table A1.

*Iron isotopes*

Magnetite and hematite samples were subjected to ion exchange chromatography to isolate Fe for isotopic analysis. Between ~0.3 and 0.7 mg of each sample was dissolved and dried down in aqua regia, again in 8N HCl, and then loaded into columns of AG1-X8 resin in 8N HCl, following the procedure described by Huang et al. (2011). Analyses were performed at the University of Illinois, Urbana-Champaign, over two sessions using a Nu Plasma HR multi collector-inductively coupled plasma-mass spectrometer (MC-ICP-MS) in dry plasma mode with

either a DSN-100 or an Aridus II Desolvating Nebulizer System. All analyses were conducted following the double-spike method of Millet et al. (2012) to correct for instrumental mass bias and increase precision. Each sample was analyzed two times, with all analyses bracketed by the international standard IRMM-14 to correct for small changes in mass bias with time (Millet et al. 2012). Iron isotope values (Table 3.3) are reported relative to IRMM-14, calculated by using equation 1:

$$\delta^{56}Fe_{sample}\ (‰) = [(^{56}Fe/^{54}Fe)_{measured} / (^{56}Fe/^{54}Fe)_{IRMM\text{-}14} - 1] * 1000 \qquad (1)$$

The in-house standard UIFe was measured to average $\delta^{56}$Fe value of 0.67 ± 0.05 ‰ ($n$ = 8, 2σ, one session over four days) in the first session using the DSN-100; the international standard BCR-2 yielded a $\delta^{56}$Fe value of 0.08 ± 0.05 ‰ ($n$ = 1, 2σ ; recommended value 0.091 ± 0.011 ‰; Craddock and Dauphas 2011) during the same session. The in-house standard UIFe was measured to average 0.65 ± 0.05 ‰ ($n$ = 2, 2σ, one session in one day) using the Aridus II; BCR-2 was not measured during this session.

*Oxygen isotopes*

Oxygen isotope analyses of magnetite and hematite were conducted at the University of Oregon by using a laser fluorination line coupled with a Thermo-Finnigan MAT 253 gas isotope ratio mass spectrometer in dual inlet mode. Magnetite and hematite grains (2–3 mg) from each sample were initially subjected to low-power lasing. Laser power was slowly increased to minimize jumping movements of the grains during fluorination with $BrF_5$. For samples that did not experience grain jumping, $O_2$ yields were close to the theoretical 100%. All data were

compared to the Gore Mountain garnet (GMG) standard, which was measured before, during, and after analysis of magnetite samples. Oxygen isotope values (Table 3.3) are reported relative to the international Vienna Standard Mean Ocean Water (VSMOW). Average values for standard GMG ($\delta^{18}O_{GMG} \pm 1\sigma$) over three days of measurements were 7.23 ± 0.10 ‰, 7.21 ± 0.11 ‰, and 7.19 ± 0.08 ‰. Analytical precision for individual analyses is ± 0.10 ‰. The analytical values were adjusted by the difference between our measured standard values for each day and the recommended $\delta^{18}O$ value for the GMG standard 6.52 ‰. Theoretical $O_2$ yields for magnetite and hematite are 7.8 and 10.4 μmol/gram and analyzed magnetite and hematite samples average 7.8 and 8.3 μmol/gram, respectively.

## RESULTS

### *Major and trace element concentrations of magnetite and hematite*

Minimum, maximum, and average concentrations are reported for Mg, Al, Si, Ca, Ti, V, Cr, Mn, and Fe in magnetite and hematite from multiple depths in Table 3.4. Backscattered electron images of magnetite and hematite representative of analyzed samples are presented in Figs. 3.2 and 3.4. All individual EPMA data are reported in supplemental Table A.3. The average concentrations of Fe in magnetite (n = 335) and hematite (n = 195) across all samples at all depths are 70.8 ± 1.0 and 68.8 ± 1.1 wt. %, respectively. Where element concentrations were below detection limit (BDL), the detection limit of that analysis was substituted when calculating average values and standard deviations for each depth. Magnesium, Ca, Cr, and Mn were commonly BDL. Magnetite across all depths contains low and similar concentrations of Mg, Al, Ca, V, Cr, and Mn (average of 0.03, 0.11, 0.08, 0.07, 0.01, and 0.01 wt. %, respectively), elevated Si (0.24 wt. %), and low Ti (0.05 wt. %) relative to hematite. Hematite across all depths

contains low and similar concentrations of Mg, Al, Ca, V, Cr, and Mn (0.02, 0.11, 0.05, 0.06, 0.01, and 0.01 wt. %, respectively), is depleted in Si (0.03 wt. %), and is elevated in Ti (0.56 wt. %) relative to magnetite.

*Fe isotope compositions of magnetite and hematite*

Stable Fe isotope ratios for magnetite and hematite are reported as $\delta^{56}$Fe in Table 3.3. The $\delta^{56}$Fe values (± 2 sigma) for magnetite range from 0.46 ± 0.04 ‰ to 0.58 ± 0.02 ‰ and average 0.51 ± 0.16 ‰ ($n$ = 10). The $\delta^{56}$Fe values (± 2 sigma) for three late stage hematite are 0.34 ± 0.10 ‰, 0.42 ± 0.09 ‰, and 0.46 ± 0.06 ‰.

*Oxygen isotope compositions of magnetite and hematite*

Stable O isotope ratios for magnetite and hematite are reported as $\delta^{18}$O in Table 3.3. The $\delta^{18}$O values (± 2 sigma) for magnetite range from 0.69 ± 0.04 to 4.61 ± 0.05 ‰ and average 2.99 ± 2.70 ‰ ($n$ = 9) and for late stage hematite range from -1.36 ± 0.05 ‰ to 5.57 ± 0.05‰ and average 0.10 ± 5.38 ‰ ($n$ = 6).

## DISCUSSION

*Trace element compositions of magnetite and hematite*

Trace element concentrations of magnetite and hematite can be useful fingerprinting tools in provenance studies and for mineral exploration (Dupuis and Beaudoin 2011; Dare et al. 2014; Nadoll et al. 2014; Knipping et al. 2015a,b). Dupuis and Beaudoin (2011) and Nadoll et al. (2014) used trace elements that substitute for Fe in the magnetite and hematite crystal lattices to develop several discriminant diagrams for magnetite and hematite from different ore forming

environments. Those authors determined that concentrations of Al, Mn, Ti, and V were most useful when discriminating primary magnetite among skarn, IOCG, Kiruna-type IOA, porphyry Cu-Mo(-Au), and orthomagmatic Fe-Ti-V deposits. The concentrations of [Al+Mn] vs [Ti+V] reported in the current study for magnetite and hematite from Mantoverde are plotted on the magnetite discriminant diagram in Fig. 3.3. Data for magnetite from the Los Colorados IOA deposit, Chile, from Knipping et al. (2015a,b), are also plotted on Fig. 3.3. The average [Ti+V] and [Al+Mn] values for all magnetite analyses from Mantoverde plot in the IOCG field on the discriminant diagram. However, [Ti+V] and [Al+Mn] concentrations within and among magnetite grains spread across all fields. There is no apparent correlation between trace element concentrations of magnetite and the depth of samples within the deposit. The average [Al+Mn] and [Ti+V] values for late-stage hematite from Mantoverde plot in the Kiruna field, and the trace element compositions of individual hematite grains plot across the Kiruna, IOCG, porphyry and Fe-Ti-V fields; these are not included in Figure 3.3. Upon inspection under BSE and FE-SEM, some magnetite grains were found to have chemical zonation (Fig. 3.4), and display concentric (Fig. 3.4 A, B) and mottled (not pictured) zoning of Si- and Al-rich and Si- and Al-poor magnetite. Several grains were found to have Si- and Al-rich cores surrounded by Si- and Al-poor rims (Fig. 3.4 E, F). In general, the average trace element composition of hematite in this study is more comparable to Fe-oxides from the porphyry and igneous environments examined by Dupuis and Beaudoin (2011).

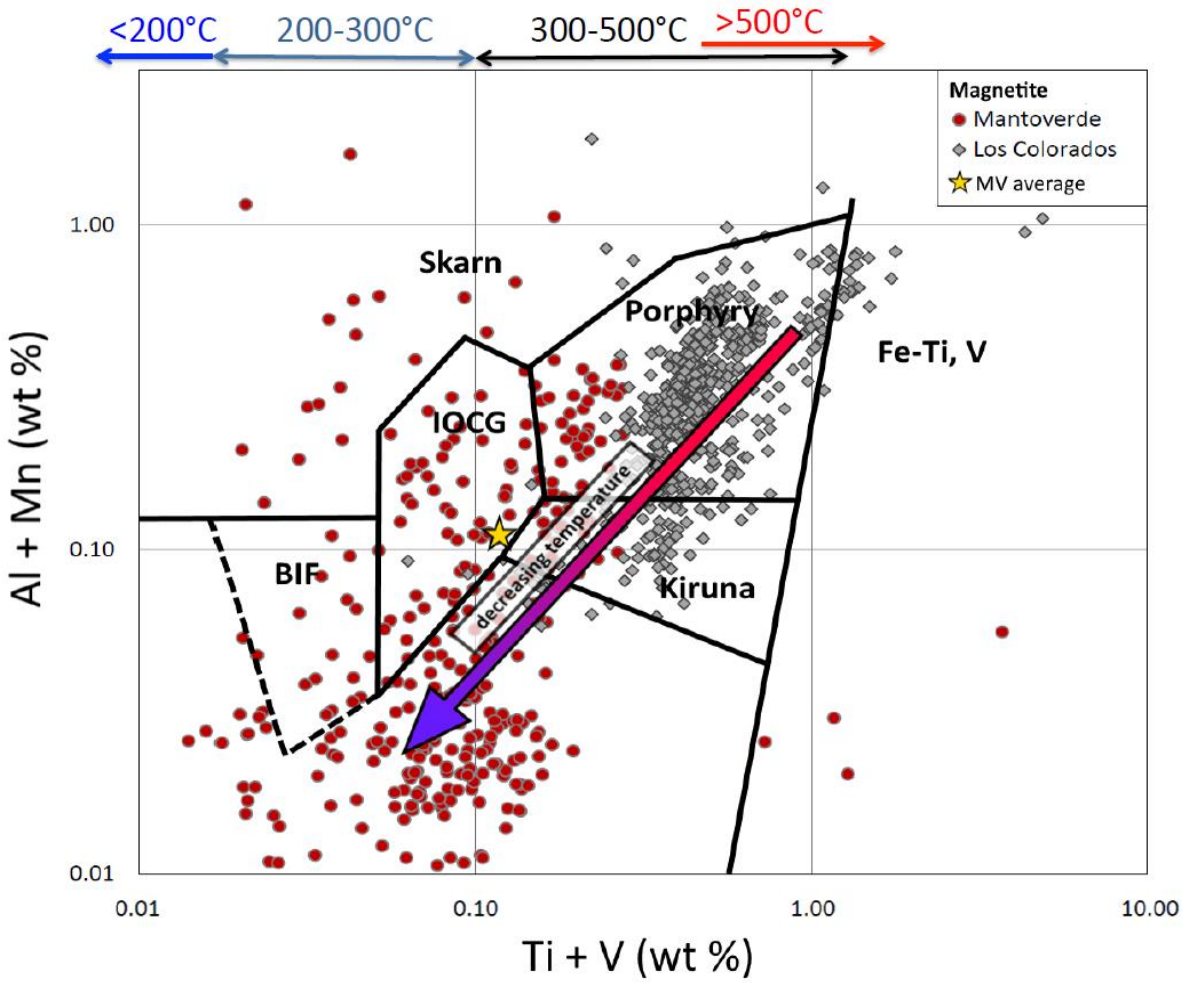


Figure 3.3: The concentrations of [Al+Mn] vs. [Ti+V] for magnetite from the Mantoverde IOCG deposit are plotted on the magnetite trace element discrimination diagram from Nadoll et al. (2014), along with [Al+Mn] vs. [Ti+V] for magnetite from the Los Colorados Kiruna-type IOA deposit in the Chilean Iron Belt. The data from Los Colorados are from Knipping et al. (2015a,b). The solid red circles and grey diamonds represent magnetite from Mantoverde and Los Colorados, respectively. The temperatures on the top abscissa are from Nadoll et al. (2014) who used homogenization temperatures for fluid inclusions trapped in paragenetically equivalent quartz to constrain temperatures of magnetite crystallization from each of the ore deposits types on the diagram. The color-graded arrow indicates the expected trend for the trace element chemistry of magnetite that grows from a cooling magmatic-hydrothermal fluid. EPMA conditions are reported in Table A1; general statistics for EPMA data located in Table 4; full list of data in supplementary Table A.3.

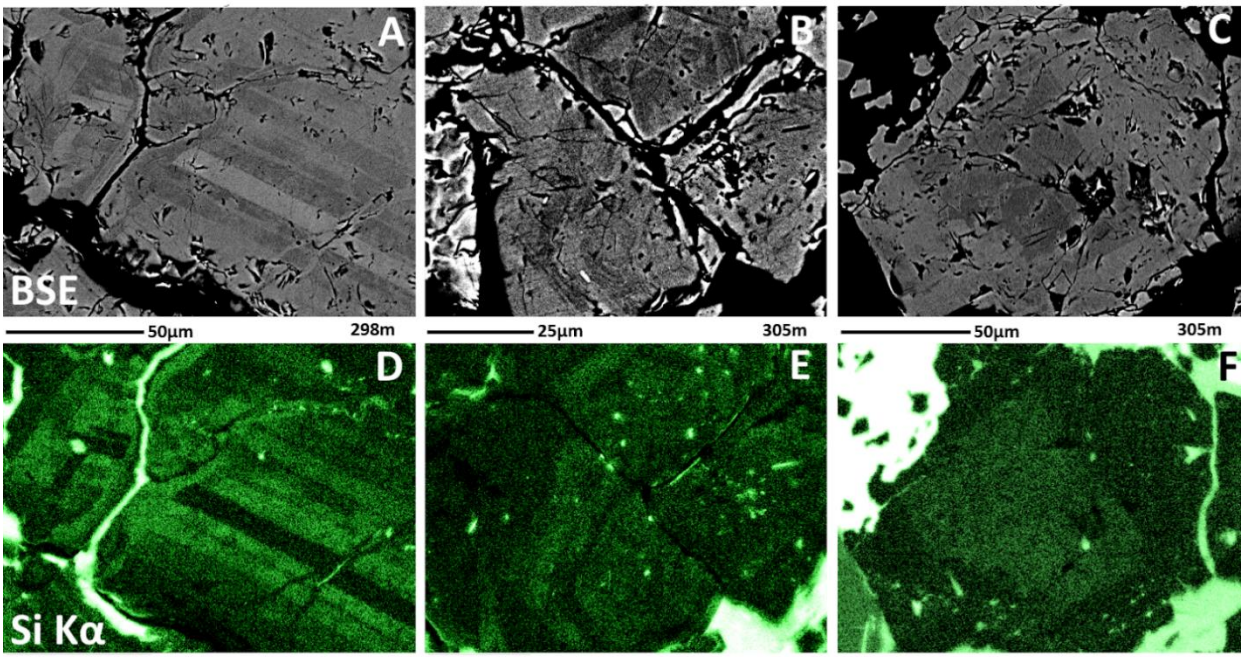


Figure 3.4: A-C: BSE images of magnetite from sample depths 298m and 305m; D-F: FE-SEM images of Si concentrations in magnetite. Panels A and D display concentric zoning of trace element rich and trace element poor growth bands. Panels B and E display similar concentric zoning as in A and D and display a trace element rich core and poor rim. Panels C and F display trace element rich core and trace element poor rim. Bright spots within magnetite are silicate inclusions, either formed in-situ or as inclusions along rims during magnetite growth.

The new trace element data for magnetite reported here are similar to the concentrations of Ti, V, Al, and Si in magnetite from Mantoverde Norte and Sur reported by Rieger et al. (2010). The large range of trace element concentrations in magnetite and hematite likely reflects the effects of oscillatory zoning during precipitation (Fig. 3.4), unresolvable nano-inclusions trapped during replacement of host rocks, and of fluids responsible for later potassic alteration, silicification, and hydrolytic alteration of the host rocks in the Mantoverde system. Care was taken during the EPMA to analyze only magnetite and hematite that appeared texturally homogeneous (i.e., grains that had no visible fluid inclusions or mineral inclusions) under BSE examination. In spite of the scatter, the values of [Al+Mn] and [Ti+V] for magnetite from Mantoverde are, generally, positively correlated with each other. Nadoll et al. (2014) used

homogenization temperatures of fluid inclusions hosted in transparent mineral phases that are paragenetically equivalent with magnetite from a wide variety of mineral deposit environments to determine approximate crystallization temperatures for magnetite that correlate with the abundances of [Al+Mn] and [Ti+V] in magnetite. Comparison of magnetite trace element chemistry with published estimates for the temperatures of magnetite crystallization allowed Nadoll et al. (2014) to determine that magnetite with [Al+Mn] of 0.001 - 0.1 wt. % and [Ti+V] of 0.0008 - 0.01 wt. % crystallized from hydrothermal fluid at <200 ℃, [Al+Mn] of 0.01 - 0.2 wt. % and [Ti+V] of 0.001 - 0.1 wt. % crystallized from hydrothermal fluid at 200 - 300 ℃, [Al+Mn] of 0.1 - 3 wt. % and [Ti+V] of 0.03 - 1 wt. % crystallized from hydrothermal fluid at 300 - 500 ℃, and [Al+Mn] >0.1 wt. % and [Ti+V] >0.3 wt. % crystallized from hydrothermal fluid at >500 ℃. Published microthermometry data for magnetite-bearing fluid inclusions in Iron Oxide Stage quartz from Mantoverde indicate that mineralization occurred over a temperature range from 278 to 530 ℃ (Rieger et al. 2012), consistent with the apparent cooling trend revealed by the [Al+Mn] and [Ti+V] data shown in Figure 3.3. The same positive correlation between [Al+Mn] and [Ti+V] values is also observed for magnetite from the Los Colorados IOA deposit (Fig. 3.3) (Knipping et al. 2015a, b). Those authors used melt inclusion homogenization temperatures, O-isotope thermometry for magnetite-actinolite pairs, and the presence of halite-saturated fluid inclusions in magnetite to conclude that the [Al+Mn] and [Ti+V] values record magnetite crystallization from a cooling magmatic-hydrothermal fluid.

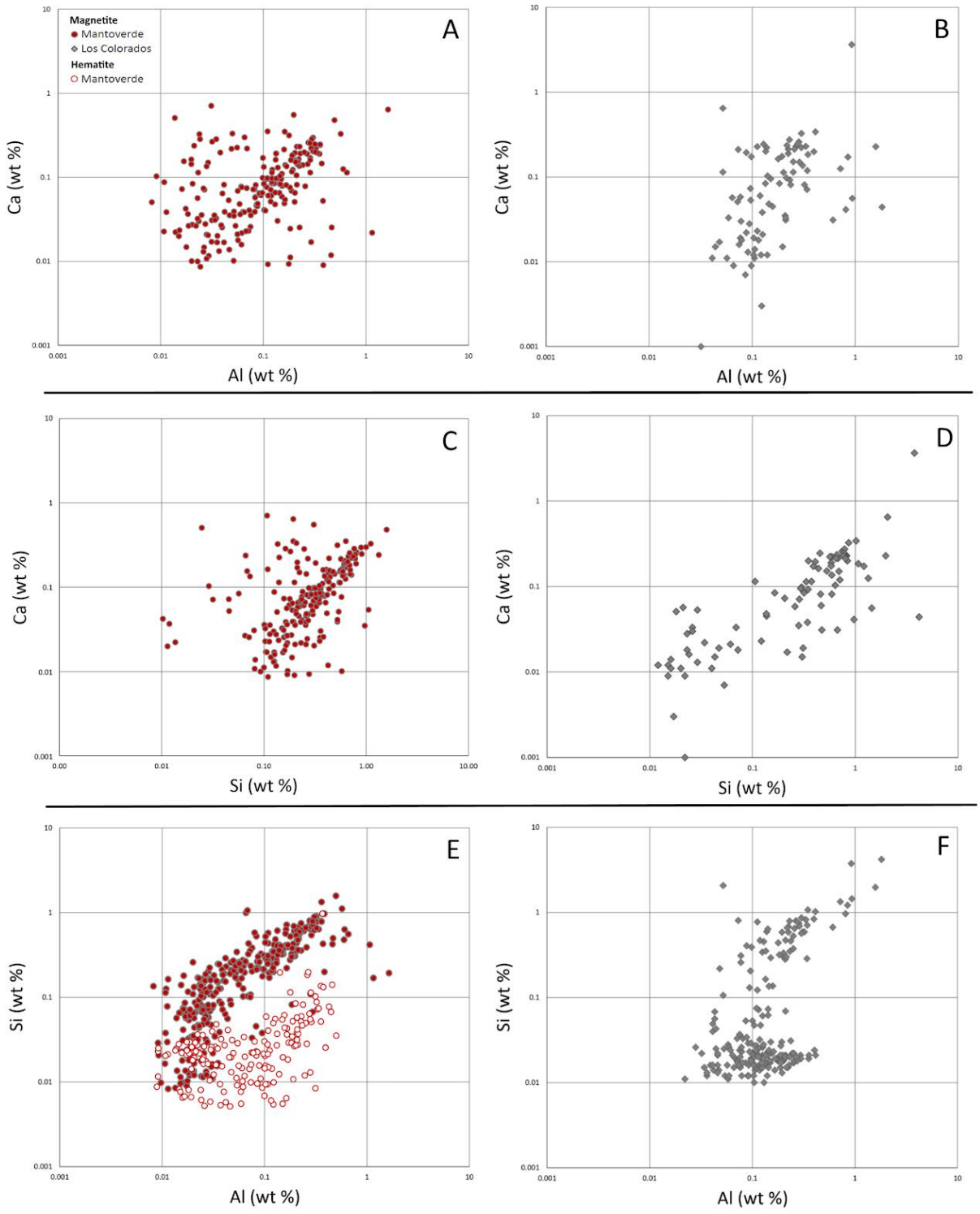


Figure 3.5: The trace element compositions of magnetite from the Mantoverde IOCG deposit and the Los Colorados IOA deposit are plotted as weight percents of Ca vs. Al (A,B), Ca vs. Si (C,D), and Si vs. Al (E,F). The symbols are the same as those used in Fig. 3.3. Only data from drill core LC-04 that intersects

the main massive magnetite ore body at Los Colorados have been plotted for clarity, although data from magnetite in drill core LC-05 from Los Colorados shows very similar trends (Knipping et al., 2015b). Hematite is only plotted in panel E owing to lack of detectable Ca concentrations. The concentrations of Mg vs. Si, not included here, show very similar correlations. Note the "elbows" in panels E and F.

Further evidence of the apparent overall cooling trend revealed by magnetite trace element chemistry is supported by Si- and Al- rich cores in some magnetite grains from Mantoverde. It is well established that minerals such as magnetite incorporate greater amounts of trace elements at higher temperatures. Shimazaki (1998) examined magnetite from over 40 skarn deposits and found four distinct types of Si-bearing (silician) magnetite. Silician magnetite poor in Al, Mg, and Ca (type-one) was found in more than half of the studied skarn deposits, whereas silician magnetite rich in Al, Mg, Ca, and other elements (type-two) was only found in four deposits. The trace elements in type-two magnetite appeared to be dissolved within the magnetite crystalline structure based on the lack of evidence of inclusions under high-magnification BSE imaging. However some type-two magnetite grains did contain very fine, dust-like inclusions that were interpreted to be either exsolution products or inclusions that were incorporated during magnetite growth. The former interpretation, combined with the observation of type-two magnetite that has no visible inclusions, is indicative of greater partitioning of trace elements into magnetite that grows in the presence of a high temperature hydrothermal fluid. Calcium, Al, and Mg concentrations in type-two magnetite were demonstrated to have positive, coupled relationships with Si (Neumann et al. 2017). Those authors examined magnetite from the Angara-Ilim IOCG located within East Siberia and found hydrothermal magnetite contains variable, but positively related, amounts of Ca, Al, Mg, and Si, variably correlated with $Fe^{2+}$ and $Fe^{3+}$ concentrations. Backscatter electron images and core-to-rim trace element analyses of concentrically zoned massive magnetite indicate an overall trace element depletion in magnetite over time, indicative of a cooling trend. The concentrations of Ca vs. Al, Ca vs. Si, and Si vs. Al

in magnetite and hematite from Mantoverde and Los Colorados are plotted next to one another in Figure 3.5. All three pairs of elemental concentrations in oxides from both deposits exhibit the same positive correlation with increasing concentration of trace elements and, when combined with the observation of Si-, Al-, Mg- and Ca-rich magnetite cores and depleted rims, indicate a systematic, progressive decrease in trace element concentrations with decreasing temperature. Hematite data only exist at Mantoverde and were only plotted in panel E of Figure 3.5 since Ca concentrations were mostly below MDL. In spite of this, both hematite and magnetite show very strong correlations between Si and Al concentrations implying that not only did magnetite precipitate from a cooling fluid, but hematite also crystallized from a cooling hydrothermal fluid. The implications for the apparent down-temperature continuity of magnetite trace element compositions at the Mantoverde IOCG and Los Colorados IOA deposits are discussed below.

We highlight that while the trace element compositions and BSE images of magnetite from Mantoverde are consistent with crystallization of magnetite from a cooling fluid, the wide distribution of trace element abundances demonstrates how susceptible trace elements in magnetite and hematite are to hydrothermal alteration. The observations reported here indicate that caution should be exercised when using discriminant diagrams to fingerprint provenance and geochemical processes. Other geochemical proxies must be used to fingerprint the fluid source(s) for magnetite and hematite.

*Iron isotopes*

The ranges of $\delta^{56}$Fe for magnetite (0.46 to 0.58 ‰) and hematite (0.34 to 0.46 ‰) from Mantoverde overlaps published $\delta^{56}$Fe values for magnetite formed by magmatic and magmatic-hydrothermal processes. In Fig. 3.6, the published global range of $\delta^{56}$Fe values from ~0.0 to 0.86

‰ are indicated for magmatic and magmatic-hydrothermal magnetite based on data from Heimann et al. (2008), Craddock and Dauphas (2010), Weis (2013), and Bilenker et al. (2016, 2017). Notably, the study by Craddock and Dauphas (2010) presents a comprehensive $\delta^{56}$Fe data set for basalt, basaltic andesite, andesite, dacite and rhyolite, their intrusive equivalents, and peridotite. Also shown in Fig. 3.6 are $\delta^{56}$Fe data for magnetite from several Kiruna-type IOA deposits that are proposed to represent the stratigraphically deeper, sulfur poor end-member of IOCG systems (see Fig. 3.6 caption for references). Importantly, published studies conclude that the magnetite-rich orebodies at Pea Ridge and Pilot Knob (Childress et al. 2016; Hofstra et al. 2016), Los Colorados, Chile (Knipping et al. 2015a,b; Bilenker et al. 2016; Reich et al. 2016), and Grängesberg, Sweden (Jonsson et al. 2013; Weis 2013) formed by magmatic-hydrothermal processes based on fluid inclusion data, and trace element and isotopic compositions of ore and gangue minerals. Data are also shown for the Plio-Pleistocene El Laco magnetite - apatite deposit, Chile (Weis 2013; Bilenker et al. 2016), for which magmatic (Tornos et al. 2016; Velasco et al. 2016) and magmatic-hydrothermal genetic models (Sillitoe 2003; Dare et al. 2015) are proposed.

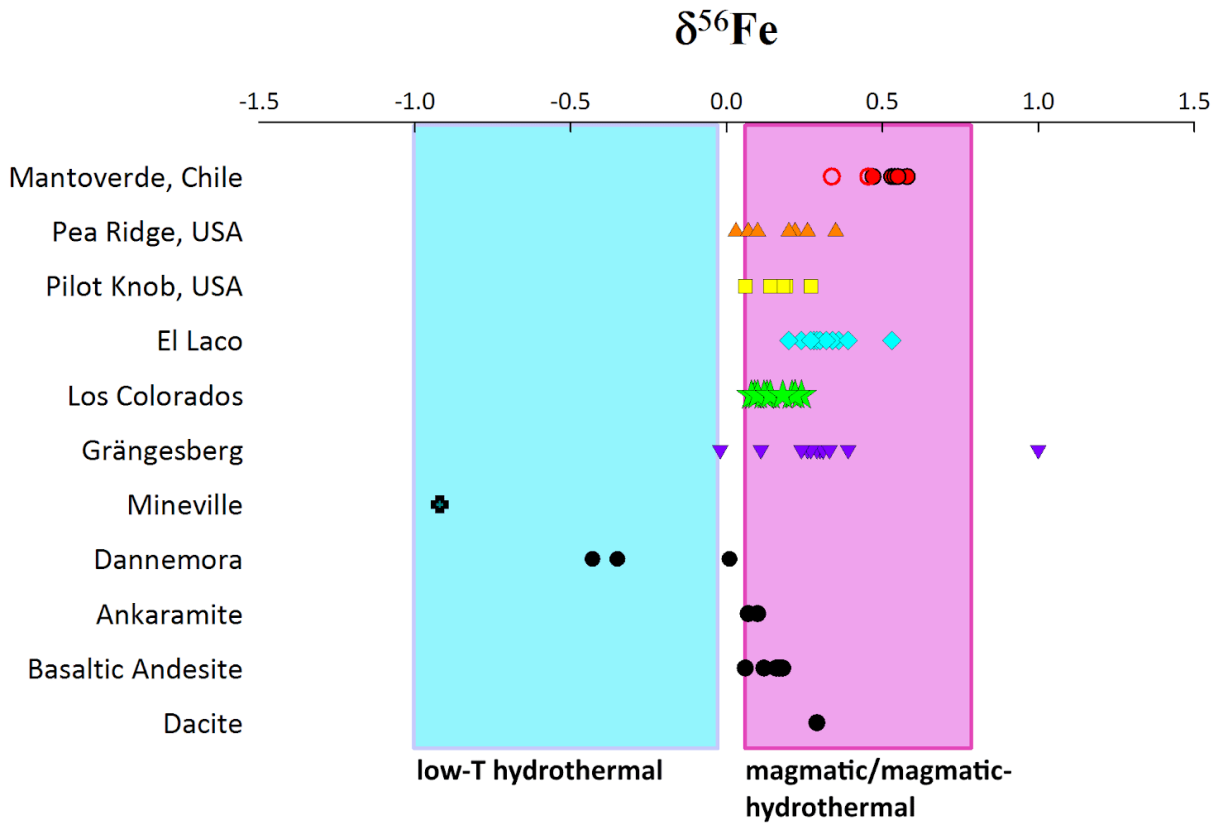


Figure 3.6: Iron isotope values ($\delta^{56}$Fe) for primary magnetite and hematite from this study along with $\delta^{56}$Fe values for magnetite from several iron oxide - apatite deposits and volcanic reference materials. The pink box represents the global range of $\delta^{56}$Fe values (~ 0.0 – 0.86 ‰) reported in the literature for igneous and magmatic-hydrothermal magnetite. The blue box represents the global range of $\delta^{56}$Fe values (-1.0 – 0.0 ‰) for magnetite that formed from low temperature hydrothermal processes. Solid symbols for Mantoverde data points represent magnetite samples and open symbols represent hematite samples. Data points and ranges from Anbar (2004), Schüßler (2008), Weis (2013), Bilenker et al. (2016), and Childress et al. (2016). Full list of data are reported in supplemental Table A.5.

Comparison of the $\delta^{56}$Fe values for magnetite from Mantoverde (0.46 to 0.58 ‰) with the global range of $\delta^{56}$Fe for magmatic and magmatic-hydrothermal magnetite (~0.0 to 0.86 ‰) suggests that the variable degrees of potassic alteration, chloritization, sericitization, silicification, and/or carbonatization of the host rocks in the Mantoverde deposit (Cornejo et al. 2000; Rieger et al. 2010) did not significantly alter the primary $\delta^{56}$Fe signatures of modally abundant magnetite (Fig. 3.6). Extensive hydrothermal alteration of magnetite, such as partial or

total dissolution, transport, and reprecipitation (Weis 2013) or Fe ion exchange between a mineral and magnetite above closure temperature (Frost et al. 2006), drives the $\delta^{56}$Fe signature to values <0.0 ‰. This has been documented for the Dannemora iron-skarn in Sweden and magnetite-rich ore deposits in the Adirondack Mountains, U.S.A. At Dannemora, Lager (2001) proposed that volcanic activity drove circulation of Fe- and Mn-rich hydrothermal fluids that migrated from a high-relief hinterland into evaporite pans which served as traps for magnetite mineralization, the traps being strata-bound to dolomitic limestone. Lager (2001) provided evidence for multiple episodes of low-temperature dissolution, mobilization, and reprecipitation of magnetite. Similarly, Valley et al. (2011) reported that magnetite ore bodies within the Lyon Mountain Granite, near Mineville, New York, were subjected to extensive sodic alteration, which resulted in albitization and complete dissolution and remobilization of originally magmatic/magmatic-hydrothermal magnetite. The U-Th-Pb abundances in hydrothermal zircon in the magnetite orebodies record at least 40 Ma of episodic sodic metasomatism, with hydrothermal fluid circulation driven by regional extension of the Adirondack Highlands (Valley et al. 2011). Weis (2013) analyzed magnetite samples from the Dannemora deposits and reported an average $\delta^{56}$Fe value of -0.28 ‰ (n = 4) for magnetite. Bilenker et al. (2016) reported that magnetite from the Mineville deposit yields a $\delta^{56}$Fe value of -0.92 ‰. The $\delta^{56}$Fe data for magnetite from Dannemora and Mineville indicate that extensive dissolution and reprecipitation of magnetite by secondary, low-temperature (i.e., <300 °C) hydrothermal processes results in progressively decreasing $\delta^{56}$Fe values for magnetite (Fig. 3.6).

The new magnetite $\delta^{56}$Fe data presented here are consistent with a magmatically derived ore fluid for the modally abundant stage-one magnetite at Mantoverde. Late-stage hematite yields an average $\delta^{56}$Fe value of 0.41 ± 0.12 ‰ (2σ, n = 3), consistent with growth from an

oxidized magmatic-hydrothermal fluid. Experimental data indicate negligible Fe isotope fractionation between oxidized $Fe^{3+}$-bearing aqueous fluid and hematite at 200 ℃ (Saunier et al. 2011). Considering that reduced isotopic partition function ratios (β-factors) for magnetite and hematite are similar (Polyakov et al. 2007; Blanchard et al. 2009), isotopic fractionation among these minerals and other phases will be similar. It is plausible that an oxidized magmatic, Fe-rich fluid precipitated hematite that exhibits a similar isotopic signature as the initial magnetite.

*Oxygen isotopes*

Several published studies report stable O isotope data for magnetite, hematite and gangue minerals from multiple deposits within the Mantoverde district. Benavides et al. (2007) report $\delta^{18}O$ values that range from 1.4 to 3.1 ‰ (n = 5) for Iron Oxide Stage magnetite from the sulfide-bearing orebodies, and range from 2.2 to 4.1 ‰ (n = 5) for magnetite from spatially associated magnetite-apatite ± pyrite bodies located along the eastern branch of the Atacama Fault Zone. Those authors report $\delta^{18}O$ values that range from -1.9 to +1.7 ‰ (n = 10) for Late Stage hematite. Benavides et al. (2007) used oxygen isotope fractionation factors for magnetite-water from Bottinga and Javoy (1975) to calculate that at temperatures from 460° to 550°C (the temperature range constrained by fluid inclusion microthermometry in paragenetically equivalent quartz), Iron Oxide Stage magnetite would have been in equilibrium with a fluid with $\delta^{18}O$ of +7.3 to +10 ‰. They reported that magnetite from the magnetite-apatite ± pyrite orebodies spatially and temporally associated with IOCG mineralization would have been in equilibrium with a fluid with $\delta^{18}O$ values of +8 to +9 ‰ at ~650 °C, a temperature that was constrained by $\delta^{18}O$ thermometry of co-genetic magnetite and apatite. Benavides et al. (2007) used their $\delta^{18}O$ data and published sulfur isotope data for pyrite from Mantoverde to conclude that Iron Oxide

Stage mineralizing fluids were magmatic-hydrothermal, and that non-magmatic fluids became prominent after magnetite mineralization, during the bulk of sulfide deposition.

Rieger et al. (2012) investigated hydrothermal quartz, K-feldspar, and calcite, which are co-depositional to the Iron Oxide (Stage 1), Sulfide (Stage 2), and Late Stage (Stage 3) mineralization, respectively, from the Manto Ruso, Mantoverde Norte, and Mantoverde Sur deposits within the Mantoverde district. Those authors report $\delta^{18}O$ values that range from 11.8 to 13.6 ‰ for quartz from the Iron Oxide stage. Rieger et al. (2012) used fractionation factors from Zheng (1993) to calculate that at 435 °C, quartz with $\delta^{18}O$ values ranging from 11.8 to 13.6 ‰ would be in equilibrium with an aqueous fluid with $\delta^{18}O$ values ranging from 7.9 to 9.7 ‰. Rieger et al. (2012) report $\delta^{18}O$ values ranging from 10.46 to 12.06 ‰ for potassium feldspar from the Sulfide Stage of mineralization, and used fractionation factors from Zheng (1993) to calculate that an aqueous fluid in equilibrium with this K-feldspar would have $\delta^{18}O$ values ranging from 6.3 to 7.9 ‰ at 300 °C, the temperature for sulfide mineralization. Late Stage calcite $\delta^{18}O$ values from the same study range from 10.8 to 13.3 ‰ and indicate that a fluid in equilibrium with calcite at 244 °C (median $T_h$) would exhibit $\delta^{18}O$ values ranging from 3.4 to 5.9 ‰ (fractionation factors from Ohmoto and Rye 1979). A second generation of calcite yielded the highest measured $\delta^{18}O$ value of 15.8 ‰, but was not studied further due to a lack of fluid inclusions. Rieger et al. (2012) concluded that the calculated $\delta^{18}O$ values for aqueous fluid in equilibrium with quartz from the Iron Oxide Stage and K-feldspar from the Sulfide Stage, which are, respectively, the main oxide and sulfide mineralizing events in the deposits, are consistent with magmatic-hydrothermal fluids derived from I-type magmatism and noted their similarity to whole-rock $\delta^{18}O$ isotope values of 6.9 – 8.6 ‰ reported for the Coastal Batholith (Marschik et al. 2003; Rieger et al. 2012).

The new $\delta^{18}O$ data reported here for magnetite and hematite from the Iron Oxide Stage and Late Stage, respectively, are presented in Fig. 3.7, together with $\delta^{18}O$ values for magnetite from IOCG deposits in the Cloncurry District and broader eastern Mt. Isa Block, NW Queensland, Australia (Marshall and Oliver 2006), as well as several Kiruna-type IOA deposits for which a magmatic or magmatic-hydrothermal genesis has been proposed in the literature (see Fig. 3.7 caption for references). Globally, $\delta^{18}O$ values for magnetite in the range of 0.9 to 5.0 ‰ fingerprint an ortho-magmatic origin for magnetite, as indicated in Fig. 3.7 (Taylor 1967). All except one $\delta^{18}O$ value for magnetite from Mantoverde are consistent with the global database for magnetite crystallized from silicate melt and magmatic-hydrothermal fluids.

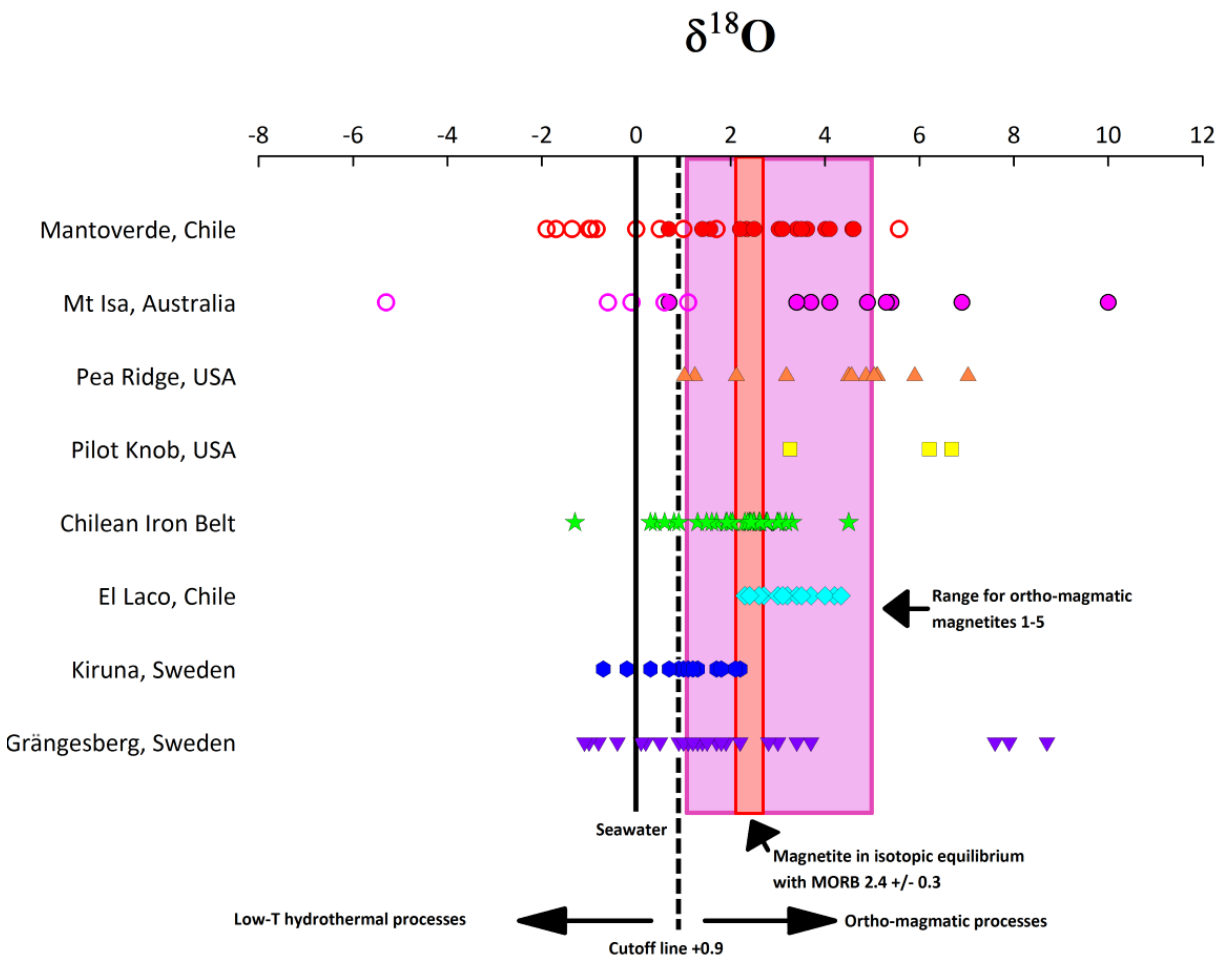


Figure 3.7: Oxygen isotope values ($\delta^{18}O$) for primary magnetite and hematite from this study along with $\delta^{18}O$ values for magnetite from the Mt Isa IOCG deposit (Australia) and several IOCG deposits including deposits from the Chilean Iron Belt. The pink box represents range the global range for $\delta^{18}O$ values (~1 – 5 ‰) for magmatic-hydrothermal magnetite. The orange box represents the $\delta^{18}O$ range (2.4 ± 0.3 ‰) for magnetite in isotopic equilibrium with MORB. The vertical dashed line at ~ $\delta^{18}O$ = 1.0 ‰ represents the divide between magmatic-hydrothermal magnetite and magnetite crystallized from non-magmatic low-temperature hydrothermal fluids. The solid line at ~ $\delta^{18}O$ = 0.0 ‰ represents the $\delta^{18}O$ value of seawater. The solid symbols represent $\delta^{18}O$ values for magnetite samples and the open symbols represent $\delta^{18}O$ values for hematite samples. Data from Marshal and Oliver (2006), Nyström et al. (2008), Weis (2013), Jonnson et al. (2014), Bilenker et al. (2016), Childress et al. (2016), and Bilenker et al. (2017). Full list of data are reported in supplemental Table A.4.

We used fractionation factors from Cole et al. (2004) to calculate that over the temperature range of 300 to 550 °C (based on published fluid inclusion microthermometry data for paragenetically equivalent quartz), magnetite in isotopic equilibrium with fluid with $\delta^{18}O$ values of 7.9 ‰ (at 300 °C) – 9.7 ‰ (at 550 °C), will have $\delta^{18}O$ values ranging from 0.9 ‰ (at

300 °C) to 2.3 ‰ (at 550 °C). The magnetite sample from Mantoverde that yielded a $\delta^{18}O$ value of 0.69 ‰ likely reflects post-mineralization alteration, an observation similar to results reported for magnetite samples from Kiruna and the Grängesberg districts, Sweden (Jonsson et al. 2013), and consistent with the trace element chemistry for Mantoverde magnetite discussed above (Fig. 3.3). One Late Stage hematite sample from Mantoverde yielded a $\delta^{18}O$ value of +5.57 ‰; however, most $\delta^{18}O$ values for late stage hematite fall below 0 ‰.

We used published values for $\delta^{18}O$ of quartz and calcite from Rieger et al. (2012) and quartz-fluid and calcite-fluid fractionation factors from Zheng (1991) and Cole et al. (2004), respectively, to calculate theoretical $\delta^{18}O$ values for Iron Oxide Stage and Late Stage fluids that would have been in equilibrium with Iron Oxide Stage magnetite and Late Stage hematite. These results are shown in Fig. 3.8, and indicate that the new $\delta^{18}O$ values for magnetite reported here are consistent with $\delta^{18}O$ values predicted by using published $\delta^{18}O$ values of quartz and quartz-fluid fractionation factors. However, the new $\delta^{18}O$ values for late-stage hematite reported here are consistent with a heavier fluid (i.e., greater magmatic component) than predicted by using published $\delta^{18}O$ values of late-stage calcite and calcite-fluid fractionation factors.

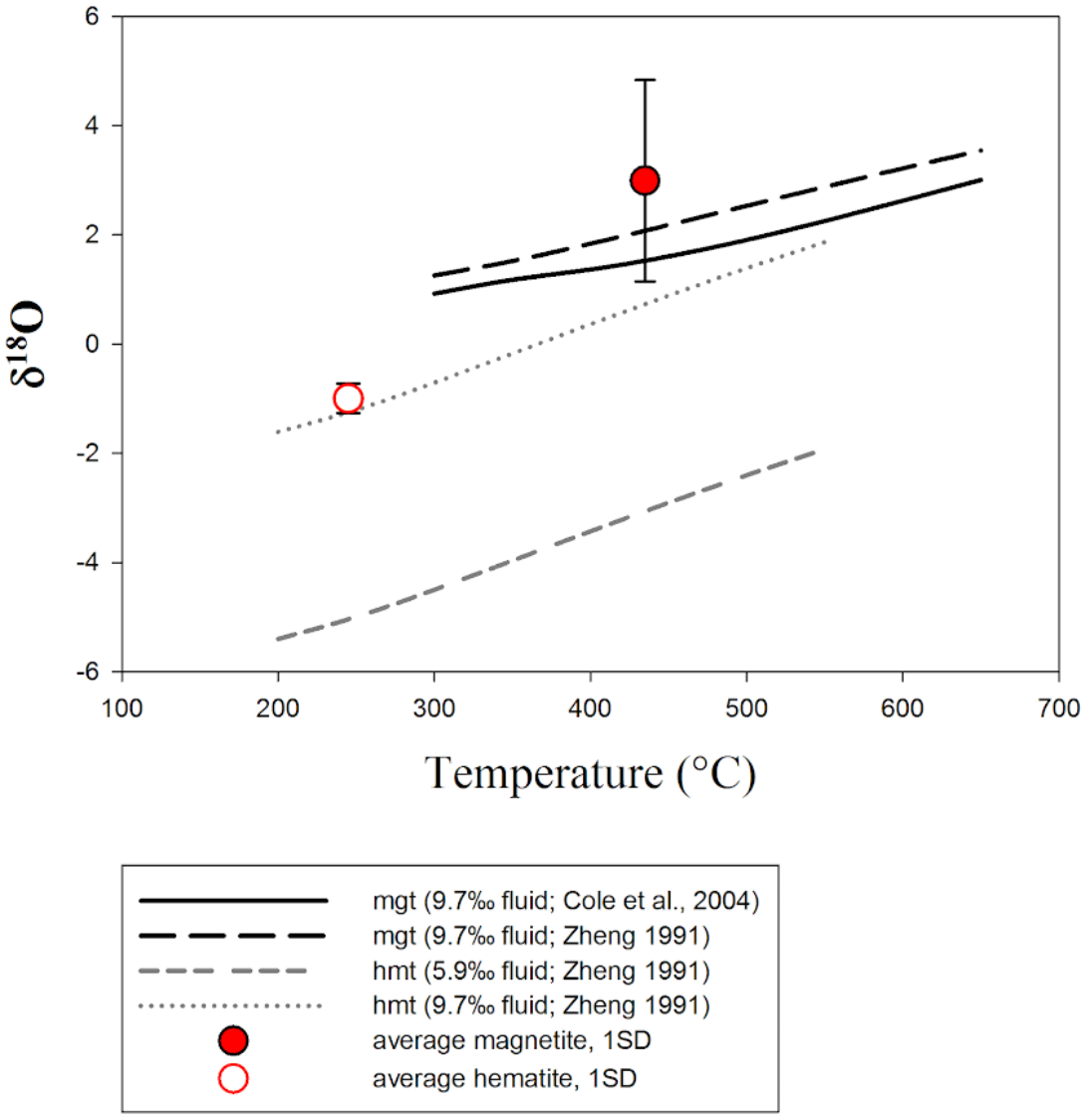


Figure 3.8: The ranges of $\delta^{18}O$ values for model (theoretical) hydrothermal fluids in equilibrium with ore-stage magnetite and late-stage hematite from this study; one sigma standard deviations are plotted and symbols are the same as were used in Fig. 3.5. The solid and long-dashed black lines were calculated by using the magnetite-$H_2O$ fractionation factors published in Zheng (1991) and Cole et al. (2004), respectively. The short-dashed and dotted grey lines were calculated by using the hematite-$H_2O$ fractionation factors published in Zheng (1991). The lines were calculated by using average $\delta^{18}O$ values for ore-stage quartz and late-stage calcite from Rieger et al. (2012).

Magnetite and hematite samples from Mantoverde yield $\delta^{18}O$ values that are similar to values reported for samples from the Cloncurry District and neighboring IOCG deposits within

the Proterozoic eastern Mt. Isa Block, Australia (Marshall and Oliver 2006). Magnetite and hematite from Cloncurry and Mt. Isa yield $\delta^{18}O$ values that range from 0.7 to 10.0 ‰ (average 4.78 ‰, $n$ = 10) and -5.3 to 1.1 ‰ (average -0.9 ‰, $n$ = 5), respectively. The majority of magnetite samples from Cloncurry and Mt. Isa yield $\delta^{18}O$ values between 1 and 5 ‰, which led Marshall and Oliver (2006) to conclude that magnetite and hematite in the Cloncurry and Mt. Isa districts precipitated from magmatically sourced ore fluids that experienced variable re-equilibration with igneous host rocks.

Magnetite and hematite $\delta^{18}O$ values reported here, and those reported by Benavides et al. (2007), indicate that the ore fluids from which these minerals precipitated were derived from a magmatic source. The $\delta^{18}O$ values for both Late Stage calcite associated with hematite (as in Rieger et al. 2012) and Stage IV post-hematite calcite (as in Benavides et al. 2007) record incursion of, and mixing with, a non-magmatic fluid.

*A magmatic-hydrothermal origin for Mantoverde*

The $\delta^{56}Fe$ and $\delta^{18}O$ data for magnetite and hematite samples from Mantoverde, plotted together in Fig. 3.9, are consistent with a magmatic source for Fe and O (e.g., Weis 2013; Bilenker et al. 2016; Childress et al. 2016). Together, the paired $\delta^{18}O$ and $\delta^{56}Fe$ values for magnetite and hematite, combined with published data for isotopes of C, O, S, Sr, Pb, Ar, Kr, Xe, and halogen ratios for samples from hypogene mineralization, all consistently fingerprint a magmatic-hydrothermal ore forming fluid for the ore bodies in the Mantoverde district. The data do indicate the presence of a non-magmatic fluid, plausibly a basinal brine, but the sum of the isotopic data indicate that such a fluid was volumetrically minor and present only during the waning stages of mineralization.

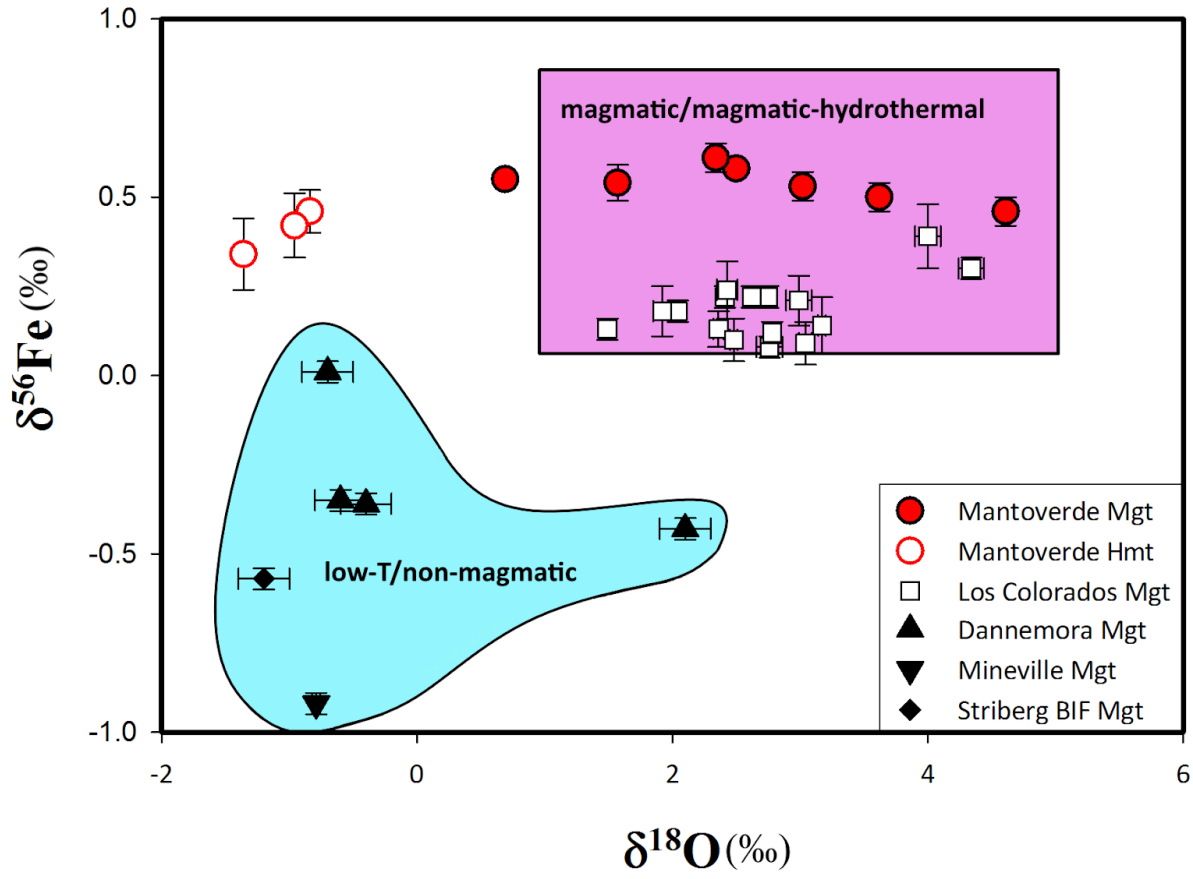


Figure 3.9: Paired oxygen ($\delta^{18}O$) and iron ($\delta^{56}Fe$) isotope values determined for the same primary magnetite and hematite samples measured in this study are plotted. The pink box represents the global range of $\delta^{18}O$ and iron $\delta^{56}Fe$ values reported for igneous and magmatic-hydrothermal magnetite. The solid and open red circles represent $\delta^{18}O$ and iron $\delta^{56}Fe$ for magnetite and hematite from Mantoverde, respectively. The white squares represent $\delta^{18}O$ and iron $\delta^{56}Fe$ values for magnetite from the Los Colorados IOA deposit, Chile (Bilenker et al., 2016). The error bars plotted for both $\delta^{18}O$ and $\delta^{56}Fe$ values are 2σ, and some $\delta^{18}O$ error bars are smaller than the symbols. Data are reported in Table 3.3. Note that not all magnetite and hematite samples were analyzed for both O and Fe stable isotopes; only those samples for which both O and Fe data were obtained are plotted on Fig. 3.9.

It has been suggested that IOCG deposits represent the more shallow, evolved endmembers of systems that contain IOA orebodies at depth (Sillitoe 2003). A genetic model linking IOCG deposits and IOA deposits has recently been proposed by Knipping et al. (2015a). Those authors used major, minor and trace element concentrations of magnetite from the Los

Colorados IOA ore deposit located within the Punta del Cobre Formation, approximately 200 km south of Mantoverde, to reveal that magnetite in the Los Colorados deposit retains both an igneous and a magmatic-hydrothermal chemical signature. The magnetite cores are chemically equivalent to magnetite grown in equilibrium with a silicate melt, and magnetite rims are chemically equivalent to magnetite grown in equilibrium with a cooling magmatic-hydrothermal fluid. Briefly, they proposed that magnetite cores crystallized from a silicate melt, that the melt subsequently reached volatile saturation, and the magnetite crystal surfaces served as nucleation sites for the exsolving magmatic volatile phase (cf. Hurwitz and Navon 1994). Initial growth of magnetite in equilibrium with silicate melt is indicated by the enrichment of trace elements such as Ti, V, Al and Mn in magnetite cores, and the presence of polycrystalline mineral inclusions that rehomogenize at >850 °C (Knipping et al. 2015a,b). Regional extension allowed the magma to ascend along pre-existing faults and, during decompression, resulted in the formation of a magnetite - fluid suspension that ascended from the source magma. Growth of the magnetite rims from an Fe-rich magmatic-hydrothermal fluid is indicated by the trace element chemistry of magnetite, and also the presence of halite-bearing fluid inclusions in the outer rims of magnetite. The abundances of trace elements such as Ti, V, Al and Mn in magnetite rims systematically decrease from core to rim, consistent with magnetite growth from a cooling magmatic-hydrothermal fluid (Fig. 3.3, 3.5) (Nadoll et al. 2014). Knipping et al. (2015a) reported model results that indicate the magnetite - fluid suspension is buoyant as long as the proportion of magnetite is <37 vol. % of the suspension Similarly, the Cretaceous age IOA El Romeral located to the south of Los Colorados was found to have zoned magnetite containing high V and Ti contents (~2500 - 2800 and ~80 - 3000 ppm respectively) rich in high-temperature (up 1020 ℃) silicate mineral inclusions rimmed by a second generation of magnetite that is relatively

inclusion free with high V and low Ti contents (2300 -2700 ppm and 50 - 400 ppm respectively) (Rojas et al. 2018a,b). Rojas et al. (2018a) interpreted this observation along with high-temperature actinolite (Ca- and Mg-rich cores), fluorapatite, and high Co:Ni (1-10) pyrite at depth within the deposit and lower temperature, low Co:Ni (<0.5) pyrite and hydroxyapatite at more shallow levels to indicate a shift from high-temperature (up to 840 ℃) magmatically derived mineralization to a lower temperature (<600 ℃) magmatic-hydrothermal fluid precipitation. The El Romeral IOA ore body was determined to be genetically linked to the nearby Romeral diorite.

Regional changes in tectonic stress can rapidly destabilize a magma body and cause the magnetite - fluid suspension to ascend through high-flux permeable channels that become well developed with increasing crystallinity of ductile magma (Hersum et al. 2005; Hautmann et al. 2014). Once the magnetite-fluid suspension evolves from its source magma, it will ascend along pre-existing faults and magnetite will drop out of the fluid suspension when it reaches a level of neutral buoyancy, forming the structurally controlled orebodies observed in the Los Colorados deposit. Depending on the permeability-porosity of the host rocks adjacent to the fault, the ore fluid may migrate into the host rocks and form disseminated orebodies, also observed at Los Colorados. We highlight that magnetite - apatite orebodies globally exhibit styles of mineralization identical to that observed at Los Colorados, and fluid inclusion microthermometry and mineral-mineral stable isotope fractionation record temperatures at the time of mineralization that range from approximately 500 to >650 °C (Bilenker et al. 2016).
The magmatic-hydrothermal ore fluid will continue to ascend via pre-existing faults, and percolate into the host rocks proximal to pre-existing faults, depending on the local porosity and permeability of fault-adjacent rocks. Importantly, data from natural systems (Williams-Jones and

Heinrich 2005) and experimental studies (Chou and Eugster 1977; Wood and Samson 1998; Simon et al. 2004; Hurtig and Williams-Jones 2014; Williams-Jones and Migdisov 2014) demonstrate that the fluid will be enriched in S and metals such as Fe, Cu and Au as it cools to temperatures < 500 °C. Thus, the ore fluid is capable of precipitating iron oxides and metal sulfides during decompression and cooling within, above, and proximal to the magnetite-rich orebodies.

Reich et al. (2016) examined the geochemistry of pyrite from the Los Colorados magnetite ore body and host diorite intrusion. Pyrite is present as disseminated grains within the orebody and host diorite, and as veins that cross-cut the main orebodies. They found anomalously high concentrations of Co and Ni (up to ~3.9 and ~1.5 wt. %, respectively) in pyrite, with Co/Ni ratios ranging from ~0.5 to >2. Reich et al. (2016) compared the pyrite chemistry from Los Colorados to published pyrite chemistry from magmatic Cu-Ni, VMS, porphyry Cu-Mo, Fe-Cu skarn, orogenic Au, and IOCG deposits, including pyrite from orebodies in the Mantoverde district, and concluded that the high Co and Ni concentrations and high Co/Ni ratios (>1) in pyrite from Los Colorados indicate growth of pyrite from a magmatic-hydrothermal ore fluid sourced from an intermediate to mafic magma. Reich et al. (2016) propose that the pyrite at Los Colorados precipitated from the same magmatic-hydrothermal ore fluid that formed the Los Colorados IOA deposit. Precipitation of pyrite likely occurred as the temperature of the ore fluid decreased below 500 °C, consistent with experimental data for the mobility of Fe and S in aqueous fluid (Wood and Samson 1998).

Pyrite from the Mantoverde IOCG deposits has Co/Ni ratios that range from about 5 to 15, overlapping the Co/Ni ratios for pyrite at Los Colorados (Reich et al. 2016). Three chemically distinct groups of pyrite were found to exist from the Mantoverde IOCG deposit,

containing Co/Ni ratios of <1, 1-20, and >90, partially overlapping Co/Ni rations from Los Colorados (Johansson et al. 2017). These ratios grade high (i.e. >90) to low (i.e. <1) from the deeper sections of the deposit to the upper sections, indicative of a cooling and evolving fluid. The elevated Co/Ni ratio for pyrite at Mantoverde is consistent with an intermediate to mafic magma source for the ore fluid. Iron oxide - copper - gold orebodies within the Mantoverde district are also spatially and temporally associated with magnetite - apatite ± pyrite mineralization (Benavides et al. 2008; Rieger et al. 2010), and it seems geologically plausible that the formation of the Mantoverde system is consistent with the combined igneous/magmatic-hydrothermal model proposed by Knipping et al. (2015a). Such a model predicts the presence of magnetite-rich mineralization at depth in the Mantoverde system, which is corroborated by geophysical data (Mantos Copper, written communication, July 4, 2017).

The igneous/magmatic-hydrothermal genetic model predicts a continuum for the trace element chemistry of magnetite in the sulfur-poor, IOA orebodies and magnetite in the sulfur-enriched, IOCG orebodies. This continuum should manifest in progressively lower concentrations of trace elements such as Ti, V, Mn and Al as a function of the temperature at which magnetite equilibrates with the evolving (cooling) magmatic-hydrothermal ore fluid (Nadoll et al. 2014). This feature is observed in the trace element chemistry for magnetite from the Los Colorados IOA deposit and the Mantoverde IOCG deposit (Fig. 3.3). Clearly, these two deposits are not themselves genetically related to each other, but the trace element composition of magnetite in each deposit is consistent with a single, down-temperature continuum from a magmatic-hydrothermal fluid. From an exploration perspective, this may allow the trace element chemistry of magnetite to be useful, provided that extensive alteration (i.e., complete dissolution-reprecipitation) has not affected the orebody. We note that field observations of the depth of

mineralization for IOCG and IOA deposits are consistent with a model wherein IOCG and IOA deposits represent end-members of a single evolving ore system (Benavides et al., 2008; Richards and Mumin 2013a; Barra et al. 2017).

Lastly, we note that the magmatic/magmatic-hydrothermal model is supported by Re-Os data for Mantoverde and a plethora of other IOCG (i.e., Candelaria, Casualidad, Diego de Almagro, and Barreal Seco) and IOA (i.e., Los Colorados, El Romeral, and Carmen) ore deposits. Barra et al. (2017) report that these deposits have low to moderate Re concentration (<250 ppb), low Os concentration (<300 ppt total Os), and are dominated by radiogenic Os (>90% Os) and variable initial Os ratios. The Re-Os systematics for the deposits are similar to those for Chilean porphyry Cu-Mo systems, which formed unequivocally from magmatic-hydrothermal fluids.

## CONCLUSIONS

New Fe and O isotope data reported here for Iron Oxide Stage magnetite and Late Stage hematite from the Mantoverde IOCG district, combined with published data for isotopes of C, O, S, Sr, Pb, Ar, Kr, and Xe for hypogene samples from the Mantoverde district, support the hypothesis that mineralization in the Mantoverde district is primarily the result of magmatic-hydrothermal fluids. Magnetite mineral cores exhibit high Si, Al, Mg, and Ca contents relative to the surrounding magnetite rim, indicating magnetite grew from an initially hotter and gradually cooling source-fluid. Oxygen isotope $\delta^{18}O$ values vary among individual magnetite and hematite samples due to variable degrees of hydrothermal alteration, supported by widely varying Al, Ca, Mn, Ti, and V concentrations in magnetite and hematite, while Fe isotope $\delta^{56}Fe$ values remain

relatively unaffected by hydrothermal alteration and, when coupled with O isotopes, are a robust tool to differentiate between magmatic and meteoric fluid sources.

**ACKNOWLEDGEMENTS**

TMC thanks the Society of Economic Geologists and the University of Michigan for providing funding, Mantos Copper for providing access to drill core and generous hospitality, and Zhenhao Zhou from the University of Illinois for amazing assistance with Fe isotope analyses. ACS acknowledges funding from NSF EAR grants #1250239 and #1264560. MR and FB acknowledge funding from Millennium Science Initiative (MSI) through Millennium Nucleus for Metal Tracing along Subduction Grant NC130065, and FONDECYT Grant #1140780 "Metallogenesis of the Mesozoic magmatic arc of northern Chile: Testing the IOCG connection using a multi-proxy geochemical approach".

**REFERENCES**

Anbar AD (2004) Iron stable isotopes: Beyond biosignatures. Earth and Planetary Science Letters, 217:223–236.

Anbar AD, Jarzecki AA, Spiro TG (2005) Theoretical investigation of iron isotope fractionation between $Fe(H_2O)_6^{3+}$ and $Fe(H_2O)_6^{2+}$: implications for iron stable isotope geochemistry. Geochimica et Cosmochimica Acta, 69:825–837.

Barra F, Reich M, Rojas P, Selby D, Simon AC, Salazar E, Palma G (2017) Unraveling the origin of the Andean IOCG Clan: A Re-Os Isotope Approach. Ore Geology Reviews, 81:62–78.

Barton MD (2014) Iron oxide (–Cu–Au–REE–P–Ag–U–Co) systems, in Scott SD, ed., Geochemistry of mineral deposits. Amsterdam, Elsevier, Treatise on Geochemistry, 2nd ed., 13:515-541

Barton MD, Johnson DA (1996) Evaporitic-source model for igneous-related Fe oxide-(REE-Cu-Au-U) mineralization. Geology, 26:259–262.

Benavides J, Kyser TK, Clark AH, Oates CJ, Zamora R, Tarnovschi R, Castillo B (2007) The Mantoverde iron oxide-copper-gold district, III Región, Chile: the role of regionally derived, non-magmatic fluids in chalcopyrite mineralization. Economic Geology, 102:415–440.

Benavides J, Kyser TK, Clark AH, Stanley C, Oates CJ (2008) Exploration guidelines for copper-rich iron oxide–copper–gold deposits in the Mantoverde area, northern Chile: the integration of host-rock molar element ratios and oxygen isotope compositions. Geochemistry, Exploration, Environment, Analysis, 8:343–367.

Bilenker LD (2015) Elucidating igneous and ore-forming processes with iron isotopes by using experimental and field-based methods. PhD dissertation, University of Michigan, 103 p.

Bilenker LD, VanTongeren JA, Lundstrom CC, Simon AC (2017) Iron isotopic evolution during fractional crystallization of the uppermost Bushveld Complex layered mafic intrusion. Geochemistry Geophysics Geosystems, 18, doi:10.1002/ 2016GC006660.

Bilenker LD, Simon AC, Reich M, Lundstrom CC, Gajos N, Bindeman I, Barra R, Munizaga R (2016) Fe-O stable isotope pairs elucidate a high-temperature origin of Chilean iron oxide-apatite deposits. Geochimica et Cosmochimica Acta, 177:94–104.

Bindeman I (2008) Oxygen isotopes in mantle and crustal magmas as revealed by single crystal analysis. Reviews in Mineralogy and Geochemistry, 69:445–478.

Blanchard M, Poitrasson F, Méheut M, Lazzeri M, Mauri F, Balan E (2009) Iron isotope fractionation between pyrite ($FeS_2$), hematite ($Fe_2O_3$) and siderite ($FeCO_3$): A first-principles density functional theory study. Geochimica et Cosmochimica Acta, 73:6565–6578.

Bottinga Y, Javoy M (1975) Oxygen isotope partitioning among the minerals in igneous and metamorphic rock. Reviews of Geophysics, 13:401–418.

Childress TM, Simon AC, Day WC, Lundstrom CC, Bindeman IN (2016) Iron and oxygen isotope signatures of the Pea Ridge and Pilot Knob magnetite-apatite deposits, Southeast Missouri, USA. Economic Geology, 111:2033-2044

Chou, IM, Eugster, HP (1977) Solubility of magnetite in supercritical chloride solutions. American Journal of Science, 277:1296–1314.

Cole DR, Horita J, Polyakov VB, Valley JW, Spicuzza MJ, Coffey DW (2004) An experimental and theoretical determination of oxygen isotope fractionation in the system magnetite-$H_2O$ from 300 to 800°C. Geochimica et Cosmochimica Acta, 68:3569–3585.

Cornejo P, Matthews S, Orrego M, Robles W (2000) Etapas de mineralización asociadas a alteración potásica en un sistema Fe-Cu-Au: Yacimiento Mantoverde, III Región de Atacama, Chile: IX Congreso Geológico Chileno, Puerto Varas, Actas, p 97–101.

Craddock PR, Dauphas N (2011) Iron isotopic compositions of geological reference materials and chondrites. Geostandards and Geoanalytical Research, 35:101–123.

Dare SAS, Barnes S-J, Beaudoin G (2014) Did the massive magnetite "lava flows" of El Laco (Chile) form by magmatic or hydrothermal processes? New constraints from magnetite composition by LA-ICP-M. Mineralium Deposita, 50:607–617.

Dupuis C, Beaudoin G (2011) Discriminant diagrams for iron oxide trace element fingerprinting of mineral deposit types. Mineralium Deposita, 46:319–335.

Fisher LA, Kendrick MA (2008) Metamorphic fluid origins in the Osborne Fe oxide-Cu-Au deposit, Australia: evidence from noble gases and halogens. Mineral Deposits, 43:483–497.

Frost CD, Blanckenburg F von, Shoenberg R, Frost BR, and Swapp SM (2007), Preservation of Fe isotope heterogeneities during diagenesis and metamorphism of banded iron formation. Contributions to Mineral Petrology, 153:211–235

Groves DI, Bierlein FP, Meinert LD, Hitzman MW (2010) Iron oxide copper-gold (IOCG) deposits through earth history: Implications for origin, lithospheric setting, and distinction from other epigenetic iron oxide deposits. Economic Geology, 105:641–654.

Hautmann S, Witham F, Christopher T, Cole P, Linde AT, Sacks S, and Sparks SJ (2014) Strain field analysis on Montserrat (W.I.) as tool for assessing permeable flow paths in the magmatic system of Soufriere Hills Volcano. Geochemistry Geophysics Geosystems, 15:676–690, doi: 10.1002/2013GC005087

Heimann A, Beard BL, Johnson CM (2008) The role of volatile exsolution and subsolidus fluid/rock interactions in producing high $^{56}Fe/^{54}Fe$ ratios in siliceous igneous rocks. Geochimica et Cosmochimica Acta, 72:4379–4396.

Hersum T, Hilpert M, Marsh B (2005) Permeability and melt flow in simulated and natural partially molten basaltic magmas. Earth and Planetary Science Letters, 237:798–814, doi: 10.1016/j.epsl.2005.07.008

Hitzman MW, Oreskes N, Einaudi MT (1992) Geological characteristics and tectonic setting of Proterozoic iron oxide (Cu-U-Au-REE) deposits. Precambrian Research, 58:241–287.

Huang F, Zhang Z, Lundstrom CC, Zhi X (2011) Iron and magnesium isotopic compositions of peridotite xenoliths from eastern China. Geochimica et Cosmochimica Acta, 75:3318–3334.

Hurtig NC, Williams-Jones AE (2014) An experimental study of the transport of gold through hydration of AuCl in aqueous vapour and vapour-like fluids. Geochimica et Cosmochimica Acta, 127:305–325.

Hurwitz S, Navon O (1994) Bubble nucleation in rhyolitic melts: experiments at high pressure, temperature, and water content, Earth Planet. Science Letters, 122:267–280.

Johansson C, Barra F, Reich M, Deditius AP, Simon AC, Rojas P (2017) The Co-Ni signature of sulfide minerals from the Mantoverde IOCG deposit, northern Chile. Goldschmidt Abstracts, 1871

Jones CE, Jenkyns HC, Coe AL, and Hasselbo SP (1994) Strontium isotopic variations in Jurassic and Cretaceous seawater. Geochimica et Cosmochimica Acta, 58:3061–3074.

Jonsson E, Valentin RT, Högdahl K, Harri C, Weis F, Nilsson KP, Skelton A (2013) Magmatic origin of giant 'Kiruna-type' apatite-iron-oxide ores in central Sweden. Scientific Reports, 3, doi: 10.1038/srep01644.

Knipping JL, Bilenker LD, Simon AC, Reich M, Barra F, Deditius AP, Lundstrom C, Bindeman I, Munizaga R (2015a) Giant Kiruna-type deposits form by efficient flotation of magmatic magnetite suspensions. Geology, 43:491–594.

Knipping JL, Bilenker LD, Simon AC, Reich M, Barra F, Deditius AP, Wälle M, Heinrich CA, Holtz F, and Munizaga R (2015b) Trace elements in magnetite from massive iron oxide-apatite deposits indicate a combined formation by igneous and magmatic hydrothermal processes. Geochimica et Cosmochimica Acta, 171:15–38.

Lager I (2001) The geology of the Palaeoproterozoic limestone-hosted Dannemora iron deposit, Sweden: The Geological Survey of Sweden, 54 p.

Lara L, Godoy E (1998) Hoja quebrada salitrosa, III Región de Atacama: Santiago, Chile. Servicio Nacional de Geología y Minería, Mapas Geológicos 4, escala 1:100,000.

Lucassen F, Kramer W, Bartsch V, Wilke HG, Franz G, Romer RL, and Dulski P (2006) Nd, Pb, and Sr isotope composition of juvenile magmatism in the Mesozoic large magmatic province of northern Chile (18-27°S): Indications for a uniform subarc mantle. Contributions to Mineralogy and Petrology, 152:571-589.

Markl G, Blanckenburg F von, Wagner T (2006) Iron isotope fractionation during hydrothermal ore deposition and alteration. Geochimica et Cosmochimica Acta, 70:2011–3030.

Marschik R, Fontboté L (2001) The Punta del Cobre Formation, Punta del Cobre-Candelaria area, northern Chile. Journal of South American Earth Sciences, 14:401–433.

Marschik R, Fontignie D, Chiaradia M, Voldet P (2003) Geochemical and Sr–Nd–Pb–O isotope composition of granitoids of the Early Cretaceous Copiapó plutonic complex (27°30’S), Chile. Journal of South American Earth Sciences, 16:381–398.

Marschik R, Kendrick MA (2015) Noble gas and halogen constraints on fluid sources in iron oxide-copper-gold mineralization: Mantoverde and La Candelaria, Northern Chile. Mineralium Deposita, 50:357–371.

Marshal LJ, Oliver NHS (2006) Monitoring fluid chemistry in IOCG - related metasomatic processes, eastern Mt Isa Block, Australia. Geofluids, 6:45–66.

Millet MA, Baker JA, Payne CE (2012) Ultra-precise stable Fe isotope measurements by high resolution multiple-collector inductively coupled plasma mass spectrometry with a 57Fe-58Fe double spike. Chemical Geology, 304:18–25.

Montreuil, J-F, Corriveau, L, Davis, WJ (2016) Tectonomagmatic evolution of the southern Great Bear Magmatic Zone (Northwest Territories, Canada); implications for the genesis of iron oxide-alkali-altered hydrothermal systems. Economic Geology, 111:2111-2138.

Mpodozis C, Ramos V (1990) The Andes of Chile and Argentina: circum-Pacific council for energy and mineral resources. Earth Science Series, 11:59–90.

Mumin AH, Somarin AK, Jones B, Corriveau L, Ootes L, Camier J (2010) The IOCG-porphyry-epithermal continuum in the Great Bear Magmatic Zone, Northwest Territories, Canada. In Exploring for Iron Oxide Coper-Gold Deposits: Canada and Global Analogues (eds. Corriveau L and Mumin AH). Geological Association of Canada, Short Course Number 20, p. 59-78

Nadoll P, Angerer T, Mauk JL, French D, Walshe J (2014) The chemistry of hydrothermal magnetite: A review. Ore Geology Reviews, 61:1–32.

Naslund HR, Henriquez F, Nyström JO, Vivallo W, Dobbs FM (2002) Magmatic iron ores and associated mineralisation: examples from the Chilean high Andes and coastal Cordillera. In Hydrothermal Iron Oxide Copper–Gold A Global Perspective, 2 (ed. Porter TM). PGC Publishing, Adelaide, Australia, p. 207–226.

Neumann E-R, Svensen HH, Polozov AG, Hammer Ø (2017) Formation of Si-Al-Mg-Ca-rich zoned magnetite in an end-Permian phreatomagmatic pipe in the Tunguska Basin, East Siberia. Mineralium Deposita, 52:1205–1222.

Nyström, JO, Henríquez F (1994) Magmatic features of iron ores of the Kiruna-type in Chile and Sweden: Ore textures and magnetite geochemistry. Economic Geology, 89:820–839.

Nyström JO, Billström K, Henríquez F, Fallick AE, Naslund HR (2008) Oxygen isotope composition of magnetite in iron ores of the Kiruna type in Chile and Sweden: GFF [Geologiska Föreningen], 130:177–188.

Ohmoto H, Rye RO (1974) Hydrogen and oxygen isotopic compositions of fluid inclusions in the Kuroko deposits, Japan. Economic Geology, 69:947–953.

Orrego M, Zamora R (1991) Manto Ruso: un yacimiento de cobre ligado a la Falla de Atacama, norte de Chile: Congreso Geológico Chileno, 6th, Viña del Mar, Resumenes Expandidos, 174–178.

Pollard PJ (2006) An intrusion-related origin for Cu-Au mineralization in iron oxide-copper-gold (IOCG) provinces. Mineralium Deposita, 41:179–187.

Polyakov VB, Clayton RN, Horita J, Mineev SD (2007) Equilibrium iron isotope fractionation factors of minerals: Reevaluation from the data of nuclear inelastic resonant X-ray scattering and Mössbauer spectroscopy. Geochimica et Cosmochimica Acta, 71:3833–3846

Porter TM, ed. (2000) Hydrothermal iron oxide copper-gold and related deposits: A global perspective. Australian mineral Foundation, Adelaide, 349 p.

Reich M, Simon AC, Deditius A, Barra F, Chryssoulis S, Lagas G, Tardani D, Knipping J, Bilenker L, Sanchez-Alfaro P, Roberts MP, Munizaga R (2016) Trace element signature of pyrite from the Los Colorados iron oxide-apatite (IOA) deposit, Chile: A missing link between Andean IOA and IOCG systems? Economic Geology, 111:743–761.

Richards, JP, Mumin AH (2013a) Lithospheric fertilization and mineralization by arc magmas: Genetic links and secular differences between porphyry copper±molybdenum±gold and magmatic-hydrothermal iron oxide copper-gold deposits. In Colpron, M, Bissig, T, Rusk, BG, Thompson, JFH (eds.); Tectonics, Metallogeny, and Discovery: The North American Cordillera and Similar Accretionary Settings. Society of Economic Geologists, Special Publication 17:277-299.

Richards JP, Mumin AH (2013b) Magmatic-hydrothermal processes within an evolving Earth: iron oxide-copper-gold and porphyry Cu ± Mo ± Au deposits. Geology. http://dx.doi.org/10.1130/G34275.1.

Rieger AA, Marschik R, Díaz M, Hölzl S, Chiaradia M, Akker B, Spangenberg JE (2010) The hypogene IOCG mineralization in the Mantoverde district, northern Chile. Economic Geology, 105:1271–1299.

Rieger AA, Marschik R, Díaz M (2012) The evolution of the hydrothermal IOCG system in the Mantoverde district, northern Chile: new evidence from microthermometry and stable isotope geochemistry. Mineral Deposits, 47:359–369.

Roberts DE, Hudson GRT (1983) The Olympic Dam copper-uranium-gold-silver deposit, Roxby Downs, South Australia. Economic Geology, 78:799–822.

Rojas PA, Barra F, Deditius A, Reich M, Simon A, Roberts M, Rojo M (2018) New contributions to the understanding of Kiruna-type iron oxide-apatite deposits revealed by

magnetite ore and gangue mineral geochemistry at the El Romeral deposit, Chile. Ore Geology Reviews, 93:413–135

Rojas, PA, Barra F, Reich M, Deditius A, Simon A, Uribe F, Romero R, Rojo M (2018) A genetic link between magnetite mineralization and diorite intrusion at the El Romeral iron oxide-apatite deposit, northern Chile. Mineralium Deposita, 1-20., https://doi-org/10.1007/s00126-017-0777-x

Saunier G, Pokrovski GS, Poitrasson F (2011) First experimental determination of iron isotope fractionation between hematite and aqueous solution at hydrothermal conditions. Geochimica et Cosmochimica Acta, 75:6629–6645.

Schüßler J (2008) Controls on stable iron isotope variations in magmatic systems — Significance of mineral-melt isotopic fractionation in experiments and nature: Unpublished Ph.D. thesis, Faculty of Natural Science, Gottfried Wilhelm Leibniz Universität, Hannover, Germany, 165 p.

Shimazaki H (1998) On the occurrence of silician magnetites. Resource Geology, 48(1):23–29

Sillitoe RM (2003) Iron oxide-copper-gold deposits: An Andean view. Mineralium Deposita, 38:787–812.

Sillitoe RM, Burrows DR (2002) New field evidence bearing on the origin of the El Laco magnetite deposit, northern Chile. Economic Geology, 97:1101–1109.

Simon AC, Pettke T, Candela PA, Piccoli PM, and Heinrich CA (2004) Magnetite solubility and iron transport in magmatic-hydrothermal environments. Geochimica et Cosmochimica Acta, 68:4905–4914.

Simon, A.C., Knipping, J., Reich, M., Barra, F., Deditius, A.P., Bilenker, L., Childress, T. (2018) Kiruna-Type Iron Oxide-Apatite (IOA) and Iron Oxide Copper-Gold (IOCG) Deposits Form by a Combination of Igneous and Magmatic-Hydrothermal Processes: Evidence from the Chilean Iron Belt. Society of Economic Geology Special Publication No. 21, pp. 89-114.

Taylor HP (1967) Oxygen isotope studies of hydrothermal mineral deposits, in Barnes, H.L., ed., Geochemistry of Hydrothermal Ore Deposits, 1st ed., New York, Holt, Rinehart and Winston, 109–142.

Tornos F, Velasco F, Hanchar JM (2016) Iron-rich melts, magmatic magnetite, and superheated hydrothermal systems: The El Laco deposit, Chile. Geology, 44(6):427–430.

Travisany V, Henriquez F, Nyström JO (1995) Magnetite lava flows in the Pleito-Melon District of the Chilean iron belt: Economic Geology, 90:438–444.

Valley PM, Hanchar JM, Whitehouse MJ (2011) New insights on the evolution of the Lyon Mountain Granite and associated Kiruna-type magnetite-apatite deposits: Adirondack Mountains, New York State. Geosphere, 7:357–389.

Velasco F, Tornos F, Hanchar JM (2016) Immiscible iron-and silica-rich melts and magnetite geochemistry at the El Laco volcano (northern Chile): Evidence for a magmatic origin for the magnetite deposits. Ore Geology Reviews 79:346–366.

Vila T, Lindsay N, and Zamora R (1996) Geology of the Mantoverde copper deposit, northern Chile: A specularite-rich hydrothermal tectonic breccia related to the Atacama fault zone. Society of Economic Geologists Special Publication 5:157–170.

Weis F (2013) Oxygen and iron isotope systematics of the Grängesberg mining district (GMD), central Sweden: Unpublished Ph.D. Dissertation, Uppsala Universitet, Uppsala, Sweden, 77p.

Williams PJ, Barton MD, Johnson DA, Fontboté L, de Haller A, Mark G, Oliver NHS. Marschik R (2005) Iron oxide copper-gold deposits: Geology, Space-time distribution, and possible modes of origin. Economic Geology 100th Anniversary Volume, 371–405.

Williams-Jones AE, Migdisov AA (2014) Experimental constraints on the transport and deposition of metals in ore-forming hydrothermal systems. Society of Economic Geologists, 18:77–96.

Williams-Jones AE, Heinrich CA (2005) Vapor transport of metals and the formation of magmatic-hydrothermal ore deposits. Economic Geology 100:1287−1312.

Wood SA, Samson IM (1998) Solubility of ore minerals and complexation of ore metals in hydrothermal solutions. In J. Richards and P. Larson, eds., Techniques in Hydrothermal Ore Deposits. Reviews in Economic Geology, 10:33–80.

Zamora R, Castillo B (2001) Mineralizació de Fe-Cu-Au en el distrito Mantoverde, Cordillera de la Costa, III Región de Atacama, Chile: Congreso Internacional de Prospectores y Exploradores, Lima, Conferencias, 2nd, Instituto de Ingenieros de Minas del Perú, Lima, Actas, 13p.

Zheng Y-F (1991) Calculation of oxygen isotope fractionation in metal oxides. Geochimica et Cosmochimica Acta 55:2299–2307.

Zheng Y-F (1993) Calculation of oxygen isotope fractionation in anhydrous silicate minerals. Geochimica et Cosmochimica Acta 57:1079–1091.

**TABLES**

**Table 3.1:** Sample descriptions determined by hand samples and transmitted and reflected microscopy. All depths were subject to EPMA. Asterisk indicates samples analyzed for both Fe and O isotopes.

| Sample | Depth(m) | Minerals present (in order of abundance) | Phases sampled | Isotope analyses |
|---|---|---|---|---|
| 1 | 262 | Magnetite, pyrite, K-feldspar, chlorite, specularite veinlets (1-3mm) | magnetite* | O, Fe |
| 2 | 276 | Pyrite, K-feldspar, chlorite, magnetite, specularite veinlets (1-2mm) | magnetite* ; hematite | O, Fe; O |
| 3 | 284 | K-feldspar, chlorite, pyrite, K-feldspar veinlets (<1mm) , magnetite, calcite veinlets (<1mm), specularite veinlets (<1mm), chalcopyrite | magnetite | O |
| 4 | 291 | Magnetite, pyrite, K-feldspar, chlorite, calcite veinlets (3-6mm), K-feldspar veinlets (<1-2mm), specularite veinlets (1mm) | magnetite | O |
| 5 | 298 | K-feldspar, magnetite, pyrite, chlorite, K-feldspar veinlets (<1-1mm), specularite | magnetite* ; hematite | O, Fe; none |
| 6 | 305 | Magnetite, K-feldspar, chlorite, pyrite, K-feldspar veinlets (<1-1mm), specularite | magnetite* ; hematite | O, Fe; none |
| 7 | 314 | K-feldspar, chlorite, pyrite, magnetite, specularite (<1-2mm) | magnetite* ; hematite | O, Fe; O |
| 8 | 324 | K-feldspar, hematite veinlets (<1mm), pyrite veinlets (<1-1mm), chalcopyrite, chlorite | hematite | none |
| 9 | 331 | K-feldspar, specularite, chalcopyrite, pyrite, magnetite | magnetite, hematite | Fe; none |

| | | | | |
|---|---|---|---|---|
| 10 | 340 | Magnetite, K-feldspar, chlorite, K-feldspar veinlets (<1-1mm), pyrite | magnetite* | O, Fe; none |
| 11 | 356 | K-feldspar, chlorite, magnetite, calcite vein (1->6mm), pyrite, specularite | hematite | none |
| 12 | 411 | K-feldspar, chlorite, magnetite, K-feldspar veinlets (<1mm), calcite veinlets (<1mm), quartz, specularite, chalcopyrite | magnetite* | O, Fe |
| 13 | 416 | K-feldspar, calcite veinlets (<1mm), chlorite, magnetite, specularite, chalcopyrite, pyrite | hematite | none |
| 14 | 423 | K-feldspar, chlorite, specularite veinlets (1mm), chalcopyrite veinlets (<1mm), pyrite, calcite | hematite | none |
| 15 | 438 | K-feldspar, chlorite, magnetite, K-feldspar veinlets (<1mm), specularite veinlets (1-4mm), calcite veinlets (<1-1.5mm), pyrite, chalcopyrite | magnetite; hematite | Fe; none |
| 16 | 449 | K-feldspar, specularite veinlets (<1-2mm), chlorite, chalcopyrite veinlets (<1mm) | hematite* | O, Fe |
| 17 | 455 | K-feldspar, specularite veinlets (<1-3mm), chalcopyrite, pyrite, chlorite | hematite* | O, Fe |
| 18 | 471 | K-feldspar, chlorite, magnetite, chalcopyrite, pyrite, specularite | magnetite | Fe |
| 19 | 489 | K-feldspar, chlorite, specularite veinlets (<1-2mm), calcite, chalcopyrite | hematite* | O, Fe, EMPA |
| 20 | 492 | K-feldspar, chlorite, specularite veinlets (<1-2mm), calcite veinlets (<1mm), chalcopyrite | hematite | O, EMPA |

**Table 3.2:** Major characteristics of deposits near drillhole DDH-18-DS91. Readers are referred to Benavides et al. (2007) and Rieger et al. (2010) for more detailed information.

| Deposit | General | Major mineralization |
|---|---|---|
| Manto Ruso | Large ore zone with both supergene and hypogene copper ore; east of Mantoverde fault; contains primarily hematite with local magnetite rich rocks | Specularite-cemented hydrothermal breccia with andesite and diorite fragments affected by strong K feldspar alteration and silicification ± chloritization. Pyrite, chalcopyrite, and, locally, bornite and digenite occur interstitial to specularite; breccia grades to specularite stockwork zone containing chalcopyrite-pyrite; host rocks characterized by strong pervasive quartz, K feldspar, or sericite alteration ± chlorite alteration. |
| Mantoverde Norte | Hosted within and proximal to the Mantoverde fault; main ore-bearing units all parallel the fault; contains supergene copper oxides | Specularite-calcite hydrothermal breccia with andesite or granitoid clasts commonly affected by variable K feldspar alteration with chloritization, sericitization, silicification, and/or carbonatization; cut by K feldspar ± quartz, tourmaline, sericite, calcite, and specularite veinlets pyrite, chalcopyrite, digenite present |
| Mantoverde Sur | Weak relation to Mantoverde fault; magnetite stockworks and disseminations; pervasive argillic alteration | magnetite-chlorite-sericite-K feldspar-cemented breccias, igneous clasts altered mainly by magnetite, K feldspar, and quartz, cut by K feldspar ± quartz, calcite, sericite, and late specularite-calcite veinlets; magnetite, mushketovite, pyrite, and chalcopyrite present |

**Table 3.3:** Oxygen and iron stable isotope ratios of magnetite and hematite measured in this study from drill hole DDH-14-DS91 in the Mantoverde district, which is located at 368875m E 7063667m N, north of Mantoverde Norte pit. Theoretical yields for magnetite are 7.8 and 10.4 µmol/gram. Blank spaces indicate samples that were not analyzed for either Fe or O.

| Sample | $\delta^{18}O$ (‰) | 2σ | µmol/gram | $\delta^{56}Fe$ (‰) | 2σ |
|---|---|---|---|---|---|
| 262m mt | 1.57 | 0.09 | 8.5 | 0.54 | 0.05 |
| 276m mt | 0.69 | 0.03 | 7.9 | 0.55 | 0.02 |
| 284m mt | 4.01 | 0.05 | 6.8 | | |
| 291m mt | 4.58 | 0.06 | 10.4 | | |
| 298m mt | 2.34 | 0.06 | 8.5 | 0.61 | 0.04 |
| 305m mt | 3.62 | 0.07 | 8.6 | 0.5 | 0.04 |
| 314m mt | 2.5 | 0.08 | 8.9 | 0.58 | 0.02 |
| 331m mt | | | | 0.37 | 0.06 |
| 340m mt | 4.61 | 0.11 | 6 | 0.46 | 0.04 |
| 411m mt | 3.02 | 0.06 | 4.9 | 0.53 | 0.04 |
| 438m mt | | | | 0.55 | 0.06 |
| 471m mt | | | | 0.38 | 0.02 |
| 276m hmt | -1.16 | 0.2* | 8 | | |
| 314m hmt | -0.67 | 0.2* | 8.6 | | |
| 449m hmt | -1.36 | 0.09 | 5.8 | 0.34 | 0.1 |
| 455m hmt | -0.96 | 0.04 | 9.2 | 0.42 | 0.09 |
| 489m hmt | -0.84 | 0.08 | 9.1 | 0.46 | 0.06 |
| 492m hmt | 5.57 | 0.11 | 9.3 | | |

**Table 3.4:** EPMA results for magnetite and hematite in weight percent. Where analyses were BLD, the detection limit was substituted for statistical calculations. Depths of magnetite samples ranges 262 to 471m. Depths of hematite samples ranges 299 to 492m. Comprehensive list of individual analyses and their respective depths are located in **Table 1.**

| | | Mg | Al | Si | Ca | Ti | V | Cr | Mn | Fe | O | Total |
|---|---|---|---|---|---|---|---|---|---|---|---|---|
| **magnetite** | **Max** | 0.55 | 1.64 | 1.59 | 0.71 | 3.62 | 0.20 | 1.40 | 0.02 | 72.64 | 22.11 | 94.40 |
| n= 323 | **Min** | 0.01 | 0.01 | 0.01 | 0.01 | 0.01 | 0.01 | 0.01 | 0.01 | 64.43 | 19.83 | 88.83 |
| | **Average** | 0.03 | 0.11 | 0.24 | 0.08 | 0.05 | 0.07 | 0.01 | 0.01 | 70.80 | 20.78 | 92.17 |
| | **SD** | 0.05 | 0.16 | 0.25 | 0.10 | 0.22 | 0.04 | 0.08 | 0.00 | 1.02 | 0.31 | 0.85 |
| **hematite** | **Max** | 1.26 | 0.50 | 0.97 | 0.30 | 3.02 | 0.53 | 0.02 | 0.08 | 70.93 | 21.74 | 92.06 |
| n= 195 | **Min** | 0.01 | 0.01 | 0.01 | 0.01 | 0.01 | 0.01 | 0.01 | 0.01 | 65.16 | 19.87 | 88.04 |
| | **Average** | 0.02 | 0.11 | 0.03 | 0.05 | 0.56 | 0.06 | 0.01 | 0.01 | 68.79 | 20.27 | 89.88 |
| | **SD** | 0.09 | 0.11 | 0.07 | 0.05 | 0.73 | 0.05 | 0.00 | 0.01 | 1.13 | 0.27 | 0.71 |

# CHAPTER IV

## TRIPLE OXYGEN, HYDROGEN, AND IRON STABLE ISOTOPES SIGNATURES INDICATE A SILICATE MAGMA SOURCE AND MAGMATIC-HYDROTHERMAL GENESIS FOR MAGNETITE ORE BODIES AT EL LACO, CHILE


## ABSTRACT

The El Laco iron oxide – apatite (IOA) ore bodies are some of the most enigmatic mineral deposits on Earth, interpreted to have formed as lava flows or hydrothermal replacements, two radically different processes. Field observations provide some support for both processes, but ultimately fail to explain all observations. Previously proposed genetic models include magnetite crystallization from an erupting immiscible Fe- and P-rich (Si-poor) melt and metasomatic replacement of andesitic lava flows by a hypogene hydrothermal fluid. A more recent interpretation of drill core at El Laco suggests a new model that invokes shallow emplacement and surface venting of a magnetite-bearing magmatic-hydrothermal fluid suspension. The 734 Mt (at 49.2% Fe) Plio-Pleistocene El Laco (IOA) deposits are hosted within a ~20-km$^2$ andesitic stratovolcano complex in northern Chile. In this study, we measured triple O, H, and Fe stable isotope abundances in bulk iron oxide (primarily magnetite with minor, secondary hematite and goethite) from five ore bodies around the El Laco volcano and used calculated values of $\delta^{18}O$, $\Delta^{17}O$, $\delta^{2}H$, and $\delta^{56}Fe$ to fingerprint the source of the ore forming fluid(s). Magnetite and bulk iron oxide from Laco Sur, Cristales Grandes, and San Vicente Alto $\delta^{18}O$ values display grouped ranges from 4.3 to 4.5‰ (n = 5), 3.0 to 3.9‰ (n = 5), and -8.5 to

-0.5‰ (n = 5), respectively. Magnetite from Rodados Negros was determined to be of the least altered samples and was also analyzed for $\delta^{17}O$ ratios, and yielded $\delta^{18}O$ values that range from 2.6 to 3.8 ‰ (n = 9), and $\Delta^{17}O$ values that range from -0.13 to 0.10 ‰ (n = 5). Bulk iron oxide from Laco Norte yielded $\delta^{18}O$ values that range from -10.2 to 4.5 ‰ (avg = 0.8 ‰, n = 18), and $\delta^{2}H$ of magnetite and bulk iron oxide (with H being in fluid inclusions and in minor goethite) from all five ore bodies ranges from -189.4 to -61.1 ‰ (n = 33). Values of $\delta^{56}Fe$ for magnetite and bulk iron oxide from all five ore bodies range from 0.04 to 0.70 ‰ (avg = 0.29, $\sigma$ = 0.15 ‰, n = 26). The Fe isotope data indicate a silicate magma source for Fe in magnetite and its alteration products from all sampled El Laco ore bodies. The O isotope data indicate a hydrous silicate magma source for O in magnetite and a volcanic degassing trend in $\delta^{2}H$ from fluid inclusions contained in magnetite from Laco Sur, Cristales Grandes, and Rodados Negros. Oxygen and H isotopic ratios for bulk iron oxide from Laco Norte and San Vicente Altos reveal a magmatic/magmatic-hydrothermal signature ($\delta^{2}H \simeq$ -60 to -80 ‰) that has been altered to meteoric values consistent with goethite in equilibrium with local O and H meteoric isotopic values ($\simeq$ -15.4 and -211 ‰, respectively). The sum of the data unequivocally fingerprint a silicate magma as the source of the ore fluids responsible for mineralization at El Laco and are consistent with a model that explains mineralization as the synergistic result of common magmatic and magmatic-hydrothermal processes during the evolution of a caldera-related explosive volcanic system.

## INTRODUCTION

Investigations to determine the genesis of iron oxide – apatite (IOA) deposits have been ongoing for decades, with proposed models that range from those that invoke purely

hydrothermal processes to those invoking purely magmatic processes. One of the most enigmatic and hotly debated deposits is the El Laco IOA deposit, located at about 5000 masl in the Chilean Altiplano (Fig. 4.1). Park (1961) documented the outcrops at El Laco and hypothesized the ore bodies represent surficial or shallow intrusion of iron oxide lava flows, citing textures among the iron oxide ore bodies that resemble aa, pahoehoe, volcanic bombs, and vesicular bubble-like shapes. At El Laco, two opposing models have been proposed and tested at length to explain the coexistence of arguably volcanic and hydrothermal features of the orebodies: liquid immiscibility (Naslund et al., 2002; Velasco et al., 2016; Tornos et al., 2016, 2017) and hydrothermal replacement of andesitic lava flows (Rhodes and Oreskes, 1995; Rhodes et al., 1999; Sillitoe and Burrows, 2002; Dare et al., 2015).

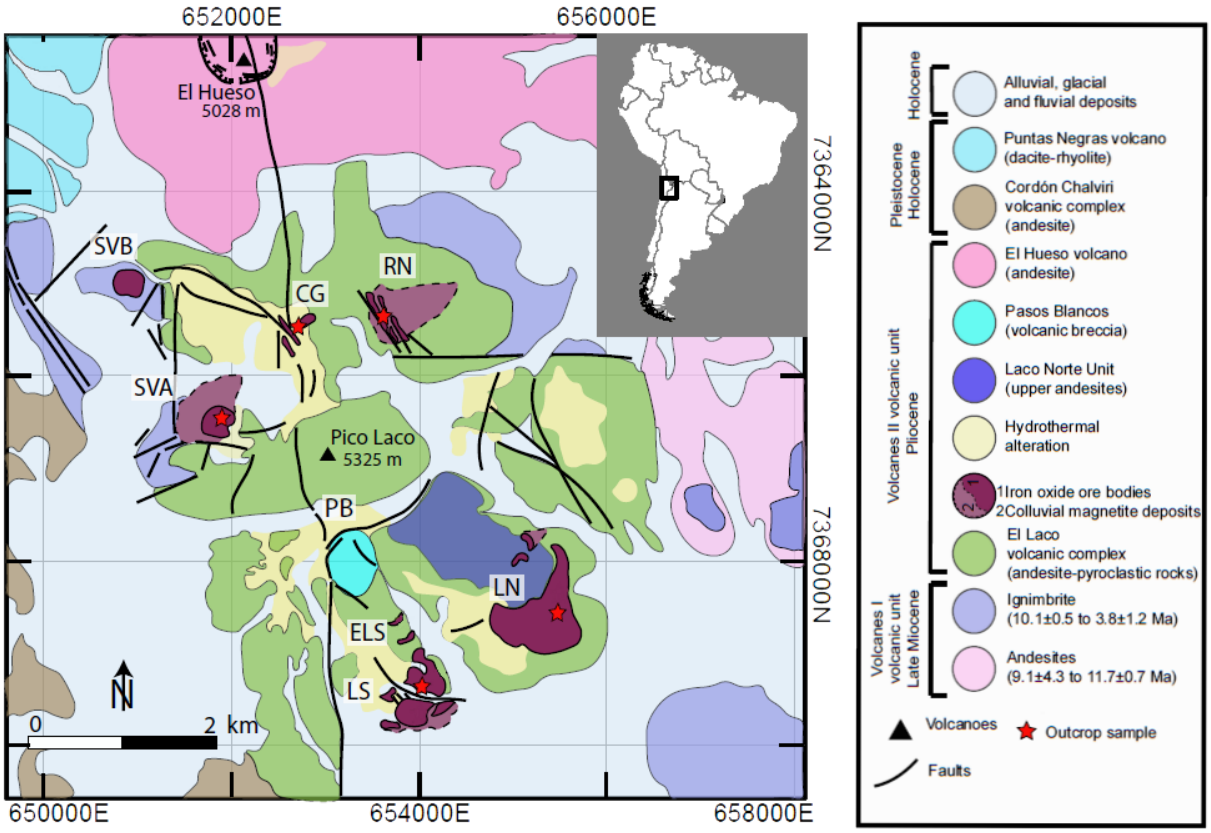


Figure 4.1: Geologic map of El Laco from Ovalle et al. (2018). The El Laco volcanic complex is primarily made up of andesite and pyroclastic rocks (green) with major iron oxide deposits (maroon). Red stars denote sampling locations. LN = Laco Norte, LS = Laco Sur, RN = Rodados Negros, CG = Cristales Grandes, SVA = San Vicente Alto, SVB = San Vicente Bajo.

The liquid immiscibility hypothesis, originally proposed by Philpotts (1967) to explain the magmatic/volcanic textures observed in many IOA deposits, invokes unmixing of a silicate melt into two physiochemically distinct melts, one Fe- and P-rich and the other Si-rich and Fe-poor (Naslund et al., 2002). In order for the Fe-P-rich melt to ascend from its source magma into the overlying crust and form an ore body, the model requires that $H_2O$ partition preferentially into the Fe-P-rich melt in order to lower its density and increase its buoyancy relative to the conjugate Si-rich melt (Tornos et al., 2016, 2017). In contrast, the replacement model calls upon a hypogene Fe-rich hydrothermal fluid to percolate through andesitic lava flows and entirely replace the host rock with magnetite and hematite and, importantly, preserve all original volcanic

textures (Rhodes et al., 1999; Sillitoe and Burrows, 2002; Dare et al., 2015). A new model by Ovalle et al. (2018) presents extensive textural and geochemical evidence for magnetite from surface and drill core samples at El Laco that is consistent with this model. Those authors propose that the El Laco ore bodies formed by eruption of a buoyant magnetite-fluid suspension that evolved from a silicate magma. Their model is based on Knipping et al. (2015a,b), who invoke crystallization of magnetite microlites from an intermediate silicate melt, followed by volatile saturation of the melt wherein the surface of magnetite microlites are preferentially wetted and swept up by the volatile phase to form a magnetite-fluid suspension (i.e., froth) that has a lower density than the surrounding melt.

In this study, we measured Fe, O, and H stable isotope compositions of magnetite, hematite, and goethite samples from five of the six largest deposits at El Laco to identify the source of the ore forming fluids and use the data to assess these three competing genetic hypotheses. In addition, we report the first $\Delta^{17}O$ values of iron oxides from an IOA deposit, and further prove that the combined use of conventional and non-conventional stable isotope tracers provide new insights on the formation of the IOA ore deposits, allowing tracing the source reservoirs for ore fluids and constraining the isotopic fractionation within and among iron oxide mineral systems.

## GEOLOGIC BACKGROUND

The El Laco volcanic complex is located in a structurally-controlled volcanic zone of the Central Andes (23°48’ S, 67°30’ W (Fig. 4.1)), and records an uncommon set of both magmatic and hydrothermal stages. It is composed by variably preserved andesitic to dacitic lava flows, pyroclastic rocks and volcanic breccias, which are the products of several stages of volcanic activity developed from the Pliocene to Pleistocene (5.3 ± 1.9 to 1.6 ± 0.5 Ma; K-Ar) (Naranjo et

al., 2010). These volcanic products host large iron oxide ore bodies with remarkably volcanic and subvolcanic features, which have been dated to 2.1 ± 0.1 Ma (apatite fission track, Maksaev et al., 1988). In addition, extensive zones of penetrative hydrothermal alteration are widespread at El Laco.

Stratigraphically from oldest to youngest, the major volcanic units are described as the lower andesites, upper andesites, dome-like edifices, and volcanic breccia bodies that crosscut the older units, The majority (>90%) of the andesitic volcanic materials are porphyritic, massive, rarely vesicular and contain abundant plagioclase and pyroxene phenocrysts. Unaltered andesites are silica oversaturated according to the total alkali-silica (TAS) classification diagram (Le Maitre et al., 2005) where they plot near the silica-saturated trachyandesite field, and are geochemically similar to nearby recent edifices such as Llullaillaco and Lascar (Matthews et al., 1999; Velasco et al,. 2016). The El Laco andesites are calc-alkaline I-type rocks that range in composition from basaltic andesite to primitive dacite, and their chemistry does not vary significantly among magmatic pulses (Velaso et al., 2016).

The magnetite orebodies are located around the central volcanic plug (Pico Laco), structurally associated with collapse-related fissures and secondary craters. (Frutos and Oyarzun, 1975; Naranjo et al., 2010; Ovalle et al., 2018). Based on their morphologies and surface textures they can be classified as stratabound (Laco Norte, Laco Sur, Laquito, San Vicente Alto), dome-shaped (San Vicente Bajo), and tabular (Rodados Negros, and Cristales Grandes). A recent study by Ovalle et al. (2018) reported that such ore bodies show a complex vertical zonation, composed by an outcropping portion of trace elements-depleted massive magnetite (e.g., Ti: 218 ppm and V: 586 ppm, average contents) partially to totally martitized (oxidized), with minor clinopyroxene, apatite and REE-rich and iron phosphates. Upper massive magnetite grades at

depth to large magnetite-(± clinopyroxene-scapolite) breccia bodies, characterized by a systematic increase of Ti in magnetite with depth (average contents of up to 7637 ppm; Ovalle et al., 2018). Magnetite from surface (focused of this study) exhibits a variety of textures. Massive stratabound ore bodies (above listed) are dominated by flow and highly vesicular textures, as well as octahedral and pyroclastic-like or friable magnetite. Whereas tabular ore bodies (above listed) are characterized by subvolcanic cooling textures such as columnar and bladed magnetite, and lack vesicularity (Figs. 4.2, 4.3A, 4.3C). Highly vesicular, friable magnetite is found in abundance at Laco Sur and occurs elsewhere to lesser degrees (Figs. 4.3B, 4.3D) (Nystrom et al., 2016). Columnar magnetite is observed locally within the deposits, and numerous vertically oriented gas escape tubes lined with octahedral magnetite are found at Laco Sur, Laco Norte, and San Vicente Alto; the tubes themselves ranging up to tens of centimeters in diameter to meters in height. Hydrothermal alteration at El Laco occurs widespread at both surface and depth, and although it appears to be spatially close to the iron bodies, there is not always a synchronous relationship between hydrothermal alteration and iron oxide mineralization (Tornos et al., 2017). Aureoles that are pervasive in the andesite surrounding the magnetite bodies consist of a magnetite-diopside-quartz assemblage (Vivallo et al., 1994; Rhodes et al., 1999). At depth, an alkali-calcic alteration assemblage is particularly well developed, and comprises intense scapolitization and diopside formation, that partially to pervasively replace andesitic fragments, which occur immersed in a magnetite-diopside-scapolite matrix (Rhodes et al., 1999; Naranjo et al., 2010; Ovalle et al., 2018). Late magnetite-clinopyroxene-pyrite and pyrite-bearing gypsum veinlets crosscut the breccia body at depth (Ovalle et al., 2018). Andesite is locally crosscut by coarse-grained veins with unidirectional growth mainly composed of diopside, magnetite, and anhydrite with crystals up to 10 cm long (Tornos et al., 2016).

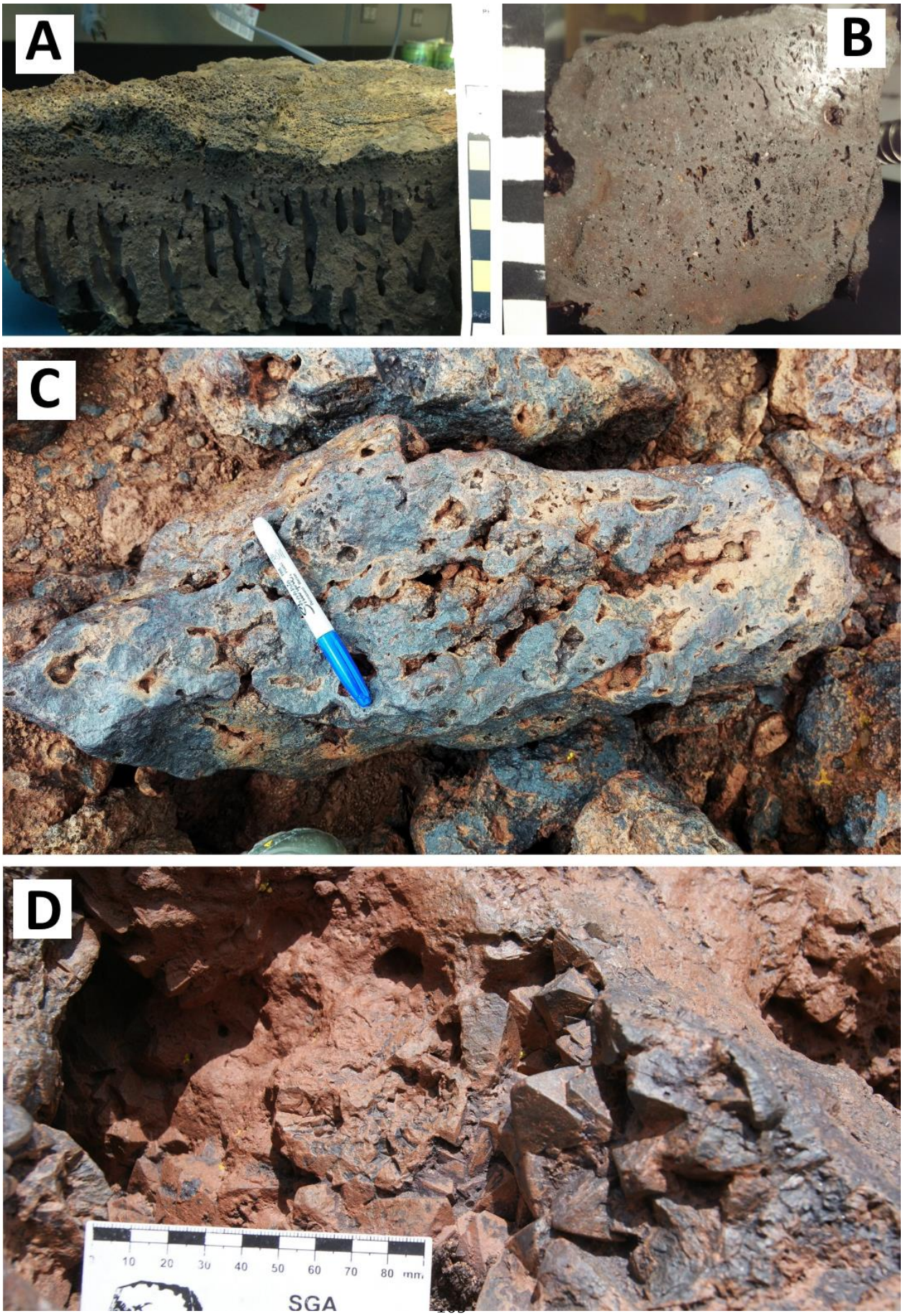
A
B
C
D
10 20 30 40 50 60 70 80 mm
SGA

Figure 4.2: Panel A shows a vesicular basalt sample from Hawaii. Panels B and C show vesicular magnetite from Laco Norte and Rodados Negros, respectively. Panel D shows octahedral magnetite from San Vicente Alto. Vesicular textures are nearly ubiquitous among the iron oxide deposits at El Laco, along with bomb and spinifex textures, demonstrating the volatile rich and fast cooling nature of these samples. Terminal euhedral magnetite tends to line the inner walls of vesicles. Scales in panels A and B are both in centimeters; marker for scale in panel C.

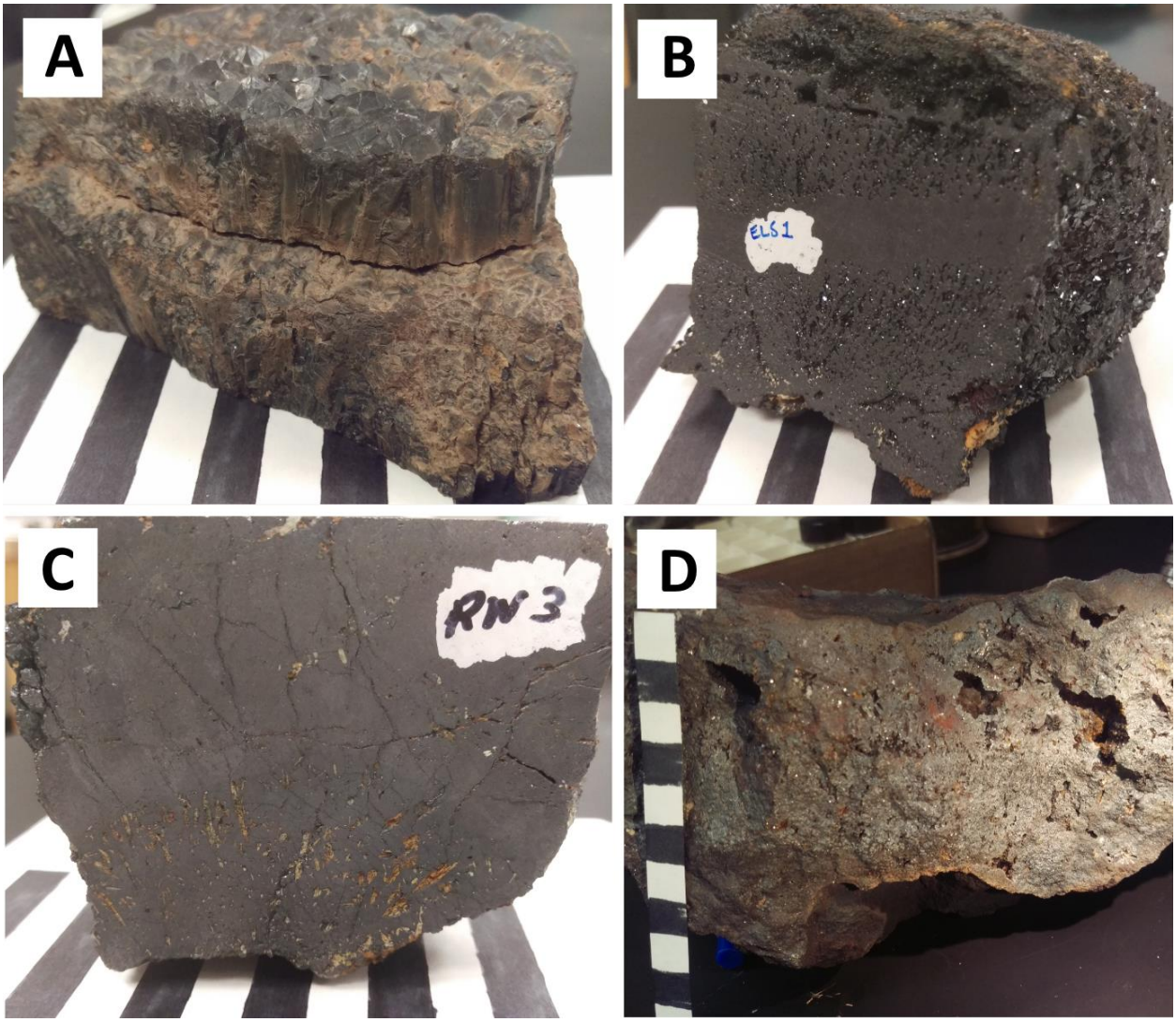


Figure 4.3: Select hand samples from El Laco. Panels A and C are hand samples RN-4 and -3, respectively, featuring columnar magnetite from Rodados Negros with octahedral terminations and oriented actinolite in panel C. Panel B shows highly vesicular magnetite from Laco Sur (LS-1). Panel D shows highly vesicular and oxidized magnetite from San Vicente Alto, similar to samples analyzed in this study. Black and white scale bars are 1 cm wide.

Weak regional propylitic alteration (chlorite-epidote-sericite; Vivallo et al., 1994; Rhodes et al., 1997) appears to temporally overlap sodic, potassic, and calcic alteration (Rhodes et al., 1999).

Widespread andesite bleaching at El Laco is a result of a late argillic alteration, which occurs as

extensive steam-heated zones marked by a penetrative replacement of andesites by argillic assemblages dominated by tridymite, cristobalite, alunite, jarosite, trace secondary copper minerals, and minor native sulfur, forming silicic vein-like structures and irregular hydrothermal breccia bodies (Vivallo et al., 1994; Sillitoe and Burrows, 2002). In addition, large exhalative deposits represented by gypsum-rich mounds, which appear to be fossil fumaroles, are located in discrete emission centers spatially associated with NW-trending collapse structures which control the late hot-spring-like geothermal activity at ELVC (Vivallo et al., 1994; Rhodes and Oreskes, 1994). Sulfate-rich alteration altered magnetite to hematite in some orebodies and replaced andesite with alunite and minor kaolinite, gypsum, and tridymite, and gypsum veins locally crosscut magnetite in several deposits (Sillitoe and Burrows, 2002).

## METHODS

### *Sample Selection*

Access to El Laco was provided by CAP Minería. Samples were collected from five of the seven surficial iron oxide deposits: Laco Norte, Laco Sur, Rodados Negros, Cristales Grandes, and San Vicente Alto. San Vicente Bajo and Laquito were not sampled. Sites range in elevation from about 4640 masl at Laco Sur to >5000 masl at Cristales Grandes. Samples at each site were selected in the field for their uniqueness in texture and appearance (e.g., columnar magnetite, octahedral magnetite, volcanic bomb-like) in order to sample a wide variety of textural types. With the exception of samples from Cristales Grandes and San Vicente Alto that contain large apatite and actinolite crystals, iron oxide hand samples were free of visible non-iron oxides.

*Sample preparation for stable isotope analysis*

Sample preparation followed the same procedure documented in Bilenker et al. (2016, 2017) and Childress et al. (2016). Samples of iron oxide were cut by diamond saw into small cubes in order to exclude as much as possible all non-iron oxide minerals. Samples were then wrapped in weighing paper and crushed with a plastic-sheathed mallet to reduce the grain size to less than 1 mm and disaggregate iron oxides and any gangue minerals. Magnetite grains were then separated from the crushed material by use of a hand magnet wrapped in a Kimwipe. The separated iron oxides grains were inspected by using a binocular microscope at ~40x magnification and only the most uniform grains were handpicked. Grain sizes of magnetite between ~0.1 and 0.8 mm were selected for H, O, and Fe isotope analyses. These grains were visually estimated to contain > 90 % magnetite for samples from Laco Sur, Cristales Grandes, and Rodados Negros. Samples from Laco Norte and San Vicente Alto were visually estimated to contain < 90 % magnetite and in some cases were primarily hematite and goethite and are referred to as bulk iron oxide samples. Figure 4.4 shows typical iron oxide textures in these samples, including magnetite replaced by hematite with goethite filling space between grains at Laco Norte (panel A), relatively homogeneous magnetite from Rodados Negros and Cristales Grandes (panels B and C), and magnetite intergrown with occasional $FePO_4$ replacing apatite at San Vicente Alto (panel D). Approximately 10 mg, 2-3 mg, and 0.5-1.5 mg of sample were used for H, O, and Fe analyses, respectively.

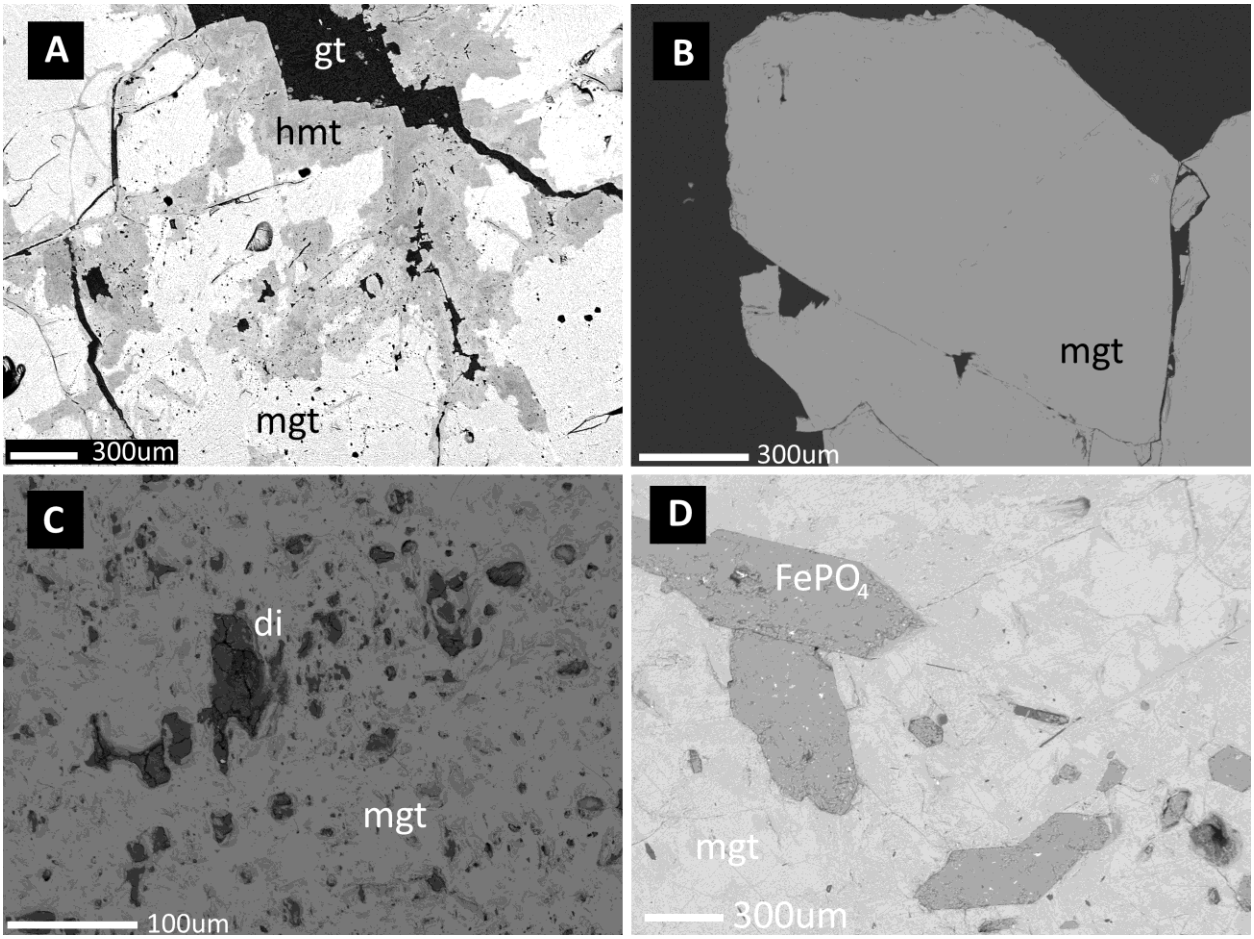


Figure 4.4: Backscatter images of typical magnetite textures from El Laco. Panel A (LN-2) shows magnetite (mgt) being replaced by hematite (hmt) on outer rims, with goethite (gt) filling space between grains. Panel B shows homogeneous magnetite from Rodados Negros (RN-1; black area is epoxy). Panel C shows magnetite intergrown with diopside (di) at Cristales Grandes (CG-5). Panel D (SVA-1) shows magnetite intergrown with $FePO_4$ that has replaced apatite.

Grains selected for Fe isotope analysis were further crushed to hasten acid digestion by use of an alumina ceramic mortar and pestle that were cleaned with ethanol and compressed air between samples to avoid contamination. Aliquots of polished magnetite and bulk iron oxide grains from all samples were inspected at high magnification using backscattered-electron (BSE) imaging on a Cameca SX-100 scanning electron microscope (SEM) and separately on a JEOL-7800FLV field emission-scanning electron microscope (FE-SEM); both instruments are located at the University of Michigan Electron Microbeam Analysis Lab (EMAL).

*Oxygen isotopes*

Oxygen isotope analyses of iron oxides were conducted at the University of Oregon by using a laser fluorination line coupled with a Thermo-Finnigan MAT 253 gas isotope ratio mass spectrometer (IRMS) in dual inlet mode. Iron oxide grains (2–3 mg) from each sample were subjected initially to low-power lasing. Laser power was slowly increased to minimize jumping movements of the grains during fluorination with $BrF_5$. For samples that did not experience grain jumping, $O_2$ yields were close to the theoretical 100%. All data were compared to the Gore Mountain garnet (in-house standard, UOG, recommended 6.52 ‰) which was measured before, during, and after analysis of iron oxide samples to correct for instrumental drift. The average value for standard UOG ($\delta^{18}O_{UOG}$) was 6.50 ‰ and the average 2σ for UOG for each day of analysis was ~0.27 ‰ (n = 14), calculated from variance. Individual sample analyses typically have 2σ of < 0.1 ‰. Theoretical $O_2$ yields for magnetite, hematite, and goethite are 7.8, 10.4, and 31.2 μmol/mg respectively. Oxygen isotope values are reported relative to the international Vienna Standard Mean Ocean Water (VSMOW) and were calculated using Equation 1:

$$\delta^{18}O_{sample}\ (‰) = [(^{18}O/^{16}O)_{measured} / (^{18}O/^{16}O)_{VSMOW} - 1] * 1000 \qquad (1)$$

The average UOG during $\Delta^{17}O$ analyses was 6.41 ± 0.01‰ (2σ, n = 3). Capital delta values were calculated using Equation 2:

$$\Delta^{17}O_{sample} = \delta^{17}O_{sample} - \delta^{18}O_{sample} * 5.305 \qquad (2)$$

where 5.305 is the slope of the reference line for minerals formed at high temperatures (Pack and Herwartz, 2014). Five samples from Rodados Negros were analyzed three times and averaged.

Triple oxygen isotopes were measured in a single session with $O_2$ gas as analyte run against calibrated reference gas, and an additional gas chromatographic purification step in a controlled He flow using 6ft long zeolite column that was added to the University of Oregon fluorination line (Bindeman et al., 2018). This procedure is needed to minimize potential $^{17}O$ contaminants (Pack and Herwartz, 2014) such as NF and organics.

*Hydrogen isotopes*

Hydrogen isotope analyses of iron oxides were also conducted at the University of Oregon by using a Thermo Scientific high temperature conversion elemental analyzer (TC/EA) with a MAT253 gas source IRMS following the procedure described in Bindeman et al. (2012). We used a glassy carbon reactor held at 1450 °C and gas chromatographic peak separation using continuous He flow and a CONFLOW gas interface. The reference materials USGS57 (biotite) and USGS58 (muscovite) (Qi et al., 2017) were measured throughout the analytical session to account for a range of $\delta^2H$ values, and were measured to be -91.0 ‰ (n = 5, 2σ = 9.7 ‰) and -28.0 ‰ (n = 5, 2σ = 4.7 ‰), respectively, with calculated wt% $H_2O$ contents of 3.6 (n = 5, 2σ = 0.1 %) and 4.1 (n = 5, 2σ = 0.0 %), respectively. Water was determined by peak integration of H and D areas relative to that of the known NBS30 and USGS57 micas (nominal $H_2O$ = 3.5 wt%). Results are reported relative to VSMOW, calculated using Equation 3:

$$\delta^2H_{sample}\ (‰) = [(^2H/^1H)_{measured} / (^2H/^1H)_{VSMOW} - 1] * 1000 \qquad (3)$$

*Iron isotopes*

Iron oxide samples were subjected to ion exchange chromatography to isolate Fe for isotopic analysis. Between ~0.5 and 1.5 mg of each sample was dissolved and dried down in aqua regia, again in 8N HCl, and then loaded into columns of AG1-X8 resin (Biorad, 200-400 mesh) in 8N HCl, following the procedure described by Huang et al. (2011). Analyses were performed at the Pacific Centre for Isotopic and Geochemical Research, University of British Columbia, Canada, using a Nu Plasma 1700 HR multi collector-inductively coupled plasma-mass spectrometer (MC-ICP-MS) in dry plasma mode with a DSN-100. The large geometry of the instrument allowed for complete separation of Ar interferences in high resolution. Cr was monitored and $^{54}$Fe and measurements were corrected because of isobaric interference with $^{54}$Cr. Each sample was analyzed three to four times, with all analyses bracketed by the international standard IRMM-14 to correct for small changes in mass bias over time. Average IRMM-14 measured 0.00 ‰, ($2\sigma = 0.077$, n = 12) (Millet et al., 2012). Iron isotope values (Table 4.1) are reported relative to IRMM-14, calculated by using Equation 4:

$$\delta^{56}Fe_{sample}\ (‰) = [(^{56}Fe/^{54}Fe)_{measured} / (^{56}Fe/^{54}Fe)_{IRMM\text{-}14} - 1] * 1000 \qquad (4)$$

**RESULTS**

*Oxygen isotope compositions*

Stable O isotope ratios for magnetite and bulk iron oxide are reported as $\delta^{18}O$ and $\Delta^{17}O$ in Tables 4.1 and 4.2, respectively. The $\delta^{18}O$ values ($\pm 2\sigma$) range from a very low meteoric -10.15 ‰ to normal magmatic 4.49 ‰. All negative values occur in samples from either Laco Norte or San Vicente Alto and correspond to a decrease in magnetite abundance and increase in

(secondary) hematite and/or goethite. The $\delta^{18}O$ values (± 2σ) for individual deposits Laco Norte, Laco Sur, Rodados Negros, Cristales Grandes, and San Vicente Alto average 0.81 ± 9.07 (n = 18), 4.41 ± 0.14 (n = 5), 3.69 ± 0.21 (n = 9), 3.65 ± 0.71 (n = 5), and -3.77 ± 8.39 ‰ (n = 5) respectively. Five samples from Rodados Negros were analyzed for $\Delta^{17}O$, yielding a nearly vertical array with values of -0.13, -0.12, -0.09, 0.03, and 0.10 ‰.

*Hydrogen isotope compositions*

Stable H isotope ratios for magnetite and bulk iron oxide are reported as $\delta^{2}H$ in Table 4.1. The $\delta^{2}H$ values (± 2σ) range from -189.4 to -78.2 ‰ and average -128.2 ± 60.8 ‰. The average $\delta^{2}H$ values (± 2σ) for individual deposits Laco Norte, Laco Sur, Rodados Negros, Cristales Grandes, and San Vicente Alto are -143.4 ± 83.1 (n = 12), 124.4 ± 18.6 (n = 6), -95.6 ± 29.0 (n = 5), -123.1 ± 25.2 (n = 5) and -133.8 ± 14.8 ‰ (n = 5), respectively. Calculated $H_2O$ contents ($H_2O_{eq}$) for Laco Norte, Laco Sur, Rodados Negros, Cristales Grandes, and San Vicente Alto average (± 2σ) 0.63 ± 1.24 (n = 12), 0.11 ± 0.13 (n = 6), 0.08 ± 0.11 (n = 5), 0.09 ± 0.18 (n = 5), and 1.06 ± 0.90 wt% (n = 5), respectively, and may originate from either fluid inclusions, H within goethite, or both.

*Fe isotope compositions*

Stable Fe isotope ratios for magnetite and bulk iron oxides are reported as $\delta^{56}Fe$ in Table 4.1. The $\delta^{56}Fe$ values (± 2σ) range from 0.04 ± 0.06 ‰ to 0.7 ± 0.03 ‰ and average 0.29 ± 0.15 ‰ (n = 26). The $\delta^{56}Fe$ values (± 2σ) for individual deposits Laco Norte, Laco Sur, Rodados Negros, Cristales Grandes, and San Vicente Alto average 0.27 ± 0.13 (n = 6), 0.35 ± 0.09 (n = 5), 0.17 ± 0.02 (n = 5), 0.20 ± 0.11 (n = 5), and 0.47 ± 0.15 ‰ (n = 5), respectively.

## DISCUSSION

### *Magmatic and magmatic-hydrothermal $\delta^{18}O$ and $\Delta^{17}O$*

One of the major issues dividing opinion on the origin of the El Laco ore bodies is the occurrence of both hydrothermal and magmatic textures of magnetite, and textures in some samples that may be interpreted as either. Rhodes and Oreskes (1999) carried out the first comprehensive stable isotope study completed at El Laco. They measured stable O isotope abundances in magnetite and bulk iron oxide via laser fluorination of 2 to 5 mg of iron oxide powders and chips from surface samples of the same five ore bodies as the current study, as well as samples from San Vicente Bajo and Laquito, and also whole rock samples of altered and unaltered andesite host rock from El Laco. A major goal of their study was to determine whether or not there were two populations of $\delta^{18}O$ values among primary magnetite samples that varied from magmatic textures to hydrothermal textures. Their analyses revealed a very narrow range of $\delta^{18}O$ values (i.e., mean ± 2σ for all samples = 4.1 ± 0.49 ‰, total range = 1.7 ‰, n = 16) in unaltered samples of both textural types of magnetite, and they concluded that both textural types formed from the same ore fluid.

Nyström et al. (2008) measured O isotope ratios in magnetite from the same ore bodies sampled by Rhodes and Oreskes (1999) and report a mean ± 2σ value for all samples of 3.0 ± 1.2 ‰ and a total range from 2.3 - 4.2 ‰ (n = 14) (Fig. 4.5). Nyström et al. (2008) report that, when categorized by their respective magmatic and hydrothermal textures, "magmatic" magnetite at San Vicente Bajo and "hydrothermal" magnetite at Cristales Grandes, respectively, show two distinct populations of magnetite with a $\Delta^{18}O_{SanVicenteBajo\text{-}CristalesGrandes}$ value of 1.3‰. Those authors used the small range of $\delta^{18}O$ values, which overlap those reported by Rhodes and Oreskes (1999), to conclude that all of the orebodies at El Laco share a common source and

proposed that the ore bodies formed from a cooling Fe-rich magma, with slightly lower magnetite $\delta^{18}O$ values for vein magnetite at Cristales Grandes (as low as 2.3 ‰) being the result of magnetite growth from a magmatic-hydrothermal fluid phase (with fluids in high-T, O and H isotope equilibrium with magma) that exsolved from the Fe-rich magma. The results presented in the current study are consistent with data from Rhodes and Oreskes (1999) and Nyström et al. (2008) and collectively indicate that magnetite in the El Laco ore bodies does not exhibit exclusively magmatic or magmatic-hydrothermal isotopic signatures, but rather both, consistent with the occurrence of igneous and hydrothermal features in these deposits (Ovalle et al., 2018).

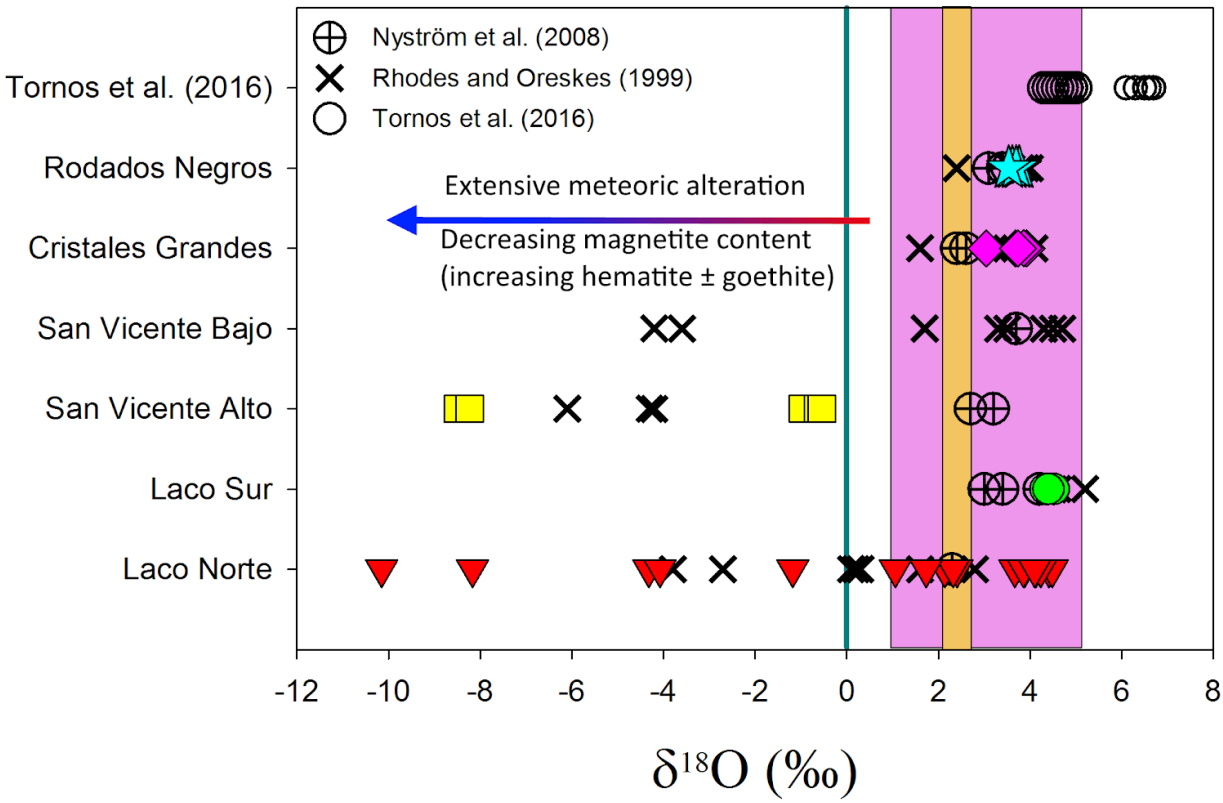


Figure 4.5: Plot of $\delta^{18}O$ values for samples from Laco Norte, Laco Sur, Rodados Negros, Cristales Grandes, and San Vicente Alto, and from previous studies. Blue line denotes seawater (0 ‰), orange box denotes magnetite in equilibrium with MORB (2.2-2.6 ‰), and pink box denotes magnetite in equilibrium with typical continental magmas (~1-5 ‰; Taylor 1967, 1968; Bindeman 2008).

High temperatures of mineralization at El Laco are indicated by homogenization temperatures of fluid inclusions hosted in pyroxene phenocrysts intimately intergrown with magnetite at Laco Sur and Cristales Grandes that reveal pyroxene growth from a fluid-saturated silicate melt occurred at >800 °C (Broman et al., 1999), and homogenization temperatures of silicate melt inclusions in pyroxene from San Vicente Alto and Laco Norte indicate mineralization temperatures that range from 820 to 840 °C (Sheets, 1997). The $\delta^{18}O$ values discussed above for magnetite ore samples from El Laco can be used with $\delta^{18}O$ values that range from 7.2 to 7.9 ‰ for unaltered (or least altered) andesite whole rock from El Laco reported by Rhodes and Oreskes (1999) to calculate equilibrium temperatures for magnetite-andesite pairs. Based on the fractionation factors reported by Zhao and Zheng (2003), magnetite in equilibrium with andesite that has $\delta^{18}O$ values of 7.2 to 7.9 ‰ at temperatures between 700 and 900 °C will range in $\delta^{18}O$ from 3 to 5 ‰, a range that encompasses the majority of unaltered magnetite samples from all five ore bodies in the current study and all published studies of El Laco. By comparison, the global range of $\delta^{18}O$ values of typical magmatic waters is 5.5 to 10 ‰ (Taylor, 1967, 1968), which could result in magmatic-hydrothermal magnetite with $\delta^{18}O$ values between 0.8 and 5.3 ‰ at 900 °C. Applying these fractionation factors (Zhao and Zheng, 2003) and comparing to $\delta^{18}O$ values from natural samples demonstrates the overlap between magmatically and magmatic-hydrothermally derived magnetite, and highlights the necessity for careful statistical analysis. Notably, the $\delta^{18}O$ values for samples from the El Laco ore bodies (Table 4.1; Fig. 4.5) overlap with $\delta^{18}O$ values for magnetite from both IOA and iron oxide-copper-gold (IOCG) deposits from the Chilean Iron Belt and IOA and IOCG deposits globally (e.g., Marshal and Oliver, 2006; Nyström et al., 2008; Weis, 2013; Jonsson et al., 2013; Bilenker et al., 2016; 2017; Childress et al., 2016, 2019), highlighting the challenge of discriminating between

magmatic and magmatic-hydrothermal magnetite using limited iron oxide sampling while in the field and analysis of bulk iron oxide for $\delta^{18}O$ rather than *in situ* analyses of individual magnetite textures and different geochemical generations of magnetite (e.g., Günther et al., 2017; Knipping et al., 2019).

In addition to the more traditional $\delta^{18}O$ analyses presented in this study, we also measured the abundance of $^{17}O$ in the least altered samples from Rodados Negros and used the calculated $\Delta^{17}O$ values to assess the source reservoir(s) for oxygen in those samples. The use of three, rather than two, isotopes allows an independent solution for the source and water-rock ratio as well as end member compositions (Pack and Herwartz, 2014; Zakharov et al., 2017; Bindeman et al., 2018).

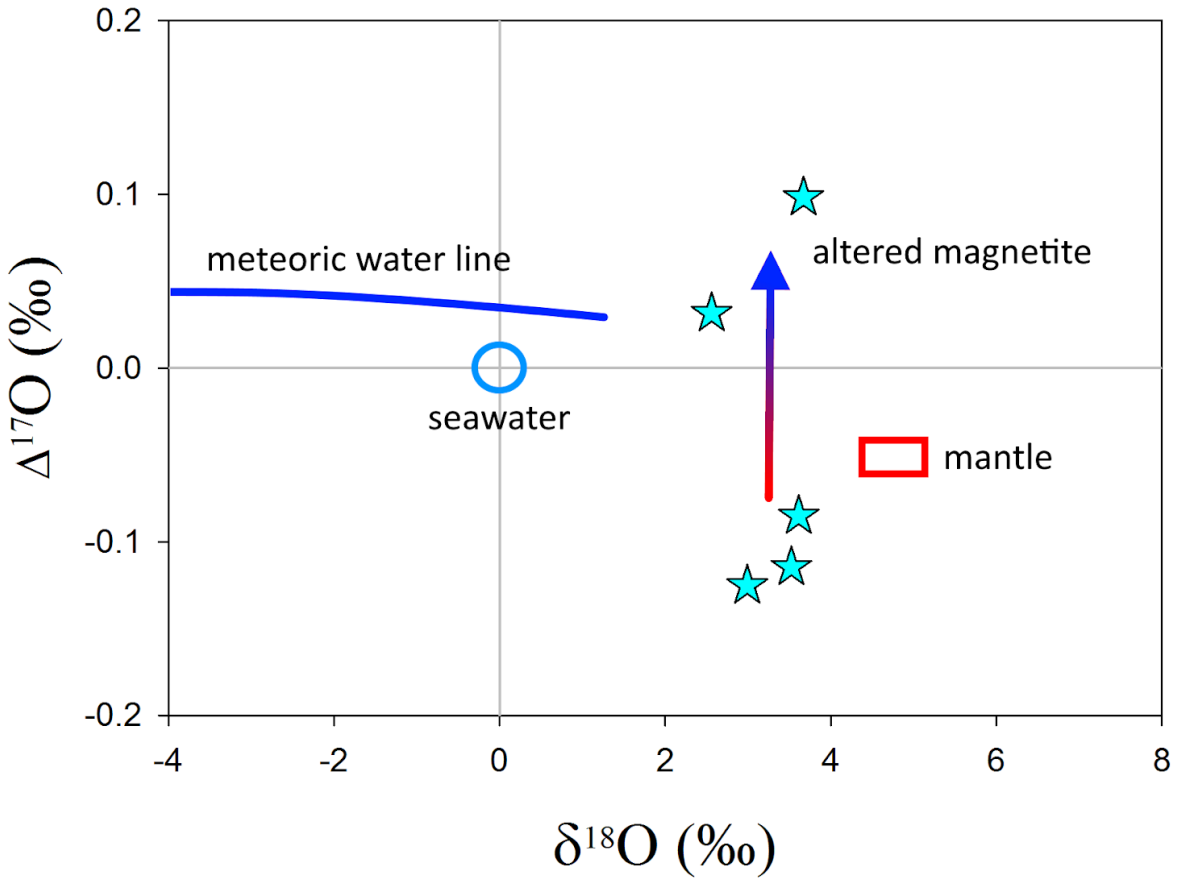


Figure 4.6: Plot of $\delta^{18}O$ and $\Delta^{17}O$ for magnetite from Rodados Negros from this study. Blue circle denotes average value of seawater, blue line is the meteoric water line, and the red box is typical mantle values (Pack and Herwartz, 2014). Samples analysed from Rodados Negros clearly exhibit a trend from magmatic values to meteoric values due to post-depositional alteration.

Rodados Negros was chosen for this analysis based on the narrow ranges of Fe and O isotopes in these samples and the lack of hematite and goethite. The $\Delta^{17}O$ data for three samples from Rodados Negros (Table 4.2), when plotted against corresponding $\delta^{18}O$ values for the same samples, reveal a near magmatic signature in agreement with igneous minerals studied by Pack and Herwartz (2014) ( Fig. 4.6), whereas two samples from Rodados Negros reveal alteration by high $\delta^{18}O$ meteoric water. Further analyses of IOA and IOCG deposits from inherently different geological settings will highlight similarities or dissimilarities between deposit types, and may

prove as a useful tool for understanding the formation of the ore deposit types, the source reservoirs for ore fluids, and isotopic fractionation within and among mineral systems.

*Hydrogen in magnetite, degassing, and meteoric alteration to goethite*

The occurrence of hematite and goethite in magnetite from the El Laco orebodies has been assumed to be hydrothermal alteration of magnetite by meteoric waters, and Rhodes et al. (1995), Rhodes et al. (1999) and Rhodes and Oreskes (1999) suggest that the orebodies themselves could be the result of metasomatic replacement of andesite lava flows by Fe-rich basinal brines or perhaps fluids from nearby saline lakes or buried evaporites in accordance with the evaporite fluid source model by Barton and Johnson (1996). To test both of these hypotheses, we measured H isotopes in all of our samples, and report the first $\delta^2H$ data for magnetite from El Laco. Hydrogen in magnetite may be present as fluid inclusions, hydrogen in goethite (FeO(OH)), or a combination of both. The $\delta^2H$ values in our samples range from -193 to -61‰ for 33 samples (Table 4.1), where Laco Norte exhibits the greatest range (135 ‰) and all other deposits exhibit significantly smaller ranges (≤39 ‰). The difference in ranges may, however, reflect sampling bias. The $\delta^2H$ values for typical magmatic waters range from about -40 to -80 ‰ (Taylor, 1974; Dixon et al., 2017) and local modern $\delta^2H$ and $\delta^{18}O$ meteoric values range from about -106 to -70.5 ‰ and -15.1 to -12.8 ‰ respectively (Waterisotopes Database, 2018), where lighter values correspond to higher elevation. For reference, goethite in equilibrium with the lightest modern $\delta^2H$ and $\delta^{18}O$ will exhibit values of -211 and -15.4 ‰ at 25 ℃, respectively (Yapp and Pedley, 1985; Müller, 1995). In volcanic rocks, early degassing results in strong fractionation of $^2H$ into the vapor phase, and will result in a range of $\delta^2H$ values of >40 ‰ towards lower values, as observed in natural samples (Taylor, 1986).

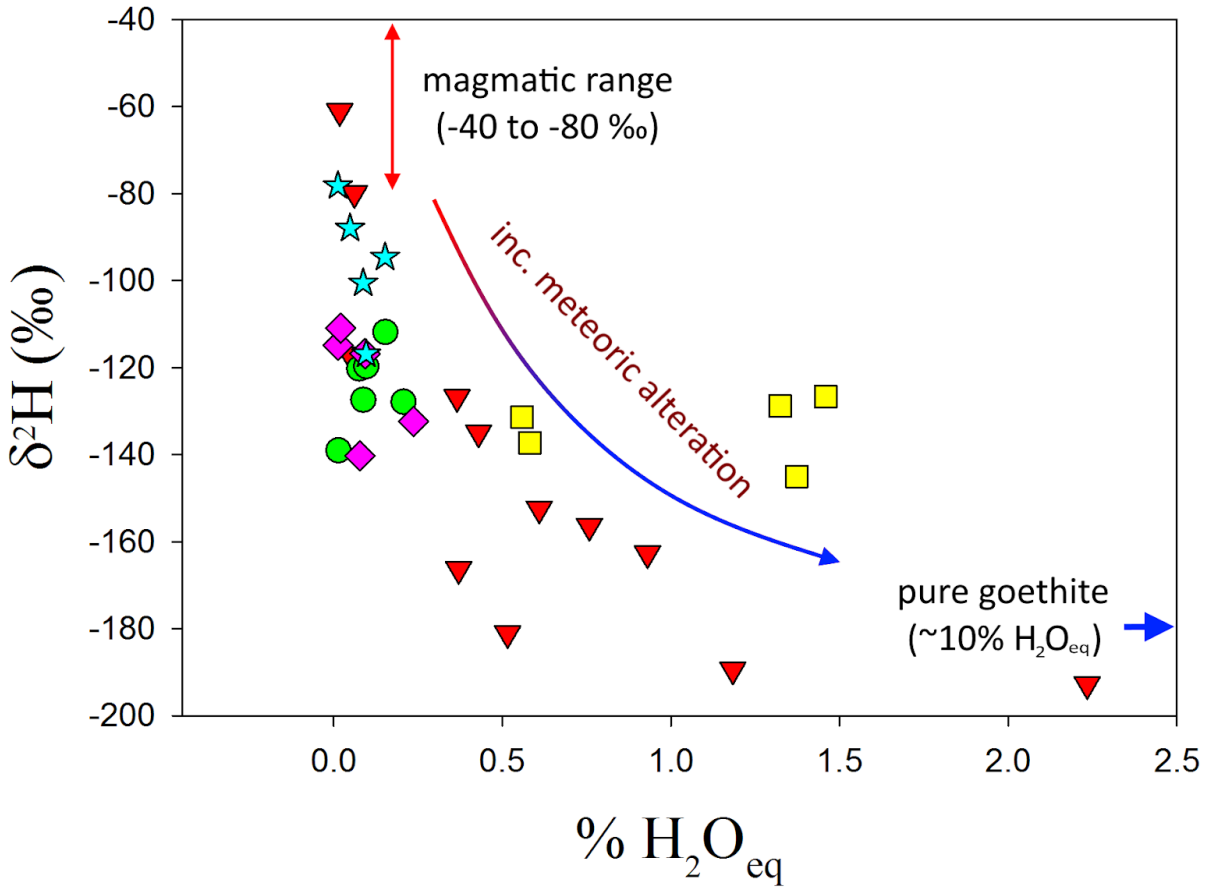


Figure 4.7: Plot of $\delta^2H$ and measured $H_2O_{eq}$ contents of hydrogen in iron oxides from Laco Norte, Laco Sur, Rodados Negros, Cristales Grandes, and San Vicente Alto (same legend as Fig. 4.5). Samples analyzed from these deposits show a clear trend from magmatic values, with increasing meteoric alteration where Laco Norte and San Vicente Alto show the highest degree of alteration of magnetite to goethite, incorporating more meteoric H. Magmatic range from Taylor and Epstein (1966).

Based on our new data, $\delta^2H$ ranges from purely magmatic to meteoric, where the large range of $\delta^2H$ values for samples from Laco Norte record the greatest degree of incorporation of meteoric fluids. Decreasing $\delta^2H$ values in samples from Laco Sur, Rodados Negros, and Cristales Grandes are consistent with initial degassing of a vapor-rich fluid (these samples also show least $\delta^{18}O$ variation), while Laco Norte and San Vicente Alto are more consistent with increasing goethite content, and therefore influence of meteoric fluids

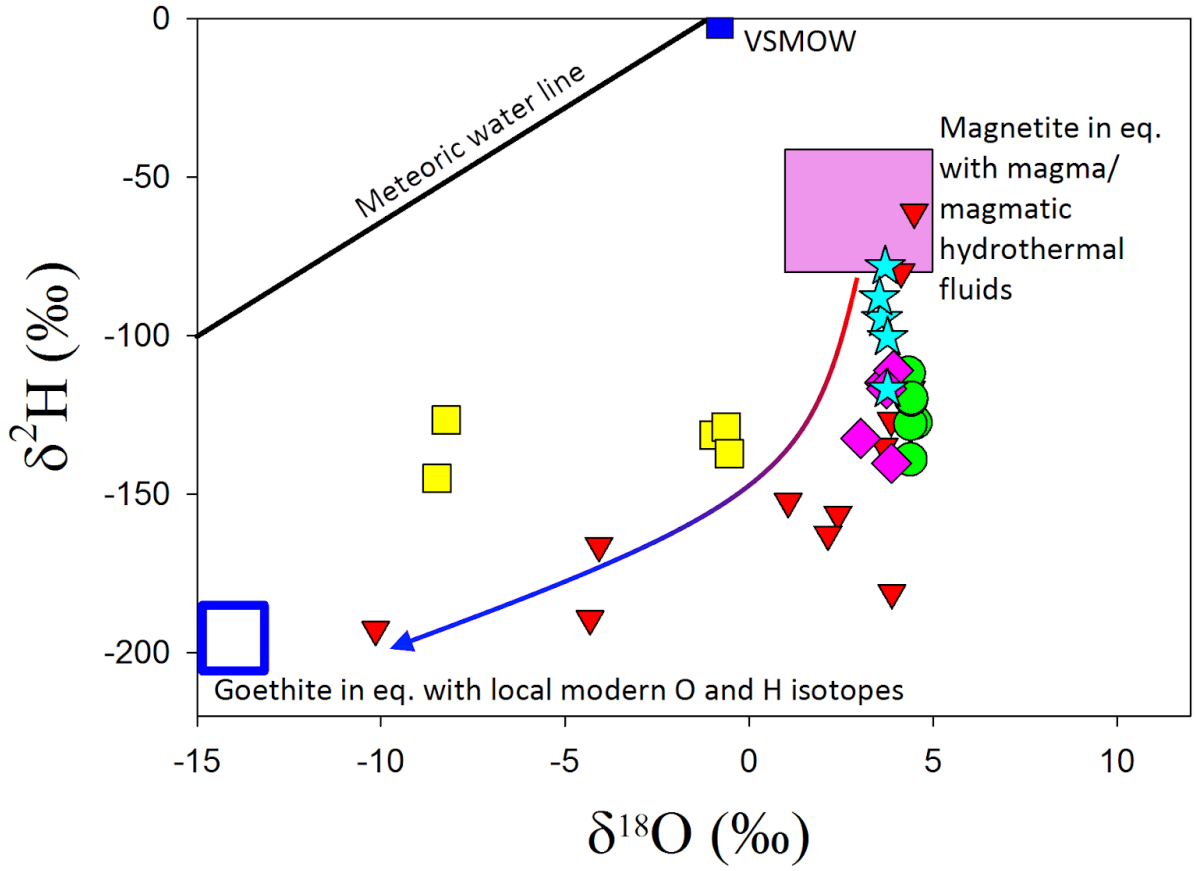


Figure 4.8: Plot of $\delta^{18}O$ and $\delta^{2}H$ from iron oxides from Laco Norte, Laco Sur, Rodados Negros, Cristales Grandes, and San Vicente Alto (same legend as Fig. 4.5). Samples show a clear trend from magmatic values to meteoric values, where Laco Norte and San Vicente Alto show highest degree of alteration of magnetite to goethite, approaching equilibrium with modern day meteorically derived goethite (Waterisotopes, 2018). Magmatic range from Taylor (1974).

The latter is demonstrated by the systematic increase of the measured $H_2O_{eq}$ content of samples (Fig. 4.7), with a maximum of 2.2 % $H_2O_{eq}$ (pure goethite = ~10% $H_2O_{eq}$) corresponding to the lightest $\delta^{2}H$ and $\delta^{18}O$ values in this study (sample LN-2) in the most altered samples from Laco Norte, which likely also underwent an initial degassing phase. When the magnetite and bulk iron oxide $\delta^{2}H$ values are combined with corresponding $\delta^{18}O$ values from the same samples, a clear trend from typical magmatic values to meteoric values is observed ( Fig. 4.8) among altered samples. Alteration of magnetite to hematite will decrease $\delta^{18}O$ values, and alteration to goethite

will decrease both $\delta^{2}H$ and $\delta^{18}O$ values. Rhodes and Oreskes (1999) reported that nearby playa lake water (Laguna Tuyajto) has a $\delta^{18}O$ value of 8.7 ‰ and suggested magnetite precipitating at low temperatures from such a fluid could yield $\delta^{18}O$ values such as those measured in samples at El Laco. While this is plausible considering O and H isotopes alone, the addition of corresponding Fe isotopes for these sample allows for a much clearer (and less altered!) look at the original isotopic signature of the iron oxides at El Laco.

*Iron isotopes - an unaltered view*

The iron isotopic system is relatively new as a tool in high-temperature systems when compared to other well-known stable isotope systems (e.g, O, H, and S), and is considered "non-traditional" due to its less developed but rapidly growing database of natural, experimental, and first principles modeled data (Dauphas et al., 2017 and references therein). Iron isotope abundances in iron oxide minerals are more resistant to secondary alteration than are the abundances of H and O (Frost et al., 2007, Weis, 2013, Bilenker et al., 2016, Childress et al., 2016, 2019), and will only significantly deviate from their original signature (to lighter values) via extensive coupled dissolution and reprecipitation reactions with hydrothermal fluids, as has been reported for the Mineville IOA deposit (Bilenker et al., 2016) and the Dannemora (Sweden) (Fig. 4.9) and Chagangnuoer (China) Fe-skarn-type deposits (Weis, 2013; Günther et al., 2017).

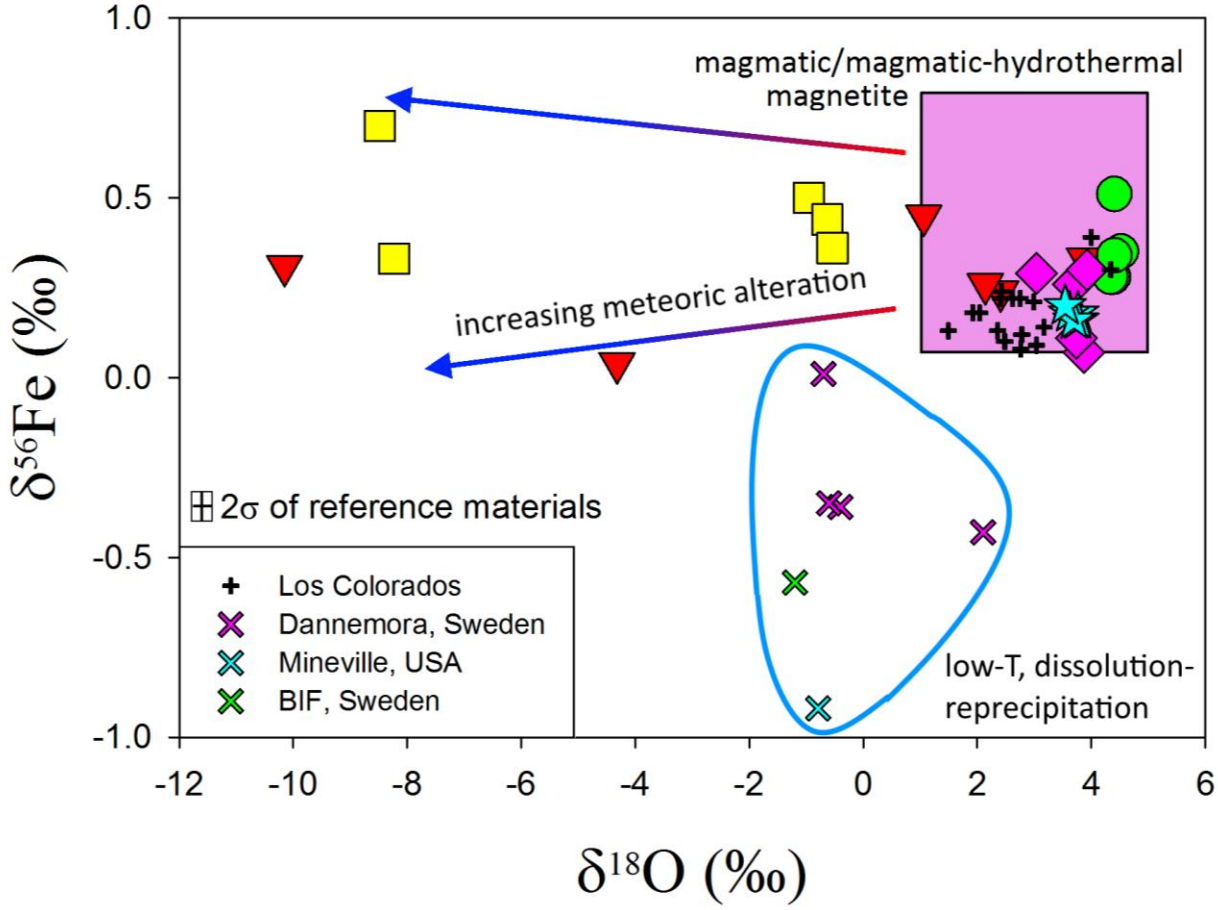


Figure 4.9: Plot of $\delta^{18}O$ and $\delta^{56}Fe$ from iron oxides from Laco Norte, Laco Sur, Rodados Negros, Cristales Grandes, and San Vicente Alto (same legend as Fig. 4.5). The majority of samples from this study plot within the magmatic range, similar to the Los Colorados deposit (Bilenker et al. 2016). Laco Norte and San Vicente Alto trend towards lower $\delta^{18}O$ values, indicating higher degrees of alteration. Low-T and dissolution-reprecipitation derived magnetite will commonly exhibit low $\delta^{56}Fe$ values. Magmatic range and additional data from Taylor (1974), Weis (2013), and Bilenker et al. (2016, 2017).

At El Laco, $\delta^{56}Fe$ values range from 0.04 to 0.70 ‰ for all samples from all five ore bodies, with the greatest variation at San Vicente Alto (0.15 ‰, 2σ) and lowest variation at Rodados Negros (0.02 ‰, 2σ) (Table 4.1). When plotted against the $\delta^{18}O$ data from the same samples (Fig. 4.9), the majority of $\delta^{56}Fe$ and $\delta^{18}O$ values lie within the established range of magmatic/magmatic-hydrothermal magnetite. The exceptions to this are samples from Laco Norte and San Vicente Alto, which largely plot outside the box due to their exceptionally low

$\delta^{18}O$ values. The fact that both $\delta^{18}O$ and $\delta^{56}Fe$ values for these two deposits exhibit the greatest ranges further implies that these deposits have experienced extensive alteration by meteoric water. The $\delta^{56}Fe$ and $\delta^{18}O$ values for samples from El Laco overlap values of magnetite from the Los Colorados IOA deposit in the Cretaceous Chilean Iron Belt, for which the original flotation model by Knipping et al. (2015a,b) was conceived. Los Colorados consists of two sub-parallel, sub-vertical magnetite-dominant orebodies hosted in dioritic and andesitic rocks. Bilenker et al. (2016) used $\Delta^{18}O$ for coexisting magnetite-actinolite separates to calculate a minimum formation temperature of 630 ℃ for Los Colorados, a temperature that is consistent with closure temperature of magmatic magnetite for O isotopes (e.g., Farquhar et al., 1993; Farquhar and Chacko, 1994). Those authors also calculated a temperature range of 610 to 820 ℃ using the Fe numbers for actinolite intergrown with magnetite. The isotopic values and calculated temperatures at Los Colorados are consistent with those at El Laco considering the $\Delta^{18}O$ between magnetite and co-genetic andesite (discussed below), and suggest Fe ore formation at El Laco occurred at < 900 ℃.

*Testing the liquid immiscibility hypothesis*

One of the proposed genetic models for the formation of El Laco and other IOA deposits invokes unmixing of a silicate melt into immiscible Fe-P-rich, Si-poor melt and conjugate Fe-poor, Si-rich melt (Philpotts, 1967, Naslund et al., 2002, Tornos et al,. 2016, Velasco et al., 2016, Hou et al. 2018). Proponents of the liquid immiscibility model cite the presence of what are interpreted to be Fe- and P-rich globules hosted exclusively in silicate melt inclusions within pyroxene and plagioclase phenocrysts in the andesite host rocks (Naslund et al., 2009, Tornos, 2016, Velasco et al., 2016). Tornos et al. (2016) reported stable $\delta^{18}O$ values for the andesite host

(7.4 to 9.6 ‰), stratabound magnetite from an undesignated ore body (4.3 to 5.0 ‰), and magnetite from a diopside-magnetite-anhydrite vein (4.4 to 6.7 ‰) (Fig. 4.5). The $\delta^{18}O$ values reported by those authors generally agree with data reported in the current study as well as Rhodes and Oreskes (1999) and Nyström et al. (2008), with the exception of heavier $\delta^{18}O$ values in magnetite from the diopside-magnetite-anhydrite vein. Tornos et al. (2016) used $\delta^{18}O$ values of coexisting magnetite and diopside from a vein that crosscuts the host andesite to calculate a temperature range of 900 to 1300 °C, with most calculated temperatures in the range 900 to 1125 °C, based on the diposide-magnetite geothermometer of Matthews et al. (1983). A temperature of 1300 °C is hotter than any shallow-level crustal igneous system except for the eruption of ultramafic lavas known as komatiites that erupted predominantly in the Proterozoic and Archean (Condie et al., 2016). Tornos et al. (2016) point out that experimental studies demonstrate that water-saturated andesite melt at low pressure crystallizes over the temperature range 1030 to 950 °C (Moore and Carmichael 1998; Blundy et al. 2006), and that the $\delta^{18}O$ values they determined for magnetite and host andesite from El Laco are consistent with magnetite that crystallized in equilibrium with andesite melt over a temperature range of 650 to 1350 °C. The liquid immiscibility hypothesis that invokes crystallization of the magnetite-rich ore bodies from an Fe- and P-rich liquid in equilibrium with host andesite at El Laco can be tested directly by using experimental data that constrain the partitioning of O isotopes between immiscible Si-rich and Fe-rich melts over the temperature range at which andesites crystallize.

Kyser et al. (1998) demonstrated experimentally at 1180 °C and 0.1 MPa that $^{18}O$ isotopes will only slightly fractionate into the Si-rich melt relative to the conjugate Fe-rich melt that forms by unmixing of an initial silicate melt in the $Fe_2SiO_4$-$KAlSi_2O_6$-$SiO_2$ system. Those authors report a $\Delta^{18}O$ value, which is defined as $\delta^{18}O_{Si\text{-}rich\text{-}melt}$- $\delta^{18}O_{Fe\text{-}rich\text{-}melt}$, of 0.5-0.6 ‰. Lester

et al. (2013b) performed experiments at 1100-1200ºC to quantify O isotope fractionation between Si-rich and Fe-rich melts and report $\Delta^{18}O$ values that vary between ~0.0 and 0.5 ‰. These experimentally constrained fractionation factors for O isotopes in Si-rich and conjugate Fe-rich melts indicate that the iron oxide ore bodies at El Laco should yield $\delta^{18}O$ values of ~7 to 9 ‰ if the ore bodies crystallized from Fe-rich liquid that had been in equilibrium with andesite host rocks, even when projected to lower temperatures. However, unaltered magnetite at El Laco yields $\delta^{18}O$ values of ~3.5 to 5 ‰, as reported in the current study as well as in Tornos et al. (2016) and Rhodes and Oreskes (1999). The $\delta^{18}O$ values for magnetite at El Laco are entirely consistent with the range of typical igneous and magmatic-hydrothermal magnetite (cf. Taylor, 1967; Loewen and Bindeman, 2016) (Fig. 4.5).

Lester et al. (2013a) performed experiments in the systems $Fe_2SiO_4$–$Fe_3O_4$–$KAlSi_2O_6$–$SiO_2$, $Fe_3O_4$–$KAlSi_2O_6$–$SiO_2$ and $Fe_3O_4$–$Fe_2O_3$–$KAlSi_2O_6$–$SiO_2$ at temperatures of 1075 - 1200 °C at 200 MPa and oxygen fugacities ($fO_2$) within the magnetite stability field to assess the possible effects of $H_2O$ alone or $H_2O$ in combination with P, S, F and Cl on liquid immiscibility. Importantly, the authors added 10 % $H_2O$ by mass to their experiments and did not measure the $H_2O$ content of the quenched immiscible Si-rich and Fe-rich liquid. The authors did quantify and report that P, S, and Cl partition preferentially into the Fe-rich immiscible liquid, with P and S strongly preferring the Fe-rich melt and F showing equal preference for the Fe-rich and Si-rich melts. Their results indicate that the addition of $H_2O$ along with P, S and F (not Cl) decreases the temperature at which liquid immiscibility occurs and expands the compositional ranges of the two-liquid field. On the contrary, the addition of only $H_2O$ and Cl resulted in formation of a single melt at all conditions except one experiment at 1200 °C. Lester et al. (2013b) reported that the addition of only $H_2O$ and Cl increases the activity of Si in the melt, hence the temperature of

the silicate mineral saturation surface, which disallows unmixing of the silicate liquid. Based on their experimental results for a hydrous assemblage and the experimental results of Naslund (1983) for anhydrous assemblages, liquid immiscibility is not expected to occur below temperatures of ~1075 °C at $fO_2$ of MH or ~1100 °C at $fO_2$ NNO and, critically, is not expected to occur in systems with $H_2O$ + Cl.

Broman et al. (1999) reported data for fluid inclusions hosted in pyroxene intergrown with magnetite at Laco Sur and from a vein cross-cutting ore breccia in a dike-vein system at Cristales Grandes that reveal the ore-associated fluids (interpreted by those authors as having exsolved from the Fe-magma after emplacement and crystallization) are Na-K chloride rich and contain anhydrite daughter crystals. They refer to the inclusions as "hydrous saline melt" and report that the inclusions homogenize at > 800 °C. Broman et al. (1999) interpret the presence of the Na-K-Cl inclusions as evidence for exsolution of a hydrous saline melt from a decompressing magma, consistent with the studies of Cline and Bodnar (1991) and Webster (1997). In light of the experimental study of Lester et al. (2013b) described above, the Cl-rich nature of the inclusions seems inconsistent with the liquid immiscibility hypothesis.

Most recently, Hou et al. (2018) used Raman spectroscopy to measure the $H_2O$ concentration of experimentally produced conjugate Fe-rich and Si-rich melts and reported that $H_2O$ preferentially partitions into the Si-rich melt, with Si-melt/Fe-melt partition coefficients that vary from 1.4 - 2.5. This finding demonstrates that even if liquid immiscibility did occur in a Cl-rich system, which is the opposite of what Lester et al. (2013b) determined experimentally, the addition of $H_2O$ to the Si-rich melt will lower its bulk density relative to its conjugate Fe-rich melt. The liquid immiscibility hypothesis invoked to explain the eruption of Fe-rich magma at El Laco requires $H_2O$ to partition preferentially into the Fe-rich melt during liquid-liquid unmixing,

such that the Fe-rich melt is less dense than its conjugate Si-rich melt and it can ascend buoyantly from the source magma. The results from Hou et al. (2018) falsify that hypothesis.

In summary, the experimental data that constrain the partitioning of O isotopes between conjugate Fe-rich and Si-rich melts and that demonstrate liquid immiscibility does not occur in $H_2O$ + Cl-bearing silicate melts appear to disallow liquid immiscibility as a plausible explanation for mineralization at El Laco.

*The origin of the El Laco magnetite-rich ore bodies*

The triple O, H, and Fe isotope data presented in this paper are consistent with the magmatic/magmatic-hydrothermal model proposed by Ovalle et al. (2018) to explain mineralization at El Laco. Those authors studied surface and drill core samples to depths of 188 m and found systematic lithological, textural, and geochemical zonation of magnetite from surface to depth where predominantly hydrothermal magnetite features exist at the surface and transition to purely igneous textures (not observed on the surface) at depth. The concentrations of Ti, V, Al, and Mn in magnetite systematically increase from the surface to depth (from ~0.0 to ~0.76 wt% Ti). Titanomagnetite crystals at 188 m exhibit triple-junctions and trellis texture ilmenite exsolution lamellae (~0.76 wt.% average, up to 1.66 wt.% Ti), which is a hallmark characteristic of orthomagmatic magnetite and has been reported in the Proterozoic Pea Ridge IOA deposit (Korfeh et al., 2016). Ovalle et al. (2018) concluded that in order to explain the occurrence of both orthomagmatic and hydrothermal magnetite in the orebodies, magnetite must have formed by a combination of igneous and hydrothermal processes. Those authors invoke the magnetite-flotation model originally proposed by Knipping et al. (2015a), wherein early magnetite crystals within a magma reservoir are remobilized by exsolving magnetite-wetting Fe-

rich hydrothermal fluids, creating a low-density magnetite-fluid suspension (i.e., froth) that rises within the magma and erupts to the surface along previously formed collapse-related structures at the El Laco volcano. The systematic change in trace element concentrations records a cooling trend wherein magnetite grew from a cooling magmatic-hydrothermal fluid as the fluid evolved from magmatic temperatures to hydrothermal temperatures. Growth of magnetite from a cooling magmatic-hydrothermal fluid explains the hydrothermal textures observed in the near-surface environment at El Laco, whereas the igneous textures are consistent with emplacement to shallow levels of a magnetite-bearing magmatic-hydrothermal fluid wherein the magnetite crystallized from silicate melt in the parent magma chamber that evolved the ore fluid. Their model predicts that magnetite should have $\delta^{18}O$ and $\delta^{56}Fe$ values consistent with growth from silicate melt and magmatic-hydrothermal fluid, which agree with the values reported here and in published studies.

## CONCLUSIONS

Triple O, H, and Fe stable isotope abundances in magnetite from the El Laco IOA deposit in northern Chile fingerprint a silicate magma as the source of these elements. Hydrogen and triple O isotopes in magnetite in some samples from the Laco Norte and San Vicente Alto ore bodies reveal alteration by meteoric water, consistent with increasing abundances of hematite and goethite in samples with lighter $\delta^{18}O$ and $\delta^{2}H$ values. The $\delta^{18}O$ values in samples from Laco Sur, Cristales Grandes, and Rodados Negros overlap magmatic values. In the case of Rodados Negros, which lacks hematite and goethite, $\Delta^{17}O$ values show the same trend of an originally magmatic signature being altered to meteoric values. The $\delta^{56}Fe$ values of magnetite from all five ore bodies sampled in this study overlap with purely igneous magnetite $\delta^{56}Fe$ values and

magnetite from other IOA deposits, such as Los Colorados, Mariela Ignacia, Pea Ridge and Pilot Knob, Kiruna, and Grängesberg. Importantly, even in bulk iron oxide samples that contain hematite and goethite and have $\delta^{18}O$ and $\delta^{2}H$ values that fingerprint alteration by meteoric water, the $\delta^{56}Fe$ values preserve original magmatic values. The $\delta^{18}O$ values reported in this and previous studies from the El Laco orebodies are consistent with having been derived from the same source as the relatively isotopically heavy andesites at El Laco at temperatures between 700 and 900 °C. The stable isotope data presented here are consistent with the model proposed by Ovalle et al. (2018) to explain the magmatic and hydrothermal chemistry and textures of magnetite at El Laco. Isotopic data presented here, coupled with reported trace element and fluid inclusion information for El Laco, preclude the possibility that the ore fluids responsible for mineralization at El Laco were derived from a non-magmatic source. The stable O isotope data also precludes formation of the Fe ore bodies via liquid immiscibility. Future isotopic studies should focus on in situ studies of statistically significant populations of individual magnetite grains in order to assess isotopic fractionation between magmatic and hydrothermal magnetite and or fractionation related to the thermal gradient from depth to surface.

## ACKNOWLEDGEMENTS

TMC thanks the Society of Economic Geologists, the American Association of Petroleum Geologists, and the University of Michigan for providing funding, CAP Mining for providing access to El Laco and plentiful tea and coffee, and the University of British Columbia Pacific Centre for Isotopic Research and LDB for access and assistance with their impeccable instruments. ACS acknowledges funding from NSF EAR grants #1250239 and #1264560. MR and FB acknowledge funding from Chile's Millennium Science Initiative (MSI) through

Millennium Nucleus for Metal Tracing along Subduction Grant NC130065, and FONDECYT Grant #1140780 “Metallogenesis of the Mesozoic magmatic arc of northern Chile: Testing the IOCG connection using a multi-proxy geochemical approach”. INB acknowledges support from NSF EAR grant #1822977.

## REFERENCES

Barton MD, Johnson DA (1996) Evaporitic-source model for igneous-related Fe oxide-(REE-Cu-Au-U) mineralization. Geology, 26:259–262

Beard BL, Johnson CM (2004) Fe isotope variations in the modern and ancient earth and other planetary bodies. Reviews in Mineralogy and Geochemistry, 55:319-357

Bilenker LD, VanTongeren JA, Lundstrom CC, Simon AC (2017) Iron isotopic evolution during fractional crystallization of the uppermost Bushveld Complex layered mafic intrusion. Geochemistry Geophysics Geosystems, 18, doi:10.1002/ 2016GC006660

Bilenker LD, Simon AC, Reich M, Lundstrom CC, Gajos N, Bindeman I, Barra R, Munizaga R (2016) Fe-O stable isotope pairs elucidate a high-temperature origin of Chilean iron oxide-apatite deposits. Geochimica et Cosmochimica Acta, 177:94–104

Bindeman I (2008) Oxygen isotopes in mantle and crustal magmas as revealed by single crystal analysis. Reviews in Mineralogy and Geochemistry, 69:445–478

Bindeman, IN, Kamenetsky, VS, Palandri, J, Vennemann, T (2012) Hydrogen and oxygen isotope behaviors during variable degrees of upper mantle melting: Example from the basaltic glasses from Macquarie Island. Chemical Geology, 310:126-136

Bindeman IN , Zakharov D , Palandri J , Greber ND, Retallack GJ, Hoffman A , Dauphas N, Lackey JS, Bekker A (2018) Rapid emergence of subaerial landmasses and onset of a modern hydrologic cycle 2.5 billion years ago. Nature 557(7706):545-548, DOI: 10.1038/s41586-018-0131-1

Blundy J, Cashman K, Humphreys M (2006) Magma heating by decompression-driven crystallization beneath andesite volcanoes: Nature, 443:76-80, doi:10.1038/nature05100

Broman C, Nyström JO, Henríquez F, Elfman M (1999) Fluid inclusions in magnetite-apatite ore from a cooling magmatic system at El Laco, Chile. Geologiska Föreningen 121(3):253-267

Cline JS, Bodnar R (1991) Can economic porphyry copper mineralization be generated by a typical calc-alkaline melt. Journal of Geophysical Research, 96:8113-8126

Childress TM, Simon AC, Day WC, Lundstrom CC, Bindeman IN (2016) Iron and oxygen isotope signatures of the Pea Ridge and Pilot Knob magnetite-apatite deposits, Southeast Missouri, USA. Economic Geology, 111:2033-2044

Childress TM, Simon AC, Reich M, Barra F, Arce M, Lundstrom CC, Bindeman IN (2019) Formation of the Mantoverde iron oxide - copper - gold deposit, Chile: Insights from Fe and O stable isotopes and comparison to iron oxide - apatite deposits, in review

Condie KC, Aster RC, van Hunen J (2016) A great thermal divergence in the mantle beginning 2.5 Ga: geochemical constraints from greenstone basalts and komatiites. Geoscience Frontiers, 7(4):543-553

Craddock PR and Dauphas N (2011) Iron isotopic compositions of geological reference materials and chondrites. Geostandards and Geoanalytical Research, 35(1):101-123.

Dare SAS, Barnes S-J, Beaudoin G, Méric J, Boutroy E, Potvin-Doucet C (2014) Trace elements in magnetite as petrogenetic indicators. Mineralium Deposita, 49:785–796

Dare SAS, Barnes S-J, Beaudoin G (2015) Did the massive magnetite “lava flows” of El Laco (Chile) form by magmatic or hydrothermal processes? New constraints from magnetite composition by LA-ICP-M. Mineralium Deposita, 50:607–617, DOI: 10.1007/s00126-014-0560-1

Dauphas N, John SG, Rouxel O (2017) Iron isotope systematics. Reviews in Mineralogy and Geochemistry, 82:415-510

Dixon JE, Bindeman IN, Kingsley RH, Simons KK, Le Roux PJ, Hajewski TR, Swart P, Langmuir CH, Ryan JG, Walowski KJ, Wada I, Wallace PJ (2017) Light stable isotopic compositions of enriched mantle sources: Resolving the dehydration paradox. Geochemistry, Geophysics, Geosystems, 18:3801-3839, doi:10.1002/2016GC006743

Farquhar J, Chacko T (1994) Exsolution-enhanced oxygen exchange: implications for oxygen isotope closure temperatures in minerals. Geology 22:751-754

Farquhar J, Chacko T, and Frost BR (1993) Strategies for high-temperature oxygen isotope thermometry: a worked example from the Laramie Anorthosite Complex, Wyoming, USA. Earth and Planetary Science Letters, 117:407-422

Frost CD, Blanckenburg F von, Shoenberg R, Frost BR, and Swapp SM (2007), Preservation of Fe isotope heterogeneities during diagenesis and metamorphism of banded iron formation. Contributions to Mineral Petrology, 153:211–235

Frutos J, Oyarzun MJ (1975) Tectonic and geochemical evidence concerning the genesis of El Laco magnetite lava flow deposits, Chile. Economic Geology, 70(5):988-90

Günther T, Klemd R, Zhang X, Horn I, Weyer S (2017) In-situ trace element and Fe-isotope studies on magnetite of the volcanic-hosted Zhibo and Chagangnuoer iron ore deposits in the Western Tianshan, NW China. Chemical Geology, 453:111-127

Henríquez F, Naslund HR, Nyström J, Naranjo J (2004) Igneous textures in magnetite eruptive products at El Laco, Chile. Internation Association of Volcanology and Chemistry of the Earth's Interior, General Assembly, Pucón-Chile. Abs.

Hitzman MW, Oreskes N, Einaudi MT (1992) Geological characteristics and tectonic setting of Proterozoic iron oxide (Cu-U-Au-REE) deposits. Precambrian Research, 58:241–287

Hou T, Charlier B, Holtz F, Veksler I, Zhang Z, Thomas R, Namur O (2018) Immiscible hydrous Fe-Ca-P melt and the origin of iron oxide-apatite ore deposits. Nature Communications 9(1) no. 1415

Huang F, Zhang Z, Lundstrom CC, Zhi X (2011) Iron and magnesium isotopic compositions of peridotite xenoliths from eastern China. Geochimica et Cosmochimica Acta, 75:3318–3334

Jonsson E, Valentin RT, Högdahl K, Harri C, Weis F, Nilsson KP, Skelton A (2013) Magmatic origin of giant 'Kiruna-type' apatite-iron-oxide ores in central Sweden. Scientific Reports, 3, doi: 10.1038/srep01644

Knipping JL, Bilenker LD, Simon AC, Reich M, Barra F, Deditius AP, Lundstrom C, Bindeman I, Munizaga R (2015a) Giant Kiruna-type deposits form by efficient flotation of magmatic magnetite suspensions. Geology, 43:491–594

Knipping JL, Bilenker LD, Simon AC, Reich M, Barra F, Deditius AP, Wälle M, Heinrich CA, Holtz F, and Munizaga R (2015b) Trace elements in magnetite from massive iron oxide-apatite deposits indicate a combined formation by igneous and magmatic hydrothermal processes. Geochimica et Cosmochimica Acta, 171:15–38

Knipping J, Fiege A, Simon AC, Oeser M, Reich M, Bilenker L, (accepted) In-situ iron isotope analyses reveal igneous and magmatic-hydrothermal growth of magnetite at the Los Colorados Kiruna-type iron oxide - apatite deposit, Chile. American Mineralogist.

Korfeh DF Jr, Simon AC, Childress TM (2016) The chemistry of magnetite from the Pea Ridge iron deposit, Missouri, USA. Geological Society of American Annual Meeting, Denver, abs.

Kyser TK, Lesher CE, Walker D (1998) The effects of liquid immiscibility and thermal diffusion on oxygen isotopes in silicate liquids. Contributions to Mineralogy and Petrology 133(4):373-381

Le Maitre RW, Streckeisen A, Zanettin B, Le Bas MJ, Bonin B, Bateman P, editors (2005) Igneous rocks: a classification and glossary of terms: recommendations of the International Union of Geological Sciences Subcommission on the Systematics of Igneous Rocks. Cambridge University Press

Lester GW, Clark AH, Kyser TK, Naslund HR (2013a) Experiments on liquid immiscibility in silicate melts with $H_2O$, P, S, F and Cl: implications for natural magmas. Contributions to Mineralogy and Petrology, 166:329-349

Lester GW., Kyser TK., Clark AH (2013b), Oxygen isotope partitioning between immiscible silicate melts with $H_2O$, P and S: Geochimica et Cosmochimica Acta, 109:306–311

Maksaev V, Gardeweg M, Ramírez CF, Zentilli M (1988) Aplicación del método trazas de fisión a la datación de cuerpos de magnetita de El Laco e Incahuasi en el Altiplano de la Región de Antofagasta: V Congreso Geológico Chileno, Actas, 1:B1–B23

Marshal LJ, Oliver NHS (2006) Monitoring fluid chemistry in IOCG - related metasomatic processes, eastern Mt Isa Block, Australia. Geofluids, 6:45–66

Matthews A, Goldsmith JR, Clayton RN (1983) Oxygen isotope fractionation involving pyroxenes: the calibration of mineral-pair geothermometers. Geochimica et Cosmochimica Acta, 47:631-644

Millet MA, Baker JA, Payne CE (2012) Ultra-precise stable Fe isotope measurements by high resolution multiple-collector inductively coupled plasma mass spectrometry with a 57Fe-58Fe double spike. Chemical Geology, 304:18–25

Moore G, Carmichael I, (1998) The hydrous phase equilibria (to 3 kbar) of an andesite and basaltic andesite from western Mexico: Constraints on water content and conditions of phenocryst growth. Contributions to Mineralogy and Petrology, 130:304-319, doi:10.1007/s004100050367

Müller J (1995) Oxygen isotopes in iron (II) oxides: a new preparation line; mineral-water fractionation factors and paleoenvironmental considerations. Isotopes in Environmental and Health Studies, 31(3):301-302

Mungall JE, Long K, Brenan JM, Smythe D, Naslund HR (2018) Immiscible shoshonitic and Fe-P-oxide melts preserved in unconsolidated tephra at El laco volcano, Chile. Geology, 46(3):255-258

Nadoll P, Angerer T, Mauk JL, French D, Walshe J (2014) The chemistry of hydrothermal magnetite: A review. Ore Geology Reviews, 61:1–32

Naranjo JA, Henríquez F, Nyström JO, (2010) Subvolcanic contact metasomatism at El Laco Volcanic Complex, Central Andes: Andean Geology, v. 37, p. 110–120

Naslund HR (1983) The effect of oxygen fugacity on liquid immiscibility in iron-bearing silicate melts. American Journal of Science, 283(10):1034-1058

Naslund HR, Henriquez F, Nyström JO, Vivallo W, Dobbs FM (2002) Magmatic iron ores and associated mineralisation: examples from the Chilean high Andes and coastal Cordillera. In Hydrothermal Iron Oxide Copper–Gold A Global Perspective, 2 (ed. T. M. Porter). PGC Publishing, Adelaide, Australia, p. 207–226

Naslund HR, Mungall JE, Henriquez F, Nyström JO, Lledó H, Lester GW, Aguirre R (2009) Melt inclusions in silicate lavas and iron-oxide tephra of the El Laco volcano. Proceedings, XII Congreso Geológico Chileno, Santiago, Chile, p. 23–26

Neumann E-R, Svensen HH, Polozov AG, Hammer Ø (2017) Formation of Si-Al-Mg-Ca-rich zoned magnetite in an end-Permian phreatomagmatic pipe in the Tunguska Basin, East Siberia. Mineralium Deposita, 52:1205–1222

Nold, JL, Davidson, P, Dudley, MA (2013) The Pilot Knob magnetite deposit in the Proterozoic St. Francois Mountains Terrane, southeast Missouri, USA: A magmatic and hydrothermal replacement iron deposit. Ore Geology Reviews, 53:446–469

Nyström JO, Billström K, Henríquez F, Fallick AE, Naslund HR (2008) Oxygen isotope composition of magnetite in iron ores of the Kiruna type in Chile and Sweden: GFF [Geologiska Föreningen], 130:177–188

Nyström JO, Henríquez F, Naranjo JA, Nasuland HR (2016) Magnetite spherules in pyroclastic iron ore at El Laco, Chile. American Mineralogist, 101(3):587-95

Ovalle JT, La Cruz NL, Reich M, Barra F, Simon AC, Konecke, BA, Rodriguez-Mustafa MA, Deditius AP, Childress TM, Morata D (2018) Formation of massive iron deposits linked to explosive volcanic eruptions. Nature Scientific Reports, 8 no. 14855

Park CF Jr. (1961) A magnetite "flow" in northern Chile. Economic Geology, 56:431-436

Pack A, Herwartz D (2014) The triple oxygen isotope composition of the Earth mantle and understanding $\delta^{17}O$ variations in terrestrial rocks and minerals. Earth and Planetary Sciences Letters 390:138–145

Philpotts AR (1967) Origin of certain iron-titanium oxide and apatite rocks. Economic Geology, 62(3):303-315

Qi H., Coplen TB, Gehre M, Vennemann TW, Brandt WA, Geilmann H, Olack G, Bindeman IN, Palandri J, Huang L, Longstaffe FJ (2017) New biotite and muscovite isotopic reference materials, USGS57 and USGS58, for $\delta^{2}H$ measurements - a replacement for NBS 30. Chemical Geology, doi:10.1016/j.chemgeo.2017.07.027

Rhodes AL, Oreskes N (1995) Magnetite deposition at El Laco, Chile: implications for Fe-oxide formation in magmatic-hydrothermal systems. In: Clark AH (ed.): Giant ore deposits - II. Controls on the scale of orogenic magmatic-hydrothermal mineralization: Proceedings of the Second Giant Ore Deposits Workshop, Queens University, April 25-27, Kingston, Ontario, Canada, p. 582-622

Rhodes A, Oreskes N (1999) Oxygen isotope composition of magnetite deposits at El Laco, Chile. Society of Economic Geologists Special Publication, 7:333-351

Rhodes A, Oreskes N, Sheets S (1999) Geology and rare earth element (REE) geochemistry of magnetite deposits at El Laco, Chile. Society of Economic Geologists Special Publication, 7:299-332

Rojas PA, Barra F, Deditius A, Reich M, Simon A, Roberts M, Rojo M (2018) New contributions to the understanding of Kiruna-type iron oxide-apatite deposits revealed by magnetite ore and gangue mineral geochemistry at the El Romeral deposit, Chile. Ore Geology Reviews, 93:413–135

Sheets, SA, Oreskes N, Rhodes AL, Bodnar RJ, Szabo C (1997) Fluid inclusion evidence for a hydrothermal origin for magnetite-apatite mineralization at El Laco, Chile. Geological Society of America, Abstracts with Programs, 2:A50

Sillitoe RM, Burrows DR (2002) New field evidence bearing on the origin of the El Laco magnetite deposit, northern Chile. Economic Geology, 97:1101–1109.

Taylor HP Jr, Epstein, S (1966) Deuterium-hydrogen ratios in coexisting minerals of metamorphic and igneous rocks. American Geophysical Union Transactions (abs), 47:213

Taylor HP Jr (1967) Oxygen isotope studies of hydrothermal mineral deposits, in Barnes, H.L., ed., Geochemistry of Hydrothermal Ore Deposits, 1st ed., New York, Holt, Rinehart and Winston, 109–142.

Taylor HP Jr (1968) The oxygen isotope geochemistry of igneous rocks. Contributions to Mineralogy and Petrology 19:1–71

Taylor HP Jr (1974) The application of Oxygen and Hydrogen Isotope Studies to Problems of Hydrothermal Alteration and Ore Deposition. Economic Geology, 69:843–883

Taylor, BE (1986) Stable isotopes in high temperature geological processes. Eds. Valley JW, Taylor HP Jr, O'Neil JR. Mineralogical Society of America, Washington DC, p. 185-225

Tornos F, Velasco F, Hanchar JM (2016) Iron-rich melts, magmatic magnetite, and superheated hydrothermal systems: The El Laco deposit, Chile. Geology, 44(6):427–430

Tornos F, Velasco F, Hanchar JM (2017) The magmatic to magmatic-hydrothermal evolution of the El Laco deposit (Chile) and its implications for the genesis of magnetite-apatite deposits. Economic Geology 112(7):1595-1628

Trumbull RB, Wittenbrink R, Hahne K, Emmermann R, Büsch W, Gerstenberger H, Siebel W (1999) Evidence for Late Miocene to Recent contamination of arc andesites by crustal melts in the Chilean Andes (25-26 S) and its geodynamic implications. Journal of South American Earth Sciences 12(2):135-155

Velasco F, Tornos F, Hanchar JM (2016) Immiscible iron-and silica-rich melts and magnetite geochemistry at the El Laco volcano (northern Chile): Evidence for a magmatic origin for the magnetite deposits. Ore Geology Reviews 79:346–366.

Vivallo W, Henríquez F, Espinoza S, (1994) Oxygen and sulfur isotopes in hydrothermally altered rocks and gypsum deposits at El Laco mining district, northern Chile: Departamento de Geología, Universidad de Chile, Comunicaciones, 45:93–100

Waterisotopes Database (2018) http://waterisotopes.org. Accessed 11/20/2018

Webster JD (1997) Exsolution of magmatic volatile phases from Cl-enriched mineralizating granitic magmas and implications for ore metal transport. Geochimica et Cosmochimica Acta, 61:1017-1029

Weis F (2013) Oxygen and iron isotope systematics of the Grängesberg mining district (GMD), central Sweden: Unpublished Ph.D. Dissertation, Uppsala Universitet, Uppsala, Sweden, 77p.

Yapp CJ, Pedley MD (1985) Stable hydrogen isotopes in iron oxides. II. D/H variations among natural goethites. Geochimica et Cosmochimica Acta, 49:487-495

Zakharov DO, Bindeman IN, Slabunov AI, Ovtcharova M, Coble MA, Serebryakov NS, Schaltegger U (2017) Dating the Paleoproterozoic snowball Earth glaciations using contemporaneous subglacial hydrothermal systems. Geology, 45(7):667-670 doi:10.1130/G38759.1

Zhao Z-F, Zheng Y-F (2003) Calculation of oxygen isotope fractionation in magmatic rocks. Chemical Geology 193:59–80

**TABLES**

**Table 4.1:** Theoretical yields of $O_2$ for magnetite, hematite, and goethite are 7.8, 10.4, and 31.2 µmol/gram respectively. Blank spaces indicate samples that were not analyzed for Fe, O, or H. $\delta^2H$ and $\delta^{18}O$ values are reported relative to VSMOW. Individual $\delta^{18}O$ typically have $2\sigma < 0.1$ ‰. $\delta^{56}Fe$ is reported relative to IRMM-14. *Sample RN-2 value reported from $\Delta^{17}O$ analysis in Table 2.

| Sample | $\delta^{18}O$ (‰) | µmol/gram | $\delta^2H$ (‰) | $H_2O$ wt% | $\delta^{56}Fe$ (‰) | 2σ |
|---|---|---|---|---|---|---|
| Laco Norte | | | | | | |
| LN-2 | -10.2 | 9.4 | -192.8 | 2.2 | 0.31 | 0.04 |
| LN-3a | 3.9 | 8.3 | -126.8 | 0.4 | | |
| LN-3b | 4.4 | 7.4 | -116.9 | 0.0 | | |
| LN-5 | 3.7 | 8.6 | -134.9 | 0.4 | | |
| LN-6a | 4.1 | 7.3 | -79.9 | 0.1 | | |
| LN-6b | 4.5 | 8.7 | -61.1 | 0.0 | | |
| LN-7 | 2.3 | 8.5 | | | | |
| LN-8 | 1.7 | 8.5 | | | | |
| LN-9 | 1.1 | 9.3 | -152.4 | 0.6 | 0.45 | 0.04 |
| LN-10a | 2.4 | 8.5 | -156.4 | 0.8 | 0.24 | 0.05 |
| LN-10b | 3.9 | 8.8 | -181.1 | 0.5 | 0.33 | 0.09 |
| LN-11a | -1.2 | 8.2 | | | | |
| LN-11b | 4.2 | 6.9 | | | | |
| LN-12 | -4.1 | 9.0 | -166.3 | 0.4 | | |
| LN-14a | 2.1 | 8.3 | -162.7 | 0.9 | 0.04 | 0.05 |
| LN-14b | -4.3 | 8.9 | -189.4 | 1.2 | 0.26 | 0.07 |
| LN-15 | 4.1 | 7.7 | | | | |
| LN-B | -8.2 | 9.7 | | | | |
| Laco Sur | | | | | | |
| LS-1 | 4.5 | 8.5 | -127.4 | 0.1 | 0.35 | 0.04 |
| LS-2a | 4.4 | 7.9 | -127.9 | 0.2 | 0.28 | 0.09 |
| LS-2b | | | -139.1 | 0.0 | | |

| | | | | | | |
|---|---|---|---|---|---|---|
| LS-3 | 4.3 | 7.0 | -111.9 | 0.2 | 0.28 | 0.07 |
| LS-t2 | 4.4 | 7.6 | -120.2 | 0.1 | 0.34 | 0.07 |
| LS-t5 | 4.4 | 7.4 | -119.7 | 0.1 | 0.51 | 0.11 |
| San Vicente Alto | | | | | | |
| SVA-1 | -1.0 | 8.5 | -131.4 | 0.6 | 0.50 | 0.04 |
| SVA-2 | -8.5 | 7.7 | -145.0 | 1.4 | 0.70 | 0.04 |
| SVA-3 | -0.6 | 9.4 | -128.8 | 1.3 | 0.44 | 0.08 |
| SVA-4 | -0.5 | 9.0 | -137.2 | 0.6 | 0.36 | 0.07 |
| SVA-t1 | -8.2 | 9.4 | -126.7 | 1.5 | 0.33 | 0.07 |
| Cristales Grandes | | | | | | |
| CG-1 | 3.7 | 8.0 | -114.9 | 0.0 | 0.26 | 0.05 |
| CG-2 | 3.9 | 7.7 | -110.9 | 0.0 | 0.30 | 0.02 |
| CG-3 | 3.0 | 8.7 | -132.4 | 0.2 | 0.29 | 0.06 |
| CG-4 | 3.9 | 8.3 | -140.3 | 0.1 | 0.07 | 0.08 |
| CG-5 | 3.7 | 8.0 | -116.8 | 0.1 | 0.11 | 0.03 |
| Rodados Negros | | | | | | |
| RN-1 | 3.8 | 8.3 | -116.9 | 0.1 | 0.18 | 0.04 |
| RN-2 | 3.6* | - | -94.6 | 0.2 | 0.18 | 0.02 |
| RN-3 | 3.8 | 8.1 | -100.5 | 0.1 | 0.14 | 0.07 |
| RN-4 | 3.7 | 8.1 | -78.2 | 0.0 | 0.16 | 0.05 |
| RN-5 | 3.5 | 7.9 | -88.0 | 0.0 | 0.20 | 0.05 |

**Table 4.2:** Samples from Rodados Negros analyzed for $\delta^{17}O$ and $\delta^{18}O$ with calculated $\Delta^{17}O$ (Eq. 3). Each sample was analyzed three times and averaged with $2\sigma$ of ≤ 0.06 ‰ for both $\delta^{17}O$ and $\delta^{18}O$ analyses.

| Sample | $\delta^{17}O$ (‰) | $\delta^{18}O$ (‰) | $\Delta^{17}O$ (‰) |
|---|---|---|---|
| RD-1 | 1.5 | 3.0 | -0.13 |
| RD-2 | 1.8 | 3.6 | -0.09 |
| RD-3 | 2.0 | 3.7 | 0.10 |
| RD-4 | 1.8 | 3.5 | -0.11 |
| RD-7 | 1.4 | 2.6 | 0.03 |

# CHAPTER V

# CONCLUSIONS

The previous three chapters have demonstrated the capability of traditional and non-traditional stable isotopes when applied to the iron oxide ore-forming minerals in IOA and IOCG deposits to test current genetic models. The simple application of the Fe–O isotope pair allows researchers to determine mineralizing fluid sources and subsequent degree of alteration of the iron oxide minerals, particularly magnetite. Measuring $^{17}O$ in iron oxides and H stable isotopes of fluid inclusions in primary magnetite and secondary hydrous iron oxides may be used as an effective redundant indicator of primary and secondary fluid sources. When used in conjunction with more traditional techniques such as reflected light microscopy, electron microscopy, and trace element analyses, stable isotopes become a powerful tool for understanding metal and fluid provenance of the most modally abundant minerals of IOAs and IOCGs, magnetite and hematite, allowing for efficient testing of current ore deposit formation models.

Due to conflicting textural observations, the iron oxide deposits at Pea Ridge and Pilot Knob have been the center of much debate concerning their origin. Porphyritic magnetite phenocrysts supported by fine grained magnetite matrix have been argued to support a purely magmatic emplacement hypothesis, while replacement textures in the magnetite orebodies have led some researchers to claim Fe-rich fluids metasomatized local volcanic rocks, entirely

replacing them with magnetite. By applying Fe and O stable isotopes to these deposits, **Chapter II** determined that magnetite from these deposits are undoubtedly magmatic in origin, whether they were precipitated directly from a magma or a magmatic-hydrothermal fluid. The addition of trace element analyses allowed for further interpretation of the multiple generations of magnetite observed at Pea Ridge, and a clear contrast was observed between low-Ti magnetite (<0.36 wt % $TiO_2$) and high-Ti (>10 wt % $TiO_2$) magnetite. This observation, in conjunction with Fe and O stable isotopes, allows for the interpretation that both orthomagmatic and magmatic-hydrothermal magnetite exist within the Pea Ridge orebody. The simultaneous occurrence of both types of magnetite (magmatic and hydrothermal) is not adequately explained by previous models applied to Pea Ridge and Pilot Knob, and the new data presented in **Chapter II** are more consistent with the newer magnetite flotation model (Knipping et al., 2015) in which magmatic and magmatic-hydrothermal magnetite may precipitate from the same evolving fluid.

Many IOCG deposits within the Chilean Iron Belt are spatially and temporally associated with Kiruna-type IOA deposits. Iron oxide–apatite deposits have been suggested to be the high-T, S- (Cu-, Au-) poor endmembers of an IOA–IOCG continuum. The Mantoverde mining district is primarily host to IOCG-type magnetite-hematite deposits with spatially associated IOA deposits forming along the same fault system. **Chapter III** presents the first Fe–O paired isotopic dataset for an IOCG deposit, along with extensive trace element analyses of the iron oxides. Previous studies agreed that the initial stages of mineralizing fluids at Mantoverde were of moderate temperature (~600℃) magmatic-hydrothermal fluids, but disagreed on the role (if any) of non-magmatic fluids at later stages of mineralization (i.e. during sulfide and hematite formation). Both the iron and the oxygen stable isotopes are in agreement that early-stage magnetite and late-stage hematite formed from cooling magmatic fluids that were much cooler

(<300℃) at later stages. Trace element contents of Ti, V, Al, and Mn show a cooling trend with decreasing trace element contents, from approximately 500-200℃, similar to the cooling trend discovered at the nearby Los Colorados IOA based on the same trace element observations. The isotopic and trace element data are nearly identical to the Los Colorados IOA, and record lower mineralization temperatures. These observations support the IOA–IOCG hypothesis, where hotter, sulfur poor magnetite, apatite, and actinolite are deposited at depth, releasing Fe- and S-rich fluids that may migrate to the surface to form the cooler, more oxidized and S-rich IOCG deposits.

The El Laco IOA deposits located in the northern Atacama of Chile are among the most enigmatic and geologically inspiring deposits on Earth. Since the first description of the surficial magnetite deposits as magnetite "flows" by Park (1961), competing hypotheses have attempted to explain the occurrence of what visually appear to be iron oxide lava flows, including the eruption and emplacement of immiscible Fe-rich melts and the metasomatic replacement of andesitic lava flows by Fe-rich hydrothermal fluids. Decades of research have gone into attempting to replicate hypothesized Fe-rich melts in the laboratory. More recent observations of magnetite in drill core that extend to 188m depth reveal a continuum of magmatic and hydrothermal textures and trace element chemistry from depth to surface, prompting a new model by Ovalle et al. (2018) based on the magnetite flotation model by Knipping et al. (2015). In **Chapter IV**, we apply triple O, H, and Fe stable isotopes to magnetite and bulk iron oxide samples from five of the six major deposits at El Laco, where only $^{16}O$ and $^{18}O$ had been analyzed previously. The application of these isotopic systems unequivocally prove that the magnetite deposits were derived from a silicate magma (with magnetite $\delta^{18}O$ values consistent with equilibrium with local andesite), with minor alteration by meteoric fluids post-deposition.

The O isotope ratios in these magnetites could only have been derived from typical magmas and magmatic-hydrothermal fluids and preclude magnetite precipitating from an immiscible Fe-melt. Additionally, the paired Fe–O isotopes are nearly identical to the nearby Los Colorados IOA. When interpreted in combination with drill core data, this new all-encompassing isotopic dataset is most in agreement with the magnetite flotation model, where orthomagmatic magnetite was deposited at depth and magmatic-hydrothermal magnetite precipitated from a cooling magmatic-hydrothermal fluid that erupted onto the surface.

The summary of the isotopic and trace element datasets from these three studies supports the conclusion that the fluids responsible for these IOA and IOCG deposits were unequivocally magmatic in origin and rule out the necessity of non-magmatic hydrothermal fluids as a major contributor to deposit formation. Oxygen isotopic ratios also disallow for magnetite to have formed via immiscible Fe-rich melts. The similarity of paired Fe–O isotopes among all deposits imply geochemically similar sources and processes for both IOA and IOCG deposits and, when applied in combination with textural and geochemical analyses of the iron oxides, support the magnetite flotation and IOA–IOCG continuum hypotheses. Further application of the paired Fe–O isotopic systems to in situ analysis of individual generations of magnetite may reveal high-T fractionation of the isotopes between orthomagmatic and magmatic-hydrothermal magnetite within individual iron oxide systems to further test the magnetite flotation hypothesis.

With growing global resource demand comes a necessity of improving the ways in which we explore for high quality ore deposits. As the largest and highest quality ore deposits become more scarce and difficult to find, we must improve our overall understanding of exactly how these ore deposits form by testing and improving upon models while both in the laboratory and in the field. Methods that are currently considered unconventional (like those presented in this

study) in the sense of traditional exploration techniques may eventually become standard practice when attempting to delineate specific deposits to maximize the throughput of exploration and mining. The days of stumbling upon significant ore deposits while mapping in the field are nearing an end, and more in-depth techniques that encompass a much broader range of geoscience will become necessary if geologists are to keep up with increasing industrialization. As we venture off-planet in search of new resources in the coming decades and the cost of failed exploration attempts becomes prohibitive to the process, scientific inquiry and understanding will be at the forefront of exploration. The research presented in this thesis is a small contribution to the overall understanding of the geologic processes that form quality ore deposits, and of a rapidly growing and much needed unification of science and the mining industry. It is this unification of conventional experience and unconventional research that will highlight new avenues for productive and responsible mining for the foreseeable future.

## REFERENCES

Knipping JL, Bilenker LD, Simon AC, Reich M, Barra F, Deditius AP, Lundstrom C, Bindeman I, Munizaga R (2015a) Giant Kiruna-type deposits form by efficient flotation of magmatic magnetite suspensions. Geology, 43:491–594

Ovalle JT, La Cruz NL, Reich M, Barra F, Simon AC, Konecke, BA, Rodriguez-Mustafa MA, Deditius AP, Childress TM, Morata D (2018) Formation of massive iron deposits linked to explosive volcanic eruptions. Nature Scientific Reports, 8 no. 14855

Park CF Jr. (1961) A magnetite “flow” in northern Chile. Economic Geology, 56:431-436

# APPENDIX

## TABLES

**Table A.1**: Oxygen isotopic data from Pea Ridge and Pilot Knob and additional data and locations of magnetite samples from previous studies.

| Location | Sample | $\delta^{18}O$ (‰) |
|---|---|---|
| **Pea Ridge, USA** | PR-18 | 2.12 |
| | PR-37 | 4.50 |
| | PR-64A | 4.87 |
| | PR-65 | 5.10 |
| | PR-73 | 1.24 |
| | PR-77A | 5.11 |
| | PR-82A | 5.90 |
| | PR-82B | 7.03 |
| | PR-144 | 5.04 |
| | PR-148 | 4.56 |
| | PR-153 | 3.18 |
| | PR-163 | 1.02 |
| **Pilot Knob, USA** | PK-1145-830.1 | 3.26 |
| | PK-1145-965.8 | 6.68 |
| | PK-1145-979.5 | 6.21 |
| **Kiruna, Sweden** | Nyström et al. 2008 | 2.2 |
| | Nyström et al. 2008 | 1.7 |
| | Nyström et al. 2008 | 1.1 |
| | Nyström et al. 2008 | 1.8 |
| | Nyström et al. 2008 | 0.9 |
| | Nyström et al. 2008 | 2.1 |
| | Nyström et al. 2008 | 0.7 |
| | Nyström et al. 2008 | 1.3 |
| | Nyström et al. 2008 | 1.1 |
| | Nyström et al. 2008 | -0.2 |
| | Nyström et al. 2008 | -0.7 |
| | Nyström et al. 2008 | 1 |
| | Nyström et al. 2008 | 1.1 |
| | Nyström et al. 2008 | 0.3 |
| | Nyström et al. 2008 | 1.2 |
| | Bilenker 2015 | 1.76 |
| **Grangensberg, Sweden** | Jonnson et al, 2014 | 1.9 |
| | Jonnson et al, 2014 | 2.2 |

| | | |
|---|---|---|
| | Jonnson et al, 2014 | 2.8 |
| | Jonnson et al, 2014 | 1.2 |
| | Jonnson et al, 2014 | 1.1 |
| | Jonnson et al, 2014 | 1 |
| | Jonnson et al, 2014 | 1.2 |
| | Jonnson et al, 2014 | 1.8 |
| | Jonnson et al, 2014 | 1.4 |
| | Jonnson et al, 2014 | 3.7 |
| | Jonnson et al, 2014 | -0.4 |
| | Jonnson et al, 2014 | 1.3 |
| | Jonnson et al, 2014 | 1.2 |
| | Jonnson et al, 2014 | 3 |
| | Jonnson et al, 2014 | 1.8 |
| | Jonnson et al, 2014 | 1.9 |
| | Jonnson et al, 2014 | 0.9 |
| | Jonnson et al, 2014 | 0.2 |
| | Jonnson et al, 2014 | 1.1 |
| | Jonnson et al, 2014 | 1.5 |
| | Jonnson et al, 2014 | 2.8 |
| | Jonnson et al, 2014 | 1.7 |
| | Jonnson et al, 2014 | 3.4 |
| | Jonnson et al, 2014 | 1.8 |
| | Jonnson et al, 2014 | 1.5 |
| | | |
| **Chilean Iron Belt** | | |
| **Carmen** | This study | 2.6 |
| | Nyström et al. 2008 | 2.4 |
| | Nyström et al. 2008 | 3.3 |
| | | |
| **El Dorado** | Nyström et al. 2008 | 3 |
| | | |
| **Romeral** | Nyström et al. 2008 | 1.6 |
| | Nyström et al. 2008 | 0.8 |
| | Nyström et al. 2008 | 1.3 |
| | Nyström et al. 2008 | 1.7 |
| | Nyström et al. 2008 | -1.3 |
| | Nyström et al. 2008 | 0.4 |
| | Nyström et al. 2008 | 2 |
| | Nyström et al. 2008 | 0.3 |
| **Algarrobo** | Nyström et al. 2008 | 1.9 |
| | Nyström et al. 2008 | 2.3 |
| | Nyström et al. 2008 | 2.5 |
| | Nyström et al. 2008 | 0.6 |

| | | |
|---|---|---|
| **El Tofo** | Nyström et al. 2008 | 4.5 |
| **Cerro Iman** | Nyström et al. 2008 | 1.7 |
| | Nyström et al. 2008 | 1.6 |
| **Los Colorados** | Bilenker 2015 | 2.41 |
| | Bilenker 2015 | 3.04 |
| | Bilenker 2015 | 2.75 |
| | Bilenker 2015 | 3.17 |
| | Bilenker 2015 | 2.36 |
| | Bilenker 2015 | 2.04 |
| | Bilenker 2015 | 2.76 |
| | Bilenker 2015 | 2.99 |
| | Bilenker 2015 | 2.78 |
| | Bilenker 2015 | 2.48 |
| | Bilenker 2015 | 1.92 |
| | Bilenker 2015 | 2.62 |
| | Bilenker 2015 | 2.43 |
| **Mariela Ignacia** | Bilenker 2015 | 1.50 |
| **El Laco, Chile** | Nyström et al. 2008 | 3.2 |
| | Nyström et al. 2008 | 4.2 |
| | Nyström et al. 2008 | 2.7 |
| | Nyström et al. 2008 | 3.4 |
| | Nyström et al. 2008 | 3.4 |
| | Nyström et al. 2008 | 2.3 |
| | Nyström et al. 2008 | 3.7 |
| | Nyström et al. 2008 | 3 |
| | Nyström et al. 2008 | 3.1 |
| | Nyström et al. 2008 | 3.5 |
| | Nyström et al. 2008 | 2.3 |
| | Nyström et al. 2008 | 2.6 |
| | Nyström et al. 2008 | 2.4 |
| | Nyström et al. 2008 | 2.4 |
| | Bilenker 2015 | 4.00 |
| | Bilenker 2015 | 4.34 |

**Table A.2:** Iron isotopic data from Pea Ridge and Pilot Knob and additional data and locations of magnetite samples from previous studies.

| Location | Sample | $\delta^{56}Fe$ (‰) | 2σ (‰) | Source |
|---|---|---|---|---|
| **Pea Ridge, USA** | PR-18 | 0.35 | 0.05 | This study |
| | PR-37 | 0.07 | 0.05 | |
| | PR-64a | 0.20 | 0.05 | |
| | PR-73 | 0.28 | | |
| | PR-77a | 0.22 | 0.02 | |
| | PR-82a | 0.10 | 0.02 | |
| | PR-82b | 0.03 | 0.02 | |
| | PR-144 | 0.26 | 0.09 | |
| | | 0.10 | 0.04 | |
| | PR-158 | 0.26 | 0.08 | |
| **Pilot Knob, USA** | PK-1145-965.8 | 0.19 | 0.04 | This study |
| | PK-1145-979.5 | 0.14 | 0.10 | |
| | PK-1098-715 | 0.18 | 0.03 | |
| | PK-1086-918 | 0.14 | 0.05 | |
| | PK-2079-1160 | 0.27 | 0.06 | |
| | PK-1174-1348 | 0.06 | 0.05 | |
| **Mineville, NY** | | -0.92 | 0.03 | Bilenker, 2015 |
| **Chilean Iron Belt** | | | | |
| Los Colorados | | | | |
| Core LC-05 | | 0.22 | 0.03 | Bilenker, 2015 |
| Core LC-05 | 05-20.7 | 0.09 | 0.06 | Bilenker, 2015 |
| Core LC-05 | 05-32 | 0.22 | 0.03 | Bilenker, 2015 |
| Core LC-05 | 05-52.2 | 0.14 | 0.08 | Bilenker, 2015 |
| Core LC-05 | 05-72.9 | 0.13 | 0.05 | Bilenker, 2015 |
| | 05-82.6 | 0.08 | 0.03 | Bilenker, 2015 |
| | 05-90 | 0.21 | 0.07 | Bilenker, 2015 |
| | 05-106 | 0.12 | 0.03 | Bilenker, 2015 |
| | 05-126.15 | 0.10 | 0.06 | Bilenker, 2015 |
| | 05-129.3a | 0.22 | 0.05 | Bilenker, 2015 |
| | 05-129.3b | 0.14 | 0.02 | Bilenker, 2015 |
| Core LC-04 | 04-38.8 | 0.18 | 0.03 | Bilenker, 2015 |
| | 04-66.7 | 0.18 | 0.07 | Bilenker, 2015 |
| | 04-104.4 | 0.24 | 0.08 | Bilenker, 2015 |
| | 04-129.3 | 0.22 | 0.03 | Bilenker, 2015 |

| | | | | |
|---|---|---|---|---|
| LC East Dike | pitE1 | 0.18 | 0.03 | |
| El Laco | LCO-39 | 0.39 | 0.09 | Bilenker, 2015 |
| | LCO | 0.29 | 0.03 | Bilenker, 2015 |
| | LCO vein | 0.30 | 0.03 | Bilenker, 2015 |
| | LCO-76 | 0.32 | 0.09 | Bilenker, 2015 |
| | LCO-78 | 0.53 | 0.03 | Bilenker, 2015 |
| | LCO-104 | 0.27 | 0.03 | Bilenker, 2015 |
| | LCO-111 | 0.20 | 0.03 | Bilenker, 2015 |
| | EJ-LS-11-1 | 0.28 | 0.04 | Weis, 2013 |
| | EJ-LS-11-2 | 0.24 | 0.03 | Weis, 2013 |
| | EJ-LS-11-3 | 0.36 | 0.03 | Weis, 2013 |
| | EJ-LS-11-4 | 0.34 | 0.03 | Weis, 2013 |
| | LS-2 | 0.27 | 0.04 | Weis, 2013 |
| | LS-52 | 0.28 | 0.03 | Weis, 2013 |
| Mariela Ignacia | M-8 | 0.13 | 0.03 | Bilenker, 2015 |
| Dannemora | DM-1 | -0.36 | 0.03 | Weis, 2013 |
| | DM-2 | 0.01 | 0.03 | Weis, 2013 |
| | DM-3 | -0.43 | 0.03 | Weis, 2013 |
| | DM-4 | -0.35 | 0.03 | Weis, 2013 |
| Grängesberg Mining District | | 0.40 | 0.03 | Weis, 2013 |
| | | 0.24 | 0.03 | Weis, 2013 |
| | | 0.33 | 0.03 | Weis, 2013 |
| DC 690 | | 0.31 | 0.03 | Weis, 2013 |
| | | 0.31 | 0.04 | Weis, 2013 |
| | | 0.30 | 0.04 | Weis, 2013 |
| | | 0.26 | 0.04 | Weis, 2013 |
| | | 0.29 | 0.03 | Weis, 2013 |
| | | 0.39 | 0.04 | Weis, 2013 |
| | | 0.27 | 0.04 | Weis, 2013 |
| DC 575 | | 1.00 | 0.03 | Weis, 2013 |
| | | 0.31 | 0.03 | Weis, 2013 |
| | | 0.27 | 0.04 | Weis, 2013 |
| Additional | waste pile | 0.33 | 0.03 | Weis, 2013 |
| | waste pile | -0.02 | 0.03 | Weis, 2013 |
| | disseminated mgt | 0.24 | 0.03 | Weis, 2013 |
| | mgt vein | 0.11 | 0.03 | Weis, 2013 |
| Striberg | BIF | -0.57 | 0.03 | Weis, 2013 |
| Volcanic Reference | | | | |

| | | | | |
|---|---|---|---|---|
| Basalt | Basalt bomb | 0.46 | 0.03 | Weis, 2013 |
| Ankaramite | TEF-NER-57 | 0.16 | 0.02 | Weis, 2013 |
| Ankaramite | TEF-NER-70 | 0.10 | 0.02 | Weis, 2013 |
| Ankaramite | TEF-NER-18 | 0.07 | 0.05 | Weis, 2013 |
| Dacite | MG-07 | 0.32 | 0.03 | Weis, 2013 |
| Dacite | MG-09 | 0.29 | 0.03 | Weis, 2013 |
| Basaltic andesite | M-BA06-KA-3 | 0.17 | 0.03 | Weis, 2013 |
| Basaltic andesite | Kelut | 0.10 | 0.04 | Weis, 2013 |
| Basaltic andesite | | 0.12 | 0.03 | Weis, 2013 |
| Basaltic andesite | | 0.06 | 0.03 | Weis, 2013 |
| Basaltic andesite | | 0.16 | 0.03 | Weis, 2013 |
| Basaltic andesite | | 0.18 | 0.05 | Weis, 2013 |
| Dolerite | 83/CRS/6 | 0.34 | 0.03 | Weis, 2013 |

**Table A.3:** EMPA results for magnetite and hematite from individual depths in elemental weight percent. Blank spaces indicate an analysis that was below detection limit. Statistical summary for magnetite and hematite is located in the main text.

| Depth | Mg | Al | Si | Ca | Ti | V | Cr | Mn | Fe | O | Total |
|---|---|---|---|---|---|---|---|---|---|---|---|
| **262m** | 0.04 | 0.16 | 0.72 | 0.14 | 0.05 | 0.01 | | | 70.41 | 21.26 | 92.80 |
| | | 0.10 | 0.18 | 0.06 | 0.03 | 0.01 | | | 71.68 | 20.88 | 92.94 |
| | | 0.04 | 0.16 | 0.03 | 0.02 | 0.02 | | | 71.92 | 20.85 | 93.03 |
| | 0.02 | 0.06 | 0.20 | 0.04 | 0.01 | 0.02 | | | 71.74 | 20.88 | 92.97 |
| | 0.01 | 0.03 | 0.15 | | | 0.01 | | | 71.48 | 20.70 | 92.41 |
| | 0.03 | 1.16 | 0.17 | 0.02 | | 0.02 | | | 68.01 | 20.75 | 90.18 |
| | | 0.05 | 0.34 | | | 0.02 | | | 71.25 | 20.87 | 92.54 |
| | | 0.38 | 0.20 | 0.01 | 0.04 | 0.02 | | | 70.88 | 20.91 | 92.44 |
| **276m** | | 0.03 | 0.11 | | 0.01 | 0.11 | | | 71.35 | 20.66 | 92.28 |
| | 0.01 | 0.27 | 0.70 | 0.14 | 0.10 | 0.11 | | | 70.29 | 21.36 | 92.99 |
| | | 0.03 | 0.03 | | | 0.11 | | | 71.72 | 20.66 | 92.57 |
| | | 0.05 | 0.26 | 0.04 | 0.03 | 0.11 | | | 70.93 | 20.74 | 92.14 |
| | 0.05 | 0.36 | 1.33 | 0.24 | 0.09 | 0.12 | | | 68.97 | 21.85 | 93.03 |
| | 0.04 | 0.29 | 0.55 | 0.11 | 0.06 | 0.10 | | | 70.22 | 21.16 | 92.53 |
| | 0.01 | 0.03 | 0.20 | 0.02 | 0.01 | 0.10 | | | 71.17 | 20.72 | 92.27 |
| | 0.09 | 0.33 | 0.78 | 0.22 | 0.09 | 0.13 | | 0.01 | 69.63 | 21.40 | 92.68 |
| | 0.12 | 0.37 | 0.43 | 0.15 | 0.15 | 0.12 | | | 69.65 | 21.07 | 92.06 |
| | | 0.02 | 0.09 | | 0.02 | 0.11 | | | 71.59 | 20.69 | 92.51 |
| | 0.01 | 0.09 | 0.33 | 0.06 | 0.04 | 0.11 | | | 70.89 | 20.87 | 92.41 |
| | | 0.02 | 0.01 | | | 0.09 | | | 69.56 | 20.01 | 89.70 |
| | | 0.03 | 0.02 | | | 0.09 | | | 69.69 | 20.06 | 89.88 |
| | | 0.02 | 0.01 | | | 0.08 | | | 71.94 | 20.68 | 92.74 |
| | | 0.06 | 0.28 | 0.08 | 0.02 | 0.10 | | | 71.09 | 20.83 | 92.44 |
| | | 0.02 | 0.02 | | | 0.10 | 0.03 | | 71.77 | 20.67 | 92.62 |
| | | 0.04 | 0.02 | | | 0.09 | | | 69.43 | 20.00 | 89.59 |
| | | 0.01 | 0.02 | | | 0.08 | 0.01 | | 71.62 | 20.59 | 92.33 |

| | | | | | | | | | | |
|---|---|---|---|---|---|---|---|---|---|---|
| | | 0.06 | 0.10 | | | 0.06 | | | 71.48 | 20.69 | 92.40 |
| | | 0.03 | 0.07 | | | 0.08 | | | 71.94 | 20.76 | 92.90 |
| | | 0.03 | 0.07 | | | 0.08 | | | 72.24 | 20.85 | 93.29 |
| | | 0.02 | 0.06 | | | 0.08 | | | 71.87 | 20.72 | 92.77 |
| | 0.02 | 0.06 | 0.23 | 0.02 | | 0.09 | | | 71.30 | 20.81 | 92.53 |
| | | 0.01 | 0.01 | | | 0.10 | | | 72.00 | 20.71 | 92.85 |
| | | 0.08 | 0.03 | | | 0.10 | | | 70.49 | 20.35 | 91.06 |
| | | 0.02 | 0.02 | | | 0.09 | | | 69.37 | 19.96 | 89.47 |
| | | 0.02 | 0.01 | | | 0.09 | | | 69.41 | 19.96 | 89.49 |
| | | 0.02 | 0.02 | | | 0.11 | | | 69.64 | 20.04 | 89.83 |
| | | 0.03 | 0.02 | | 0.04 | 0.11 | 0.01 | | 69.81 | 20.13 | 90.15 |
| | | 0.01 | 0.03 | | 0.01 | 0.10 | 0.01 | | 71.85 | 20.68 | 92.68 |
| | | 0.01 | 0.08 | | | 0.08 | | | 71.22 | 20.55 | 91.94 |
| | | 0.05 | 0.17 | 0.03 | 0.01 | 0.10 | | | 71.50 | 20.79 | 92.67 |
| | | | 0.02 | | | 0.10 | | | 71.86 | 20.67 | 92.66 |
| | | 0.29 | 0.07 | | | 0.09 | | | 70.90 | 20.70 | 92.06 |
| | 0.03 | 0.13 | 0.48 | 0.08 | 0.03 | 0.10 | | | 70.55 | 21.00 | 92.40 |
| **284m** | | 0.03 | 0.02 | | 1.09 | 0.08 | | | 68.59 | 20.46 | 90.28 |
| | | 0.03 | 0.02 | | 0.64 | 0.09 | 0.02 | | 68.46 | 20.14 | 89.39 |
| | | 0.02 | 0.01 | | 1.25 | 0.03 | 0.01 | | 67.79 | 20.31 | 89.42 |
| | | 0.03 | 0.08 | | | 0.06 | | | 70.77 | 20.42 | 91.37 |
| | 0.17 | 0.23 | 0.36 | 0.03 | 0.01 | 0.04 | 0.04 | | 69.46 | 20.67 | 91.00 |
| | | 0.20 | 0.31 | 0.55 | | 0.04 | 0.05 | 0.02 | 67.63 | 20.18 | 88.97 |
| | 0.04 | 0.16 | 0.63 | 0.35 | 0.03 | 0.07 | 0.04 | | 67.90 | 20.55 | 89.76 |
| | | 0.60 | 0.63 | 0.12 | 0.02 | 0.03 | 0.01 | | 67.63 | 20.72 | 89.79 |
| | | 0.13 | 0.32 | 0.19 | 0.01 | 0.07 | 0.02 | | 68.60 | 20.28 | 89.64 |
| | | 0.03 | 0.11 | 0.71 | | 0.04 | 0.01 | 0.02 | 70.41 | 20.63 | 91.96 |
| | | 0.50 | 1.59 | 0.48 | | 0.04 | 0.02 | 0.01 | 68.56 | 22.11 | 93.31 |
| | | 1.64 | 0.19 | 0.64 | | 0.04 | 0.02 | 0.01 | 68.05 | 21.47 | 92.08 |
| | | 0.11 | 0.19 | 0.35 | | 0.04 | 0.01 | | 70.58 | 20.71 | 92.01 |
| | | 0.10 | 0.21 | 0.17 | 0.01 | 0.04 | | | 71.17 | 20.82 | 92.52 |
| | 0.03 | 0.03 | 0.07 | | 0.01 | 0.09 | 0.04 | | 69.08 | 19.99 | 89.34 |

| | | | | | | | | | | | |
|---|---|---|---|---|---|---|---|---|---|---|---|
| | | 0.08 | 0.38 | 0.03 | 0.02 | 0.08 | 0.05 | | 70.43 | 20.78 | 91.86 |
| | | 0.01 | 0.02 | | | 0.08 | 0.04 | 0.01 | 71.70 | 20.64 | 92.52 |
| | | 0.01 | 0.04 | | | 0.09 | 0.03 | | 71.48 | 20.59 | 92.23 |
| | | 0.08 | 0.53 | 0.04 | 0.03 | 0.08 | 0.14 | | 70.28 | 20.95 | 92.13 |
| | | 0.03 | 0.03 | | | 0.08 | 0.04 | | 71.27 | 20.54 | 92.00 |
| | | 0.10 | 0.31 | 0.10 | 0.02 | 0.07 | 1.40 | 0.01 | 69.44 | 21.07 | 92.51 |
| **291m** | | 0.01 | 0.07 | | | 0.06 | | | 71.57 | 20.63 | 92.34 |
| | | 0.02 | 0.07 | | | 0.06 | | | 71.85 | 20.72 | 92.72 |
| | | 0.02 | 0.05 | | 0.04 | 0.06 | | | 71.56 | 20.63 | 92.34 |
| | | 0.02 | 0.04 | | 0.01 | 0.06 | | | 71.48 | 20.58 | 92.18 |
| | | 0.05 | 0.21 | | 0.02 | 0.06 | | | 71.69 | 20.86 | 92.90 |
| | | 0.03 | 0.07 | | 0.01 | 0.07 | | | 71.84 | 20.71 | 92.70 |
| | 0.02 | 0.09 | 0.26 | 0.05 | 0.02 | 0.07 | | | 71.07 | 20.81 | 92.37 |
| | | 0.02 | 0.04 | | 0.02 | 0.07 | | | 72.00 | 20.73 | 92.86 |
| | | 0.02 | 0.12 | 0.01 | | 0.07 | | | 71.17 | 20.58 | 91.96 |
| | 0.04 | 0.11 | 0.57 | 0.08 | 0.03 | 0.07 | | | 70.34 | 21.01 | 92.25 |
| | | 0.02 | 0.07 | | | 0.07 | | | 71.66 | 20.66 | 92.47 |
| | | 0.02 | 0.07 | | | 0.07 | | | 71.66 | 20.66 | 92.48 |
| | | 0.02 | 0.15 | | | 0.07 | | | 71.62 | 20.75 | 92.62 |
| | 0.09 | 0.32 | 0.90 | 0.25 | 0.08 | 0.07 | | | 69.34 | 21.43 | 92.50 |
| | 0.55 | 0.07 | 1.00 | 0.30 | 0.01 | 0.06 | | | 69.58 | 21.65 | 93.21 |
| | | 0.07 | 0.35 | 0.02 | 0.01 | 0.06 | | | 71.01 | 20.85 | 92.38 |
| | | | 0.04 | | | 0.05 | | 0.01 | 71.70 | 20.63 | 92.46 |
| | 0.02 | 0.15 | 0.33 | 0.06 | 0.04 | 0.03 | | | 70.60 | 20.81 | 92.05 |
| | 0.05 | 0.24 | 0.61 | 0.14 | 0.12 | 0.02 | | | 69.73 | 21.06 | 91.97 |
| | 0.06 | 0.22 | 0.55 | 0.15 | 0.06 | 0.03 | | | 69.66 | 20.94 | 91.67 |
| | 0.02 | 0.10 | 0.21 | 0.07 | 0.24 | 0.03 | | | 70.72 | 20.80 | 92.19 |
| | 0.05 | 0.29 | 0.62 | 0.17 | 0.07 | 0.04 | | 0.01 | 69.85 | 21.14 | 92.23 |
| | 0.04 | 0.06 | 0.23 | 0.08 | 0.05 | 0.03 | | 0.01 | 70.46 | 20.61 | 91.58 |
| | 0.02 | 0.16 | 0.41 | 0.05 | 0.12 | 0.03 | | 0.01 | 69.14 | 20.56 | 90.52 |
| | 0.03 | 0.23 | 0.59 | 0.14 | 0.12 | 0.04 | | 0.01 | 69.21 | 20.88 | 91.24 |
| | | 0.04 | 0.13 | 0.01 | 0.05 | 0.05 | | | 71.19 | 20.64 | 92.12 |

| | | | | | | | | | | | |
|---|---|---|---|---|---|---|---|---|---|---|---|
| | 0.06 | 0.35 | 0.80 | 0.19 | 0.09 | 0.05 | | | 69.41 | 21.31 | 92.27 |
| | | 0.03 | 0.01 | | | 0.02 | | | 71.95 | 20.66 | 92.68 |
| | 0.10 | 0.57 | 1.11 | 0.33 | 0.02 | 0.02 | | 0.02 | 68.68 | 21.68 | 92.53 |
| | | 0.19 | 0.31 | 0.07 | 0.01 | 0.02 | | | 71.05 | 20.92 | 92.57 |
| | 0.05 | 0.14 | 0.42 | 0.13 | | 0.02 | | | 70.75 | 20.97 | 92.48 |
| | 0.10 | 0.28 | 0.80 | 0.26 | 0.01 | 0.02 | | | 69.54 | 21.27 | 92.28 |
| | | 0.02 | 0.01 | 0.04 | | 0.02 | | | 72.03 | 20.69 | 92.82 |
| | | 0.02 | 0.01 | 0.02 | | 0.03 | | | 69.50 | 19.96 | 89.52 |
| | | 0.01 | 0.01 | 0.02 | | 0.03 | | | 69.64 | 20.00 | 89.72 |
| | 0.08 | 0.31 | 0.89 | 0.29 | 0.02 | 0.02 | | 0.01 | 69.78 | 21.47 | 92.87 |
| | | 0.03 | 0.08 | 0.03 | | 0.02 | | | 71.72 | 20.70 | 92.60 |
| **299m** | | 0.02 | 0.01 | | | 0.06 | 0.01 | | 71.66 | 20.60 | 92.37 |
| | | 0.03 | 0.01 | | | 0.07 | 0.01 | | 71.76 | 20.64 | 92.52 |
| | | 0.02 | 0.01 | | | 0.06 | | | 71.40 | 20.52 | 92.04 |
| | | | 0.01 | | | 0.06 | | | 71.71 | 20.60 | 92.38 |
| | | 0.02 | 0.08 | | | 0.06 | 0.01 | | 71.40 | 20.62 | 92.21 |
| | | 0.03 | 0.05 | | | 0.07 | | | 71.51 | 20.61 | 92.29 |
| | | | 0.01 | | | 0.06 | | 0.01 | 71.80 | 20.63 | 92.53 |
| | | 0.02 | 0.01 | | | 0.06 | | | 71.53 | 20.55 | 92.17 |
| | | 0.02 | 0.01 | | | 0.07 | | | 71.69 | 20.59 | 92.37 |
| | | 0.03 | 0.12 | | | 0.06 | | 0.01 | 71.68 | 20.74 | 92.65 |
| | | 0.02 | 0.03 | | | 0.07 | | | 71.82 | 20.67 | 92.62 |
| | | 0.04 | 0.06 | | | 0.06 | 0.01 | 0.01 | 71.48 | 20.62 | 92.28 |
| | | 0.02 | 0.01 | | | 0.06 | | | 71.87 | 20.65 | 92.62 |
| | | 0.02 | 0.08 | | | 0.07 | | | 71.40 | 20.60 | 92.19 |
| | | 0.02 | 0.03 | | | 0.06 | | | 70.41 | 20.27 | 90.82 |
| | | 0.28 | 0.11 | | 0.02 | 0.01 | | | 68.76 | 20.10 | 89.28 |
| | | 0.19 | 0.42 | 0.12 | 0.06 | 0.02 | | 0.02 | 70.64 | 21.01 | 92.50 |
| | | 0.02 | 0.07 | | | 0.06 | 0.01 | | 71.81 | 20.71 | 92.69 |
| | | 0.02 | 0.03 | | 0.02 | 0.06 | | | 71.44 | 20.57 | 92.16 |
| | | 0.06 | 0.26 | 0.02 | 0.02 | 0.07 | | | 71.23 | 20.81 | 92.48 |
| | | 0.04 | 0.09 | | 0.02 | 0.07 | | | 71.41 | 20.64 | 92.26 |

| | | | | | | | | | | |
|---|---|---|---|---|---|---|---|---|---|---|
| | | 0.05 | 0.09 | | | 0.06 | | | 71.49 | 20.66 | 92.35 |
| | | 0.04 | 0.13 | | 0.02 | 0.07 | | | 71.71 | 20.77 | 92.74 |
| | 0.02 | 0.20 | 0.35 | 0.07 | 0.04 | 0.07 | | 0.01 | 70.70 | 20.94 | 92.39 |
| | 0.01 | 0.03 | 0.05 | | 0.01 | 0.07 | | 0.01 | 71.68 | 20.67 | 92.53 |
| | | 0.03 | 0.06 | | 0.01 | 0.06 | | 0.01 | 71.79 | 20.70 | 92.66 |
| | 0.02 | 0.26 | 0.39 | 0.08 | 0.02 | 0.05 | | 0.01 | 70.87 | 21.06 | 92.76 |
| | | 0.18 | 0.28 | 0.01 | 0.07 | 0.06 | 0.02 | | 70.64 | 20.80 | 92.04 |
| | | 0.04 | 0.13 | 0.02 | 0.01 | 0.06 | 0.10 | 0.01 | 71.43 | 20.74 | 92.54 |
| | | 0.12 | 0.25 | 0.06 | 0.05 | 0.03 | | 0.01 | 71.26 | 20.88 | 92.67 |
| | | 0.02 | 0.05 | | 0.03 | 0.05 | | | 71.60 | 20.64 | 92.40 |
| | | 0.04 | 0.06 | | 0.03 | 0.06 | 0.01 | | 71.73 | 20.72 | 92.66 |
| | | 0.02 | 0.09 | | 0.05 | 0.06 | | | 71.68 | 20.71 | 92.59 |
| | | 0.02 | 0.01 | | 0.01 | 0.07 | | | 71.73 | 20.63 | 92.48 |
| | | 0.02 | 0.01 | | 0.01 | 0.07 | | | 71.82 | 20.65 | 92.58 |
| | | 0.05 | 0.19 | 0.04 | 0.03 | 0.04 | | | 71.55 | 20.82 | 92.74 |
| | | | 0.01 | | 0.03 | 0.07 | | | 71.97 | 20.69 | 92.78 |
| | | 0.04 | 0.04 | | 0.03 | 0.07 | | | 71.63 | 20.65 | 92.45 |
| | | 0.03 | 0.02 | | 0.02 | 0.07 | | 0.02 | 71.71 | 20.64 | 92.50 |
| **299m hmt** | | 0.16 | | | 0.07 | 0.01 | | | 69.09 | 19.99 | 89.32 |
| | | 0.02 | 0.01 | | 1.78 | 0.07 | | | 67.07 | 20.47 | 89.42 |
| | | 0.06 | 0.01 | | 0.89 | 0.04 | | | 68.50 | 20.30 | 89.80 |
| | | 0.03 | | | 0.29 | 0.09 | | | 68.75 | 19.96 | 89.11 |
| | | 0.04 | | | 0.08 | 0.08 | | | 69.44 | 20.02 | 89.65 |
| | | 0.04 | 0.01 | | 0.07 | 0.08 | | | 69.36 | 20.00 | 89.55 |
| | | 0.03 | | | 0.19 | 0.09 | | | 69.02 | 19.98 | 89.31 |
| | | 0.04 | | | 0.15 | 0.09 | | 0.01 | 69.01 | 19.95 | 89.25 |
| | | 0.03 | 0.01 | | 2.43 | 0.11 | 0.01 | | 66.29 | 20.70 | 89.58 |
| | | 0.17 | 0.04 | | 0.15 | 0.06 | | | 68.92 | 20.07 | 89.40 |
| | | 0.10 | 0.02 | | 0.79 | 0.08 | | | 68.15 | 20.20 | 89.35 |
| | | 0.04 | 0.01 | | 1.74 | 0.08 | | | 67.32 | 20.53 | 89.71 |
| | | 0.04 | | | 2.25 | 0.07 | | 0.01 | 66.43 | 20.62 | 89.43 |
| | | 0.21 | 0.04 | | 0.03 | | | | 69.24 | 20.09 | 89.61 |

| | | | | | | | | | | | |
|---|---|---|---|---|---|---|---|---|---|---|---|
| | | 0.04 | 0.01 | | 0.25 | 0.09 | | | 68.98 | 20.02 | 89.40 |
| | | 0.02 | | | 2.97 | 0.06 | | | 66.35 | 21.05 | 90.45 |
| | | 0.21 | 0.04 | | 0.58 | 0.15 | | | 68.46 | 20.31 | 89.75 |
| | | 0.21 | 0.03 | | 0.35 | 0.02 | | | 68.89 | 20.19 | 89.67 |
| | | 0.28 | 0.11 | | 0.02 | 0.01 | | | 68.76 | 20.10 | 89.28 |
| **305m** | 0.02 | 0.15 | 0.37 | 0.08 | 0.04 | 0.08 | 0.03 | | 70.70 | 20.94 | 92.42 |
| | 0.03 | 0.12 | 0.35 | 0.07 | 0.11 | 0.07 | 0.03 | | 71.00 | 21.01 | 92.79 |
| | | 0.02 | 0.06 | | 0.01 | 0.07 | 0.02 | | 71.78 | 20.70 | 92.67 |
| | 0.02 | 0.08 | 0.20 | 0.04 | 0.02 | 0.08 | 0.02 | 0.01 | 71.19 | 20.78 | 92.44 |
| | | 0.02 | 0.02 | | 0.01 | 0.08 | | 0.01 | 71.79 | 20.66 | 92.60 |
| | 0.03 | 0.06 | 0.23 | 0.07 | 0.02 | 0.08 | 0.03 | | 71.19 | 20.82 | 92.52 |
| | | 0.03 | 0.19 | 0.01 | 0.03 | 0.08 | 0.03 | | 71.45 | 20.78 | 92.59 |
| | 0.03 | 0.18 | 0.32 | 0.08 | 0.05 | 0.08 | 0.02 | | 70.73 | 20.93 | 92.43 |
| | 0.01 | 0.02 | 0.13 | 0.03 | 0.02 | 0.08 | 0.02 | | 71.62 | 20.77 | 92.70 |
| | 0.03 | 0.11 | 0.29 | 0.06 | 0.03 | 0.08 | 0.02 | | 70.96 | 20.87 | 92.45 |
| | 0.07 | 0.14 | 0.37 | 0.08 | 0.04 | 0.08 | 0.01 | | 70.74 | 20.97 | 92.53 |
| | | 0.05 | 0.19 | 0.05 | 0.02 | 0.08 | 0.01 | | 71.52 | 20.83 | 92.76 |
| | | 0.02 | 0.03 | | 0.02 | 0.08 | 0.02 | | 71.86 | 20.70 | 92.74 |
| | 0.04 | 0.07 | 0.32 | 0.07 | 0.01 | 0.07 | 0.02 | | 71.09 | 20.91 | 92.61 |
| | | 0.03 | 0.12 | 0.01 | 0.02 | 0.08 | 0.02 | | 71.52 | 20.71 | 92.50 |
| | | 0.05 | 0.17 | 0.01 | 0.04 | 0.08 | 0.02 | | 71.44 | 20.78 | 92.59 |
| | | 0.03 | 0.15 | 0.03 | 0.01 | 0.09 | 0.02 | | 71.47 | 20.76 | 92.57 |
| | | 0.07 | 0.23 | 0.04 | 0.04 | 0.08 | 0.02 | | 71.66 | 20.95 | 93.10 |
| | 0.03 | 0.08 | 0.26 | 0.08 | 0.08 | 0.13 | | | 71.21 | 20.94 | 92.83 |
| | 0.01 | 0.09 | 0.30 | 0.05 | 0.02 | 0.12 | | | 70.80 | 20.80 | 92.20 |
| | | 0.03 | 0.13 | 0.01 | 0.03 | 0.10 | | | 71.26 | 20.67 | 92.24 |
| | 0.01 | 0.02 | 0.13 | 0.03 | | 0.11 | | | 70.81 | 20.53 | 91.66 |
| | | 0.04 | 0.23 | 0.04 | | 0.11 | | 0.01 | 71.05 | 20.73 | 92.22 |
| | 0.01 | 0.04 | 0.08 | | | 0.11 | | | 71.48 | 20.68 | 92.43 |
| | 0.05 | 0.22 | 0.49 | 0.14 | 0.07 | 0.12 | | 0.01 | 70.47 | 21.14 | 92.72 |
| | 0.07 | 0.22 | 0.58 | 0.16 | 0.09 | 0.13 | | 0.01 | 70.05 | 21.17 | 92.49 |
| | 0.07 | 0.21 | 0.56 | 0.16 | 0.07 | 0.12 | | 0.01 | 70.14 | 21.14 | 92.50 |

| | | | | | | | | | | |
|---|---|---|---|---|---|---|---|---|---|---|
| 0.11 | 0.21 | 0.67 | 0.23 | 0.09 | 0.12 | | 0.01 | 69.56 | 21.17 | 92.18 |
| 0.03 | 0.11 | 0.44 | 0.09 | 0.06 | 0.11 | | 0.01 | 70.75 | 21.02 | 92.62 |
| 0.03 | 0.12 | 0.29 | 0.10 | 0.06 | 0.12 | | | 70.90 | 20.90 | 92.51 |
| 0.10 | 0.23 | 0.62 | 0.19 | 0.06 | 0.12 | 0.01 | 0.02 | 70.16 | 21.25 | 92.75 |
| 0.11 | 0.21 | 0.59 | 0.15 | 0.09 | 0.12 | | 0.01 | 70.36 | 21.27 | 92.92 |
| 0.09 | 0.10 | 0.44 | 0.13 | 0.06 | 0.12 | | 0.01 | 70.83 | 21.10 | 92.90 |
| 0.08 | 0.12 | 0.42 | 0.12 | 0.05 | 0.11 | | 0.02 | 70.79 | 21.06 | 92.77 |
| 0.07 | 0.19 | 0.61 | 0.18 | 0.08 | 0.12 | | | 70.13 | 21.20 | 92.60 |
| 0.04 | 0.15 | 0.36 | 0.09 | 0.05 | 0.12 | | | 70.84 | 21.00 | 92.68 |
| 0.08 | 0.13 | 0.41 | 0.16 | 0.07 | 0.12 | | 0.01 | 70.85 | 21.10 | 92.93 |
| 0.04 | 0.10 | 0.29 | 0.08 | 0.09 | 0.12 | | 0.01 | 70.88 | 20.91 | 92.52 |
| 0.04 | 0.15 | 0.37 | 0.11 | 0.05 | 0.12 | | 0.01 | 70.60 | 20.95 | 92.41 |
| 0.09 | 0.20 | 0.62 | 0.20 | 0.06 | 0.12 | 0.01 | 0.02 | 69.96 | 21.18 | 92.46 |
| 0.07 | 0.27 | 0.65 | 0.19 | 0.09 | 0.13 | | 0.02 | 69.88 | 21.25 | 92.56 |
| 0.06 | 0.22 | 0.59 | 0.15 | 0.08 | 0.12 | | 0.01 | 70.04 | 21.15 | 92.44 |
| 0.08 | 0.25 | 0.66 | 0.20 | 0.07 | 0.12 | | 0.01 | 69.58 | 21.16 | 92.14 |
| 0.10 | 0.36 | 0.79 | 0.24 | 0.13 | 0.13 | | 0.01 | 69.07 | 21.32 | 92.16 |
| 0.12 | 0.30 | 0.77 | 0.28 | 0.14 | 0.13 | | 0.01 | 69.13 | 21.30 | 92.18 |
| 0.03 | 0.09 | 0.22 | 0.05 | 0.05 | 0.11 | | | 71.06 | 20.81 | 92.42 |
| 0.02 | 0.13 | 0.27 | 0.05 | 0.04 | 0.11 | | | 70.92 | 20.86 | 92.41 |
| 0.03 | 0.08 | 0.22 | 0.06 | 0.12 | 0.11 | | 0.01 | 70.93 | 20.83 | 92.40 |
| 0.03 | 0.21 | 0.36 | 0.08 | 0.16 | 0.12 | | 0.01 | 70.59 | 21.05 | 92.62 |
| 0.04 | 0.11 | 0.28 | 0.10 | 0.11 | 0.11 | | 0.01 | 70.49 | 20.81 | 92.06 |
| 0.05 | 0.15 | 0.32 | 0.08 | 0.10 | 0.11 | | 0.01 | 70.57 | 20.90 | 92.29 |
| 0.06 | 0.17 | 0.39 | 0.13 | 0.13 | 0.12 | | 0.01 | 70.48 | 21.03 | 92.53 |
| 0.07 | 0.21 | 0.44 | 0.16 | 0.12 | 0.11 | | 0.01 | 70.20 | 21.05 | 92.37 |
| 0.03 | 0.12 | 0.36 | 0.08 | 0.05 | 0.11 | | | 70.75 | 20.93 | 92.44 |
| 0.05 | 0.29 | 0.70 | 0.16 | 0.08 | 0.11 | | 0.01 | 69.80 | 21.26 | 92.47 |
| 0.11 | 0.28 | 0.69 | 0.25 | 0.15 | 0.12 | | 0.01 | 69.57 | 21.30 | 92.49 |
| 0.06 | 0.19 | 0.43 | 0.12 | 0.10 | 0.12 | | 0.01 | 70.34 | 21.02 | 92.39 |
| | 0.03 | 0.10 | 0.02 | 0.04 | 0.07 | 0.03 | | 71.96 | 20.84 | 93.09 |
| 0.10 | 0.13 | 0.61 | 0.19 | 0.05 | 0.07 | | 0.01 | 70.62 | 21.26 | 93.06 |

| | | | | | | | | | | | |
|---|---|---|---|---|---|---|---|---|---|---|---|
| | 0.08 | 0.19 | 0.38 | 0.16 | 0.05 | 0.13 | | | 70.25 | 20.94 | 92.19 |
| | 0.05 | 0.12 | 0.24 | 0.09 | 0.09 | 0.12 | | | 71.02 | 20.91 | 92.65 |
| | | 0.07 | 0.10 | 0.02 | 0.02 | 0.13 | | | 72.05 | 20.90 | 93.30 |
| | 0.10 | 0.29 | 0.73 | 0.22 | 0.12 | 0.10 | 0.01 | 0.02 | 69.97 | 21.43 | 92.99 |
| | 0.03 | 0.66 | 0.56 | 0.11 | 0.04 | 0.09 | | 0.01 | 69.96 | 21.40 | 92.85 |
| **305m hmt** | 0.02 | 0.04 | 0.03 | | 2.21 | 0.09 | | 0.02 | 66.13 | 20.56 | 89.11 |
| | | 0.33 | 0.07 | | 0.30 | 0.04 | | 0.01 | 67.91 | 20.05 | 88.72 |
| | | 0.02 | 0.01 | | 3.01 | 0.10 | | 0.08 | 65.16 | 20.79 | 89.17 |
| | | 0.19 | 0.05 | | 0.70 | 0.05 | | | 68.23 | 20.27 | 89.49 |
| | 0.01 | 0.26 | 0.18 | | 0.55 | 0.05 | | 0.03 | 67.48 | 20.19 | 88.76 |
| | | 0.05 | 0.03 | | 1.07 | 0.08 | | 0.02 | 67.82 | 20.27 | 89.33 |
| | | 0.46 | 0.14 | | 0.39 | 0.03 | | | 66.98 | 20.03 | 88.04 |
| | | 0.17 | 0.03 | | 0.43 | 0.07 | | | 68.50 | 20.14 | 89.35 |
| | | 0.18 | 0.11 | | 0.92 | 0.07 | | | 67.57 | 20.31 | 89.18 |
| | | 0.02 | 0.03 | | 0.93 | 0.10 | | | 67.96 | 20.19 | 89.23 |
| | | 0.04 | 0.04 | | 0.92 | 0.09 | | | 67.73 | 20.15 | 88.99 |
| **314m** | | 0.01 | 0.03 | 0.10 | 0.01 | 0.02 | | | 71.34 | 20.54 | 92.06 |
| | | 0.02 | 0.11 | 0.16 | 0.03 | 0.02 | | 0.01 | 71.22 | 20.65 | 92.23 |
| | | 0.03 | 0.22 | 0.15 | 0.06 | 0.03 | | | 70.95 | 20.72 | 92.15 |
| | 0.08 | 0.18 | 0.52 | 0.31 | 0.04 | 0.03 | | | 69.89 | 21.00 | 92.06 |
| | | 0.03 | 0.07 | 0.13 | | 0.02 | | | 70.62 | 20.42 | 91.32 |
| | 0.04 | 0.05 | 0.21 | 0.33 | 0.09 | 0.02 | | | 70.55 | 20.72 | 92.01 |
| | | 0.04 | 0.25 | 0.28 | 0.02 | 0.02 | | | 70.58 | 20.68 | 91.88 |
| | 0.02 | 0.02 | 0.14 | 0.11 | 0.02 | 0.02 | | | 71.18 | 20.66 | 92.19 |
| | 0.02 | 0.07 | 0.43 | 0.22 | 0.02 | 0.02 | | | 70.25 | 20.81 | 91.84 |
| | | 0.02 | 0.07 | 0.15 | 0.02 | 0.02 | | | 71.31 | 20.62 | 92.23 |
| | | 0.02 | 0.14 | 0.32 | 0.03 | 0.02 | | | 71.26 | 20.75 | 92.55 |
| | | 0.02 | 0.07 | 0.24 | 0.06 | 0.02 | | | 71.03 | 20.59 | 92.02 |
| | | 0.03 | 0.18 | 0.26 | 0.01 | 0.02 | | | 70.73 | 20.63 | 91.88 |
| | | 0.06 | 0.14 | 0.23 | 0.06 | 0.02 | | | 69.02 | 20.13 | 89.66 |
| | | 0.01 | 0.02 | 0.51 | 0.03 | 0.02 | | | 70.57 | 20.49 | 91.66 |
| | 0.11 | 0.16 | 0.56 | 0.21 | 0.05 | 0.02 | | 0.01 | 69.86 | 21.01 | 92.00 |

| | | | | | | | | | |
|---|---|---|---|---|---|---|---|---|---|
| | 0.02 | 0.18 | 0.07 | 0.01 | 0.02 | | 71.08 | 20.64 | 92.03 |
| | 0.03 | 0.03 | 0.07 | 0.05 | 0.02 | | 71.39 | 20.59 | 92.18 |
| 0.02 | 0.05 | 0.27 | 0.22 | 0.03 | 0.02 | 0.01 | 70.85 | 20.79 | 92.26 |
| | 0.02 | 0.26 | 0.14 | 0.01 | 0.03 | 0.01 | 71.10 | 20.76 | 92.33 |
| | 0.01 | 0.13 | 0.09 | | 0.02 | | 71.08 | 20.56 | 91.89 |
| | 0.01 | 0.13 | 0.05 | | 0.02 | 0.01 | 71.24 | 20.61 | 92.09 |
| | 0.01 | 0.16 | 0.04 | 0.01 | 0.02 | | 71.26 | 20.64 | 92.15 |
| | 0.01 | 0.11 | 0.02 | | 0.03 | | 71.37 | 20.61 | 92.15 |
| | 0.02 | 0.14 | 0.02 | | 0.02 | | 70.99 | 20.53 | 91.73 |
| | 0.03 | 0.16 | 0.03 | 0.02 | 0.02 | | 71.14 | 20.63 | 92.03 |
| | 0.02 | 0.06 | 0.08 | 0.04 | 0.03 | | 71.23 | 20.57 | 92.03 |
| | 0.12 | 0.20 | 0.11 | 0.04 | 0.02 | | 70.85 | 20.72 | 92.08 |
| 0.02 | 0.02 | 0.16 | 0.28 | 0.02 | 0.02 | | 71.14 | 20.73 | 92.40 |
| | 0.04 | 0.21 | 0.20 | 0.01 | 0.02 | | 71.51 | 20.86 | 92.86 |
| | 0.02 | 0.01 | 0.04 | 0.04 | 0.02 | | 71.69 | 20.62 | 92.44 |
| | 0.03 | 0.10 | 0.04 | 0.03 | 0.02 | | 71.53 | 20.67 | 92.42 |
| 0.01 | 0.04 | 0.29 | 0.08 | 0.05 | 0.02 | | 71.11 | 20.83 | 92.45 |
| | 0.08 | 0.05 | 0.07 | 0.01 | 0.02 | | 71.26 | 20.59 | 92.08 |
| 0.02 | 0.03 | 0.11 | 0.04 | 0.06 | 0.02 | 0.01 | 71.11 | 20.62 | 92.03 |
| | 0.03 | 0.16 | 0.07 | 0.02 | 0.02 | | 71.51 | 20.74 | 92.55 |
| 0.01 | 0.04 | 0.19 | 0.06 | 0.02 | 0.02 | | 71.08 | 20.68 | 92.11 |
| | 0.04 | 0.19 | 0.03 | 0.03 | 0.02 | | 71.40 | 20.74 | 92.44 |
| 0.02 | 0.02 | 0.17 | 0.03 | 0.03 | 0.02 | | 71.36 | 20.71 | 92.35 |
| | 0.02 | 0.17 | 0.06 | 0.01 | 0.03 | | 71.33 | 20.69 | 92.29 |
| | 0.02 | 0.11 | 0.01 | 0.04 | 0.02 | 0.01 | 71.67 | 20.73 | 92.63 |
| 0.04 | 0.14 | 0.40 | 0.07 | 0.04 | 0.02 | | 70.96 | 21.00 | 92.67 |
| | 0.03 | 0.08 | 0.01 | 0.03 | 0.02 | | 71.77 | 20.71 | 92.66 |
| | 0.04 | 0.18 | | 0.04 | 0.02 | | 71.56 | 20.78 | 92.63 |
| 0.02 | 0.17 | 0.42 | 0.08 | 0.04 | 0.03 | | 70.39 | 20.87 | 92.00 |
| 0.03 | 0.08 | 0.21 | 0.06 | 0.12 | 0.02 | | 70.70 | 20.71 | 91.94 |
| 0.05 | 0.12 | 0.34 | 0.10 | 0.16 | 0.02 | 0.01 | 70.22 | 20.81 | 91.84 |
| 0.01 | 0.03 | 0.11 | 0.03 | 0.02 | 0.02 | | 71.38 | 20.65 | 92.25 |

| | | | | | | | | | | | |
|---|---|---|---|---|---|---|---|---|---|---|---|
| | | 0.02 | 0.09 | 0.01 | 0.07 | 0.02 | | | 70.34 | 20.34 | 90.90 |
| | | 0.09 | 0.26 | 0.05 | 0.07 | 0.02 | | | 70.88 | 20.77 | 92.15 |
| | 0.13 | 0.23 | 0.75 | 0.23 | 0.07 | 0.02 | | 0.01 | 69.79 | 21.29 | 92.51 |
| | 0.11 | 0.19 | 0.69 | 0.18 | 0.05 | 0.03 | | | 69.88 | 21.17 | 92.31 |
| | | 0.07 | 0.26 | 0.04 | 0.02 | 0.02 | | | 70.79 | 20.68 | 91.88 |
| | | 0.03 | 0.01 | | | 0.02 | | | 71.56 | 20.56 | 92.19 |
| | | 0.03 | 0.01 | | | 0.02 | | | 71.64 | 20.58 | 92.29 |
| | | 0.02 | 0.06 | | | 0.02 | | | 71.63 | 20.61 | 92.34 |
| | | 0.05 | 0.08 | 0.01 | 0.03 | 0.02 | | | 71.75 | 20.73 | 92.68 |
| | | 0.01 | 0.01 | | | 0.02 | | | 71.66 | 20.56 | 92.25 |
| | | 0.01 | 0.01 | | | 0.02 | | 0.01 | 71.69 | 20.57 | 92.31 |
| | | 0.03 | 0.03 | | | 0.02 | | | 71.40 | 20.53 | 92.01 |
| | | 0.04 | 0.07 | | | 0.02 | | 0.01 | 71.61 | 20.65 | 92.41 |
| | | 0.20 | 0.54 | 0.05 | | 0.02 | | | 69.48 | 20.74 | 91.06 |
| | | 0.03 | 0.01 | | | 0.02 | | | 71.82 | 20.63 | 92.51 |
| | | 0.02 | 0.03 | | 0.01 | 0.02 | | | 71.74 | 20.62 | 92.45 |
| **324m hmt** | | 0.10 | 0.02 | 0.04 | | 0.05 | | | 70.35 | 20.30 | 90.86 |
| | | 0.09 | 0.02 | 0.03 | | 0.04 | | | 70.10 | 20.21 | 90.49 |
| | | 0.07 | 0.01 | 0.01 | 0.02 | 0.05 | | | 70.46 | 20.29 | 90.91 |
| | | 0.06 | | | 0.04 | 0.06 | | | 70.16 | 20.20 | 90.53 |
| | 0.02 | 0.05 | 0.01 | | 0.05 | 0.07 | | | 70.39 | 20.28 | 90.86 |
| | | 0.05 | 0.01 | 0.04 | | 0.05 | | | 70.31 | 20.23 | 90.68 |
| | | 0.18 | 0.03 | | 0.38 | | | | 70.06 | 20.50 | 91.14 |
| | | 0.01 | 0.01 | | 0.89 | 0.01 | | | 69.42 | 20.49 | 90.82 |
| | | 0.20 | 0.03 | | 0.17 | 0.05 | | | 70.34 | 20.47 | 91.22 |
| | | 0.17 | 0.04 | 0.01 | 1.54 | 0.06 | | | 68.37 | 20.82 | 90.99 |
| **331m** | 0.01 | 0.03 | 0.17 | 0.02 | | 0.14 | 0.01 | | 70.32 | 20.45 | 91.16 |
| | | 0.03 | 0.06 | | 0.01 | 0.14 | 0.01 | | 71.01 | 20.51 | 91.77 |
| | | 0.02 | 0.03 | | | 0.12 | | | 70.85 | 20.41 | 91.43 |
| | | 0.02 | 0.03 | | | 0.13 | 0.01 | | 68.80 | 19.83 | 88.83 |
| | | 0.10 | 0.52 | 0.04 | 0.02 | 0.14 | 0.01 | 0.01 | 70.27 | 20.94 | 92.08 |
| | | 0.02 | 0.02 | | | 0.14 | 0.01 | | 71.31 | 20.54 | 92.03 |

| | | | | | | | | | | | |
|---|---|---|---|---|---|---|---|---|---|---|---|
| | | 0.02 | 0.03 | | | 0.12 | | | 71.12 | 20.49 | 91.80 |
| | | 0.02 | 0.02 | | | 0.13 | | | 71.31 | 20.53 | 92.02 |
| | | 0.02 | 0.04 | | | 0.14 | 0.01 | | 71.28 | 20.57 | 92.07 |
| | | 0.02 | 0.02 | | | 0.14 | 0.01 | | 71.39 | 20.57 | 92.16 |
| | | 0.02 | 0.03 | | | 0.14 | 0.01 | | 71.11 | 20.49 | 91.80 |
| | 0.05 | 0.31 | 0.62 | 0.20 | 0.09 | 0.16 | 0.01 | | 69.74 | 21.22 | 92.40 |
| | 0.04 | 0.34 | 0.64 | 0.19 | 0.07 | 0.15 | | | 69.29 | 21.11 | 91.86 |
| | 0.02 | 0.13 | 0.32 | 0.10 | 0.03 | 0.15 | | 0.01 | 69.90 | 20.66 | 91.32 |
| | | 0.02 | 0.04 | | 0.01 | 0.15 | | | 71.16 | 20.53 | 91.92 |
| | 0.05 | 0.32 | 0.66 | 0.20 | 0.09 | 0.16 | | | 69.47 | 21.20 | 92.17 |
| | 0.02 | 0.15 | 0.35 | 0.10 | 0.05 | 0.16 | | | 70.38 | 20.86 | 92.07 |
| | 0.01 | 0.12 | 0.21 | 0.05 | 0.03 | 0.15 | | | 70.84 | 20.76 | 92.18 |
| | | 0.02 | 0.07 | | | 0.12 | | | 71.34 | 20.60 | 92.17 |
| | | 0.04 | 0.15 | 0.02 | 0.03 | 0.14 | | | 70.70 | 20.57 | 91.66 |
| | | 0.06 | 0.21 | 0.05 | 0.02 | 0.16 | | 0.02 | 70.64 | 20.65 | 91.83 |
| | | 0.02 | 0.03 | | 0.01 | 0.12 | 0.01 | | 71.02 | 20.47 | 91.68 |
| | 0.05 | 0.21 | 0.47 | 0.15 | 0.05 | 0.15 | | | 69.59 | 20.86 | 91.53 |
| | 0.04 | 0.21 | 0.48 | 0.10 | 0.03 | 0.11 | | | 68.75 | 20.56 | 90.29 |
| | | 0.03 | 0.02 | | 3.62 | 0.08 | | 0.02 | 64.43 | 20.97 | 89.18 |
| | | 0.03 | 0.06 | | | 0.15 | 0.01 | | 71.13 | 20.56 | 91.96 |
| | 0.02 | 0.06 | 0.17 | 0.04 | 0.01 | 0.15 | | | 70.91 | 20.67 | 92.03 |
| | | 0.11 | 0.27 | 0.04 | 0.02 | 0.15 | 0.01 | | 70.73 | 20.77 | 92.11 |
| | | 0.03 | 0.07 | | 0.01 | 0.16 | | | 71.16 | 20.58 | 92.02 |
| | 0.01 | 0.13 | 0.25 | 0.07 | 0.02 | 0.15 | 0.01 | | 70.78 | 20.81 | 92.23 |
| | | 0.06 | 0.13 | 0.02 | 0.01 | 0.14 | | | 70.81 | 20.58 | 91.76 |
| | | 0.03 | 0.05 | | | 0.13 | | | 70.77 | 20.43 | 91.42 |
| | | 0.03 | 0.05 | | | 0.13 | | | 71.36 | 20.59 | 92.18 |
| | | 0.02 | 0.02 | | | 0.12 | 0.01 | | 70.77 | 20.38 | 91.33 |
| **331m hmt** | | 0.02 | 0.01 | | 2.33 | 0.04 | | | 66.23 | 20.57 | 89.19 |
| | | 0.06 | 0.01 | | 1.74 | 0.05 | | | 66.84 | 20.40 | 89.10 |
| | | 0.05 | 0.01 | | 2.48 | 0.04 | | 0.01 | 66.25 | 20.71 | 89.54 |
| | | 0.13 | 0.04 | | 1.36 | 0.03 | | | 67.29 | 20.36 | 89.22 |

| | | | | | | | | | | |
|---|---|---|---|---|---|---|---|---|---|---|
| | | 0.02 | 0.01 | | 2.68 | 0.02 | | | 66.07 | 20.75 | 89.54 |
| | | 0.02 | 0.01 | | 2.70 | 0.03 | | | 66.11 | 20.77 | 89.63 |
| | | 0.02 | 0.01 | | 2.55 | 0.03 | | | 66.34 | 20.75 | 89.70 |
| | | 0.07 | | | 0.91 | 0.09 | | | 68.21 | 20.26 | 89.55 |
| | | 0.02 | | | 2.05 | 0.07 | | | 66.82 | 20.57 | 89.54 |
| | | 0.21 | | | 0.37 | 0.09 | | | 68.54 | 20.11 | 89.32 |
| | | 0.01 | | | 1.91 | 0.07 | | | 67.13 | 20.55 | 89.67 |
| | | 0.25 | 0.01 | | 0.10 | 0.01 | | | 68.89 | 20.04 | 89.29 |
| | | 0.09 | 0.01 | | 0.10 | 0.03 | | | 68.99 | 19.94 | 89.17 |
| | | 0.19 | 0.01 | | 0.69 | 0.13 | | | 68.25 | 20.26 | 89.54 |
| | | 0.01 | 0.01 | | 2.47 | 0.10 | 0.01 | | 66.11 | 20.66 | 89.36 |
| | | 0.05 | 0.01 | | 2.18 | 0.07 | | | 66.02 | 20.47 | 88.81 |
| | | 0.08 | 0.02 | | 2.06 | 0.04 | | 0.02 | 66.78 | 20.63 | 89.63 |
| | | 0.12 | 0.01 | | 0.81 | 0.53 | 0.02 | | 67.49 | 20.25 | 89.23 |
| | | 0.11 | 0.01 | | 0.05 | 0.03 | | | 69.21 | 19.97 | 89.36 |
| | | 0.15 | 0.01 | | 0.03 | 0.02 | | | 69.14 | 19.97 | 89.30 |
| | | 0.01 | | | 1.29 | 0.09 | | | 67.72 | 20.32 | 89.43 |
| | | 0.17 | 0.02 | | 0.04 | 0.01 | | | 69.06 | 19.99 | 89.30 |
| | | 0.16 | 0.06 | | 1.93 | 0.04 | | | 66.75 | 20.64 | 89.56 |
| | | 0.14 | 0.01 | | 0.04 | 0.03 | | | 69.25 | 20.02 | 89.50 |
| | | 0.25 | 0.05 | | 0.80 | 0.19 | 0.01 | | 68.02 | 20.39 | 89.71 |
| | | 0.12 | 0.01 | | 0.04 | 0.03 | | | 69.16 | 19.97 | 89.32 |
| | | 0.15 | | | 0.15 | 0.06 | | | 68.90 | 20.00 | 89.27 |
| | | 0.16 | | | 0.06 | 0.04 | | | 69.21 | 20.03 | 89.49 |
| | | 0.45 | 0.07 | | 0.04 | 0.11 | | | 68.50 | 20.17 | 89.33 |
| | | 0.32 | 0.01 | | 0.05 | 0.12 | | | 68.27 | 19.93 | 88.68 |
| | | 0.20 | 0.03 | | 0.62 | 0.04 | | | 68.19 | 20.18 | 89.26 |
| | | 0.15 | | | 0.04 | 0.13 | | | 68.72 | 19.91 | 88.96 |
| | | 0.12 | 0.01 | | 0.05 | 0.11 | | | 68.69 | 19.87 | 88.84 |
| | | 0.11 | 0.01 | | 0.01 | 0.03 | | | 69.02 | 19.91 | 89.10 |
| **340m** | 0.43 | 0.46 | 0.43 | 0.01 | | 0.04 | | | 70.35 | 21.36 | 93.10 |
| | | 0.02 | 0.07 | | | 0.06 | | | 72.29 | 20.84 | 93.29 |

| | | | | | | | | | | | |
|---|---|---|---|---|---|---|---|---|---|---|---|
| | | 0.11 | 0.17 | 0.01 | 0.04 | 0.06 | | | 71.04 | 20.71 | 92.16 |
| | | 0.14 | 0.36 | 0.03 | 0.02 | 0.05 | | | 71.38 | 21.04 | 93.02 |
| | | 0.03 | 0.05 | | | 0.05 | | | 72.05 | 20.75 | 92.94 |
| | 0.09 | 1.06 | 0.42 | | 0.12 | 0.05 | | | 69.95 | 21.63 | 93.33 |
| **356m hmt** | | 0.29 | 0.05 | 0.14 | 0.08 | 0.08 | | 0.04 | 68.89 | 20.21 | 89.79 |
| | | 0.36 | 0.14 | 0.10 | 0.15 | 0.06 | | 0.01 | 67.85 | 20.09 | 88.76 |
| | | 0.28 | 0.11 | 0.10 | 0.29 | 0.06 | | 0.02 | 68.74 | 20.34 | 89.95 |
| | | 0.27 | 0.20 | 0.10 | 0.54 | 0.08 | | 0.02 | 68.27 | 20.48 | 89.96 |
| | | 0.24 | 0.08 | 0.10 | 0.48 | 0.09 | | 0.01 | 68.86 | 20.44 | 90.29 |
| | | 0.28 | 0.06 | 0.10 | 0.18 | 0.07 | | 0.01 | 69.12 | 20.33 | 90.17 |
| | | 0.23 | 0.06 | 0.10 | 0.06 | 0.05 | | 0.02 | 69.30 | 20.24 | 90.06 |
| | | 0.16 | 0.04 | 0.10 | 0.68 | 0.19 | | 0.01 | 68.39 | 20.38 | 89.96 |
| | | 0.36 | 0.05 | 0.10 | 0.06 | 0.09 | | 0.01 | 69.12 | 20.31 | 90.11 |
| | | 0.34 | 0.07 | 0.10 | 0.04 | 0.10 | | 0.01 | 68.52 | 20.15 | 89.34 |
| | | 0.38 | 0.13 | 0.10 | 0.11 | 0.10 | | 0.01 | 68.77 | 20.36 | 89.96 |
| | | 0.15 | 0.05 | 0.10 | 0.09 | 0.17 | | 0.01 | 68.99 | 20.15 | 89.71 |
| **411m** | | 0.09 | 0.04 | | | 0.17 | 0.03 | | 71.54 | 20.72 | 92.61 |
| | 0.45 | 0.60 | 0.48 | | | 0.09 | 0.02 | | 69.06 | 21.22 | 91.93 |
| | | 0.02 | 0.05 | 0.03 | | 0.15 | 0.02 | | 71.87 | 20.76 | 92.92 |
| | | 0.16 | 0.22 | 0.05 | 0.03 | 0.13 | 0.01 | | 72.51 | 21.28 | 94.40 |
| **416m** | | 0.12 | 0.22 | | | 0.10 | 0.01 | | 71.89 | 21.00 | 93.34 |
| | | 0.02 | 0.10 | | | 0.20 | 0.01 | | 72.15 | 20.90 | 93.38 |
| **416m hmt** | | 0.08 | 0.02 | 0.05 | 0.08 | 0.24 | 0.01 | | 69.59 | 20.23 | 90.31 |
| | | 0.10 | 0.02 | 0.04 | 0.07 | 0.08 | | | 69.36 | 20.07 | 89.74 |
| | | 0.02 | 0.04 | 0.04 | 0.03 | 0.04 | | | 69.73 | 20.08 | 89.97 |
| | | 0.02 | 0.04 | 0.07 | 0.65 | 0.14 | | | 68.58 | 20.24 | 89.74 |
| | | 0.02 | 0.03 | 0.08 | 1.31 | 0.08 | | | 68.37 | 20.57 | 90.46 |
| | | 0.05 | 0.02 | 0.09 | 0.04 | 0.13 | | | 69.58 | 20.13 | 90.05 |
| | | 0.08 | 0.02 | 0.04 | 0.14 | 0.07 | | | 69.24 | 20.07 | 89.66 |
| | | 0.03 | 0.04 | | 1.04 | 0.20 | 0.01 | | 68.15 | 20.37 | 89.82 |
| **423m hmt** | | 0.02 | 0.02 | 0.21 | 0.03 | 0.05 | | 0.02 | 69.18 | 20.01 | 89.55 |
| | | 0.02 | 0.02 | 0.30 | 0.01 | 0.05 | | 0.02 | 69.28 | 20.05 | 89.76 |

| | | | | | | | | | | | |
|---|---|---|---|---|---|---|---|---|---|---|---|
| | | 0.05 | 0.03 | 0.15 | 0.42 | 0.05 | | 0.02 | 68.43 | 20.06 | 89.22 |
| | | 0.10 | 0.01 | 0.09 | 0.19 | 0.05 | | 0.02 | 69.01 | 20.05 | 89.51 |
| | | 0.10 | 0.06 | 0.09 | 0.14 | 0.04 | | 0.01 | 68.72 | 19.98 | 89.14 |
| | 0.01 | 0.09 | | 0.09 | 0.18 | 0.05 | | | 68.95 | 19.99 | 89.34 |
| | 0.02 | 0.09 | 0.01 | 0.09 | 0.20 | 0.05 | | 0.01 | 68.94 | 20.03 | 89.42 |
| | | 0.02 | 0.02 | 0.10 | 0.13 | 0.06 | | 0.02 | 69.40 | 20.08 | 89.84 |
| | | 0.03 | 0.05 | 0.09 | 1.73 | 0.06 | | 0.01 | 67.34 | 20.60 | 89.91 |
| | | 0.03 | 0.03 | 0.10 | 1.33 | 0.05 | | 0.01 | 67.98 | 20.49 | 90.02 |
| | | 0.04 | 0.02 | 0.10 | 0.92 | 0.05 | | 0.01 | 68.01 | 20.23 | 89.38 |
| | | 0.01 | 0.03 | 0.10 | 0.82 | 0.06 | | 0.01 | 68.97 | 20.43 | 90.44 |
| | | 0.01 | 0.01 | 0.09 | 0.62 | 0.04 | | 0.01 | 69.05 | 20.26 | 90.07 |
| | | 0.01 | 0.02 | 0.10 | 0.55 | 0.06 | | 0.02 | 68.76 | 20.18 | 89.70 |
| | | 0.03 | 0.02 | 0.09 | 0.29 | 0.05 | | 0.01 | 68.92 | 20.04 | 89.44 |
| | | 0.02 | 0.02 | 0.10 | 0.12 | 0.03 | | 0.01 | 69.30 | 20.04 | 89.64 |
| | | 0.03 | 0.02 | 0.10 | 0.12 | 0.04 | | 0.01 | 69.03 | 19.97 | 89.32 |
| | | 0.02 | 0.03 | 0.10 | 0.90 | 0.08 | | 0.01 | 68.42 | 20.33 | 89.89 |
| **438m** | 0.02 | 0.07 | 1.06 | | 0.04 | 0.11 | 0.01 | | 68.85 | 21.07 | 91.22 |
| | 0.13 | 0.29 | 0.79 | 0.02 | 0.05 | 0.11 | 0.02 | | 69.35 | 21.20 | 91.95 |
| | | 0.07 | 0.11 | | | 0.09 | 0.01 | | 72.51 | 21.00 | 93.79 |
| | | 0.01 | 0.06 | | | 0.12 | 0.01 | | 72.64 | 20.94 | 93.77 |
| | | 0.02 | 0.06 | 0.03 | | 0.12 | 0.01 | 0.01 | 72.36 | 20.87 | 93.46 |
| | | 0.02 | 0.07 | 0.01 | | 0.09 | | | 72.61 | 20.92 | 93.71 |
| | 0.11 | 0.08 | 0.58 | 0.07 | 0.02 | 0.11 | 0.01 | | 70.74 | 21.16 | 92.88 |
| | 0.02 | 0.05 | 0.23 | 0.03 | 0.01 | 0.11 | 0.02 | | 70.62 | 20.63 | 91.72 |
| | 0.32 | 0.38 | 0.97 | 0.05 | 0.05 | 0.12 | 0.02 | | 69.11 | 21.57 | 92.58 |
| **438m hmt** | | 0.06 | 0.01 | | 0.01 | 0.04 | | | 70.33 | 20.22 | 90.66 |
| | | 0.03 | 0.02 | | 0.01 | 0.06 | | | 70.25 | 20.19 | 90.55 |
| | | 0.06 | 0.02 | | 0.02 | 0.08 | | | 70.19 | 20.20 | 90.53 |
| | | 0.03 | 0.01 | | 0.08 | 0.07 | | | 70.44 | 20.29 | 90.92 |
| **449m hmt** | | 0.04 | 0.01 | | 0.15 | 0.03 | | | 70.93 | 20.46 | 91.60 |
| | | 0.28 | 0.05 | | 0.14 | | | | 70.73 | 20.65 | 91.86 |
| | | 0.23 | 0.05 | | 0.22 | 0.01 | | | 70.70 | 20.64 | 91.82 |

| | | | | | | | | | | | |
|---|---|---|---|---|---|---|---|---|---|---|---|
| | | 0.21 | 0.06 | 0.04 | 0.10 | 0.01 | | 0.01 | 70.42 | 20.50 | 91.34 |
| | | 0.27 | 0.06 | | 0.19 | 0.01 | | | 70.33 | 20.58 | 91.43 |
| | | 0.10 | | | | 0.02 | | | 70.61 | 20.32 | 91.04 |
| | | 0.23 | 0.05 | | 0.31 | 0.05 | | | 70.23 | 20.60 | 91.46 |
| | | 0.21 | 0.04 | | 0.21 | 0.02 | | | 70.44 | 20.55 | 91.45 |
| | | 0.09 | 0.01 | | 0.22 | 0.04 | | | 70.52 | 20.45 | 91.32 |
| | | 0.03 | 0.01 | | 1.04 | 0.03 | 0.01 | | 69.93 | 20.76 | 91.79 |
| | | 0.02 | 0.01 | | 1.99 | 0.01 | | | 68.86 | 21.07 | 91.94 |
| **455m hmt** | | 0.10 | 0.01 | | 0.46 | 0.01 | | | 70.02 | 20.46 | 91.05 |
| | | 0.12 | 0.01 | | 0.53 | 0.01 | | | 69.76 | 20.44 | 90.85 |
| | | 0.15 | 0.02 | | 0.53 | | | | 69.67 | 20.45 | 90.81 |
| | | 0.26 | 0.03 | | 0.21 | | | | 69.77 | 20.38 | 90.63 |
| | | 0.10 | 0.01 | | 0.36 | | | | 70.08 | 20.39 | 90.91 |
| | | 0.13 | 0.06 | | 0.29 | | | | 69.86 | 20.36 | 90.67 |
| | | 0.07 | 0.02 | | 0.26 | 0.01 | | | 70.22 | 20.37 | 90.93 |
| | | 0.07 | 0.01 | 0.01 | 0.27 | 0.02 | | | 70.33 | 20.40 | 91.10 |
| | | 0.06 | 0.01 | | 0.29 | 0.02 | | | 70.09 | 20.32 | 90.76 |
| | | 0.06 | 0.01 | | 0.23 | 0.02 | | | 70.52 | 20.41 | 91.23 |
| **471m** | | 0.18 | 0.30 | 0.02 | | 0.06 | | | 71.18 | 20.93 | 92.68 |
| | | 0.06 | 0.27 | | | 0.10 | | | 71.64 | 20.92 | 92.99 |
| | | 0.47 | 0.50 | 0.03 | | 0.11 | | | 70.15 | 21.15 | 92.41 |
| | | 0.02 | 0.07 | | | 0.14 | | | 72.03 | 20.78 | 93.03 |
| | | 0.06 | 0.25 | 0.02 | | 0.05 | | | 71.25 | 20.77 | 92.40 |
| | | 0.03 | 0.16 | | | 0.11 | | | 72.10 | 20.91 | 93.31 |
| | | 0.02 | 0.08 | | | 0.11 | | | 72.40 | 20.88 | 93.47 |
| | | 0.18 | 0.08 | 0.01 | | 0.07 | | | 69.67 | 20.24 | 90.25 |
| | | 0.07 | 0.10 | | | 0.12 | | | 71.88 | 20.82 | 92.98 |
| | 0.02 | 0.11 | 0.25 | | | 0.09 | | | 71.53 | 20.92 | 92.92 |
| | 0.02 | 0.04 | 0.25 | 0.02 | | 0.10 | | | 71.65 | 20.89 | 92.95 |
| | | 0.11 | 0.31 | | | 0.12 | | | 71.67 | 21.02 | 93.22 |
| **489m hmt** | | 0.11 | 0.02 | 0.09 | 0.16 | 0.08 | | 0.01 | 69.42 | 20.20 | 90.11 |
| | 0.03 | 0.04 | 0.02 | 0.10 | 0.42 | 0.05 | | | 68.50 | 20.03 | 89.18 |

| | | | | | | | | | | |
|---|---|---|---|---|---|---|---|---|---|---|
| | 0.01 | 0.02 | 0.10 | 1.65 | 0.05 | | 0.01 | 67.77 | 20.63 | 90.26 |
| | 0.09 | 0.02 | 0.10 | 0.18 | 0.13 | | 0.01 | 68.63 | 19.99 | 89.16 |
| | 0.06 | 0.03 | 0.10 | 0.16 | 0.07 | | 0.01 | 68.89 | 20.02 | 89.34 |
| | 0.02 | 0.02 | 0.10 | 0.23 | 0.04 | | 0.02 | 69.58 | 20.20 | 90.21 |
| | 0.03 | 0.03 | 0.10 | 1.35 | 0.07 | | 0.02 | 67.71 | 20.44 | 89.75 |
| | 0.08 | 0.03 | 0.10 | 0.36 | 0.09 | 0.01 | 0.01 | 68.33 | 20.02 | 89.03 |
| | 0.10 | 0.03 | 0.10 | 0.02 | 0.06 | | | 69.22 | 20.05 | 89.60 |
| | 0.12 | 0.05 | 0.10 | 0.04 | 0.04 | | | 68.81 | 19.98 | 89.17 |
| | 0.11 | 0.03 | 0.10 | 0.01 | 0.03 | | 0.01 | 69.71 | 20.17 | 90.17 |
| | 0.11 | 0.02 | 0.10 | 0.06 | 0.05 | | 0.01 | 69.19 | 20.05 | 89.60 |
| | 0.02 | 0.02 | 0.10 | 1.64 | 0.07 | | 0.01 | 67.82 | 20.65 | 90.33 |
| | 0.11 | 0.04 | 0.10 | 0.05 | 0.11 | | 0.02 | 69.06 | 20.06 | 89.56 |
| | 0.05 | 0.02 | 0.10 | 0.47 | 0.09 | | 0.01 | 68.95 | 20.22 | 89.90 |
| | 0.02 | 0.02 | 0.09 | 0.82 | 0.06 | | 0.01 | 68.56 | 20.31 | 89.91 |
| | 0.40 | 0.03 | 0.09 | 0.19 | 0.09 | | 0.02 | 69.01 | 20.37 | 90.19 |
| | 0.01 | 0.03 | 0.12 | 0.03 | 0.03 | | 0.01 | 69.30 | 19.99 | 89.52 |
| | 0.02 | 0.02 | 0.11 | 0.03 | 0.05 | | 0.01 | 69.36 | 20.02 | 89.63 |
| | 0.01 | 0.02 | 0.10 | 0.62 | 0.06 | | 0.01 | 68.66 | 20.20 | 89.68 |
| | 0.03 | 0.02 | 0.11 | 0.02 | 0.02 | | 0.01 | 69.46 | 20.03 | 89.71 |
| | 0.02 | 0.02 | 0.10 | 0.01 | 0.04 | | | 69.46 | 20.01 | 89.65 |
| | 0.05 | 0.02 | 0.10 | 0.31 | 0.05 | | 0.01 | 69.30 | 20.20 | 90.04 |
| | 0.02 | 0.03 | 0.11 | 0.04 | 0.03 | | 0.01 | 69.39 | 20.03 | 89.66 |
| | 0.04 | 0.03 | 0.16 | 0.76 | 0.06 | | 0.01 | 68.27 | 20.24 | 89.58 |
| | 0.02 | 0.03 | 0.15 | 0.38 | 0.05 | | 0.01 | 69.04 | 20.18 | 89.86 |
| | 0.02 | 0.03 | 0.14 | 0.02 | 0.05 | | 0.01 | 69.59 | 20.09 | 89.96 |
| | 0.02 | 0.02 | 0.12 | 0.06 | 0.05 | | 0.01 | 69.23 | 20.00 | 89.52 |
| | 0.02 | 0.02 | 0.10 | 0.04 | 0.06 | | 0.02 | 69.50 | 20.05 | 89.80 |
| | 0.02 | 0.02 | 0.10 | 0.04 | 0.05 | | 0.01 | 69.28 | 19.99 | 89.51 |
| | 0.03 | 0.02 | 0.09 | 0.19 | 0.05 | | 0.01 | 68.74 | 19.93 | 89.05 |
| | 0.03 | 0.02 | 0.10 | 0.14 | 0.05 | | 0.01 | 69.37 | 20.09 | 89.81 |
| | 0.02 | 0.02 | 0.10 | 0.18 | 0.05 | | 0.02 | 69.32 | 20.10 | 89.82 |
| | 0.03 | 0.03 | 0.10 | | 0.05 | | 0.02 | 69.37 | 20.00 | 89.59 |

| | | | | | | | | | | | |
|---|---|---|---|---|---|---|---|---|---|---|---|
| | | 0.08 | 0.02 | 0.11 | 0.10 | 0.05 | | 0.02 | 69.14 | 20.05 | 89.57 |
| | | 0.02 | 0.02 | 0.10 | 0.05 | 0.05 | | 0.02 | 69.42 | 20.03 | 89.70 |
| | | 0.06 | 0.02 | 0.10 | 0.21 | 0.09 | | 0.01 | 69.49 | 20.22 | 90.22 |
| | | 0.01 | 0.02 | 0.19 | 0.01 | 0.03 | | 0.01 | 69.54 | 20.06 | 89.88 |
| | | 0.01 | 0.02 | 0.18 | 0.92 | 0.06 | | 0.01 | 68.39 | 20.36 | 89.97 |
| | | 0.02 | 0.02 | 0.15 | 0.02 | 0.05 | | 0.01 | 69.19 | 19.97 | 89.45 |
| | | 0.31 | 0.10 | 0.10 | 0.28 | 0.14 | | 0.01 | 68.67 | 20.37 | 89.99 |
| | 1.26 | 0.37 | 0.97 | 0.12 | 0.11 | 0.11 | | 0.01 | 67.38 | 21.74 | 92.06 |
| | | 0.20 | 0.08 | 0.12 | 1.44 | 0.24 | 0.01 | 0.02 | 67.29 | 20.69 | 90.08 |
| | | 0.02 | 0.02 | 0.10 | 0.60 | 0.07 | | 0.01 | 68.63 | 20.19 | 89.66 |
| | | 0.14 | 0.20 | 0.09 | 0.59 | 0.09 | | 0.02 | 68.25 | 20.38 | 89.77 |
| | | 0.13 | 0.03 | 0.10 | 3.02 | 0.08 | | 0.02 | 65.75 | 21.09 | 90.24 |
| | | 0.32 | 0.09 | 0.10 | 0.72 | 0.09 | | 0.02 | 67.81 | 20.38 | 89.53 |
| | | 0.50 | 0.04 | 0.09 | 0.14 | 0.05 | | 0.01 | 68.89 | 20.38 | 90.11 |
| | | 0.21 | 0.03 | 0.11 | 0.24 | 0.12 | | 0.02 | 68.99 | 20.26 | 89.97 |
| | | 0.43 | 0.08 | 0.10 | 0.30 | 0.08 | | 0.02 | 68.46 | 20.37 | 89.84 |
| **492m hmt** | | 0.28 | 0.01 | | 0.16 | 0.04 | | | 69.14 | 20.19 | 89.81 |
| | | 0.19 | 0.03 | | 0.50 | 0.04 | | | 68.59 | 20.20 | 89.53 |
| | | 0.02 | 0.01 | | 0.20 | 0.04 | | | 69.83 | 20.19 | 90.29 |
| | | 0.03 | 0.01 | | 0.04 | 0.02 | | | 69.96 | 20.11 | 90.15 |
| | | 0.16 | 0.01 | | 0.15 | 0.02 | | | 69.68 | 20.23 | 90.25 |
| | | 0.03 | | 0.01 | 0.07 | 0.05 | | | 69.93 | 20.14 | 90.23 |
| | | 0.03 | 0.02 | 0.01 | 0.03 | 0.02 | | | 69.78 | 20.07 | 89.95 |
| | | 0.06 | 0.01 | | 0.37 | 0.04 | | | 69.54 | 20.26 | 90.29 |

**Table A.4:** Oxygen isotope values for Mantoverde and additional data and locations of magnetite samples from previous studies.

| Location | Sample | $\delta^{18}O$ (‰) | $O_2$ yield (µmol/gram) |
|---|---|---|---|
| **Mantoverde** | 262m mt* | 1.57 | 8.5 |
| | 276m mt* | 0.69 | 7.9 |
| | 284m mt | 4.01 | 6.8 |
| | 291m mt | 4.58 | 10.4 |
| | 298m mt | 2.34 | 8.5 |
| | 305m mt* | 3.62 | 8.6 |
| | 314m mt* | 2.50 | 8.9 |
| | 340m mt* | 4.61 | 6.0 |
| | 411m mt* | 3.02 | 4.9 |
| | 276m hmt | -1.16 | 8.0 |
| | 314m hmt | -0.67 | 8.6 |
| | 449m hmt* | -1.36 | 5.8 |
| | 455m hmt* | -0.96 | 9.2 |
| | 489m hmt* | -0.84 | 9.1 |
| | 492m hmt | 5.57 | 9.3 |
| | Benavides et al., 2007 | 1.4 | |
| | Benavides et al., 2007 | 1.4 | |
| | Benavides et al., 2007 | 3.4 | |
| | Benavides et al., 2007 | 3.1 | |
| | Benavides et al., 2007 | 2.5 | |
| | Benavides et al., 2007 | 4.1 | |
| | Benavides et al., 2007 | 2.2 | |
| | Benavides et al., 2007 | 3.5 | |
| | Benavides et al., 2007 | 2.5 | |
| | Benavides et al., 2007 | 3.1 | |
| | Benavides et al., 2007 | 1.7 (hmt) | |
| | Benavides et al., 2007 | -1.7 (hmt) | |
| | Benavides et al., 2007 | 1.0 (hmt) | |
| | Benavides et al., 2007 | -1.7 (hmt) | |
| | Benavides et al., 2007 | -1.9 (hmt) | |
| | Benavides et al., 2007 | -1.0 (hmt) | |
| | Benavides et al., 2007 | -1.0 (hmt) | |
| | Benavides et al., 2007 | 0.5 (hmt) | |
| | Benavides et al., 2007 | 0.0 (hmt) | |
| | Benavides et al., 2007 | -1.9 (hmt) | |
| **Mt Isa, Australia** | Marshall & Oliver, 2006 | 3.4 | |
| | Marshall & Oliver, 2006 | 6.9 | |
| | Marshall & Oliver, 2006 | 5.4 | |

| | | |
|---|---|---|
| | Marshall & Oliver, 2006 | 5.3 |
| | Marshall & Oliver, 2006 | 4.1 |
| | Marshall & Oliver, 2006 | 4.9 |
| | Marshall & Oliver, 2006 | 10 |
| | Marshall & Oliver, 2006 | 0.7 |
| | Marshall & Oliver, 2006 | 3.7 |
| | Marshall & Oliver, 2006 | 3.4 |
| | Marshall & Oliver, 2006 | 0.6 (hmt) |
| | Marshall & Oliver, 2006 | -0.1 (hmt) |
| | Marshall & Oliver, 2006 | -0.6 (hmt) |
| | Marshall & Oliver, 2006 | 1.1 (hmt) |
| | Marshall & Oliver, 2006 | -5.3 (hmt) |
| **Pea Ridge, USA** | Childress et al., 2016 | 2.12 |
| | Childress et al., 2016 | 4.50 |
| | Childress et al., 2016 | 4.87 |
| | Childress et al., 2016 | 5.10 |
| | Childress et al., 2016 | 1.24 |
| | Childress et al., 2016 | 5.11 |
| | Childress et al., 2016 | 5.90 |
| | Childress et al., 2016 | 7.03 |
| | Childress et al., 2016 | 5.04 |
| | Childress et al., 2016 | 4.56 |
| | Childress et al., 2016 | 3.18 |
| | Childress et al., 2016 | 1.02 |
| | Childress et al., 2016 | 5.50 |
| **Pilot Knob, USA** | Childress et al., 2016 | 3.26 |
| | Childress et al., 2016 | 6.68 |
| | Childress et al., 2016 | 6.21 |
| **Chilean Iron Belt** | | |
| **Carmen** | Childress et al., 2016 | 3.3 |
| | Nyström et al., 2008 | 2.4 |
| | Nyström et al., 2008 | 2.6 |
| | Nyström et al., 2008 | 0.9 |
| **El Dorado** | Nyström et al., 2008 | 3 |
| **Romeral** | Nyström et al., 2008 | 1.6 |
| | Nyström et al., 2008 | 0.8 |
| | Nyström et al., 2008 | 1.3 |
| | Nyström et al., 2008 | 1.7 |
| | Nyström et al., 2008 | -1.3 |

| | | |
|---|---|---|
| | Nyström et al., 2008 | 0.4 |
| | Nyström et al., 2008 | 2 |
| | Nyström et al., 2008 | 0.3 |
| **Algarrobo** | Nyström et al., 2008 | 1.9 |
| | Nyström et al., 2008 | 2.3 |
| | Nyström et al., 2008 | 2.5 |
| | Nyström et al., 2008 | 0.6 |
| **El Tofo** | Nyström et al., 2008 | 4.5 |
| **Cerro Iman** | Nyström et al., 2008 | 1.7 |
| | Nyström et al., 2008 | 1.6 |
| **Los Colorados** | Bilenker et al., 2016 | 2.41 |
| | Bilenker et al., 2016 | 3.04 |
| | Bilenker et al., 2016 | 2.75 |
| | Bilenker et al., 2016 | 3.17 |
| | Bilenker et al., 2016 | 2.36 |
| | Bilenker et al., 2016 | 2.04 |
| | Bilenker et al., 2016 | 2.76 |
| | Bilenker et al., 2016 | 2.99 |
| | Bilenker et al., 2016 | 2.78 |
| | Bilenker et al., 2016 | 2.48 |
| | Bilenker et al., 2016 | 1.92 |
| | Bilenker et al., 2016 | 2.62 |
| | Bilenker et al., 2016 | 2.43 |
| **Mariela Ignacia** | Bilenker et al., 2016 | 1.50 |
| **El Laco, Chile** | Nyström et al. 2008 | 3.2 |
| | Nyström et al. 2008 | 4.2 |
| | Nyström et al. 2008 | 2.7 |
| | Nyström et al. 2008 | 3.4 |
| | Nyström et al. 2008 | 3.4 |
| | Nyström et al. 2008 | 2.3 |
| | Nyström et al. 2008 | 3.7 |
| | Nyström et al. 2008 | 3 |
| | Nyström et al. 2008 | 3.1 |
| | Nyström et al. 2008 | 3.5 |
| | Nyström et al. 2008 | 2.3 |
| | Nyström et al. 2008 | 2.6 |
| | Nyström et al. 2008 | 2.4 |
| | Nyström et al. 2008 | 2.4 |

| | | |
|---|---|---|
| | Bilenker et al., 2016 | 4.00 |
| | Bilenker et al., 2016 | 4.34 |
| **Kiruna, Sweden** | Nyström et al., 2008 | 2.2 |
| | Nyström et al., 2008 | 1.7 |
| | Nyström et al., 2008 | 1.1 |
| | Nyström et al., 2008 | 1.8 |
| | Nyström et al., 2008 | 0.9 |
| | Nyström et al., 2008 | 2.1 |
| | Nyström et al., 2008 | 0.7 |
| | Nyström et al., 2008 | 1.3 |
| | Nyström et al., 2008 | 1.1 |
| | Nyström et al., 2008 | -0.2 |
| | Nyström et al., 2008 | -0.7 |
| | Nyström et al., 2008 | 1 |
| | Nyström et al., 2008 | 1.1 |
| | Nyström et al., 2008 | 0.3 |
| | Nyström et al., 2008 | 1.2 |
| **Grängesberg, Sweden** | | |
| | Jonnson et al., 2014 | 1.9 |
| | Jonnson et al., 2014 | 2.2 |
| | Jonnson et al., 2014 | 2.8 |
| | Jonnson et al., 2014 | 1.2 |
| | Jonnson et al., 2014 | 1.1 |
| | Jonnson et al., 2014 | 1 |
| | Jonnson et al., 2014 | 1.2 |
| | Jonnson et al., 2014 | 1.8 |
| | Jonnson et al., 2014 | 1.4 |
| | Jonnson et al., 2014 | 3.7 |
| | Jonnson et al., 2014 | -0.4 |
| | Jonnson et al., 2014 | 1.3 |
| | Jonnson et al., 2014 | 1.2 |
| | Jonnson et al., 2014 | 3 |
| | Jonnson et al., 2014 | 1.8 |
| | Jonnson et al., 2014 | 1.9 |
| | Jonnson et al., 2014 | 0.9 |
| | Jonnson et al., 2014 | 0.2 |
| | Jonnson et al., 2014 | 1.1 |
| | Jonnson et al., 2014 | 1.5 |
| | Jonnson et al., 2014 | 2.8 |
| | Jonnson et al., 2014 | 1.7 |
| | Jonnson et al., 2014 | 3.4 |
| | Jonnson et al., 2014 | 1.8 |

| | |
|---|---|
| Jonnson et al., 2014 | 1.5 |
| Weis, 2013 | 1.2 |
| Weis, 2013 | 1.8 |
| Weis, 2013 | 0.9 |
| Weis, 2013 | 2.8 |
| Weis, 2013 | 1.2 |
| Weis, 2013 | 1.1 |
| Weis, 2013 | 1.0 |
| Weis, 2013 | 1.2 |
| Weis, 2013 | 1.8 |
| Weis, 2013 | 0.5 |
| Weis, 2013 | 8.7 |
| Weis, 2013 | 0.2 |
| Weis, 2013 | 7.6 |
| Weis, 2013 | 1.8 |
| Weis, 2013 | 1.5 |
| Weis, 2013 | 7.9 |
| Weis, 2013 | 0.1 |
| Weis, 2013 | -0.8 |
| Weis, 2013 | -1.0 |
| Weis, 2013 | -1.1 |

Samples taken for this study are from drill core DDH-14-DS91, located at 368875m E 7063667m N and approximately 1008m (AMSL) elevation core is oriented west at an unknown angle. Asterisks indicate samples analyzed for both O and Fe isotopes. Full references of works cited here are located in the reference section of the main text.

**Table A.5:** Iron isotope values for magnetite and hematite from Mantoverde and additional data and locations of magnetite samples from previous studies.

| Location | Sample | $\delta^{56}Fe$ (‰) | 2σ | Source |
|---|---|---|---|---|
| **Mantoverde, Chile** | 262m mt* | 0.54 | 0.05 | This study |
| | 276m mt* | 0.55 | 0.02 | This study |
| | 298m mt* | 0.61 | 0.04 | This study |
| | 305m mt* | 0.50 | 0.04 | This study |
| | 314m mt* | 0.58 | 0.01 | This study |
| | 331m mt | 0.37 | 0.06 | This study |
| | 340m mt* | 0.46 | 0.04 | This study |
| | 411m mt* | 0.53 | 0.04 | This study |
| | 438m mt | 0.55 | 0.06 | This study |
| | 471m mt | 0.38 | 0.02 | This study |
| | 449m hmt* | 0.34 | 0.10 | This study |
| | 455m hmt* | 0.42 | 0.09 | This study |
| | 489m hmt* | 0.46 | 0.06 | This study |
| **Pea Ridge, USA** | PR-18 | 0.35 | 0.05 | Childress et al. 2016 |
| | PR-37 | 0.07 | 0.05 | Childress et al. 2016 |
| | PR-64A | 0.20 | 0.05 | Childress et al. 2016 |
| | PR-77A | 0.22 | 0.02 | Childress et al. 2016 |
| | PR-82A | 0.10 | 0.02 | Childress et al. 2016 |
| | PR-82B | 0.03 | 0.02 | Childress et al. 2016 |
| | | 0.07 | 0.05 | Childress et al. 2016 |
| | PR-144 | 0.26 | 0.09 | Childress et al. 2016 |
| | | 0.10 | 0.02 | Childress et al. 2016 |
| | PR-158 | 0.26 | 0.08 | Childress et al. 2016 |
| **Pilot Knob, USA** | PK-1086-918 | 0.14 | 0.05 | Childress et al. 2016 |
| | PK-1098-715 | 0.18 | 0.03 | Childress et al. 2016 |
| | PK-1145-965.8 | 0.19 | 0.04 | Childress et al. 2016 |
| | PK-1145-979.5 | 0.14 | 0.10 | Childress et al. 2016 |
| | PK-1174-1348 | 0.06 | 0.05 | Childress et al. 2016 |
| | PK-2079-1160 | 0.27 | 0.06 | Childress et al. 2016 |
| **Mineville, NY** | | -0.92 | 0.03 | Bilenker et al., 2016 |
| **Chilean Iron Belt** | | | | |
| Los Colorados | | | | |
| Core LC-05 | | 0.22 | 0.03 | Bilenker et al., 2016 |

| | | | | |
|---|---|---|---|---|
| Core LC-05 | 05-20.7 | 0.09 | 0.06 | Bilenker et al., 2016 |
| Core LC-05 | 05-32 | 0.22 | 0.03 | Bilenker et al., 2016 |
| Core LC-05 | 05-52.2 | 0.14 | 0.08 | Bilenker et al., 2016 |
| Core LC-05 | 05-72.9 | 0.13 | 0.05 | Bilenker et al., 2016 |
| | 05-82.6 | 0.08 | 0.03 | Bilenker et al., 2016 |
| | 05-90 | 0.21 | 0.07 | Bilenker et al., 2016 |
| | 05-106 | 0.12 | 0.03 | Bilenker et al., 2016 |
| | 05-126.15 | 0.10 | 0.06 | Bilenker et al., 2016 |
| | 05-129.3a | 0.22 | 0.05 | Bilenker et al., 2016 |
| | 05-129.3b | 0.14 | 0.02 | Bilenker et al., 2016 |
| Core LC-04 | 04-38.8 | 0.18 | 0.03 | Bilenker et al., 2016 |
| | 04-66.7 | 0.18 | 0.07 | Bilenker et al., 2016 |
| | 04-104.4 | 0.24 | 0.08 | Bilenker et al., 2016 |
| | 04-129.3 | 0.22 | 0.03 | Bilenker et al., 2016 |
| LC East Dike | pitE1 | 0.18 | 0.03 | |
| | | | | |
| El Laco | LCO-39 | 0.39 | 0.09 | Bilenker et al., 2016 |
| | LCO | 0.29 | 0.03 | Bilenker et al., 2016 |
| | LCO vein | 0.30 | 0.03 | Bilenker et al., 2016 |
| | LCO-76 | 0.32 | 0.09 | Bilenker et al., 2016 |
| | LCO-78 | 0.53 | 0.03 | Bilenker et al., 2016 |
| | LCO-104 | 0.27 | 0.03 | Bilenker et al., 2016 |
| | LCO-111 | 0.20 | 0.03 | Bilenker et al., 2016 |
| | EJ-LS-11-1 | 0.28 | 0.04 | Weis, 2013 |
| | EJ-LS-11-2 | 0.24 | 0.03 | Weis, 2013 |
| | EJ-LS-11-3 | 0.36 | 0.03 | Weis, 2013 |
| | EJ-LS-11-4 | 0.34 | 0.03 | Weis, 2013 |
| | LS-2 | 0.27 | 0.04 | Weis, 2013 |
| | LS-52 | 0.28 | 0.03 | Weis, 2013 |
| | | | | |
| Mariela Ignacia | M-8 | 0.13 | 0.03 | Bilenker et al., 2016 |
| | | | | |
| Dannemora | DM-1 | -0.36 | 0.03 | Weis, 2013 |
| | DM-2 | 0.01 | 0.03 | Weis, 2013 |
| | DM-3 | -0.43 | 0.03 | Weis, 2013 |
| | DM-4 | -0.35 | 0.03 | Weis, 2013 |
| | | | | |
| Grangensberg Mining District | | 0.40 | 0.03 | Weis, 2013 |
| | | 0.24 | 0.03 | Weis, 2013 |
| | | 0.33 | 0.03 | Weis, 2013 |
| DC 690 | | 0.31 | 0.03 | Weis, 2013 |
| | | 0.31 | 0.04 | Weis, 2013 |

| | | | | |
|---|---|---|---|---|
| | | 0.30 | 0.04 | Weis, 2013 |
| | | 0.26 | 0.04 | Weis, 2013 |
| | | 0.29 | 0.03 | Weis, 2013 |
| | | 0.39 | 0.04 | Weis, 2013 |
| | | 0.27 | 0.04 | Weis, 2013 |
| DC 575 | | 1.00 | 0.03 | Weis, 2013 |
| | | 0.31 | 0.03 | Weis, 2013 |
| | | 0.27 | 0.04 | Weis, 2013 |
| Additional | waste pile | 0.33 | 0.03 | Weis, 2013 |
| | waste pile | -0.02 | 0.03 | Weis, 2013 |
| | disseminated mgt | 0.24 | 0.03 | Weis, 2013 |
| | mgt vein | 0.11 | 0.03 | Weis, 2013 |
| Striberg | BIF | -0.57 | 0.03 | Weis, 2013 |
| | | | | |
| Volcanic Reference | | | | |
| Basalt | Basalt bomb | 0.46 | 0.03 | Weis, 2013 |
| Ankaramite | TEF-NER-57 | 0.16 | 0.02 | Weis, 2013 |
| Ankaramite | TEF-NER-70 | 0.10 | 0.02 | Weis, 2013 |
| Ankaramite | TEF-NER-18 | 0.07 | 0.05 | Weis, 2013 |
| Dacite | MG-07 | 0.32 | 0.03 | Weis, 2013 |
| Dacite | MG-09 | 0.29 | 0.03 | Weis, 2013 |
| Basaltic andesite | M-BA06-KA-3 | 0.17 | 0.03 | Weis, 2013 |
| Basaltic andesite | Kelut | 0.10 | 0.04 | Weis, 2013 |
| Basaltic andesite | | 0.12 | 0.03 | Weis, 2013 |
| Basaltic andesite | | 0.06 | 0.03 | Weis, 2013 |
| Basaltic andesite | | 0.16 | 0.03 | Weis, 2013 |
| Basaltic andesite | | 0.18 | 0.05 | Weis, 2013 |
| Dolerite | 83/CRS/6 | 0.34 | 0.03 | Weis, 2013 |

Samples taken for this study are from drill core DDH-14-DS91, located at 368875m E 7063667m N and approximately 1008m (AMSL) elevation core is oriented west at an unknown angle. Asterisks indicate samples analyzed for both O and Fe isotopes. Full references of works cited here are located in the reference section of the main text.